

Defect engineering on inorganic oxides for Lithium-ion batteries

Zhong SU

B. Eng., M. Eng.

School of Environment and Science
Gold Coast Campus, Griffith University

Submitted in fulfilment of the requirements of the
degree of Doctor of Philosophy



April 2021

ABSTRACT

Inorganic oxides have received wide attention as a new type of functional energy storage material, but their application prospects are usually limited due to their intrinsic properties, such as poor conductivity, limited active sites, and unstable crystal structure. Defect engineering is able to fine tune the concentration, mobility, and spatial distribution of carriers and electrons within crystalline structures, and these changed features radically optimize the electronic structure and physicochemical properties of the oxides. These optimized properties of oxides help to solve the kinetic problems of ion diffusion during the charge-storage process. However, defect engineering in oxides still faces the restriction of bottlenecks, which includes but is not limited to, defect preparation, defect preservation, and defect concentration adjustment. Defect preparation refers to the complicated process and harsh conditions required in the process of defect formation; these unstable defects will gradually recover or be refilled if the oxide is exposed to air or water leading to the disappearance of optimized properties; Controllable defect concentration is a further requirement for orderly regulation of oxide intrinsic properties in the development of defect engineering.

In the first study, vacancy concentration varies with temperature exponentially according to the formation mechanism of defects. But these vacancies will gradually recover or be refilled in the slow cooling process. Based on this, commercial spinel-type lithium titanium oxide (LTO) was selected and quenched in this work, and we found the rapid cooling could interrupt the recovery of defects and preserve the defect state at high temperatures in the crystal lattice. More importantly, these preserved defects (oxygen vacancies and Li/Ti redistributions) can allow for an extraordinary capacity of 201.7 mAh g⁻¹ beyond the theoretical value of pristine bulk LTO (175 mAh g⁻¹) at a rate of 1 C with the voltage range of 1.0-2.5 V. This work establishes a new mechanism for Li⁺ charge storage and opens up a new avenue for the control of oxygen vacancy

and Li/Ti redistribution in electrode materials for the enhancement of electrochemical performance of LTO anode materials.

Traditional defect introduction involves high-temperature calcination, vacuum or inert environments and expensive reducing agents, which are not cost-effective and have great energy consumption. Hence, we proposed a universal defect preparation strategy via a simple redox reaction at room temperature. N-Butyl lithium, a powerful nucleophile and reducing agent, was selected in this work and easily realized defect engineering construction in oxide lattices by a simple soaking method. More importantly, such a simple defect preparation method is suitable for common oxides but not limited to LTO, TiO_2 , SnO_2 , CeO_2 , Sb_2O_5 , and Nb_2O_5 . Also, the controllable defect concentration was achieved by adjusting the reaction time. Here, the defective LTO was selected to further study its electrochemical lithium storage at low temperatures. A highly reversible discharge specific capacity of 109.9 mAh g^{-1} can be obtained at a rate of 10 C in a severe environment of $-10 \text{ }^\circ\text{C}$ after 200 cycles, which is significantly better than the pristine LTO. Such a simple, efficient, and universal defect method is a breakthrough innovation in terms of the current status of defect engineering.

Compared with silicon anodes, silicon oxide (SiO_2) possesses relatively smaller volume expansion. In addition, the O atoms in silicon oxides can generate an inert buffer matrix phase (Li_2O and Li_4SiO_4) around the silicon particles, which can further effectively alleviate the stress caused by volume expansion. However, crystalline SiO_2 cannot be used for Li^+ insertion and is excluded as a promising anode for Li-ion batteries due to inherently poor conductivity. Hence, we extract crystalline SiO_2 from natural precursors (montmorillonite and sand) and introduce defects into crystalline SiO_2 via quenching and carbon-reduction strategies. Such a simple process enables defective SiO_2 to possess a higher electrochemical activity for Li^+ reversible deintercalation. The defective SiO_2 from montmorillonite delivers a high initial capacity of

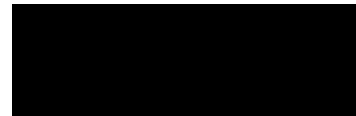
2774.3 mAh g⁻¹ at 100 mA g⁻¹ and an excellent cycle stability (734.8 mAh g⁻¹ at 500 mA g⁻¹ after 200 cycles), while the defective SiO₂ from sand also shows a highly reversible capacity of 558.1 mAh g⁻¹ at 500 mA g⁻¹ after 500 cycles with superior cycling stability. To the best of our knowledge, this work is the first to demonstrate such outstanding lithium storage performance in crystalline SiO₂ anodes. More importantly, the wide availability of SiO₂ in the natural environment indicates considerable potential for commercial applications.

In summary, several techniques developed for defect engineering on inorganic oxide materials are explored to enhance the electrochemical performance of LIBs through optimizing the intrinsic properties of oxides. The simple operation, low cost, moderate condition, abundant resources, and excellent lithium storage performance in the series of defective oxides presented in this thesis provide a wide range of application prospects.

STATEMENT

This work has not previously been submitted for a degree or diploma in any university. To the best of my knowledge and belief, the thesis contains no material previously published or written by another person except where due references is made in the thesis itself.

Signature of Candidate

A solid black rectangular box used to redact the candidate's signature.

(Date) 15/April/2021

TABLE OF CONTENTS

ABSTRACT.....	iii
STATEMENT	vi
TABLE OF CONTENTS	viii
ACKNOWLEDGEMENTS	x
ACRONYMS	xii
PUBLICATIONS	xiv
CHAPTER 1.....	1
1.1. SIGNIFICANCE OF THE PROJECT	2
1.2. RESEARCH OBJECTIVES	3
1.3. THESIS OUTLINE.....	3
1.4. REFERENCES	5
CHAPTER 2 DEFECT ENGINEERING IN TITANIUM-BASED OXIDES FOR ELECTROCHEMICAL ENERGY STORAGE DEVICES	6
2.1. INTRODUCTORY REMARKS.....	7
2.2. STATEMENT OF CONTRIBUTION.....	8
2.3 ARTICLE 1.....	9
CHAPTER 3 OUTPERFORMING CAPACITY LIMIT OF LITHIUM TITANATE ANODE VIA QUENCHING-INDUCED OXYGEN VACANCIES AND CATION REDISTRIBUTION	68
3.1. INTRODUCTORY REMARKS	69

3.2	STATEMENT OF CONTRIBUTION	70
3.3	ARTICLE 2	71
CHAPTER 4 TUNING DEFECTS IN METAL OXIDES VIA REDOX REACTION		
FOR LITHIUM ION BATTERY		121
4.1.	INTRODUCTORY REMARKS	122
4.2	STATEMENT OF CONTRIBUTION	123
4.3.	ARTICLE 3.....	124
CHAPTER 5 ENGINEERING DEFECTS INTO NATURAL SiO₂ FOR		
SUSTAINABLE LITHIUM STORAGE		161
5.1	INTRODUCTORY REMARKS	162
5.2	STATEMENT OF CONTRIBUTION	163
5.3	ARTICLE 4.....	164
CHAPTER 6 CONCLUSIONS AND FUTURE WORK		204
6.1.	GENERAL CONCLUSIONS	205
6.2.	FUTURE WORKS.....	207

ACKNOWLEDGEMENTS

The writing and completion of this thesis would be impossible without the help and support of many special people during my Ph.D.

Firstly, I would like to extend my heartfelt gratitude and highest respect to my supervisor, Prof. Shanqing Zhang for allowing me to join his research group here in Australia. His broad academic ideas, rigorous research attitude, and approachable personality have benefitted me immensely academically and personally. Under his guidance and help, I gradually adapted to life in Australia and achieved my PhD research goals. His ingenious academic insights and suggestions constantly inspire me and promote the solution of academic problems. My outstanding academic achievements would not have been realized without his help and support. I would also like to express my sincere thanks to my associate supervisor Prof. Huijun Zhao and external supervisor Prof. Chao Lai for their effective and patient supervision of my research work. I greatly appreciate their guidance, encouragement, suggestions, and help throughout my entire PhD study.

The realization of my academic achievements would not be possible without the team collaboration from the computational group of Prof. Feng Pan at Peking University and the advanced synchrotron radiation technology group of Prof. Jun Lu at Argonne National Laboratory. Under the help of Prof. Feng Pan and Prof. Jun Lu, the plagued academic bottleneck was finally broken, and the chemical mechanism was presented. I also appreciate other members of these two groups, Dr. Lu Ma, Dr. Tao Zhang, and Dr. Shunning Li. Their helpful discussions and suggestions helped solve academic problems and made my academic life full of fun.

My sincere thanks for the help from my group members, especially Mr. Meng Li, and Mr. Shangshu Qian. The Density Functional Theory calculations from Mr. Meng Li's theoretical simulation helped me understand the mechanism of electrochemical energy storage; Drawing of the cover image from Mr. Shangshu Qian increased the characteristics of the article and helped attract more readers' attention. I also show my gratitude to other team members: Mr. Han Yeu Ling, Mr. Luke Hencz, Mr. Hao Chen, Mr. Oluwatobi David Adekoya, Ms. Yuxuan Zhu, Mr. Meng Zu, Mr. Yuhui Tian, Ms. ZhenZhen Wu, Ms. Mengting Zheng, Ms. Yubai Zhang and Ms. Ding Yuan. The caring in life and academic mutual assistance made us as warm as a family.

I also express many thanks to the CCEE members and all ENV, CCEE, EFRI staff and students for their help and suggestions, especially Dr. Sean Lowe, Dr. Lei Zhang, Dr. Yuhai Dou, Dr. Mohammad Al-Mamun, Dr. Yun Wang and Dr. Robert Liu. I also want to show my sincere gratitude to the secretaries in CCEE and ESC, Ms. Christina Perry and Ms. Michelle Ryan, respectively, for their help during my whole PhD. I am grateful for the financial support of Griffith University through a Griffith University Postgraduate Research Scholarship (GUPRS) and Griffith University International Postgraduate Research Scholarship (GU-IPRS).

Finally, I want to express my deepest appreciation to my family including my parents and my brother for their meticulous care, support, and encouragement during my PhD study and over the years.

ACRONYMS

BET	Brunauer Emmett Teller
CeO ₂	Cerium dioxide
CE	Coulombic efficiency
CV	Cyclic voltammetry
DEC	Diethyl carbonate
DFT	Density functional theory
DLi	Lithium diffusion coefficient
DMC	Dimethyl carbonate
DOS	Density of states
EVs	Electric vehicles
EC	Ethylene carbonate
EDS	Energy dispersive x-ray spectroscopy
EIS	Electrochemical impedance spectroscopy
EV	Electric vehicle
FTIR	Fourier Transform infrared spectroscopy
Hz	Hertz
HRTEM	High resolution transmission electron microscopy
ICE	Initial coulombic efficiency
JCPDS	Joint committee on powder diffraction standards
LIBs	Lithium-ion batteries
LiCoO ₂	Lithium cobalt oxides
LiPF ₆	Lithium hexafluorophosphate
LTO	Lithium titanate

Nb ₂ O ₅	Niobium pentoxide
n-BuLi	N-butyllithium
NMP	N-methyl-pyrrolidone
PTFE	Poly(tetrafluoroethylene)
PVDF	Polyvinylidene fluoride
R_e	Electrolyte resistance
R_{ct}	Charge-transfer resistance
Sb ₂ O ₅	Antimony peroxide
SEI	Solid electrolyte interphase
SEM	Scanning electron microscopy
SiO ₂	Silicon dioxide
SnO ₂	Stannic oxide
TEM	Transmission electron microscopy
TiO ₂	Titanium dioxide
TGA	Thermogravimetric analysis
W_o	Warburg coefficient
XRD	X-ray diffraction spectroscopy
XPS	X-ray photoelectron spectroscopy
XANES	X-ray Absorption Near-Edge Structure

PUBLICATIONS

Acknowledgement of Papers included in this Thesis

Section 9.1 of the Griffith University Code for the Responsible Conduct of Research (“Criteria for Authorship”), in accordance with Section 5 of the Australian Code for the Responsible Conduct of Research, states:

To be named as an author, a researcher must have made a substantial scholarly contribution to the creative or scholarly work that constitutes the research output, and be able to take public responsibility for at least that part of the work they contributed. Attribution of authorship depends to some extent on the discipline and publisher policies, but in all cases, authorship must be based on substantial contributions in a combination of one or more of:

- Conception and design of the research project
- Analysis and interpretation of research data
- Drafting or making significant parts of the creative or scholarly work or critically revising it so as to contribute significantly to the final output.

Section 9.3 of the Griffith University Code (“Responsibilities of Researchers”), in accordance with Section 5 of the Australian Code, states:

Researchers are expected to:

- Offer authorship to all people, including research trainees, who meet the criteria for authorship listed above, but only those people.
- Accept or decline offers of authorship promptly in writing.
- Include in the list of authors only those who have accepted authorship
- Appoint one author to be the executive author to record authorship and manage correspondence about the work with the publisher and other interested parties.
- Acknowledge all those who have contributed to the research, facilities, or materials but who do not qualify as authors, such as research assistants, technical staff, and advisors on cultural or community knowledge. Obtain written consent to name individuals.

Chapter Publications

This thesis consists of four published and unpublished papers from Chapters 2, 3, 4, and 5. My contribution to each co-authored paper is outlined at the front of the relevant chapter.

(Note IF: Impact factor 2020)

Chapter 2:

Su Z., Liu H., Li M., Zhu Y., Qian S., Weng M., Zheng J., Zhong Y., Pan P., Zhang S., Defects Engineering of Titanium-based Oxides for Electrochemical Energy Storage Devices. *Electrochemical Energy Reviews*, 2020, 3(2):286-343. (IF: 27.31)

Chapter 3:

Su Z., Li, M., Li S., Ma L., Qian, S., Zhang T., Dong C., Lu J., Pan F., Zhang S., Outperforming theoretical capacity limit of lithium titanate anode via quenching-induced oxygen vacancies and cation redistribution. To be submitted to *Nature Energy*, (IF: 46.5)

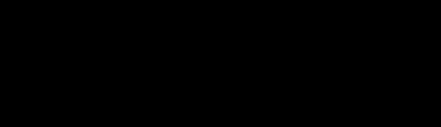
Chapter 4:

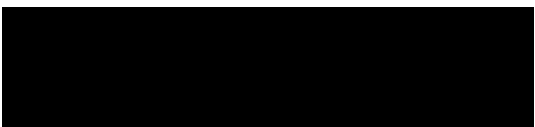
Su Z., Li, M., Qian, S., Ma L., Zhang T., Lai C., Lu J., Zhang S. Tuning defects in metal oxides via redox reaction for lithium ion battery. To be submitted to *Nature Communications*, (IF: 12.21)

Chapter 5:

Su Z., Li, M., Qian, S., Lai C., Lu J., Zhang S. Engineering defects into natural SiO₂ for sustainable Lithium storage. To be submitted to *Nature Sustainability*.

Appropriate acknowledgements of those who contributed to the research but did not qualify as authors are included in each paper.

— 
Zhong Su



Supervisor: Prof. Shanqing Zhang

Additional Relevant Publications

In addition to the published works that formed the research chapters of this thesis, a series of other co-authored publications were relevant, but did not form part of the thesis itself.

1. Zhang S.; **Su Z.** Australian Patent No 2019903786 (Approved and Authorized).
2. Zhang S.; **Su Z.** International patent No PCT AU2020 051080 (Approved).
3. **Su Z.**, Wei Z., Lai C., Deng H., Liu Z., Ma J., Robust pseudo-capacitive Li-I₂ battery enabled by catalytic, adsorptive N-doped graphene interlayer. *Energy Storage Materials*, 2018, 14:129-135.
4. **Su Z.**, Ling, H. Y., Li, M., Qian, S., Chen, H., Lai, C., & Zhang, S. Honeycomb-like carbon materials derived from coffee extract via a “salty” thermal treatment for high-performance Li-I₂ batteries. *Carbon Energy*, 2020, 2:265-275.
5. Li M., Tim G., **Su Z.**, Li S., Pan F., Zhang S., Electrochromic properties of Li₄Ti₅O₁₂: From visible to infrared spectrum. *Applied Physics Letters* 2019, 115(7):073902.
6. Chen H., Wu Z., **Su Z.**, Chen S., Yan C., Al-Mamun M., Tang Y., Zhang S. A mechanically robust self-healing binder for silicon anode in lithium ion batteries, *Nano Energy*, 2021, 81:105654.
7. Ling, H. Y., **Su, Z.**, Chen, H., Hencz, L., Zhang, M., Tang, Y., & Zhang, S. Biomass-Derived Poly (Furfuryl Alcohol)-Protected Aluminum Anode for Lithium-Ion Batteries. *Energy Technology*, 2019, 7:800995.
8. Ling, H. Y., Wang, C., **Su, Z.**, Chen, S., Chen, H., Qian, S., Li, D., Yan, C., Kiefel, M., Lai, C., & Zhang, S. Amylopectin from Glutinous Rice as a Sustainable Binder for High-Performance Silicon Anodes. *Energy & Environmental Materials*, 2020, 0:1-6. <https://doi.org/10.1002/eem2.12143>, (New Journal by John Wiley & Sons., Inc.)

CHAPTER 1

INTRODUCTION

1.1. SIGNIFICANCE OF THE PROJECT

Escalating demand for green vehicles such as electric vehicles (EVs) and hybrid electric vehicles (HEVs) has accelerated innovation in Li-ion battery technology^{1, 2}. The current commercial lithium-ion batteries with graphite anodes are far from being able to meet the current equipment needs due to their lower theoretical capacity (372 mAh g⁻¹) and poor cycle stability. Inorganic oxides normally possess a higher energy density, and their phase-transition reaction with smaller volume change enables inorganic oxides to have a fast kinetic process, thereby achieving excellent cycle stability and long cycle life during Li⁺ charge storage^{3, 4}. However, low electrical conductivity, a ubiquitous intrinsic property of inorganic oxides, severely limits their application in electrochemical energy storage. Studies have shown that when certain atoms in the oxides crystal are missing, the formed defects will produce many dangling bonds with unsaturated characteristics^{5, 6}. Such an unsaturated environment easily induces surface electron spins and interactions between electrons, and ultimately promotes the charge transfer and improves physicochemical activity. Among the many types of defects, oxygen as a typical volatile element is relatively easy to be deprived of to form vacancies in inorganic oxides. The formed oxygen vacancies in the crystal lattice of inorganic oxides can effectively change their density of states, induce impurity states in the bandgap, adjust its electronic properties and significantly optimize electronic conductivity^{7, 8}. These improvements in defect-inducing intrinsic properties have enabled inorganic oxides to show a wide range of applications in the field of energy storage and conversion^{9, 10}. Therefore, effective construction of defects and an in-depth understanding of the internal mechanism of defect formation are critical, especially for the improvement of the intrinsic properties of oxides and their influence on kinetic behavior in the energy storage process¹¹

1.2. RESEARCH OBJECTIVES

The central focus of this thesis is to explore the defect formation mechanism and design a series of defective oxides to explore the mechanism of Li-ion charge storage. More specifically, the objectives are:

- To explore a novel defect preparation method via quenching and develop a supersaturated defective LTO from the reversible mechanism of oxygen vacancy formation and recovery.
- To explore the influence of oxygen vacancies on the inherent properties of LTO through DFT calculation, and then study how the oxygen vacancies in the LTO lattice improve the Li⁺ charge storage.
- To prepare a series of defective oxides through a simple redox process at room temperature, adjust the defect concentration of oxides by controlling the reaction time, and conduct low-temperature performance tests with defect LTO as an example.
- To extend the quenching method to the natural SiO₂ dominated precursors (montmorillonite and sand) and design a defective crystalline SiO₂ with electroactivity for reversible Li-ion charge storage.

1.3. THESIS OUTLINE

The initial aim of this project is to explore new strategies to resolve the bottlenecks of current defect development, i.e., defect preparation, defect preservation, and defect concentration adjustment, and to further study the effect of defects on the intrinsic properties of oxides. The next aim is to evaluate the electrochemical performance of the defective oxides in Li-ion batteries. Detailed research objectives for each chapter are shown as follows:

- 1) Describe the significance of this thesis, summarize the research objectives, contributions to the research of defects in inorganic oxides for Li-ion batteries and the structure of the thesis (Chapter 1).
- 2) Provide a detailed review of defect types, defect formation mechanism, defect preparation and electrochemical application of defects in metal oxides (Chapter 2).
- 3) Develop a simple quenching strategy to retain the defects generated by high temperature in bulk LTO oxide, and verify the role of defects in the LTO lattice for surpassing theoretical capacity during Li^+ charge storage (Chapter 3).
- 4) Develop a universal defect preparation strategy where oxygen vacancies can be easily formed in the lattice of inorganic oxides by soaking in n-butyl lithium solution at room temperature. These inorganic oxides include but are not limited to LTO, TiO_2 , CeO_2 , SnO_2 , Sb_2O_5 , and Nb_2O_5 . In addition, defective LTO was selected to further study the role of defects in low-temperature Li^+ charge storage (Chapter 4).
- 5) Develop defective SiO_2 from natural precursors (montmorillonite and sand) via simple quenching and carbon reduction strategies, and verify the effect of defects on activating Li^+ insertion and the carbon layer on inhibiting the volume expansion of SiO_2 electrodes (Chapter 5).
- 6) Summarize and understand the importance of defects in inorganic oxides and continue to promote the development of defective oxides in other fields such as photocatalysis, sewage treatment, and supercapacitors (Chapter 6).

1.4. REFERENCES

1. Janek, J., Zeier, W. G. A solid future for battery development. *Energy* **500**, 300 (2016).
2. Lu, J. *et al.* The role of nanotechnology in the development of battery materials for electric vehicles. *Nature nanotechnology* **11**, 1031 (2016).
3. Wang, L. *et al.* Morphological and Chemical Tuning of High-Energy-Density Metal Oxides for Lithium Ion Battery Electrode Applications. *ACS Energy Lett.* **2**, 1465-1478 (2017).
4. Jiang, J. *et al.* Recent advances in metal oxide-based electrode architecture design for electrochemical energy storage. *Adv. Mater.* **24**, 5166-5180 (2012).
5. Tong, Y. *et al.* The optical properties of ZnO nanoparticles capped with polyvinyl butyral. *Journal of sol-gel science and technology* **30**, 157-161 (2004).
6. Yu, Z. Q. *et al.* Blue photoluminescent properties of pure nanostructured γ -Al₂O₃. *Journal of Materials Research* **16**, 1890-1893 (2001).
7. Pacchioni, G. Oxygen vacancy: the invisible agent on oxide surfaces. *ChemPhysChem* **4**, 1041-1047 (2003).
8. Kalinin, S. V., Spaldin, N. A. Functional ion defects in transition metal oxides. *Science* **341**, 858-859 (2013).
9. Xie, C. *et al.* Insight into the design of defect electrocatalysts: From electronic structure to adsorption energy. *Mater. Today* **31**, 47-68 (2019).
10. Andersson, O. E. *et al.* Structure and electronic properties of graphite nanoparticles. *Phys. Rev. B* **58**, 16387 (1998).
11. Su, Z. *et al.* Defect engineering in titanium-based oxides for electrochemical energy storage devices. *Electrochem. Energy Rev.* **3**, 286-343 (2020).

CHAPTER 2

**DEFECT ENGINEERING IN TITANIUM-BASED OXIDES FOR
ELECTROCHEMICAL ENERGY STORAGE DEVICES**

Electrochemical Energy Reviews, 2020, 3(2):286-343

2.1. INTRODUCTORY REMARKS

As a full literature review of this thesis, this chapter is presented as a published review article in *Electrochemical Energy Reviews*.

Defect engineering affects the concentration, mobility, and spatial distribution of carriers and electrons within crystalline structures in oxides. At present, extensive research has focused on defects to optimize the electronic structure of oxides. This review highlights defect types, defect formation mechanism, the influence of defect on intrinsic properties, defect preparation and applications in electrochemical energy storage, and then summarizes the bottleneck of current defect development and proposes future development prospects for defects in the fields of energy storage, catalysis, and sewage treatment.

2.2. STATEMENT OF CONTRIBUTION

This chapter includes one first-authored paper. The bibliographic details of the co-authored paper, including all authors, are:

Zhong Su, Jiahua Liu, Meng Li, Yuxuan Zhu, Shangshu Qian, Mouyi Weng, Jiaxin Zheng, Yulin Zhong, Feng Pan, Shanqing Zhang*

Defect Engineering in Titanium-based Oxides for Electrochemical Energy Storage Devices.
Electrochemical Energy Reviews, 2020, 3(2):286-343.

My contribution to the paper included:

Collection and organization of information, data and references; Writing and preparation of manuscript.

(Signed) _____ (Date) 15/04/2021

Name of Student: Zhong Su

(Countersigned) _____ (Date) 15/04/2021

Corresponding author of paper: Shanqing Zhang


(Countersigned) _____ (Date) 15/04/2021

Supervisor: Shanqing Zhang

2.3 ARTICLE 1



Defect Engineering in Titanium-Based Oxides for Electrochemical Energy Storage Devices

Zhong Su¹ · Jiahua Liu² · Meng Li¹ · Yuxuan Zhu¹ · Shangshu Qian¹ · Mouyi Weng² · Jiaxin Zheng² · Yulin Zhong¹ · Feng Pan² · Shanqing Zhang¹ 

Received: 6 August 2019 / Revised: 28 September 2019 / Accepted: 20 January 2020
© Shanghai University and Periodicals Agency of Shanghai University 2020

Abstract

Defect engineering involves the manipulation of the type, concentration, mobility or spatial distribution of defects within crystalline structures and can play a pivotal role in transition metal oxides in terms of optimizing electronic structure, conductivity, surface properties and mass ion transport behaviors. And of the various transition metal oxides, titanium-based oxides have been keenly investigated due to their extensive application in electrochemical storage devices in which the atomic-scale modification of titanium-based oxides involving defect engineering has become increasingly sophisticated in recent years through the manipulation of the type, concentration, spatial distribution and mobility of defects. As a result, this review will present recent advancements in defect-engineered titanium-based oxides, including defect formation mechanisms, fabrication strategies, characterization techniques, density functional theory calculations and applications in energy conversion and storage devices. In addition, this review will highlight trends and challenges to guide the future research into more efficient electrochemical storage devices.

Keywords Defect engineering · Ti-based oxides · Optimized intrinsic properties · Electrochemical energy storage

1 Introduction

The increasing prominence of local and global environmental challenges has stimulated growing demand for clean, renewable energy sources [1, 2]. To address this demand, electrochemical energy conversion and storage devices have been recognized as ideal alternatives to traditional fossil fuels because they are environmentally friendly, inexpensive, portable and scalable [3, 4]. And of these devices, lithium-ion batteries [5–7], metal-ion (Na^+ , Mg^{2+} and Al^{3+}) batteries [8, 9] and electrochemical supercapacitors [10, 11]

have all become significant energy storage systems that have been successfully applied in portable devices. However, these systems often suffer from low energy storage efficiency and struggle to meet the demands of high energy-consuming devices such as electric and hybrid electric vehicles. To address these problems, great efforts have been devoted to developing low-cost novel oxide nanomaterials to improve electrochemical energy storage performance metrics such as energy density, power density and cycle life spans. And among various oxides, Ti-based oxides have been extensively studied as multifunctional materials for electrochemical energy storage devices [12, 13] as well as for water splitting, solar cells, hydrogen energy and rechargeable battery/supercapacitor applications due to their natural abundance, lack of toxicity and low costs [14–17].

As an important class of Ti-based oxides, titanium dioxide (TiO_2) has attracted extensive attention as an important semiconductor material after being initially reported by Fujishima et al. [18] for water splitting in which anatase, rutile, brookite and $\text{TiO}_2(\text{B})$ (bronze) all show potential in electrochemical energy storage applications regardless of being in bulk or nanostructured forms [19–26]. In addition, anatase and bronze phases are more electrochemically

Zhong Su and Jiahua Liu have contributed equally to this work.

✉ Feng Pan
panfeng@pkusz.edu.cn

✉ Shanqing Zhang
s.zhang@griffith.edu.au

¹ Centre for Clean Environment and Energy, School of Environment and Science, Griffith University, Gold Coast Campus, Gold Coast, QLD 4222, Australia

² School of Advanced Materials, Peking University Shenzhen Graduate School, Shenzhen 518055, Guangdong, China

active for Li^+ intercalation due to their open crystal structure and low Li^+ diffusion energy barrier. However, TiO_2 also suffers from poor electron and Li^+ conductivity and tends to display large polarization, irreversible capacity loss and poor cyclic stability. Here, researchers suggest that higher specific surface areas, nanoparticle sizes and special nanostructures can alleviate these issues. For example, Li et al. [27] synthesized $\text{TiO}_2(\text{B})$ nanowires with an ultrahigh surface area of $210 \text{ m}^2 \text{ g}^{-1}$ through a facile hydrothermal route and reported that rapid Li^+ insertion/extraction can be achieved if the nanowires were used as anodes in LIBs in which high BET surface areas can provide larger reaction areas and promote charge transfer and collection, thus increasing battery rate performance. In another example, Rai et al. [28] prepared extremely small TiO_2 nanoparticles (8.6 nm) through a simple urea-assisted auto-combustion synthesis method under different calcination temperatures and reported that the resulting small particle size was able to provide a larger contact surface area with the electrolyte to enhance Li^+ de-intercalation and therefore improve Li storage capability. Aside from these examples, an array of TiO_2 nanostructures including 0D nanoparticles [14], 1D nanowires and nanotubes [29], 2D nanosheets [30] and 3D hierarchical structures [31] have also been investigated over the years with studies ranging from preparation techniques and material characterizations to implementation in energy storage applications, resulting in outstanding electrochemical performances due to large reaction areas and rapid Li^+ transport pathways as provided by corresponding nanostructures. (The methods to construct nanostructures and composite materials to enhance the conductivity, reaction area and Li^+ transport in electrode materials have been discussed and reviewed). Despite these promising results however, fundamental drawbacks of TiO_2 such as slow charge carrier transfer rates and wide band gaps (3.2 eV) remain unchanged and seriously hinder development and application [32].

As another important class of Ti-based oxides, $\text{Li}_4\text{Ti}_5\text{O}_{12}$ (LTO) is widely considered to be a promising anode material in Li batteries due to its structural stability with “zero strain” in its lattice parameter during charge/discharge [33–35] and a higher flat Li insertion/extraction potential at $\sim 1.55 \text{ V}$, which enhances safety in LTO-based LIBs by avoiding Li dendrite formation. In addition, wide operating temperatures and high reversibility make LTO practical in various energy storage systems. And as a result of these desirable characteristics, LTO-based LIBs have been successfully commercialized and applied to portable energy storage devices. Despite this, the further development of LTO in LIBs is severely constrained by its lower theoretical capacity (175 mAh g^{-1}) as well as its low electronic conductivity and Li^+ diffusion coefficient [12]. Here, great efforts have been devoted to resolving these issues, including the development of novel nanostructures [36], carbon or oxide coatings [37] and composites [38].

For example, He et al. [39] prepared ultrathin LTO hierarchical microspheres composed of nanosheets through a simple hydrothermal procedure and reported that the resulting ultrathin nanosheets possessed larger reaction areas and enhanced Li^+ and electron transport. In another example, Shen et al. [40] synthesized mesoporous LTO/C nanocomposites using nanocasting technology with a porous carbon material (CMK-3) as a hard template and reported that the interpenetrating conductive carbon network of the CMK-3 can serve as a carrier to effectively promote electron transfer and improve the utilization of active materials. Furthermore, Wang et al. [41] synthesized a well-defined LTO nanosheet coating with a rutile- TiO_2 layer using a facile solution-based method and reported that as compared with a carbon layer, the resulting rutile- TiO_2 nanocoating layer can enhance the kinetic performance of LTO for rapid Li^+ de-intercalation. Similar to TiO_2 however, these methods can only alleviate and improve the properties of LTO electrode materials and cannot resolve the underlying issues of LTO (lower electron and ionic conductivity) (Fig. 1).

Based on the above discussions, the empty 3d orbital of Ti^{4+} in TiO_2 and LTO lattices appears to be the root cause of poor electron and ion conductivity, limiting application in energy storage devices. For example, Li^+ charge storage in Ti-based oxides involves charge-transfer reactions occurring at the interface and bulk accompanied by electron and ion diffusion kinetics. Here, numerous studies have suggested that the introduction of defects is the most effective method to enhance ionic diffusion and electronic conductivity in TiO_2 and LTO [42–45] in which the introduction of defects can narrow band gaps and provide additional energy levels (the intermediate band), thus expanding light absorption to longer wavelengths. In addition, defects can alter the electronic structure of TiO_2/LTO and optimize electron and ion transport kinetics. Moreover, the formation of disorder layers can modify the surface properties of Ti-based oxides (e.g., ion adsorption and surface activity) and enhance ion desolvation in electrolytes to improve kinetic performance in charge storage processes. Overall, the modified inherent properties of Ti-based oxides as induced by defects offer enormous potential for electrochemical energy storage applications. As a result, defect structures in Ti-based oxides have been widely investigated both experimentally and theoretically in which the defect type, concentration and distribution are important factors that determine the activity and selectivity of ion adsorption and storage, whereas the intrinsic properties of Ti-based oxides determine the formation condition, the location and property of defects.

In this review, recent advances in defective Ti-based oxides and their application in electrochemical energy storage devices will be summarized and discussed. In addition, the types of defects in Ti-based oxides including intrinsic defects [46–48], extrinsic defects [49–52] and

Defective Ti-based oxides for electrochemical energy storage

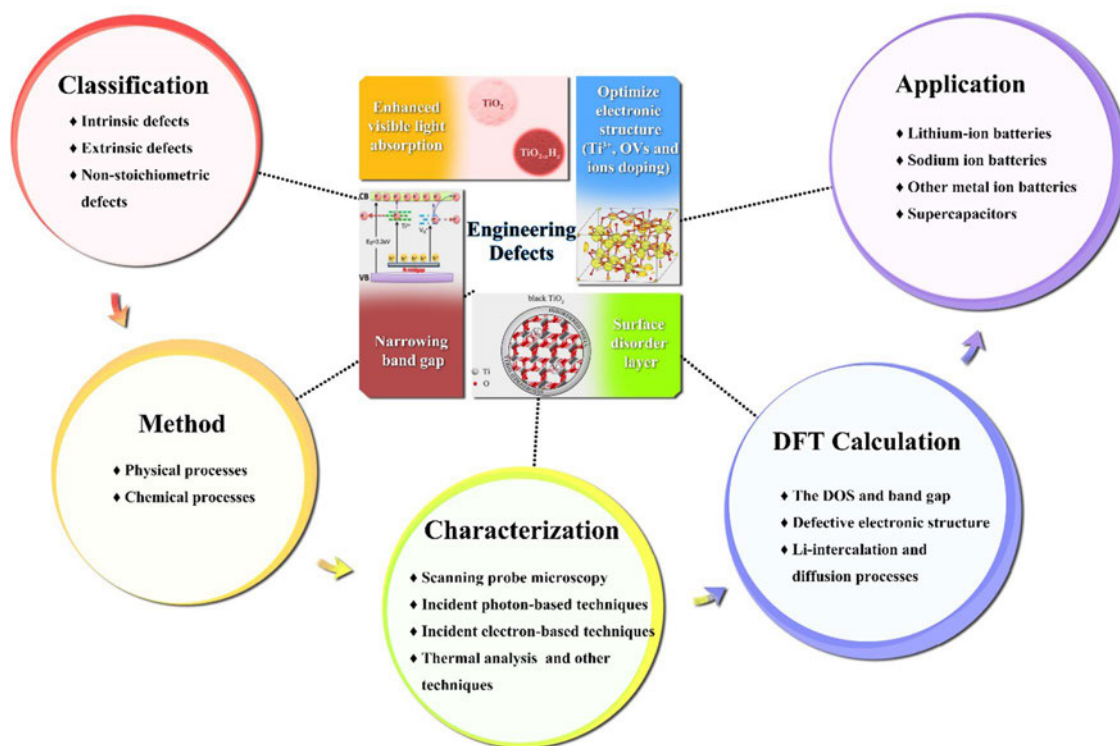


Fig. 1 Overview of key topics in Ti-based oxide defect chemistry for electrochemical energy storage

non-stoichiometric defects [53–56] will be introduced and their methods of preparation will be discussed. Furthermore, modified inherent properties such as optimized electronic structures, enhanced visible light absorptions, narrowed band gaps and surface disordered layers will also be discussed along with various techniques for characterization. Subsequently, density functional theory (DFT) calculations that provide theoretical explanations for these modified intrinsic properties and their effects on electrochemical energy storage will be outlined. Overall, this review will provide new insights into the role of defects in Ti-based oxides and facilitate their expansion into other fields.

2 Classification

Defect structures in metal oxides include intrinsic [46–48], extrinsic [49–52] and non-stoichiometric defects [53–56]. Of these defects, intrinsic defects (point defects) consist of lattice vacancies and do not alter the composition or stoichiometry of the overall crystal but affect the atoms around the vacancies and cause local lattice relaxation. Alternatively, extrinsic defects involve foreign atoms or ions being forced into crystal lattices to break the original atomic arrangement and induce partial lattice distortion, which can cause charge

redistribution and the modification of electronic structures. Here, extrinsic defect concentrations can be controlled and material properties can be optimized by adjusting the number of doped heteroatoms. As for non-stoichiometric defects, these can alter both the composition and structure of crystals and exist mainly in compounds containing volatile elements such as oxides, sulfides and chlorides and are greatly affected by ambient atmosphere and temperature. In addition, non-stoichiometric defects tend to be found at the surface of lattices and can alter inherent properties such as electronic structure, optical absorption, ionic adsorption and surface activity.

2.1 Intrinsic Defects

Intrinsic defects (point defects) are the most frequently studied in Ti-based oxides and can serve as charge carrier traps, important adsorption and active sites and can affect the kinetics of electron and ion transport in electrochemical applications. And of the various point defects, Frenkel and Schottky defects (Fig. 2) are two main types that have been studied in detail.

Schottky defects normally occur if smaller size differences exist between cations and anions and involve cation and anion pairs being forced to leave original lattice

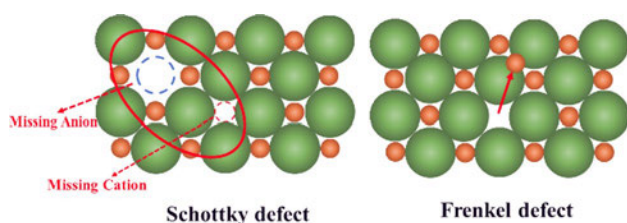


Fig. 2 Typical intrinsic defects: the Schottky defect and the Frenkel defect

Table 1 Defects in TiO_2 lattices and corresponding Kröger–Vink valence notation. Reprinted (adapted) with permission from Ref. [59], copyright (2011) American Chemical Society

Description	Kröger–Vink notation
Ti^{4+} ions in TiO_2 lattice sites	$\text{Ti}_{\text{Ti}}^{\times}$
Ti^{3+} ions in TiO_2 lattice sites (quasi-free electrons)	e'
Titanium vacancies	$\text{V}_{\text{Ti}}^{\prime\prime\prime}$
Ti^{3+} ions in TiO_2 lattice interstitial sites	$\text{Ti}_{\text{i}}^{\prime\prime}$
Ti^{4+} ions in TiO_2 lattice interstitial sites	$\text{Ti}_{\text{i}}^{\prime\prime\prime}$
O^{2-} ions in oxygen lattice sites	$\text{O}_{\text{o}}^{\times}$
Oxygen vacancies	$\text{V}_{\text{o}}^{\prime\prime}$
O^- ions in oxygen lattice sites (quasi-free electrons)	h^{\cdot}

positions to create lattice vacancies (Fig. 2) [57]. In addition, Schottky defects do not affect the stoichiometry or overall neutral charge in corresponding crystal lattices. As for Frenkel defects, these usually occur if large size differences exist between cations and anions because smaller ions (usually cations) can easily migrate from original lattice sites to interstitial positions, leaving vacancies in original locations and forming interstitial defects in new positions [58]. And in terms of Ti-based oxides, Frenkel and Schottky defects do not alter crystal structures but will lead to electron redistribution. For example, defect equilibria can be used to describe the formation of defects in TiO_2 (Tables 1, 2) [59] in which oxygen vacancies (OVs), Ti^{3+} and Ti^{4+} ions in interstitial sites are prone to form in TiO_2 lattices (Eqs. 1–3, 5 in Table 2). Furthermore, the formation of Ti vacancies is

a slow process (Eq. 4), illustrating that defect formation is a complex process usually accompanied by oxygen vacancies, interstitial defects and quasi-free electrons.

2.2 Extrinsic Defects

In contrast to intrinsic defects, extrinsic defects (doping defects) are caused by external atoms or ions entering the crystal lattice to replace original atoms or entering interstitial positions, resulting in local lattice distortion [48, 60–62]. Furthermore, corresponding charge compensation will occur in defective structures to maintain electrical neutrality if the valence state of impurity atoms is different from replaced atoms. Here, the concentration of extrinsic defects can be controlled by adjusting the number of heteroatoms to optimize material properties, and based on the properties of doped ions, extrinsic defects can be classified as either anion or cation doping defects. For example, metal cation doping defects in TiO_2 can introduce additional dopant-induced impurity energy levels within band gaps, which reduces the energy required for electronic excitation in which Carneiro et al. [63] studied Fe-doped TiO_2 and reported that two configuration energy levels were formed within the TiO_2 band gap by introducing Fe ions as a dopant. Here, these researchers suggested that because the oxidation level of $\text{Fe}^{3+}/\text{Fe}^{4+}$ exceeded the valence band edge of TiO_2 and the reduction level of $\text{Fe}^{3+}/\text{Fe}^{2+}$ was lower than the conduction energy level of TiO_2 , the formation of electron–hole pairs can be facilitated through the capture and loss of electrons in the conduction band and valence band edge of TiO_2 (Fig. 3a). Researchers have also reported that other high-valence doping cations (V^{5+} , Sn^{4+} and Co^{3+}) can also adjust the band gap of TiO_2 and reduce the energy required for electronic excitation [56–58].

Compared with cation doping, the aim of anion doping is to overlap the S and P orbitals of anions with the intrinsic conduction and valence bands of TiO_2 to reduce band gaps and produce highly active electron–hole pairs on the surface [64–66]. For example, Czoska et al. [49] reported that in F-doped TiO_2 , the exotic substitution of an O atom with a F atom can introduce an excess electron that reduces Ti^{4+} to Ti^{3+} and proposed two F- TiO_2 models in which one involves

Table 2 Basic defect reactions in TiO_2 (n and p denote the concentration of electrons and electron holes, respectively). Reprinted (adapted) with permission from Ref. [59], copyright (2011) American Chemical Society

	Defect reaction	Constant	ΔH° (kJ mol $^{-1}$)	ΔS° [J (mol K) $^{-1}$]
1	$\text{O}_{\text{o}}^{\times} \leftrightarrow \text{V}_{\text{o}}^{\prime\prime} + 2e' + 1/2\text{O}_2$	$K_1 = [\text{V}_{\text{o}}^{\prime\prime}]n^2p(\text{O}_2)^{1/2}$	493.1	106.5
2	$\text{Ti}_{\text{Ti}}^{\times} + 2\text{O}_{\text{o}}^{\times} \leftrightarrow \text{Ti}_{\text{i}}^{\prime\prime} + 3e' + \text{O}_2$	$K_2 = [\text{Ti}_{\text{i}}^{\prime\prime}]n^3p(\text{O}_2)$	879.2	190.8
3	$\text{Ti}_{\text{Ti}}^{\times} + 2\text{O}_{\text{o}}^{\times} \leftrightarrow \text{Ti}_{\text{i}}^{\prime\prime\prime} + 4e' + \text{O}_2$	$K_3 = [\text{Ti}_{\text{i}}^{\prime\prime\prime}]n^4p(\text{O}_2)$	1025.8	238.3
4	$\text{O}_2 \leftrightarrow \text{V}_{\text{Ti}}^{\prime\prime\prime} + 4h^{\cdot} + 2\text{O}_{\text{o}}^{\times}$	$K_4 = [\text{V}_{\text{Ti}}^{\prime\prime\prime}]p^4(\text{O}_2)^{-1}$	354.5	−202.1
5	$\text{nil} \leftrightarrow e' + h^{\cdot}$	$K_i = np$	222.1	44.6
	$\ln K = [(\Delta S^\circ)/R] - [(\Delta H^\circ)/RT]$			

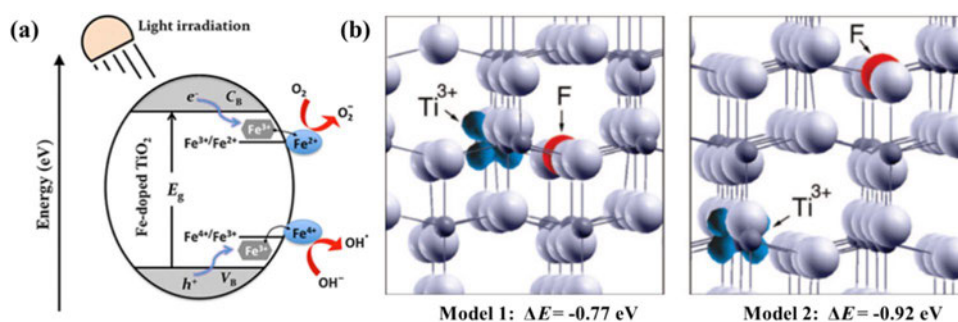


Fig. 3 **a** Diagram of the different energy levels for Fe–TiO₂. C_B and V_B correspond to the conduction and valence bands of the semiconductor. Reprinted with permission from Ref. [63], copyright (2014) Springer Nature. **b** Ball and stick models for F-doped anatase TiO₂.

The left panel: a Ti³⁺ cation directly neighboring a F dopant. The right panel: a Ti³⁺ cation at ~7 Å distance from a F dopant. Reprinted with permission from Ref. [49], copyright (2008) American Chemical Society

a Ti³⁺ atom adjacent to a F atom (Model 1), whereas the other involves Ti³⁺ being separated from the F atom (Model 2) (Fig. 3b). Here, the relative position (ΔE) of the defect Ti 3d_{xz} state in Model 1 is much smaller than that in Model 2, indicating that excess electrons from F atoms can reduce neighboring Ti⁴⁺ to maintain a stable structure. Researchers have also introduced a series of nonmetallic elements such as B, C, N and S to replace O or to enter interstitial sites in TiO₂ lattices based on the valence and the radius of the doping atom [14, 67, 68] and have reported that multi-ion doping can generate additional synergistic effects to further optimize impurity energy levels and defect structures to improve performance in energy storage applications [69, 70].

Overall in TiO₂, metal cation doping can cause lattice distortion and reduce electron–hole pair formation to improve photon utilization, whereas nonmetallic anion doping can alter the response to visible light absorption and optimize quantum efficiency by reducing the band gap width and utilizing energy level staggered coupling.

2.3 Non-stoichiometric Defects

Different from intrinsic defects, non-stoichiometric defects can alter structural and stoichiometric compositions by creating sufficient vacancies and interstitial defects [53, 54]. Non-stoichiometric defects are also more prevalent in Ti-based oxides (e.g., LTO and TiO₂) because their oxygen atoms are more prone to be removed at low oxygen activities. In addition, non-stoichiometric defects are usually accompanied by the formation of intrinsic defects (Frenkel and Schottky defects). For example, Zhen et al. [71] compared stoichiometric and non-stoichiometric TiO₂ through calcination in air and Ar gas and reported that the ratio of O to Ti on the surface (1.98–1.78) calcined in air was near a perfect stoichiometric value of 2, whereas the ratio (1.70–1.67) prepared in Ar was below ideal stoichiometry, suggesting that lower oxygen pressures in Ar can result in

the loss of lattice oxygen (Fig. 4). Researchers have also reported that non-stoichiometric TiO_{2-x} possesses a complex defect structure and can demonstrate excellent adsorption properties and electrochemical activities due to an amorphous surface layer with abundant defective sites such as reduced Ti³⁺, Ti⁴⁺ interstitials and OV. However, non-stoichiometric defects can also gradually be repaired in higher oxygen activity atmospheres at high temperatures, leading to the recovery of a stoichiometric structure.

3 Engineering of Defects

Methods to engineer defects in Ti-based oxides can be divided into physical and chemical processes (Fig. 5). In terms of physical processes, the creation of high activation energy and the doping of foreign atoms are important methods to achieve lattice distortion and deformation. Here, corresponding changes include the introduction of OVs, interstitial defects and the partial reduction of Ti⁴⁺ to Ti³⁺ [49, 72–74]. And although the lower defect concentrations associated with physical methods are undesirable

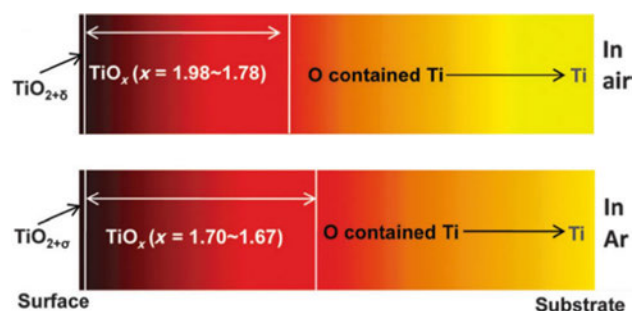


Fig. 4 Schematic showing compositional changes from the surface to the substrate in TiO₂ during calcination in air or Ar. Reprinted with permission from Ref. [71], copyright (2013) Royal Society of Chemistry

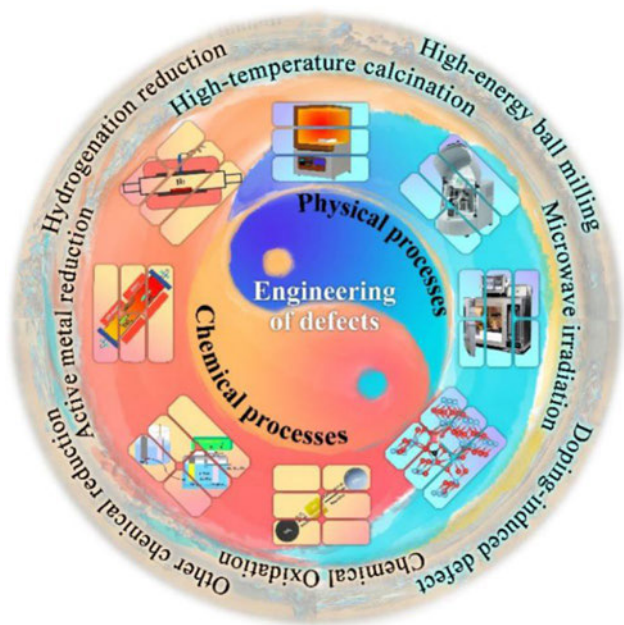


Fig. 5 Methods for engineering defects

in terms of improving the intrinsic properties of Ti-based oxides, the reduction of high-valence state Ti from Ti^{4+} to Ti^{3+} or Ti^{2+} and the oxidization of low-valence state Ti from Ti^{2+} or Ti^{3+} to Ti^{4+} are reported to be effective chemical methods to induce high defect concentrations in Ti-based oxides [44, 75–77]. Despite this, specific conditions in terms of temperature, pressure and atmosphere are required for these redox reactions to occur. Therefore, the formation of defects is a complex physicochemical process and detailed

understandings of these methods can elucidate defect formation mechanisms and allow for the optimization of intrinsic properties associated with various applications.

3.1 Physical Processes

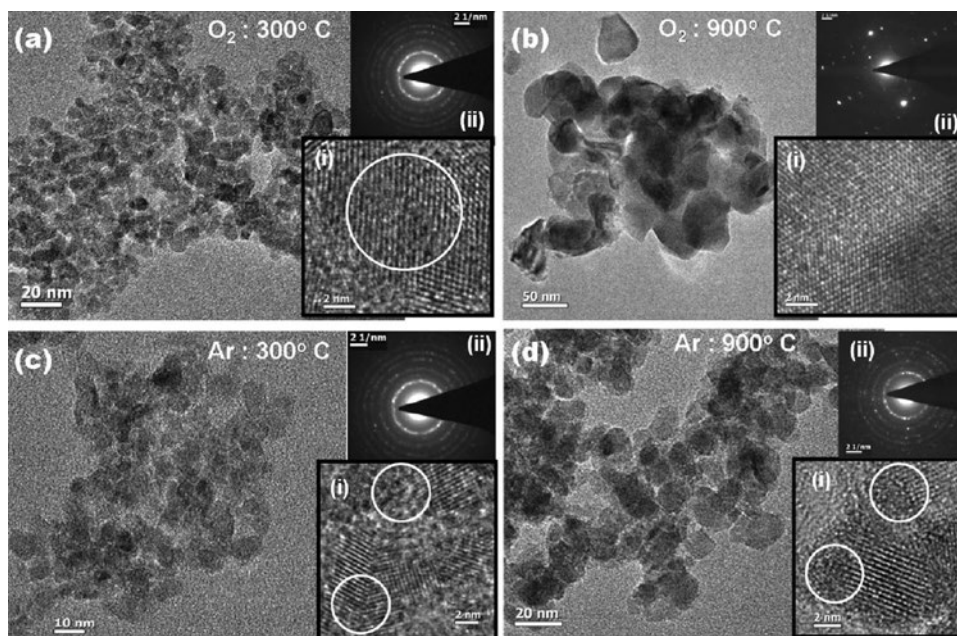
3.1.1 High-Temperature Calcination

Although intrinsic defects (Frenkel and Schottky defects) are found in low concentrations, defect density can usually be controlled by adjusting temperature [72, 78]. Equation (1) summarizes the relationship between structural defect concentration and temperature:

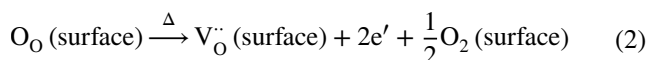
$$\frac{N_v}{N} = \exp\left(-\frac{Q_v}{k_B T}\right) \quad (1)$$

In which N_v is the number of defects in the lattice, N is the number of potential defect sites, Q_v is the activation energy for vacancy formation, k_B is the Boltzmann's constant, and T is the temperature. And because defect concentrations increase exponentially with temperature, calcination is considered to be an effective method to create structural defects in Ti-based oxides in which oxygen atoms in Ti-based oxides tend to diffuse to the surface or the subsurface layer and thereby form OV's [79]. However, these OV's are unstable and can easily be refilled by oxygen in air or H_2O [80]. For example, Ghosh et al. [81] analyzed the evolution of OV's in TiO_2 calcined in air and Ar atmospheres (Fig. 6) and reported obvious structural defects or lattice imperfections in TiO_2 samples calcined at 300 °C in air, whereas samples gradually evolved into single crystalline phases as

Fig. 6 TEM micrographs of TiO_2 nanoparticles annealed at different temperatures in **a, b** air or **c, d** Ar gas. Inset (i) HRTEM images (white circles indicate lattice defects) and (ii) corresponding selected area electron diffraction (SAED) patterns. Reprinted with permission from Ref. [81], copyright (2013) American Chemical Society



annealing temperatures reached 900 °C (Fig. 6a, b), demonstrating that high temperature calcinations in the presence of sufficient oxygen can repair partial OV's and increase crystallinity. Alternatively, these researchers reported different results in Ar-annealed samples in which defects or imperfections were still present after annealing at 300 and 900 °C (Fig. 6c, d), which may be explained with reference to the balance between surface oxygen in TiO₂ and oxygen in the atmosphere (Eq. 2) in which not only are OV's in TiO₂ unable to receive enough replenishing oxygen in a severely oxygen-deficient atmosphere, but high temperatures can also tilt the balance toward producing more OV's.



Researchers have also studied oxygen-deficient atmospheres including Ar, N₂, He or vacuum to create OV's in Ti-based oxides during calcination at high temperatures [81–84]. For example, Xia et al. [82, 83] prepared vacuum-treated TiO₂ to analyze the effects of vacuum heating and reported that the vacuum-treated TiO₂ was yellow in color (Fig. 7a) and that its absorption range for visible light was extended from the original 400–1100 nm (Fig. 7b) in which a disordered amorphous shell formed at the edge of the crystalline region after vacuum treatment (Fig. 7c, d). Guillemot et al. [84] also reported that TiO₂ exhibited a typical n-type defective structure (TiO_{2-x}) if calcined in vacuum and similarly; Chen et al. [85] reported that Li₄Ti₅O_{12-y} can be synthesized through calcination in N₂ atmosphere at 500 °C for 2 h. Overall, defect concentrations increase with calcination temperature in vacuum.

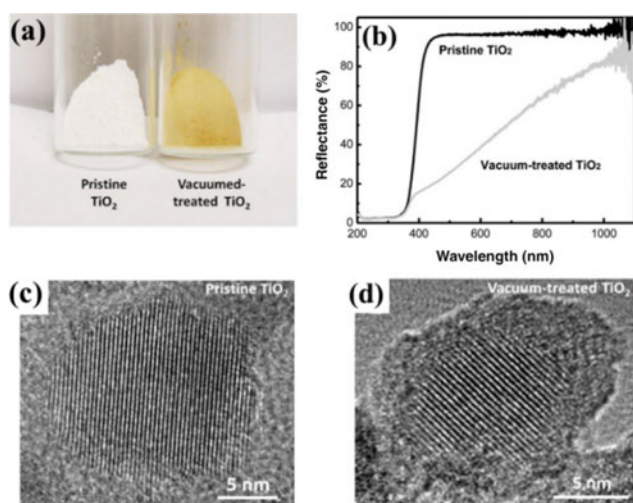
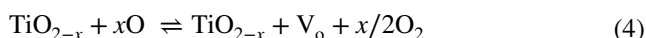


Fig. 7 **a** Digital image, **b** UV–Vis reflectance spectra, **c**, **d** HRTEM images of pristine and vacuum-treated TiO₂. Reprinted with permission from Ref. [83], copyright (2013) John Wiley and Sons

3.1.2 High-Energy Ball Milling

In addition to providing activation energy for the formation of defects through high temperatures, high-energy ball milling is another efficient method to gain grain refinement, defects and lattice distortions through repetitive deformation, fragmentation and cold welding under mechanical activation [73, 86–90]. Here, high-energy ball milling is an extensively investigated mechanochemical reaction technique in which a ball and powder are confined in a closed container and subjected to mechanical revolution and rotation, resulting in kinetic energy and mechanical stress, which leads to particle pulverization, lattice distortion and structural defects. For example, Indris et al. [89] dry-milled TiO₂ using a SPEX8000 ball mill in air for up to 4 h and reported that the partial Ti–O bonds at the surface of TiO₂ can be broken through mechanical activation to release oxygen atoms as O₂, thus forming OV's and allowing for a transition from Ti⁴⁺ to Ti³⁺ in the TiO₂ lattice (Eq. 3 and 4):



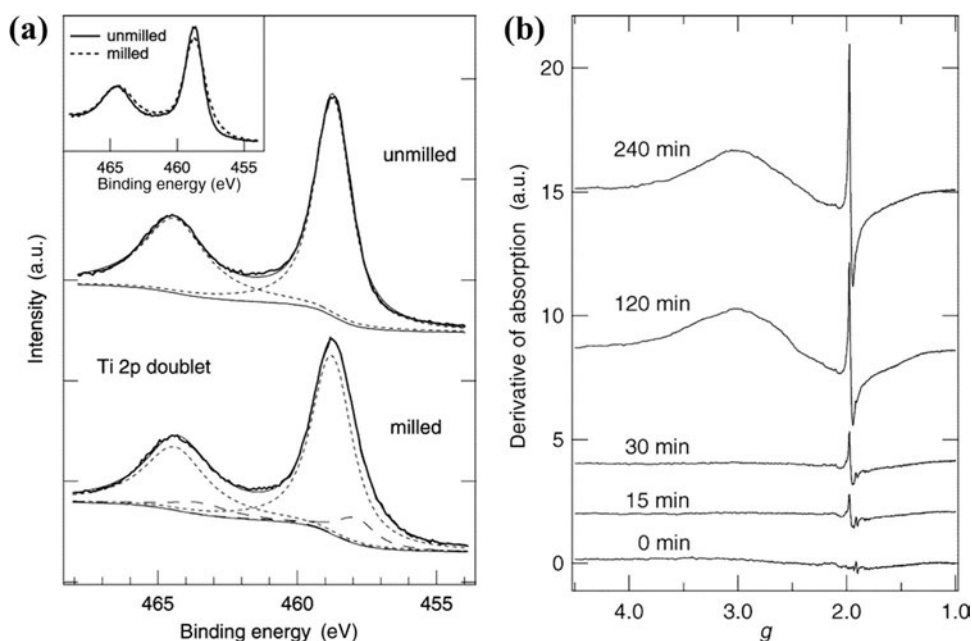
These researchers also studied the influence of high-energy ball milling on TiO₂ by examining XPS Ti 2p spectra (Fig. 8a) and reported that milled TiO₂ presented an additional peak at 456.9 eV that can be attributed to Ti³⁺. In addition, EPR measurements were taken in this study to confirm the formation of Ti³⁺ after milling (Fig. 8b) in which a narrow signal at *g* = 1.96 was observed in the un-milled TiO₂ that gradually increases in intensity with increasing milling times. More importantly, the results showed that a broad peak related to Ti³⁺ at *g* = 2.42 started to appear after milling for 2 h. Overall, both the XPS and EPR results in this study demonstrated that high-energy ball milling can create lattice distortions and generate OV's and Ti³⁺ in TiO₂ lattices.

Milling atmosphere also has important effects on high-energy ball milling induced defects. For example, Pan et al. [87] prepared milled TiO₂ at 220 rpm for 40 h in air and nitrogen atmospheres and found that the low oxygen pressure in the nitrogen atmosphere can affect the balance of defect reactions in Eqs. 3 and 4 and was more conducive to the formation of oxygen defects during high-energy ball milling.

3.1.3 Microwave Irradiation

Compared with conventional heating, microwave irradiation is a more rapid heating method that can generate spin among polar molecules through an electromagnetic field and convert electromagnetic energy into thermal

Fig. 8 **a** XPS spectra of unmilled anatase and anatase milled for 4 h at 100 K. **b** EPR spectra of ball-milled TiO_2 (rutile). Reprinted with permission from Ref. [89], copyright (2005) American Chemical Society



energy. In addition, the molecular vibration caused by microwave radiation can break the ionic bonds in TiO_2 and help to form defect structures [91–93]. For example, Ishida et al. [93] synthesized black TiO_2 powder by subjecting a water-soluble Ti complex to microwave-induced plasma at 100 W for 60 min and reported strong absorption in all visible light regions (Fig. 9a). Marinel et al. [91] also reported the dielectric properties of microwave-treated TiO_2 in which their microwave-treated TiO_2 was synthesized through the manual grinding of TiO_2 powder in an agate mortar and pressed into a disk through uniaxial pressing (90 MPa) followed by microwave treatment (200 W), resulting in the color of the TiO_2 disk to change from white to yellowish brown (Fig. 9b).

3.1.4 Doping-Induced Defect Processes

Ion doping in Ti-based oxide lattices is an effective method to achieve lattice distortion and introduce impurity states in band gaps, thereby extending absorption into the visible light region [49, 74, 94–97]. Overall, interstitial and substitutional dopings in TiO_2 lattices are complex processes and metal and nonmetal doping processes are discussed in this section to illustrate the formation of doping-induced defect structures. In general, nonmetal atoms (B, N, S, F, etc.) can replace O atoms and metal atoms can displace Ti ions in doping processes. This is generally accompanied by large amounts of ions entering interstitial positions, resulting in corresponding charge compensation in doping areas and the reorganization of electronic structures.

Fig. 9 **a** UV–Vis spectra of black and white TiO_2 nanoparticles (the inset: a photo of black TiO_2 powder). Reprinted with permission from Ref. [93], copyright 2015, Chemical Society of Japan(CSJ). **b** Picture of white TiO_2 turning to yellowish brown after microwave treatment. Reprinted with permission from Ref. [91], copyright 2013, Elsevier

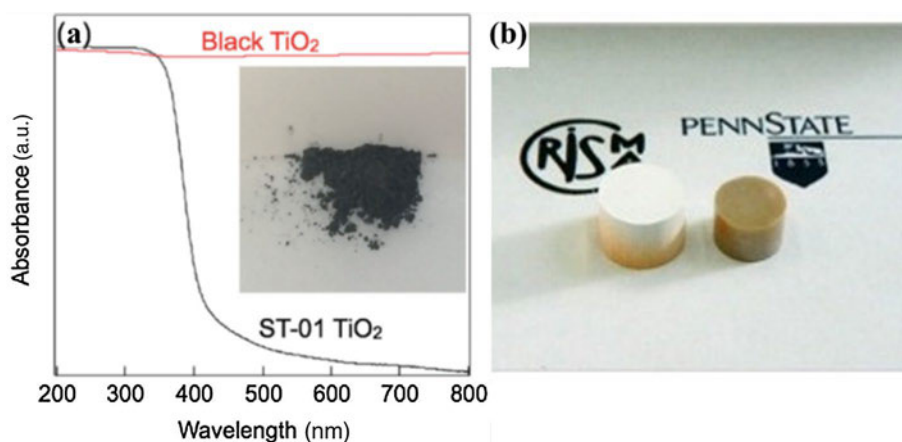
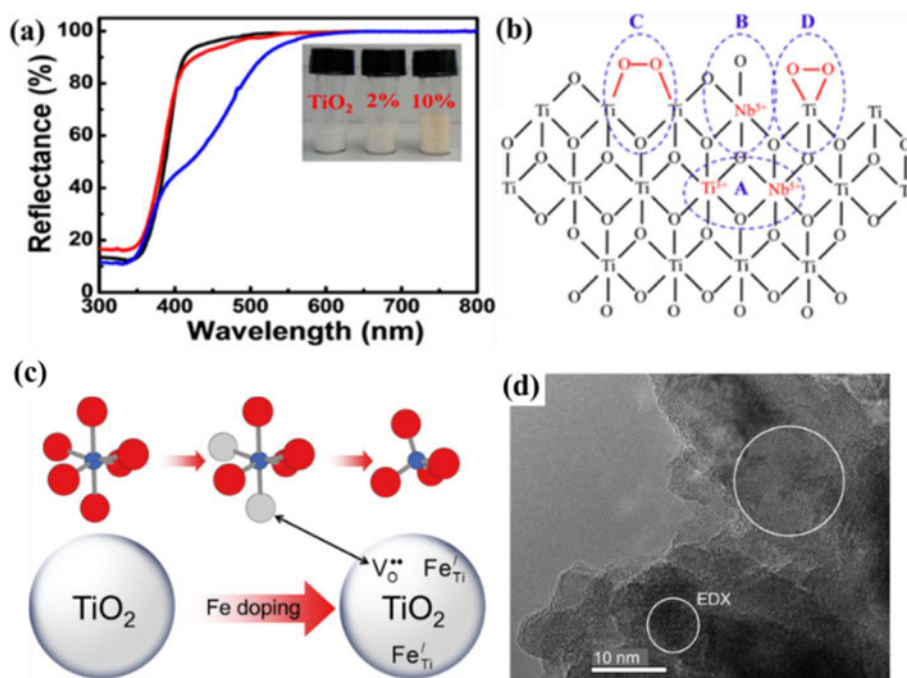


Fig. 10 **a** UV–Vis diffuse reflectance spectra of undoped and Nb-doped TiO_2 samples and **b** the defect structure of Nb-doped TiO_2 : A = the Ti^{3+} and Nb^{5+} defect couple, B = surface Nb^{5+} defects, C and D = surface peroxide defects. Reprinted with permission from Ref. [52], copyright (2015) American Chemical Society. **c** Transformation from octahedral to tetrahedral-coordinated Ti^{4+} in Fe– TiO_2 and **d** high-resolution TEM image of 10% Fe/ TiO_2 after annealing in air. Reprinted with permission from Ref. [74], copyright (2012) American Chemical Society



3.1.4.1 Metal Ion Doping In one study, Kong et al. [52] obtained defect-induced yellow TiO_2 by introducing Nb to partially replace Ti and reported that the color of the solution gradually deepened to yellow with increasing Nb concentrations (Fig. 10a), which these researchers attributed to the fact that the introduced Nb^{5+} can not only replace Ti^{4+} but also lead to neighboring Ti^{4+} transitioning to Ti^{3+} in the TiO_2 lattice (Fig. 10b). In another study, Wu et al. [74] obtained defective TiO_{2-x} by introducing Fe^{3+} to replace Ti^{4+} in TiO_2 lattices corresponding to the formation of OVs. Here, these researchers suggested that Fe^{3+} can serve as an acceptor-type dopant to partially remove and rearrange oxygen ions in TiO_6 octahedra and form OVs and TiO_4 tetrahedra (Fig. 10c). These researchers also observed an obvious amorphous region in the high-resolution TEM image of Fe-doped TiO_2 nanoparticles (Fig. 10d), which clearly revealed the formation of large numbers of OVs after the introduction of Fe^{3+} into TiO_2 . In a further study, Pathak et al. [98] prepared Al-doped TiO_2 by replacing Ti^{3+} with Al^{3+} due to similar atomic radii as well as the instability of Ti^{3+} . And in addition to these mentioned cations, researchers have also reported that other cations such as Cu^{2+} [99], Zn^{2+} [100], Co^{2+} [101, 102], Cr^{3+} [94], Mn^{5+} [103, 104] and V^{5+} [105] can also be used as effective doping ions to create defective TiO_2 structures. Here, researchers suggested that high-valence ions (M^{4+} or M^{5+}) can lead to the transition of neighboring Ti^{4+} to Ti^{3+} and contribute to the stabilization of Ti^{3+} but do not produce OVs, whereas low-valence ions (M^{1+} , M^{2+} or M^{3+}) can form OVs but are not conducive to the formation of Ti^{3+} .

3.1.4.2 Nonmetal Ion Doping Similar to metal-doping ions, nonmetal ions (B, C, N, S, etc.) have also been introduced to replace O atoms or into interstitial positions in TiO_2 lattices [49, 95, 106], resulting in the extension of the visible light absorption region of materials by narrowing band gaps, forming impurity energy levels and creating OVs. For example, Feng et al. [107] prepared B- TiO_{2-x} through a simple hydrolysis reaction and reported that the color of the TiO_2 changed from white to gray and subsequently to blue with the increasing B content (Fig. 11). In another example, Irie et al. [108] synthesized $\text{TiO}_{2-x}\text{N}_x$ nanoparticles through annealing at 550, 575 and 600 °C for 3 h under NH_3 atmos-

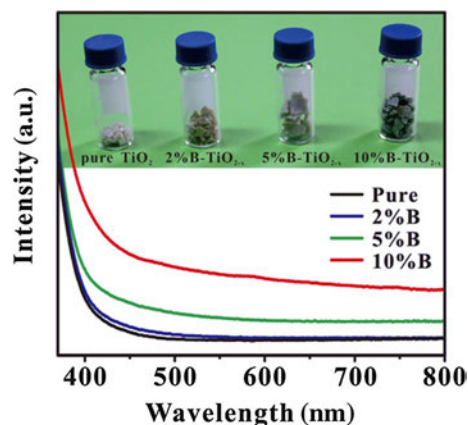


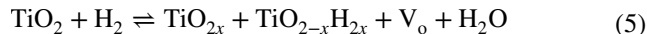
Fig. 11 UV–Vis absorption spectra of pure TiO_2 and B- TiO_{2-x} samples with various B-doping contents along with corresponding photographs. Reprinted with permissions from Ref. [107] under Creative Commons

phere and reported that the N concentration in TiO_{2-x} gradually increased with calcination temperatures. Moreover, Czoska et al. [49] prepared F-doped TiO_2 through a typical impregnation technique in which TiO_2 powder was placed in aqueous HF (1 L) with continuous stirring for 1 h followed by repeated washing with water and drying at 40 °C for 4 h and similarly, Qi et al. [109] prepared $\text{Li}_4\text{Ti}_5\text{O}_{12-x}\text{Br}_x$ samples through a conventional high-temperature solid-state reaction in which $\text{LiOH}\cdot\text{H}_2\text{O}$, $\text{LiBr}\cdot\text{H}_2\text{O}$ and TiO_2 were ground together for 1 h and heated at 900 °C for 12 h in air.

3.2 Chemical Processes

3.2.1 Hydrogenation Reduction

Because high-valence oxidation state Ti species are the main forms of Ti-based oxides, the partial reduction of Ti^{4+} to Ti^{3+} through chemical methods is an effective strategy to create defect structures. Here, hydrogenation is able to capture oxygen and maintain OV's in Ti-based oxides, corresponding to the incomplete reduction process from high-valence-state Ti species [44, 75]. Using the hydrogenation process of TiO_2 as an example, TiO_2 can exhibit different colors from white to blue to black with increasing defect concentrations and the hydrogenation process can be summarized as:



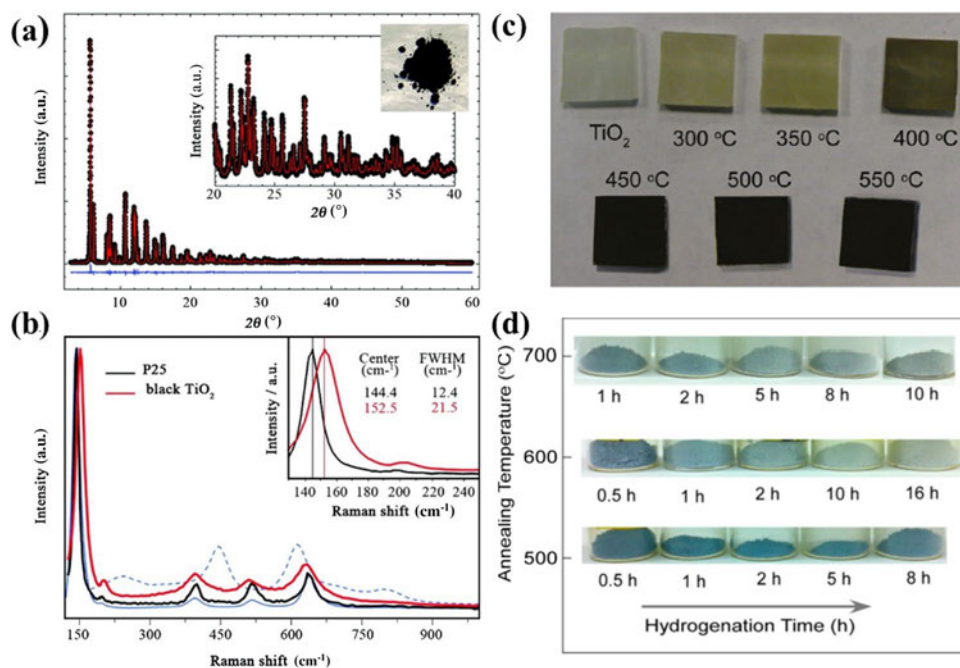
And although according to Eq. 5, hydrogenation should be simple, the full hydrogenation mechanism is actually

complex and is affected by temperature, reaction time, pressure, H_2 partial pressure, hydrogen plasma and ion doping, all of which play a vital role in inducing TiO_2 /LTO defect structures during hydrogenation. In addition, the defect concentrations and related physiochemical properties of TiO_2 /LTO can exhibit different characteristics due to these conditions [110].

3.2.1.1 High-Temperature Hydrogenation As an example of high-temperature hydrogenation, Naldoni et al. [42] obtained black TiO_2 through hydrogen reduction at 500 °C for 1 h (Fig. 12a) and reported that although the Raman results of white and black TiO_2 both presented similar phase compositions, a smaller peak shift appeared in the black TiO_2 that can be attributed to the defect structure after hydrogenation (Fig. 12b). Jiang et al. [111] also reduced white P25 TiO_2 nanoparticles through annealing at 400 °C for 10 h under a pure hydrogen gas (99.99%) atmosphere to obtain a gray-colored H-P25 and attributed the different coloration to the cooling rate after hydrogenation.

Reaction times and calcination temperatures are also important factors affecting the hydrogenation effect. For example, Wang et al. [112] studied hydrogenated TiO_2 nanowire films synthesized at various temperatures from 300 to 550 °C for 0.5 h and found that white untreated TiO_2 turned yellowish green at 300 to 350 °C and finally black at 450 °C and up (Fig. 12c), suggesting that the increased visible light absorption is a result of high-temperature activation and hydrogenation. In another study, Yu et al. [44] also observed the gradual color change of TiO_2 from white to blue to gray by controlling annealing temperatures

Fig. 12 **a** SXRPD pattern and photo of black TiO_2 and **b** micro-Raman spectra of P25 and black TiO_2 . Reprinted with permission from Ref. [42], copyright (2012) American Chemical Society. **c** Photographs of pristine TiO_2 and H- TiO_2 nanowires annealed in hydrogen at various temperatures from 300 to 550 °C. **d** Gradual changes in the color of TiO_2 from blue to gray at different annealing temperatures and annealing times in a hydrogen atmosphere. Reprinted with permission from Ref. [44], copyright (2013) American Chemical Society



(500–700 °C) and hydrogenation times (0.5–16 h) in which white untreated TiO₂ turned blue at the starting stages (0.5–1 h) of hydrogenation and gradually turned gray with increasing hydrogenation times (8–16 h) (Fig. 12d). Here, these researchers reported that temperature can also determine color change to some extent in which blue TiO₂ can be retained longer (over 8 h) at 500 °C but turns to pale gray at 600 and 700 °C.

3.2.1.2 High-Pressure Hydrogenation As an example of high-pressure hydrogenation, Chen et al. [75] obtained black TiO₂ nanocrystals through calcination at 200 °C for 5 days under high pressure hydrogen (20.0 bar H₂) and reported that a thin amorphous layer formed on the crystalline TiO₂ after hydrogenation, resulting in an obvious color change from white to black (Fig. 13a–d). In addition, Qiu et al. [113] obtained blue rutile TiO₂ through typical hydrogenation at 450 °C for 1 h with 40 bar hydrogen pressure (Fig. 13e) and reported that their white and blue TiO₂ showed similar diffraction peaks, indicating that hydrogenation does not change the rutile framework and that color changes can be attributed to OV. Qiu et al. [110] in another study also prepared hydrogenated LTO through calcination at 500 °C (50 °C min^{−1}) under 40 bar H₂ atmosphere for 1 h and reported that the color of the sample changed from white to blue as a result of OV (Fig. 13f, g). Furthermore, Lu et al. [114] prepared multiple colors of TiO₂ based on different hydrogenation times at room temperature (35 bar H₂, 3–17 days) in which white TiO₂ shifted to pale yellow

after 3 days and gradually changed into much deeper colors with increasing hydrogenated times (Fig. 13h). The resulting enhanced visible light absorption in this study was also confirmed by UV–Vis spectra (Fig. 13i).

3.2.1.3 Mixed Atmosphere Hydrogenation As for mixed atmosphere hydrogenation, Cai et al. [115] obtained hydrogenated TiO₂ through calcination in a mixed atmosphere (10 vol% H₂/N₂) at 650 °C for 5 h in which a disordered shell formed on the surface of TiO₂ during high-temperature hydrogenation accompanied by the transition of TiO₂(B)-anatase heterophase junctions (Fig. 14a). Su et al. [116] also prepared colored TiO₂ nanocrystals through hydrogen thermal treatments (1 °C min^{−1}) at 300, 400, 500 and 600 °C for 5 h under a mixed atmosphere (10% H₂ and 90% N₂) and suggested that the enhanced visible region absorbance associated with temperature was caused by OV (Fig. 14b). These researchers also reported that band gap values decreased with increasing calcination temperatures and that the color of the sample gradually transformed from white to light yellow and subsequently to darker gray (Fig. 14c). In a further study, Wu et al. [117] compared the effects of different calcination atmospheres on TiO₂ including air, nitrogen (99.999%) and a hydrogen/nitrogen mixture (15% H₂–85% N₂) under various temperatures from 400 to 600 °C for 2 h and reported that white TiO₂ turned black in N₂ and H₂/N₂ mixed atmospheres at high temperatures (400 °C and above) (Fig. 14d). Liu et al. [118] also studied the effects of pressure and atmosphere on TiO₂ color under

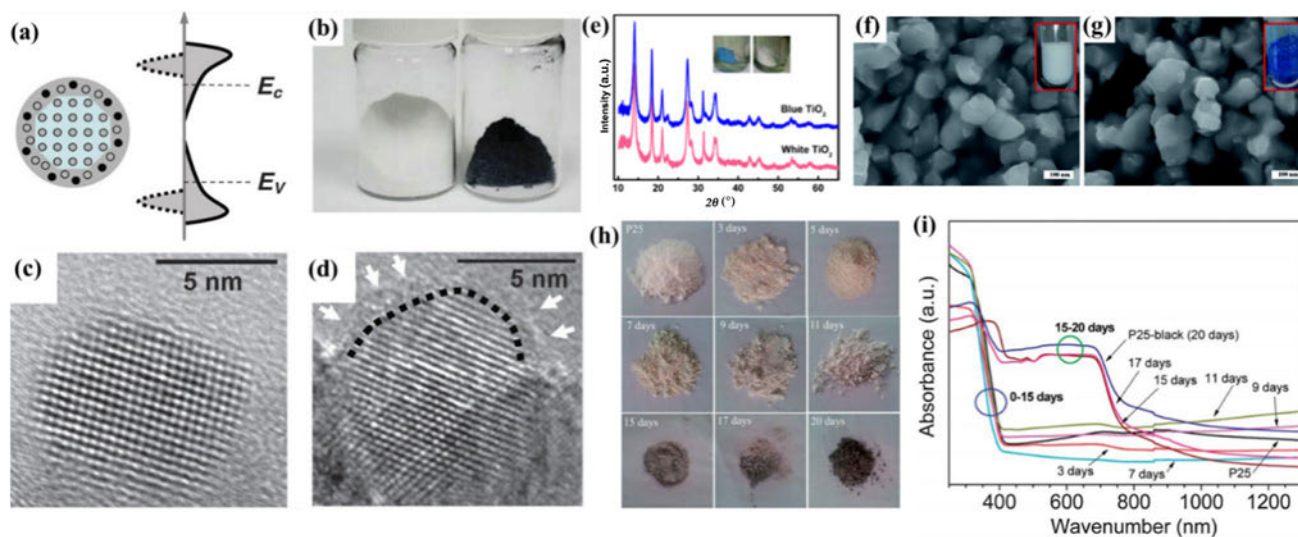


Fig. 13 **a** Schematic of the formation of black TiO₂. **b** Photographs of white and black TiO₂. **c**, **d** HRTEM images of white and black TiO₂ nanocrystals. Reprinted with permission from Ref. [75], copyright (2011) American Association for the Advancement of Science. **e** XRD spectra of blue and white TiO₂ along with corresponding photographs. Reprinted with permission from Ref. [113], copyright (2014)

American Chemical Society. **f**, **g** SEM images of pristine and blue H-LTO. Reprinted with permission from Ref. [110], copyright (2014) Royal Society of Chemistry. **h** Photographs and **i** UV–Vis spectra of P25 treated at different hydrogenation times (35 bar, H₂) at room temperature. Reprinted with permission from Ref. [114], copyright (2014) Royal Society of Chemistry

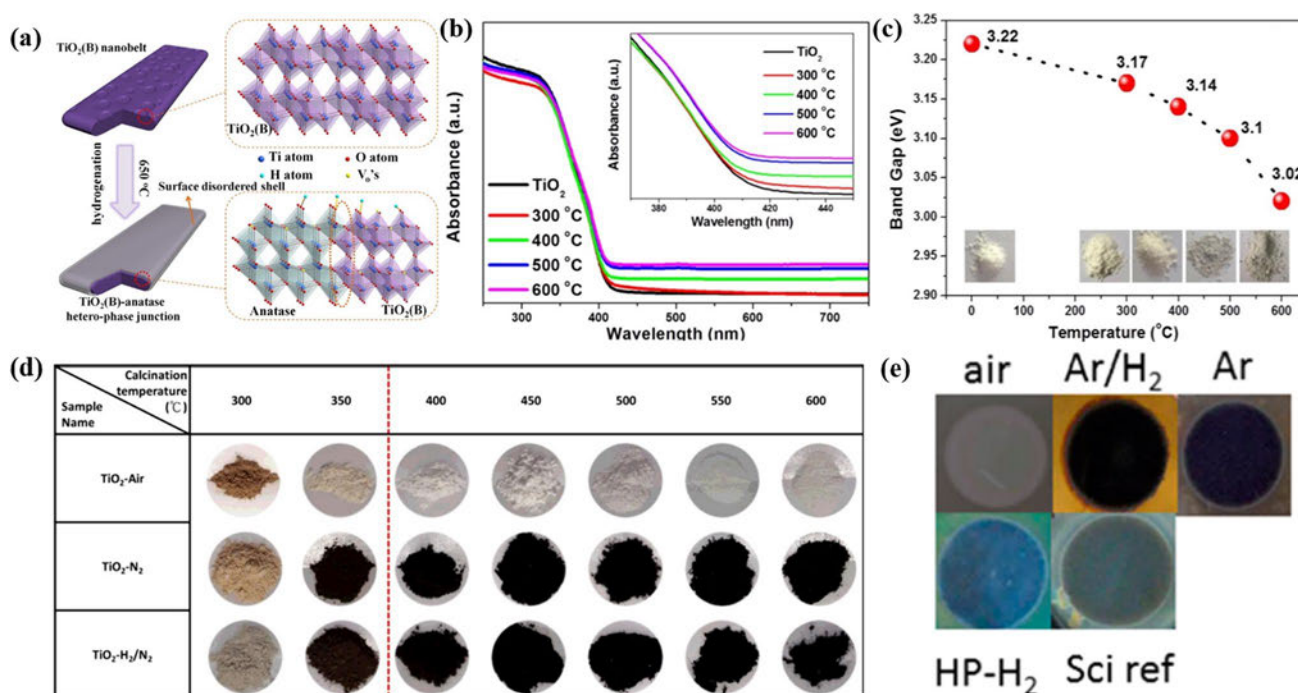


Fig. 14 **a** Simplified schematic showing defects and the $\text{TiO}_2(\text{B})$ -anatase heterophase junction. Reprinted with permission from Ref. [115], copyright (2015) American Chemical Society. **b** UV-Vis spectra of obtained samples and **c** band gap energy at different temperatures. Reprinted with permission from Ref. [116], copyright (2015) American Chemical Society. **d** Color change of

TiO_2 nanocrystals calcined at various temperatures for 2 h under different atmospheres of air, nitrogen and a hydrogen/nitrogen mixture. Reprinted with permission from Ref. [117], copyright (2016) Elsevier. **e** TiO_2 nanotubes annealed in air, Ar/H_2 or high pressure H_2 . Reprinted with permission from Ref. [118], copyright (2014) American Chemical Society

different hydrogenation conditions including calcination at 450 °C for 1 h in air, calcination in Ar (Ar) or H_2/Ar at atmospheric pressure, high-pressure H_2 treatment (20 bar, 500 °C for 1 h) and high pressure but low-temperature treatment (H_2 , 20 bar, 200 °C for 5 d) and reported that white TiO_2 gradually turned black under Ar (Ar) or H_2/Ar atmospheres but was light blue in the high pressure H_2 treatment (20 bar, 500 °C for 1 h) and gray in the high pressure but low temperature atmosphere treatment (H_2 , 20 bar, 200 °C for 5 d) (Fig. 14e).

3.2.1.4 Ion Doping Hydrogenation Ion doping has been reported to be able to modify band structures by producing additional dopant-induced impurity energy levels. And by combining hydrogenation with ion doping, band gap structures can be further optimized and visible light adsorption can be further enhanced. For example, Wang et al. [119] prepared a series of F-, NF-, HF- and NHF-doped TiO_2 through various processes, including the hydrothermal reaction of tetrabutyl titanate at 180 °C for 24 h with HF as an additive to produce TiO_2 -F, the mixing of TiO_2 -F with urea followed by calcination at 400 °C for 2 h in air to produce TiO_2 -NF and the hydrogenation of TiO_2 -F and TiO_2 -NF at 400 °C for 2 h to produce TiO_2 -HF and TiO_2 -NHF and reported

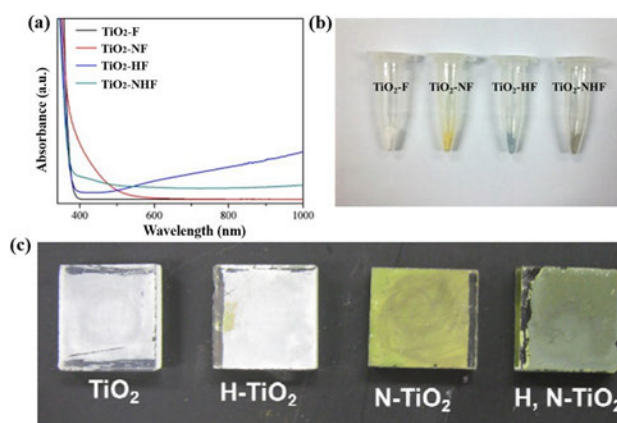


Fig. 15 **a** UV-Visible absorption spectra of TiO_2 -N, TiO_2 -NF, TiO_2 -HF and TiO_2 -NHF and **b** corresponding colors. Reprinted with permission from Ref. [119], copyright (2012) Elsevier. **c** TiO_2 , H- TiO_2 , N- TiO_2 and H, N- TiO_2 nanowire arrays. Reprinted with permission from Ref. [120], copyright (2012) American Chemical Society

that completely different visible light absorption spectra can be observed for each sample (Fig. 15a, b) in which TiO_2 -F possessed a white color but changed to bright yellow and

dark blue after N-doping and H-doping, respectively, before finally taking on a brown color as $\text{TiO}_2\text{-NHF}$. Here, these obvious color changes can be attributed to the modified band structures as induced by ion doping in which only a few F ions can enter the $\text{TiO}_2\text{-F}$ lattice, resulting in a mild defect band state, whereas if N atoms were doped into the lattice, relatively serious structural distortions will occur, and Ti^{3+} and two independent N 2p defect states will form between the conduction band and the valence band. As for $\text{TiO}_2\text{-HF}$, H_2 can capture O and F atoms to generate large amounts of vacancies and corresponding Ti^{3+} in the TiO_2 lattice. Similarly, H_2 can react with N, F and O atoms in $\text{TiO}_2\text{-NF}$ lattices and maintain the amount of OV_s (N), OV_s (F) and OV_s (H) as well as different Ti^{3+} (N), Ti^{3+} (F), Ti^{3+} (H) and Ti^{3+} (H'), leading to a dark brown color. In another example, Hoang et al. [120] obtained TiO_2 nanowire arrays through calcination in various atmospheres including H- TiO_2 (500 °C in H_2/Ar for 1 h), N- TiO_2 (500 °C in NH_3 for 2 h) and H, N- TiO_2 (500 °C in H_2/Ar for 1 h followed by NH_3 at 500 °C for 2 h) and reported no obvious color change after hydrogenation as compared with pristine TiO_2 but that the color changed to green after nitridation and dark green after both nitridation and hydrogenation (Fig. 15c).

3.2.1.5 Plasma-Enhanced Hydrogenation For plasma-enhanced hydrogenation, Yan et al. [121] obtained various colored TiO_2 after treatment with hydrogen plasma in which white TiO_2 was treated by using an inductively coupled

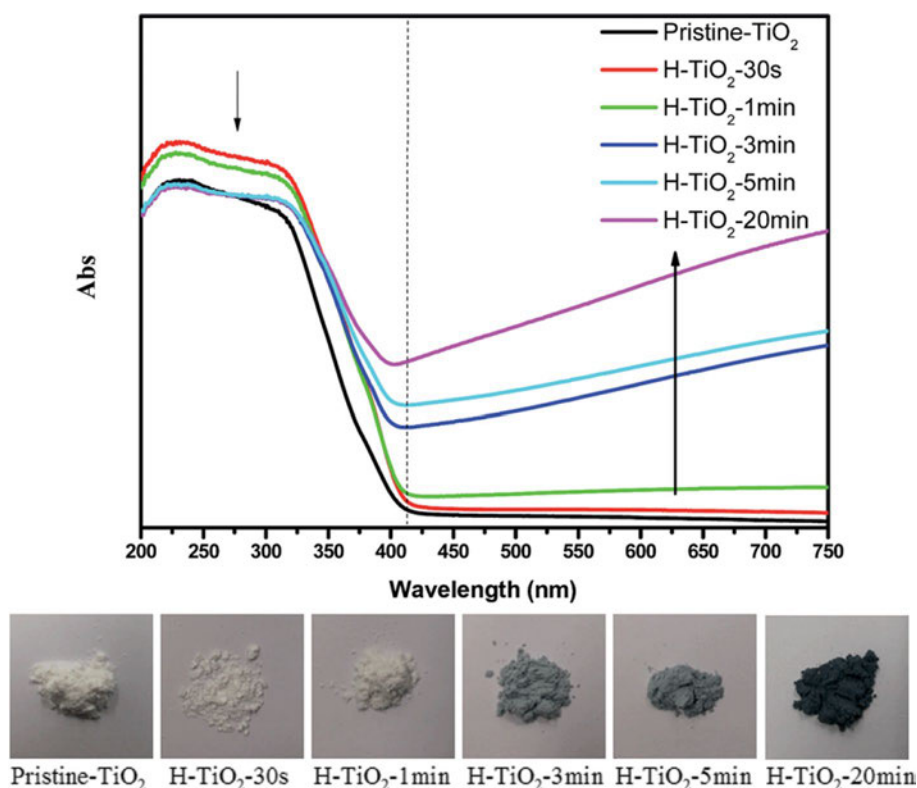
plasma instrument at 150 °C for 30 s, 1 min, 3 min, 5 min and 20 min and reported that the color of TiO_2 gradually deepened from white to blue (3 min) to dark blue (5 min) and finally to black (20 min) (Fig. 16) as confirmed by the increasing visible light absorbance in the UV–Vis spectra. Wu et al. [122] also prepared blue TiO_2 through hydrogen plasma treatment in which white TiO_2 was preheated in a vacuum at 320 °C for 0.5 h and subsequently treated with hydrogen plasma for 1.5 h under 50 Pa H_2 gas, and they observed a similar color evolution from white to blue.

3.2.2 Active Metal Reduction

Compared with hydrogen, metal elements such as Li, Al, Mg and Zn possess relatively high reducing activities and can partially capture oxygen atoms to leave OV_s and Ti^{3+} centers in lattices [79, 123–126]. In addition, significant advantages such as low costs and simple and safe preparation methods have attracted widespread attention for metal reduced TiO_2 .

3.2.2.1 Li-Based Reduction As an example of Li-based reduction, Ou et al. [79] obtained black TiO_2 through a simple grinding process in which the initial white TiO_2 turned blue with the addition of 1 wt% Li powder and subsequently changed to black as the amount of Li powder increased (Fig. 17a). Here, these researchers reported that this obvious color change did not affect the crystal structure of TiO_2

Fig. 16 UV–Vis absorption spectra and related photographs of obtained TiO_2 with H_2 plasma treatment for 30 s, 1 min, 3 min, 5 min and 20 min, respectively. Reprinted with permission from Ref. [121], copyright (2014) Royal Society of Chemistry



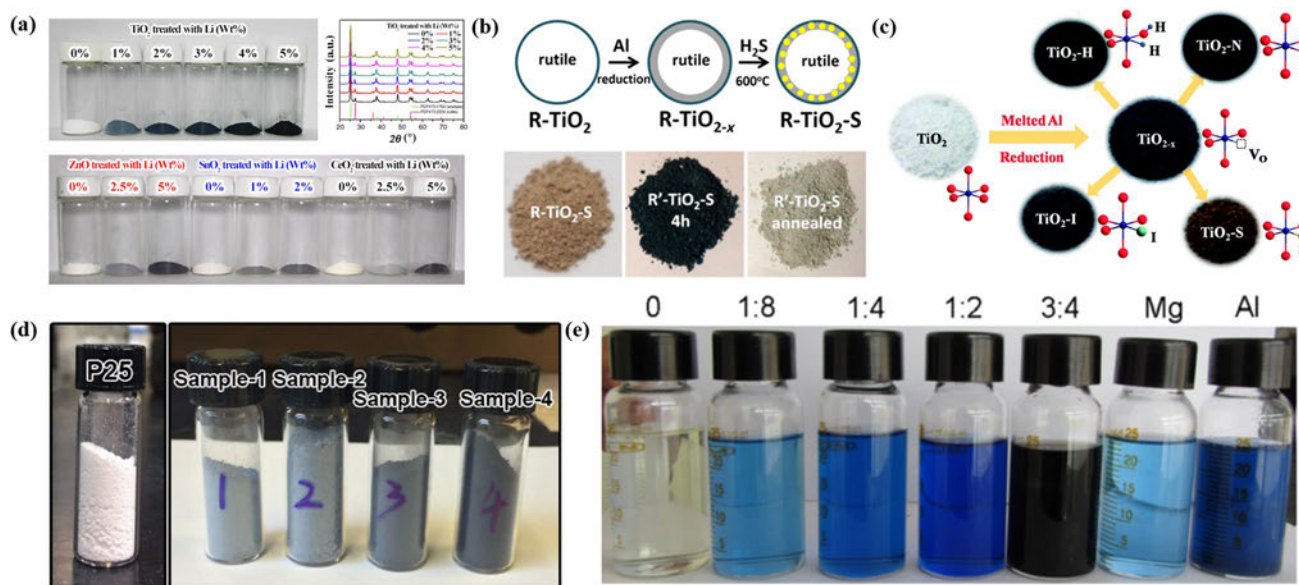


Fig. 17 **a** Photographs of pristine and Li-reduced oxide nanoparticles: TiO_2 , ZnO , SnO_2 and CeO_2 . Reprinted with permission from Ref. [79], copyright (2018) Springer Nature. **b** Schematic of the synthesis of rutile TiO_2 (R-TiO_2) with a sulfurized surface along with photographs of $\text{R-TiO}_2\text{-S}$, $\text{R'-TiO}_2\text{-S-4 h}$ and $\text{R'-TiO}_2\text{-S}$ annealed at 800°C in an Ar atmosphere through Al reduction. Reprinted with permission from Ref. [123], copyright (2013) American Chemical Society. **c** Evolution from pristine TiO_2 to TiO_{2-x} and to x -doped TiO_{2-x} ($x=\text{H}$,

N , S , I). Reprinted with permission from Ref. [124], copyright (2014) Royal Society of Chemistry. **d** TiO_2 obtained by adding 60 mg (sample 1), 120 mg (sample 2), 240 mg (sample 3) and 400 mg (sample 4) Mg powder. Reprinted with permission from Ref. [125], copyright (2017) John Wiley and Sons. **e** TiCl_4 solutions in ethanol after adding Zn powder at different ratios and Mg, Al powder ($\text{Mg/Al:TiCl}_4=2:1$). Reprinted with permission from Ref. [126], copyright (2013) Royal Society of Chemistry

as shown in XRD results and that this lithiation effect with TiO_2 can also occur for oxides such as ZnO , SnO_2 and CeO_2 .

3.2.2.2 Al-Based Reduction As for Al-based reduction, Yang et al. [123] prepared a core-shell structured black TiO_2 through a two-step reducing process in which Al powder and pristine TiO_2 were separately placed in an evacuated two-zone furnace at 800°C (Al) and 500°C (TiO_2) for 6 h followed by reheating at 600°C for 4 h under a H_2S atmosphere (1000 Pa) in which a surface disorder layer formed on rutile TiO_2 through the initial molten Al reductive treatment and S atoms were incorporated into the disordered shell under subsequent heating in a H_2S atmosphere (Fig. 17b). Here, these researchers reported that the sulfurized TiO_2 possessed a light brown or black color based on the TiO_2 surface phase and that the black rutile $\text{TiO}_2\text{-S}$ returned to gray after annealing. Lin et al. [124] also obtained black TiO_2 through a two-step synthesis process involving Al-based reduction and ion doping in which black TiO_{2-x} was initially prepared through Al reduction in a two-zone evacuated furnace at 800°C followed by reheating at 500°C for 4 h in atmospheres of hydrogen plasma, S and I_2 , and a mixed atmosphere of NH_3 and Ar (2:1) to form H-doped black titania ($\text{TiO}_2\text{-H}$), S- and I-doped black titania ($\text{TiO}_2\text{-S}$, I), and N-doped black titania ($\text{TiO}_2\text{-N}$), respectfully (Fig. 17c).

3.2.2.3 Mg-Based Reduction In terms of Mg-based reduction, Ye et al. [125] prepared colored TiO_{2-x} through calcination at 500, 600 and 700°C in Ar atmosphere for 4 h under a controlled ratio of TiO_2 and Mg powder and reported that white TiO_2 (P25) gradually changed to gray, blue-gray, light black or dark black with increasing amounts of Mg powder (Fig. 17d). Sinhamahapatra et al. [127] also prepared black TiO_2 through a similar process in which mixed TiO_2 and Mg powder was transferred to a tube furnace and heated at 650°C for 5 h under a 5% H_2/Ar atmosphere, and reported that the reduced TiO_2 presented different colors based on the amount of Mg powder added.

3.2.2.4 Zn-Based Reduction As an example of Zn-based reduction, Zheng et al. [126] synthesized Ti^{3+} self-doped TiO_2 through a facile Zn powder reduction process and reported that the solution color gradually changed from light blue to dark blue and to black based on the different Zn/ TiCl_4 molar ratios of 0, 1:8, 1:4, 1:3, 1:2 or 3:4 (Fig. 17e). In addition, these researchers also used Mg and Al powders in place of Zn and reported that the resulting solutions turned light blue and dark blue, respectively. Here, these solutions were transferred into a Teflon autoclave and heated at 180°C for 24 h to obtain Ti^{3+} self-doped TiO_2 .

Table 3 Comparison of reducing agents in the induction of defect structures in TiO₂/LTO

Pristine TiO ₂ /LTO color	Reductant	Defect TiO ₂ /LTO color	References
White	NaBH ₄	Gray and black	[128, 129]
White	C ₂ H ₅ OH	Blue or black	[130, 131]
White	CaH ₂	Black	[132]
White	N ₂ H ₄	Black	[133]
White	Diethylene glycol	Black	[134]
White	Imidazole	Gray	[135]
White	Electrochemical reduction	Brown or black	[136, 137]

3.2.3 Other Chemical Reduction Processes

In addition to H₂ and metal reducing agents, other reducing agents can also capture oxygen atoms and create defect structures in TiO₂/LTO, resulting in corresponding color changes from white to blue or black (Table 3).

3.2.3.1 NaBH₄ As an example of NaBH₄ as a reducing agent, Ariyanti et al. [128] prepared defective black TiO₂ through a sealing-transfer reduction process using NaBH₄ as a reducing agent followed by annealing at 300–450 °C under an Ar atmosphere for 1 h and reported that white TiO₂ gradually changed to gray and black with increasing temperatures (Fig. 18a). Similarly, Xu et al. [129] also prepared

defective black TiO₂ through a NaBH₄ high-temperature reducing process at 425 °C for 2 h under an Ar atmosphere.

3.2.3.2 C₂H₅OH As for C₂H₅OH as a reducing agent, Chen et al. [130] were able to prepared black TiO₂ through a facile synthetic procedure in which TiO₂ nanoparticles (0.5 g) were dispersed in ethanol (50 mL) to form a milky-white suspension followed by heating at 400 °C for 3 h, which led to an obvious color change from white to black. Nasara et al. [131] also obtained highly oxygen-deficient Li₄Ti₅O₁₂ using a facile C₂H₅OH reducing strategy in which TiO₂ and Li₂CO₃ (a molar ratio of Ti/Li = 5:4) were mixed through wet ball milling and heated to 800 °C for 0–8 h under ambient atmosphere. Here, these researchers reported that anatase TiO₂ tended to transform into a rutile phase and

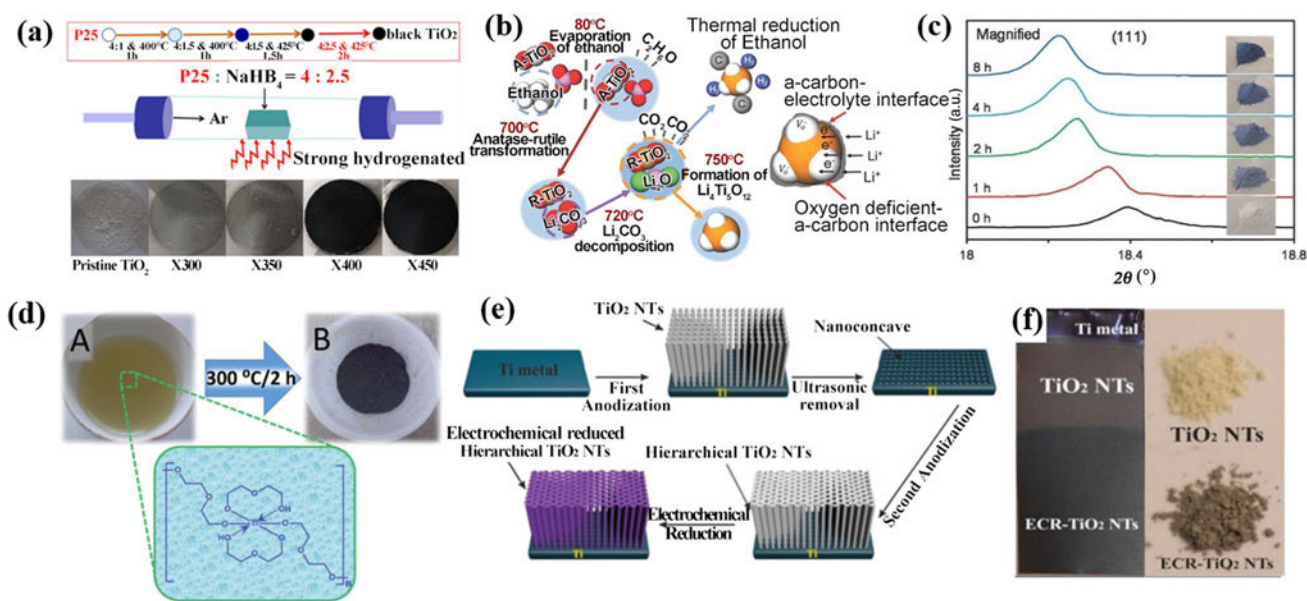
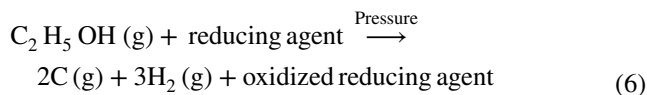


Fig. 18 **a** Schematic for the preparation of black TiO₂ and photographs of colored TiO_{2-x}. Reprinted with permission from Ref. [129], copyright (2017) IOP Publishing. **b** Formation mechanism of defective-LTO and **c** XRD of LTO calcined at 800 °C for various time periods. Reprinted with permission from Ref. [131], copyright (2017) John Wiley and Sons. **d** Photographs of (A) Ti glycolate gel

and (B) black anatase TiO_{2-x} with the Ti glycolate gel structure highlighted. Reprinted with permission from Ref. [134], copyright (2016) Royal Society of Chemistry. **e** Ti³⁺ self-doped TiO₂ NT synthesis and **f** photographs of TiO₂ NTs and detached ECR-TiO₂ NT powders. Reprinted with permission from Ref. [136], copyright (2013) Royal Society of Chemistry

Li_2CO_3 will thermally decompose to form CO_2 and Li_2O at high temperatures (Fig. 18b), allowing Li_2O to react with TiO_2 to form $\text{Li}_4\text{Ti}_5\text{O}_{12}$ and the accelerated thermal reduction of $\text{C}_2\text{H}_5\text{OH}$ with evolved CO_2 gas in which the reducing agent can capture oxygen atoms and form highly oxygen-deficient $\text{Li}_4\text{Ti}_5\text{O}_{12-x}$ (Eq. 6). And based on XRD results of LTO at 800 °C with different calcination times, the anatase and rutile- TiO_2 gradually disappeared and transformed into the LTO phase with increasing calcination times, corresponding to a change in the LTO color from light to dark blue (Fig. 18c).



3.2.3.3 CaH_2 In terms of CaH_2 , Tominaka et al. [132] synthesized TiO_{2-x} through a simple CaH_2 reducing process involving the mixing of TiO_2 and CaH_2 at a weight ratio of 1:4 under an Ar atmosphere followed by heating at 350 °C for 15 days and the washing of the obtained product with NH_4Cl and drying in air.

3.2.3.4 N_2H_4 Using N_2H_4 as a reducing agent, Mao et al. [133] in their study were able to fabricate higher Ti^{3+} self-doped TiO_{2-x} . In this synthesis process, Ti foil was briefly soaked in an aqueous HCl solution and hydrothermally treated at 220 °C for 18 h. Subsequently, the sample was washed with water, dried in Ar gas and reheated at 550 °C for 150 min under Ar. Finally, the sample was placed in a N_2H_4 solution (20%, 10 mL), preheated at 220 °C for 20 h and washed with water to remove residual N_2H_4 to obtain the final TiO_{2-x} .

3.2.3.5 Organic Reducing Agents In terms of organic reducing agents, Ullattila et al. [134] reported that Ti^{3+} self-doped black TiO_2 can be prepared by using a gel combustion strategy in which by mixing 0.2 M Ti(IV), butoxide (6.8 g) and diethylene glycol (50 mL), a yellow ethyl glycolate gel can be formed. Deionized water (14.4 mL) can subsequently be added to form a hydrated Ti glycolate gel, which if heated in a muffle furnace at 300 °C for 2 h, can produce black TiO_2 (Fig. 18d). In another example, Zou et al. [135] reduced TiO_2 with imidazole in which TiO_2 (0.5 g), imidazole (1 g) and HCl (37 wt%, 3 mL) were mixed, heated at 450 °C for 6 h and cooled to room temperature to form defective TiO_2 .

3.2.3.6 Electrochemical Reducing Agents As for electrochemical reducing agents, Zhang et al. [136] prepared Ti^{3+} self-doped TiO_2 through a two-step anodization and one-step reduction process. Here, a Ti sheet was anodized at

60 V for 30 min to remove the as-grown nanotube layer and the resulting nanoconcave Ti sheet was again anodized at 80 V for 5 min and heated at 450 °C for 1 h in air to obtain hierarchical TiO_2 nanotubes (TiO_2 NTs) (Fig. 18e). And during the electrochemical reduction process, the TiO_2 NTs were reduced at -0.4 V in a 1 M Na_2SO_4 electrolyte for 30 min in which the Ti^{4+} in the TiO_2 NTs captured electrons and converted to Ti^{3+} , causing a color change from white to brown (Fig. 18f). Dong et al. [137] also prepared defective TiO_{2-x} through a similar anodization technique in which a TiO_2 layer was grown on Ti foil through a two-step anodization process at 60 V for 10 h followed by heating at 450 °C for 1 h in ambient atmosphere to obtain black TiO_{2-x} .

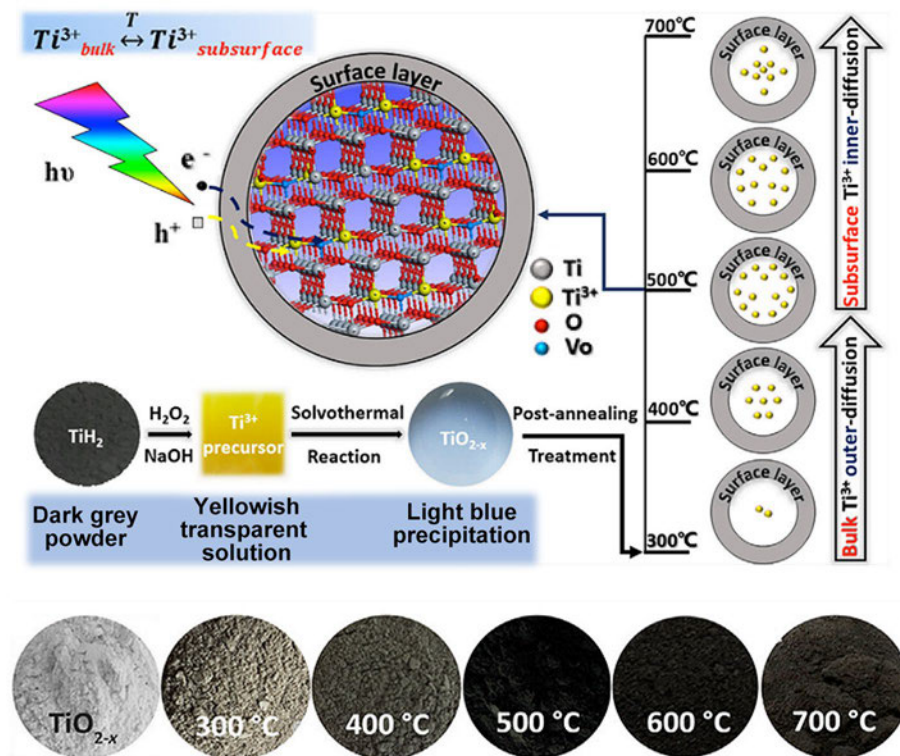
3.2.4 Chemical Oxidization

In addition to the reduction of Ti^{4+} to Ti^{3+} , the oxidation of low-valence state Ti (Ti^{2+} or Ti^{3+}) to Ti^{4+} and the maintenance of remaining partial low-valence states (Ti^{2+} or Ti^{3+}) in Ti-based oxides are also effective strategies to produce black defective TiO_{2-x} . Here, because low-valence state Ti (Ti^{2+} or Ti^{3+}) is relatively unstable and prone to being oxidized to Ti^{4+} , reducing agents are needed to ensure the formation of defective structures.

3.2.4.1 TiH_2 As an example of chemical oxidation by using TiH_2 , Xin et al. [76] prepared Ti^{3+} self-doped black TiO_2 through a typical oxidation process in which TiH_2 , H_2O and H_2O_2 were mixed to form a yellowish gel-like precursor followed by the addition of NaBH_4 and heating at 180 °C for 24 h to obtain light blue TiO_{2-x} . This TiO_{2-x} sample was subsequently heated at 300–700 °C for 3 h under a N_2 atmosphere to obtain various colors of TiO_{2-x} (Fig. 19). In other examples, Grabstanowicz et al. [138] conducted a similar oxidative conversion of TiH_2 to black TiO_{2-x} by adding H_2O_2 and Liu et al. [139] prepared Ti^{3+} self-doped TiO_{2-x} nanoparticles through a H_2O_2 oxidation-based method.

3.2.4.2 TiCl_3 As for TiCl_3 , Chen et al. [77] obtained dark-colored rutile TiO_2 using a solvothermal method in which Mg powder, TiCl_3 and isopropanol were uniformly mixed and treated with a hydrothermal process at 180 °C for 6 h to form a dark-gray TiO_2 powder. Zhu et al. [140] also prepared blue TiO_{2-x} through a facile solvothermal method in which TiF_4 and TiCl_3 were briefly dissolved in anhydrous alcohol and treated with a hydrothermal process at 180 °C for 24 h. These researchers in the same study also prepared a series of Ti^{3+} self-doped TiO_{2-x} samples by controlling the molar ratio of TiF_4 to TiCl_3 at 0, 1:5, 1:20, 1:40, 1:80 and 1:120, and Zhao et al. [141] prepared blue TiO_{2-x} through a

Fig. 19 Mechanism of Ti^{3+} distribution in as-prepared TiO_{2-x} and corresponding images of Ti^{3+} self-doped TiO_2 samples prepared with heating between 300 and 700 °C for 3 h in a N_2 gas flow. Reprinted with permission from Ref. [76], copyright 2015, Elsevier



hydrothermal reaction by mixing TiCl_3 with Zn powder in isopropanol.

3.2.4.3 TiO and Ti_2O_3 TiO and Ti_2O_3 can also be used for chemical oxidation. For example, Pei et al. [142] synthesized defective TiO_{2-x} through a simple hydrothermal process in which TiO and HCl solutions were mixed uniformly and treated with a hydrothermal process at 160 °C for 24 h. In another example, Dong et al. [143] prepared Ti^{3+} self-doped $\text{Li}_4\text{Ti}_5\text{O}_{12}$ through a novel solid-state strategy in which a stoichiometric ratio of Li_2CO_3 to Ti_2O_3 was mixed by ball milling for 4 h with ethanol as an additive and annealed at 800 °C for 6 h to obtain Ti^{3+} self-doped $\text{Li}_4\text{Ti}_5\text{O}_{12}$.

4 Characterization of Defects in TiO_2 and LTO

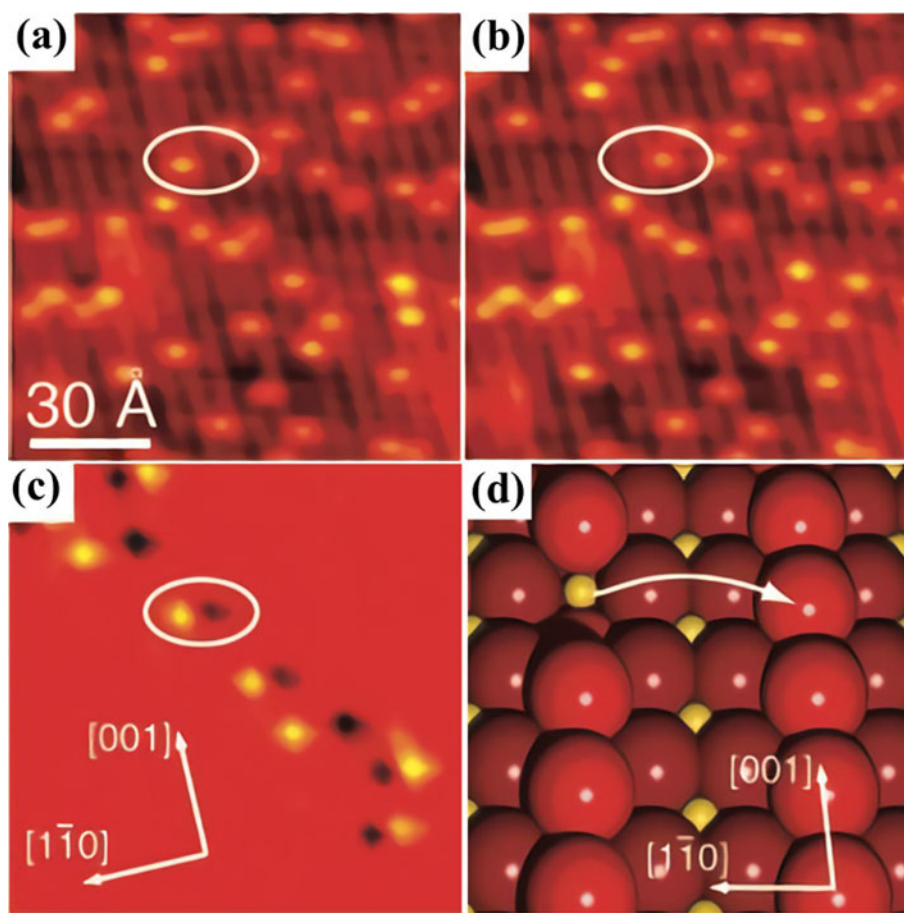
Nanoscale dimensions and extremely low concentrations of defects make their qualitative characterization and quantitative determination difficult. Overall, the most widely used characterization techniques for defects can be classified into scanning probe microscopy (SPM), incident photon-based techniques, incident electron-based techniques, thermal analysis and other techniques. Here, SPM can be directly used to visualize OV's at the nanoscale and molecular level and

indirect detection techniques can be applied with the help of incident photons or electrons. However, semiconductors with OV's possess different magnetic and electronic properties, which can lead to changes in spectroscopic response. As for thermal analysis and other related techniques, these can be used to monitor weight changes and reaction products during defect-inducing processes. In general, characterization techniques are powerful tools to investigate the impact of defects on the properties of Ti-based oxides and will be briefly discussed in this session.

4.1 Scanning Probe Microscopy (SPM)

Scanning probe microscopy (SPM) includes a range of techniques that can image surfaces and structures down to the atomic level by using a physical probe to scan samples. During the scanning process, a computer is used to gather data concerning the interaction between probes and surface changes with position in which minor changes in surfaces can greatly alter surface properties and affect interactions, which is the basic mechanism underlying atomic resolutions. And of the various SPM techniques, scanning tunneling microscopy (STM) and atomic force microscopy (AFM) are among the most widely used. As for Ti-based oxides, the conduction and valence bands of TiO_2 are usually dominated by Ti-3d and O-2p orbitals, respectively, and under applied voltage, electrons from the tip of an STM first tunnel to

Fig. 20 **a, b** Consecutive STM images of TiO_2 with a bridging OV marked by a circle. **c** Difference image constructed by subtracting **b** from **a**. **d** Ball model for the TiO_2 (110) surface. The arrow represents an observed vacancy diffusion pathway. Reprinted with permission from Ref. [144], copyright (2003) American Association for the Advancement of Science



the Ti-3d orbital in the conduction band before being transported away, allowing for the detection of Ti and O atoms (typically represented by bright or dark colors, respectively). Furthermore, OVs can create shallow donor states in band gaps and the Fermi level is elevated next to the conduction band minimum (CBM), causing these defects to appear as bright spots between bright Ti rows. As an example, two STM micrographs of a rutile TiO_2 (110) surface can indicate the existence of a diffusion pathway for OVs, which becomes more evident in the corresponding difference image (Fig. 20a–c, the ball model of this process is presented in Fig. 20d) [144].

4.2 Incident Photon-Based Techniques

4.2.1 X-Ray Diffraction (XRD) Pattern Analysis

As a widely used technique, XRD can detect changes in crystal structure as induced by OVs and dopants in which defects can be confirmed by XRD peak shifts. And unlike techniques that measure properties that have a direct association with OVs, XRD results need to be confirmed with other techniques (XPS, EPR, etc.) to eliminate other possibilities and provide direct evidence of OVs. For example,

Choudhury et al. [145] prepared Co-doped TiO_2 nanoparticles and found a slight shift of the (101) peak toward lower angles (Fig. 21a) as well as a larger full width at half maximum (FWHM) in which the decrease in peak intensity confirmed structural irregularity after doping. Here, the altered position of the diffraction peak can be explained by considering the different chemical valence states of Ti^{4+} and Co^{2+} in which as OVs are formed after doping to maintain charge neutrality, changes in the local structure surrounding Co^{2+} ions occur in accordance with other reported studies [146–148]. A similar phenomenon was also observed in defective LTO (Fig. 21b) in which the characteristic blue color as well as the shifting of (111) and (311) peaks toward lower angles was consistent with the presence of OVs as confirmed by XPS [131].

4.2.2 X-Ray Absorption Fine Structure (XAFS) Spectroscopy

The irradiation of samples with high intensity X-ray beams can cause sharp increases in absorption to produce absorption edges at certain energy. The oscillatory feature above the edge is called X-ray absorption fine structure (XAFS) and is caused by interferences between photoelectrons and surrounding atoms [149]. In addition, this energy-dependent

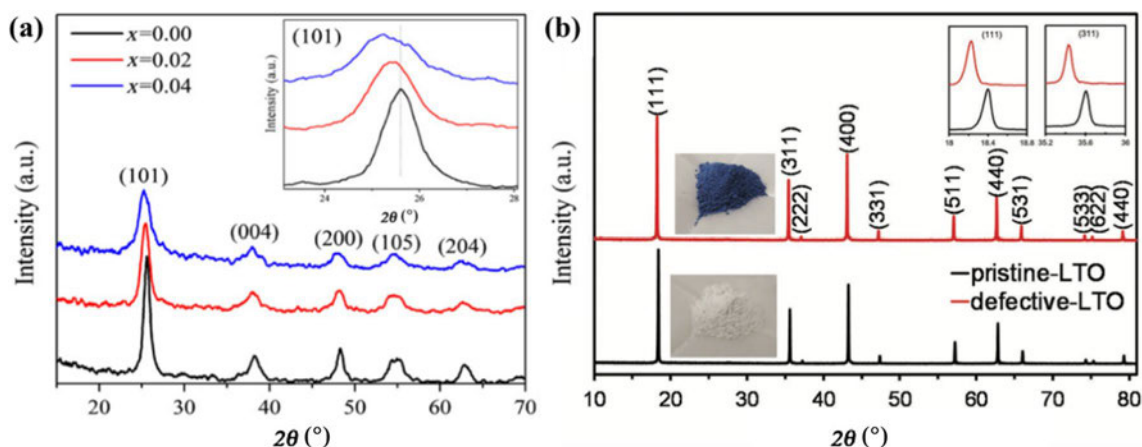


Fig. 21 **a** XRD patterns of undoped and Co-doped TiO_2 nanoparticles. Reprinted with permission from Ref. [145], copyright 2012, Elsevier. **b** Pristine and defective LTO synthesized in a reducing

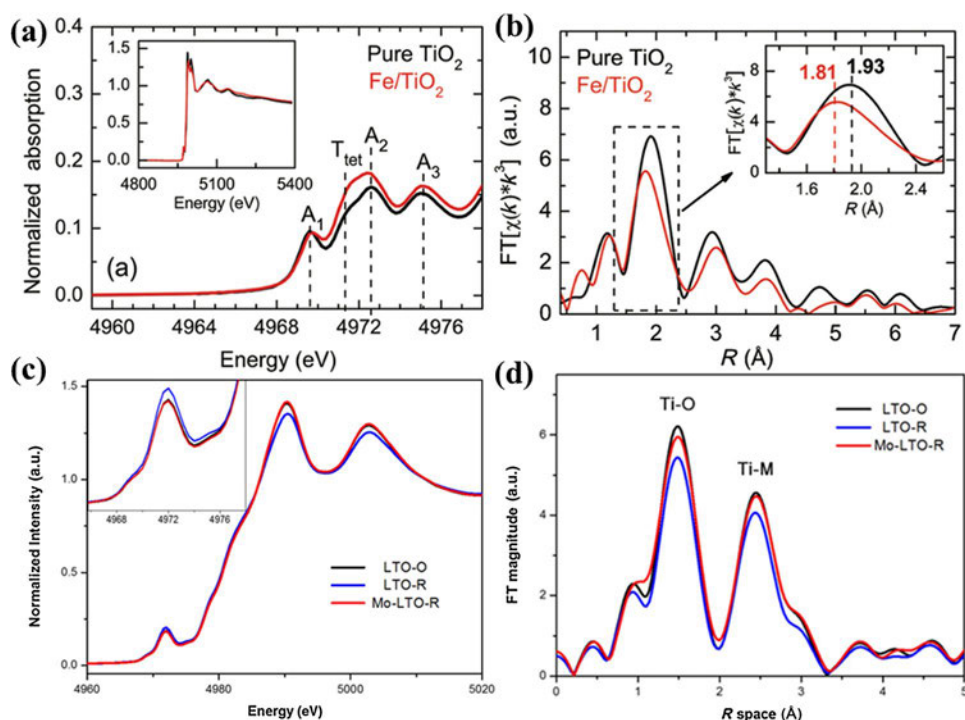
atmosphere at 800 °C under high pressure. Reprinted with permission from Ref. [131], copyright (2017) John Wiley and Sons

variation in the X-ray absorption spectrum can be divided into X-ray absorption near-edge spectroscopy (XANES) and extended X-ray absorption fine-structure spectroscopy (EXAFS) in which the former (from the edge to 30–50 eV) contains information concerning the electronic structure and the oxidation state of absorbing atoms, whereas the latter (from 30–50 eV to 1000 eV) is sensitive to the bond length, the coordination number and surrounding species of absorbing lattice atoms. Here, the presence of defects can change the coordination number and the chemical bond length of Ti–O to alter the chemical environment of nearby atoms, and

therefore, XAFS can be an effective technique to investigate defects in TiO_x .

For example, Wu et al. [74] investigated the transformation of Ti^{4+} local structures induced by OV's using XANES and EXAFS and reported three low-density pre-edge peaks (A_1 , A_2 , A_3) characteristic of the octahedral coordination of Ti (Fig. 22a). Here, these researchers attributed this to the transition from the Ti 1s orbital to different molecular orbitals ($1t_{1g}$, $2t_{2g}$ and $3e_g$) [150, 151]. In addition, these researchers reported that as compared with pure TiO_2 , a new absorption shoulder peak (T_{tet}) between A_1 and A_2

Fig. 22 **a** Ti K-edge XANES spectra and **b** the magnitude component of Fourier transformed k^3 -weighted $\chi(k)$ of the Ti K-edge EXAFS spectra for pure TiO_2 and Fe-doped TiO_2 . Reprinted with permission from Ref. [74], copyright (2012) American Chemical Society. **c** Ti K-edge XANES spectra and **d** EXAFS spectra of undoped $\text{Li}_4\text{Ti}_5\text{O}_{12}$ in an oxidizing atmosphere (LTO-O), undoped $\text{Li}_4\text{Ti}_5\text{O}_{12}$ in a reducing atmosphere (LTO-R) and Mo-doped $\text{Li}_4\text{Ti}_5\text{O}_{12}$ in a reducing atmosphere (Mo-LTO-R). Reprinted with permission from Ref. [155] under Creative Commons



can be observed for Fe-doped TiO_2 , indicating the presence of tetrahedrally coordinated Ti ions in which Ti ions remained in the form of Ti^{4+} instead of Ti^{3+} because the first maximum of the first derivative for the main edge jump did not shift to lower energy [152, 153]. These researchers also reported that the Ti–O bond length shrank from 1.93 to 1.81 Å (Fig. 22b), which is close to the Ti–O distance in TiO_4 tetrahedra [150, 154], clearly providing evidence of the existence of tetrahedrally coordinated Ti^{4+} . In another example, Song et al. [155] used XANES to study changes in the OV concentration in $\text{Li}_4\text{Ti}_5\text{O}_{12}$ in which the obtained pre-edge peak centered at 4972 eV corresponded to the pure electric quadrupole $1s \rightarrow 3d$ transition and the peak for LTO-R was found to be higher than that for LTO-O, indicating the increased distortion of the TiO_6 octahedral structure for LTO-R (Fig. 22c). Here, these researchers suggested that the intensity of the pre-edge peak was directly related to a break in central symmetry, which can be attributed to OVs, demonstrating that LTO-R possesses a higher OV content. The same conclusion was also drawn after analyzing the peak position at ~4990 eV, which represented the $1s \rightarrow 4p$ transition in which the hybridization of Ti $p - t_{2g}$ orbitals was enhanced due to severer distortions, leading to the lower probability of $1s \rightarrow 4p$ transition. Furthermore, the results of the Ti K-edge EXAFS analysis in this study also demonstrated that the distortion of the TiO_6 octahedral structure in LTO-R was intenser than that in the other two (as calculated by using Debye–Waller factors) (Fig. 22d) [155].

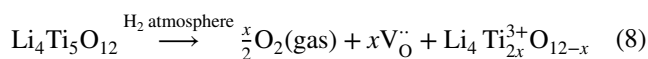
4.2.3 X-Ray Photoelectron Spectroscopy (XPS)

XPS, also known as electron spectroscopy for chemical analysis (ESCA), is a quantitative technique to analyze the surface of a sample and provide information concerning elemental composition, chemical valence states, electronic states and so on. The basic principle of XPS is to simultaneously measure kinetic energy and the number of photoelectrons ejected from a surface through monoenergetic X-rays (for Al $K\alpha$ X-rays, $h\nu = 1486.7$ eV) under high vacuum conditions in which the kinetic energy (E_K) of electrons depends on the irradiating photon energy ($h\nu$), the binding energy (E_B) between electrons and nuclei relative to the Fermi level and the work function (ϕ), which is an adjustable instrumental correction factor calculated by using Eq. 7 [156]:

$$h\nu = E_K + E_B + \phi \quad (7)$$

And based on the value of E_B and the chemical shift, elemental composition and chemical bonding states can be calculated quantitatively because binding energy is related to the structure of electron shells and the surrounding environment of atoms in question. For example, Kang et al. [157] studied TiO_2 nanotube arrays (NTAs) with OVs prepared

through NaBH_4 treatment using XPS and reported similar shifts of O 1s and Ti 2p, indicating the migration of electrons from O and Ti ions to OVs that can be regarded as electron traps (Fig. 23a, b). These researchers also used valence band XPS (VBXPS) to investigate the density of states (DOS) and the occupation of electronic states in the valence band and reported that the introduction of OVs can lead to the narrowing of band gaps from 2.03 to 1.50 eV as well as the presence of a slight band tail at ~0.97 eV (Fig. 23c). Here, these researchers suggested that the band tail represented localized defect states in the band gap at 0.75–1.18 eV below the CBM (Fig. 23d). In addition to peak shifts and defect states, XPS can also be used to confirm the existence of defects through peaks in deconvolved spectra [158] in which new peaks were observed at 684.8 eV (F^-) [148], 485.8 eV (Sn^{2+}) and 486.4 eV (Sn^{4+}) [159] as compared with pristine TiO_2 . And as for reference $\text{Li}_4\text{Ti}_5\text{O}_{12}$ (R-LTO), the deconvolved XPS spectrum could only be fitted with two single peaks, implying that all Ti ions were Ti^{4+} (Fig. 23e), whereas for LTO with OVs (Fig. 23f), each of the two peaks could be deconvolved into two component peaks, indicating the existence of Ti^{3+} that formed with OVs through Eq. 8:



4.2.4 Raman Spectroscopy

Raman spectroscopy is a nondestructive technique based on the inelastic scattering of monochromatic light, usually from a high-intensity laser source in which laser light photons are initially absorbed by analyte and subsequently re-emitted. This re-emitted light of the same wavelength as the laser source is called the Rayleigh scattered light (elastic scattering) and does not contain structural information concerning samples but does constitute most of the scattered light. Here, only a small proportion of photons shift up or down frequencies due to interactions with chemical bonds in materials. These photons are called Raman scattered light (inelastic scattering), and changes in frequency can provide information concerning vibrational, rotational and other low-frequency transitions in samples [160]. In terms of TiO_2 , the main Raman active mode centered around 142 cm^{-1} (E_g) possesses a blueshift and a larger FWHM for partially reduced TiO_2 that becomes more evident with increasing reaction temperatures (Fig. 24a) [161]. This phenomenon is generally attributed to the small size effect of crystalline grains (< 10 nm) or the decreased correlation lengths as induced by defects in which the former can be excluded because the size of nanoparticles is not less than 19 nm. And considering that the liquid reduction process does not introduce any impurities as shown in energy dispersive X-ray results (Fig. 27a), the only practical conclusion is that OVs

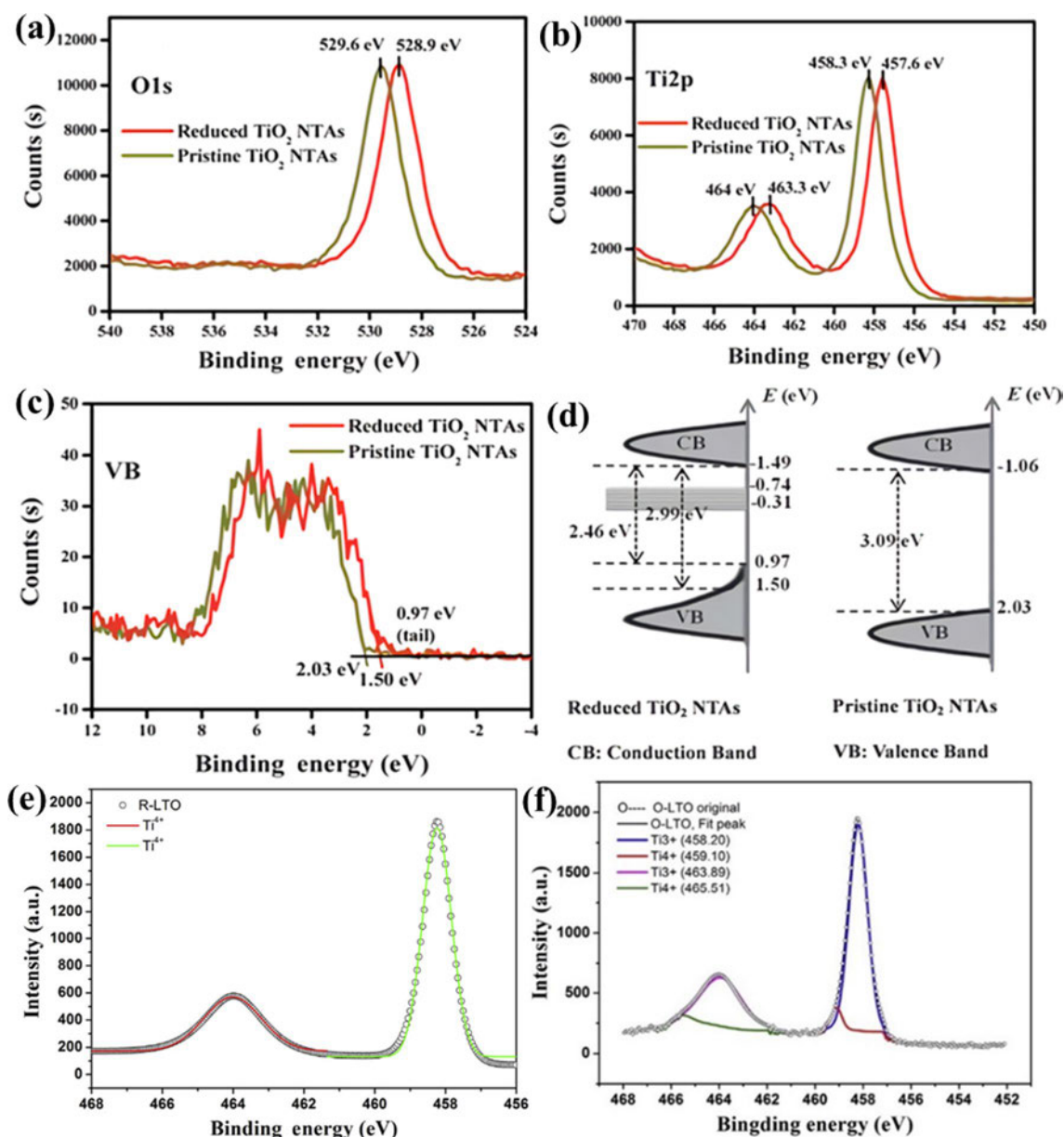


Fig. 23 **a** O 1s, **b** Ti 2p and **c** valence band XPS spectra of pristine and NaBH_4 reduced TiO_2 NTAs. **d** Schematic of the DOS of reduced and pristine TiO_2 NTAs. Reprinted with permission from Ref. [157], copyright 2013, Royal Society of Chemistry. **e** Deconvoluted XPS

spectra of reference $\text{Li}_4\text{Ti}_5\text{O}_{12}$ (R-LTO) and **f** $\text{Li}_4\text{Ti}_5\text{O}_{12}$ with OV (O-LTO) synthesized under 5 vol% H_2/Ar atmosphere. Reprinted with permission from Ref. [158], copyright 2017, Elsevier

led to the blueshift and larger FWHM. Furthermore, a similar blueshift at 144 cm^{-1} can also be observed in F-doped TiO_2 [148], and as for $\text{Li}_4\text{Ti}_5\text{O}_{12}$ nanoparticles [162], the Raman peaks possess a blueshift from 674 to 680 cm^{-1} , which corresponds to the Ti–O vibration mode (Fig. 24b), meaning that more OV are produced under an Ar/H_2 reducing atmosphere (8% mol). Moreover, the correlation between shifts/broadening of Raman peaks and the presence of OV has also been observed in other studies [74, 163–165].

4.2.5 Fourier Transform Infrared (FTIR) Spectroscopy

FTIR spectroscopy can be used to obtain the spectra of infrared light absorption or emission in samples. Here, different vibration modes of various bonds can selectively absorb the radiation of specific wavelengths and these wavelengths can cause changes in dipole moments and elevate vibrational energy levels in which the frequency of absorption peaks is based on the vibrational energy gap between ground states and excited states. In addition, the number of vibrational

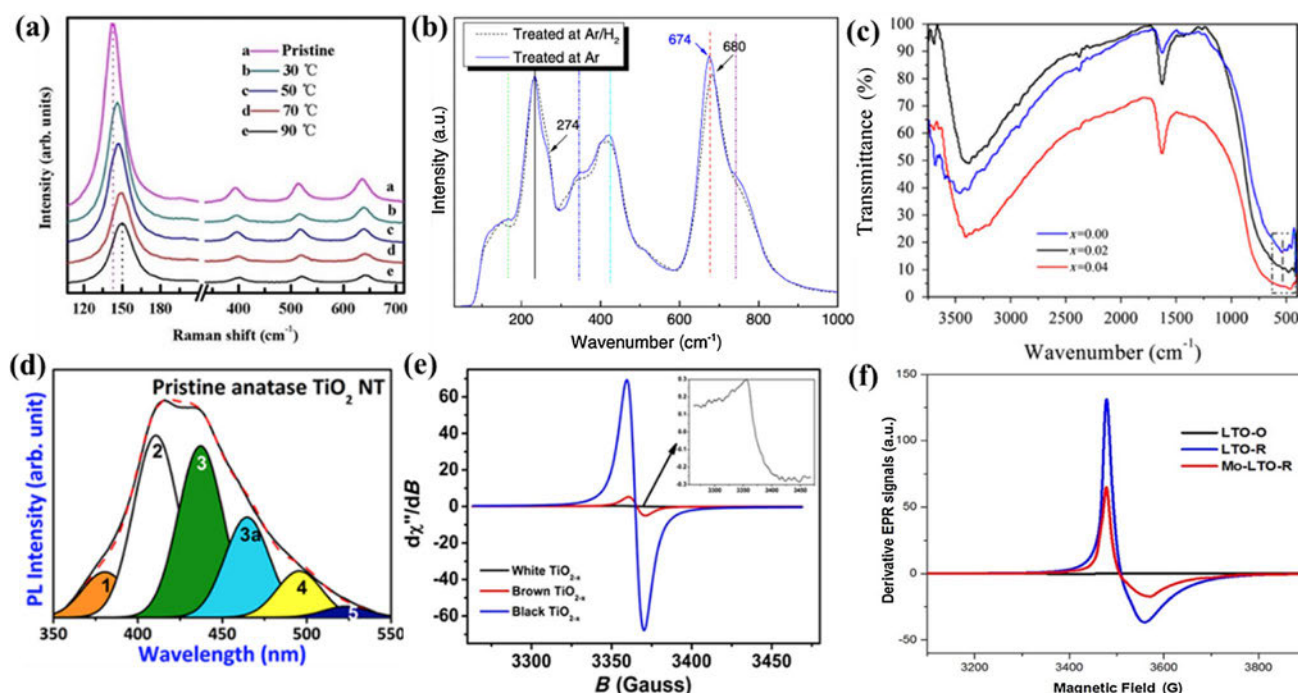


Fig. 24 **a** Raman spectra of the pristine anatase phase of TiO_2 nanotube arrays (TNAs) and partially reduced TNAs (PR-TNAs) in NaBH_4 solution at different temperatures. Reprinted with permission from Ref. [161], copyright 2015, IOP Publishing. **b** Raman spectra of $\text{Li}_4\text{Ti}_5\text{O}_{12}$ synthesized under different atmospheres. Reprinted with permission from Ref. [162], copyright 2011, Springer Nature. **c** FTIR spectra of undoped and Co^{2+} doped TiO_2 nanoparticles. Reprinted with permission from Ref. [145], copyright 2012, Elsevier. **d** Gaussian peak fitted PL spectra of TiO_2 nanotubes. Reprinted with permis-

sion from Ref. [166], copyright (2017) American Chemical Society. **e** EPR spectra of defective TiO_2 nanoparticles reduced by L-ascorbic acid (0, 0.3 and 0.7 g corresponding to white, brown and black TiO_{2-x}). Reprinted with permissions from Ref. [167] under Creative Commons. **f** Derivative EPR spectra of undoped LTO in oxidizing (LTO-O) and reducing atmospheres (LTO-R) as well as Mo-doped LTO in reducing atmosphere (Mo-LTO-R). Reprinted with permissions from Ref. [155] under Creative Commons

freedom degrees of chemical bonds can determine the number of absorption peaks. Therefore, by analyzing FTIR spectra, vibration modes in TiO_2 or $\text{Li}_4\text{Ti}_5\text{O}_{12}$ crystal lattices can be investigated, which are affected by synthesis conditions, doped ions, presence of OV, etc. Furthermore, FTIR spectroscopy can be used to confirm the presence of OV in doped Ti oxides. In general, absorption peaks around $400\text{--}800\text{ cm}^{-1}$ can be attributed to the bending and stretching vibration modes of Ti-O-Ti and Ti-O bonds [168, 169]. For example, Choudhury et al. [145] found a redshift for doped TiO_2 nanoparticles in the peak position of Ti-O from 454 cm^{-1} (undoped TiO_2) to 425 cm^{-1} and 423 cm^{-1} (0.02 and 0.04 Co^{2+} -doped TiO_2 , respectively) (Fig. 24c). And because of charge neutrality, OV were undoubtedly introduced into the Co^{2+} -doped samples, which can decrease the number of O ions available to form chemical bonds with metal ions, meaning bond strengths and force constant values (k) will decrease according to Eq. (9):

$$\nu = \frac{1}{2\pi c} \left(\frac{k}{\mu} \right)^{\frac{1}{2}} \quad (9)$$

in which ν is the wave number, k is the force constant of the chemical bond and μ is the reduced mass of the bond associated with the elements, meaning that lowered k or increased μ will lead to redshifting in corresponding FTIR peaks. Similar results for redshifting in FTIR spectra peaks were also reported for Zn- and Mn-co-doped TiO_2 [170].

4.2.6 Photoluminescence (PL) Spectroscopy

Photoluminescence (PL) is a process in which electrons are excited to higher electronic states after absorbing photons and subsequently return to lower energy states and radiate photons. PL spectroscopy can allow for the characterization of properties at the surface/interface of samples, especially those related to impurities and defects. For example, Sarkar et al. [166] conducted room-temperature PL emission spectra for TiO_2 nanotubes by exciting samples with 325 nm wavelength photons. Here, the obtained Gaussian curve fitted PL spectra (Fig. 24d) showed several peaks in which peak 1, positioned around 380 nm (3.26 eV), matched well with the band gap energy of anatase TiO_2 whereas peak 2 (411 nm, 3.01 eV) and peak

4 (496 nm, 2.5 eV) can be assigned to free exciton recombination and band tails, respectively, and peak 3 (437 nm, 2.84 eV) and peak 5 (523 nm, 2.37 eV) are related to surface defects or surface OV, which can further become F and F⁺ centers. In addition, these researchers suggested that peak 3a centered around 465 nm (2.66 eV) originated from shallow and deep surface traps, which are associated with Ti³⁺ states that are a result of the combination of electrons in F centers and adjacent Ti⁴⁺ ions based on Eqs. (10–13) [171]:



And as a result of these findings, it can be confirmed that visible light PL emission peaks in TiO₂ are closely related to OV defects. Moreover, researchers have also reported that for Co-doped TiO₂, an obvious decrease in intensity ratios of UV to visible emission peaks with dopant concentration can be observed [145].

4.2.7 Electron Paramagnetic Resonance (EPR)

Electron paramagnetic resonance (EPR), also known as electron spin resonance (ESR), is another powerful and nondestructive method to study materials with unpaired electrons based on the fact that every electron possesses a magnetic moment and a spin quantum number ($m_s = \pm 1/2$). Here, in the presence of an external magnetic field (B_0), separation between lower and upper states of unpaired electrons occurs with energy differences being calculated based on $\Delta E = g \mu_B B_0$ in which g is the Landé g -factor, μ_B is the Bohr magneton ($\mu_B = e\hbar/2m_e = 5.7884 \times 10^{-5} \text{ eV T}^{-1}$), and B_0 is the strength of the applied magnetic field. And based on this equation, the splitting of energy levels is directly proportional to the strength of the applied magnetic field. In addition, unpaired electrons can move between two energy levels by absorbing or emitting photons with a frequency of ν with the condition $\Delta E = h\nu$ (h is Planck's constant). Based on this, the fundamental equation of EPR spectroscopy is: $h\nu = g \mu_B B_0$. Moreover, aside from original absorption spectra, the first derivative of EPR signals is the most common method to report results. Overall, multiple studies have confirmed that EPR is an extraordinarily powerful technique to identify OVs and OV-related defect states [155, 158, 167, 172–177] in which for reduced TiO₂ nanoparticles, F⁺ centers (OVs containing a single electron) and Ti³⁺ ([Ar]3d¹)

can be directly detected. And based on Eq. (11) in which Ti³⁺ ions are formed after Ti⁴⁺ ions gain an electron from adjacent OVs (F centers), the presence of Ti³⁺ ions can be regarded as a sign of the presence of OVs. For example, defective TiO_{2-x} and Mo-doped Li₄Ti₅O₁₂ samples show strong EPR signals around $g=2$, which can be ascribed to single electron-trapped OVs (F⁺ centers) (Fig. 24e, f), and in general, g values around 1.96–1.99 correspond to Ti³⁺ ions on surfaces. Furthermore, large increases in EPR signal intensities for brown and black TiO_{2-x} can also indicate the increased production of OVs with increasing reduction from L-ascorbic acid (Fig. 24e). Similar increases can also be observed for LTO-O (in oxidizing atmosphere) and LTO-R (in reducing atmosphere) (Fig. 24f). Alternatively, the EPR signal intensity for Mo-doped LTO is markedly lower than that for LTO-R however, indicating a decrease in OVs. This can be explained by the fact that because the Mo dopant is in its Mo⁶⁺ state (confirmed by XPS), the partial reduction of Ti⁴⁺ ions is caused by charge compensation (the high valence dopant) similar to n-type doping rather than the introduction of OVs in reducing atmospheres.

4.3 Incident electron-based techniques

4.3.1 Positron Annihilation Spectroscopy (PAS)

Positron annihilation spectroscopy (PAS) is a nondestructive technique with high sensitivity to voids and defects in solids, especially to those that cannot be detected with other characterization methods. PAS operates on the principle that as a positron interacts with its antiparticle electron, they annihilate and release gamma rays that can be detected. Here, the lifetime of a positron can be calculated by recording the time difference between the emission of positrons from the radioactive source (e.g., ²²Na) and the detection of the produced gamma rays. And because positrons prefer to be trapped by atomic defects, leading to different lifetimes and diffusion lengths, these results can provide information concerning the electronic environment of annihilation sites, which correspond to various vacancies with different sizes, concentrations and so on. Overall, the three widely performed PAS techniques include positron annihilation lifetime spectroscopy (PALS), Doppler broadening spectroscopy (DBS) and angular correlation of annihilation radiation (ACAR). As an example, Jiang et al. [111] investigated the OVs of pristine and hydrogenated TiO₂ using PALS and found that in the obtained spectra, the first component (τ_1) represented the free annihilation of positrons in a defect-free crystal (Fig. 25) in which for pristine TiO₂, monovacancies naturally existed in the crystal lattice and τ_1 was 140.5 ps, whereas τ_1 for hydrogenated TiO₂ was significantly longer at 188.1 ps, with an increase of over 33%. And because OVs or shallow positron traps can

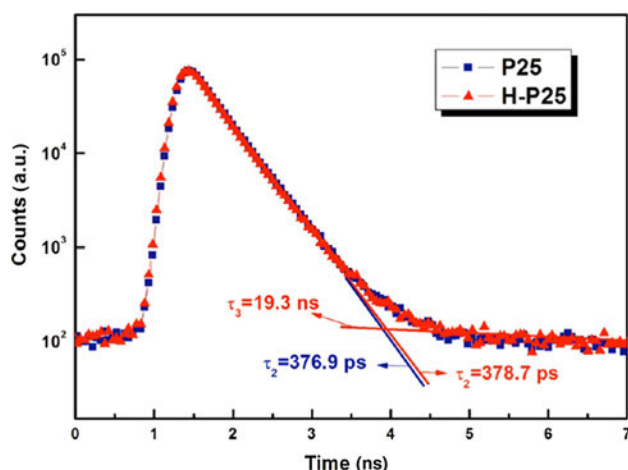


Fig. 25 Positron lifetime spectra with fitting lines for pristine (P25, blue) and hydrogenated (H-P25, red) TiO_2 nanoparticles. Reprinted with permission from Ref. [111], copyright (2012) American Chemical Society

reduce surrounding electron density, positron lifetimes and diffusion lengths are increased, meaning that the prolonged τ_1 of hydrogenated TiO_2 can demonstrate the existence of large numbers of Ti^{3+} -OVs in TiO_2 lattices as induced by hydrogenation. These researchers also reported that the corresponding relative intensity (I_1) also increased from 11.22% to 14.30% after reduction and that the longer lifetime component (τ_2) belonged to positrons captured by larger-sized defects (boundary-like defects) in which the average electron

density is much lower than that in smaller-sized defects, leading to decreases in annihilation rates and remarkable increases in positron lifetime. And because of a larger percentage of boundary-like defects as compared with monovacancies, the relative intensity possesses the relation $I_2 > I_1$. As for the longest lifetime component (τ_3), these researchers reported that this was only detected in the hydrogenated sample at extremely low relative intensity, which they attributed to the annihilation of orthopositronium atoms in which the intensity was so low that the few voids of OV associates were created in the grains of hydrogenated TiO_2 . As a result, OVs led to comparatively low nearby electron densities and therefore increased the value of τ_1 . In addition, OV associates can form larger size clusters, which explains the longer lifetime components (τ_2 and τ_3) (Table 4).

4.3.2 Transmission Electron Microscopy (TEM)

Transmission electron microscopy can directly visualize atoms by using transmitting electrons through a specimen at high resolutions due to the small de Broglie wavelength of electrons. Here, spherical aberration corrected high-resolution transmission electron microscopy (C_s -corrected HRTEM) and spherical aberration corrected scanning transmission electron microscopy (STEM) are among the most widely used techniques in which the latter can be used with different detectors to obtain high-angle annular dark-field (HAADF), annular bright-field (ABF) and annular dark-field

Table 4 Positron lifetimes and relative intensities of pristine and hydrogenated TiO_2 nanoparticles. Reprinted with permission from Ref. [111], copyright (2012) American Chemical Society

Sample	τ_1 (ps)	τ_2 (ps)	τ_3 (ns)	I_1 (%)	I_2 (%)	I_3 (%)
Pristine TiO_2	140.5	376.9	NA	11.22	88.78	NA
Hydrogenated TiO_2	188.1	378.7	19.3	14.30	85.45	0.25

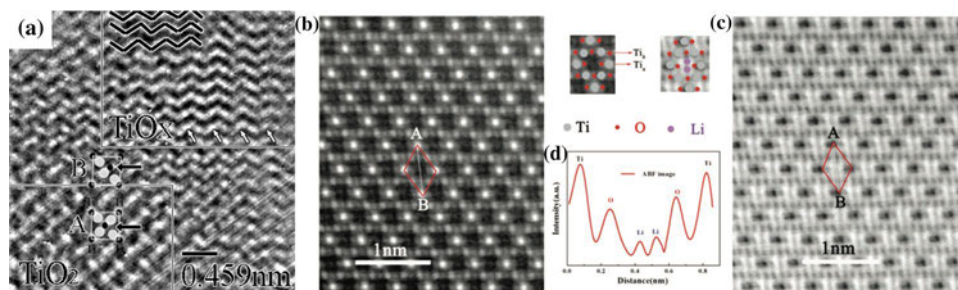


Fig. 26 **a** C_s -corrected HRTEM image of TiO_2 and reduced TiO_x [178]. **b** Enlarged HAADF-STEM image of $\text{Li}_4\text{Ti}_5\text{O}_{12}$. **c** ABF-STEM image and **d** the corresponding line profile of $\text{Li}_4\text{Ti}_5\text{O}_{12}$ along the

[110] zone axis. The image contrast of the dark dots is inverted and represented as peaks. Reprinted with permission from Ref. [179], copyright (2012) John Wiley and Sons

(ADF) STEM images, all of which are effective and possess better image resolution, sensitivity and improved signal to noise ratios as compared with conventional TEM. For example, Yoshida et al. [178] obtained HRTEM images of TiO_2 and reduced TiO_x (Fig. 26a) in which small black and large white dots represented Ti and O atoms, respectively, and reported that as compared with pristine TiO_2 (marked “A”), one O atom was missing in the reduced TiO_x (marked “B”), thus providing direct evidence of OV in TiO_2 . Similar conclusions were also obtained in other studies (Fig. 26b, c) [179], and corresponding line profiles (Fig. 26d) can also reveal atom distributions on the surface with two pronounced Li^+ ion peaks.

4.3.3 Energy-Dispersive X-Ray Spectroscopy (EDS)

Energy-dispersive X-ray spectroscopy (EDS, EDX, EDXS or XEDS), sometimes referred to as energy dispersive X-ray analysis (EDXA) or energy dispersive X-ray microanalysis (EDXMA), is a surface analytical technique that uses an electron beam to eject electrons into inner shells to create electron holes. Electrons from the outer shell will subsequently fill these holes and release the energy difference in the form of X-rays. Here, the energy signature of this emission is unique for each element and can be detected by an

energy-dispersive spectrometer. In principle, all elements from the atomic number 5 (Boron) to 92 (Uranium) can be detected with poorer accuracy for “lighter” elements (atomic number less than 10). And in general, EDS is coupled with SEM, TEM or STEM. For example, Zhang et al. [161] in their study on the reduction of TiO_2 nanotube arrays used EDS to demonstrate that the NaBH_4 -based reducing process is pollution free with no impurities introduced (Fig. 27a, b) in which EDS revealed that a decrease in the atomic ratio of O:Ti with higher reduction temperatures originated from increasing OVs and that the non-integral stoichiometric ratio of O:Ti (1.97:1) was mainly due to the annealing process (low temperature and short annealing time in air). EDS can also be regarded as a tool to indirectly assist in the determination of oxygen defects provided that other possibilities are excluded. In addition, EDS can provide information concerning atomic composition (%) and can easily detect doped cations and anions such as Co^{2+} [145], Mo^{6+} [180], F^- [181] and N^{3-} [182].

4.3.4 Electron Energy Loss Spectroscopy (EELS)

When a beam of electrons with specific kinetic energy passes through a thin sample, the majority of electrons can interact elastically with the sample and a fraction will lose

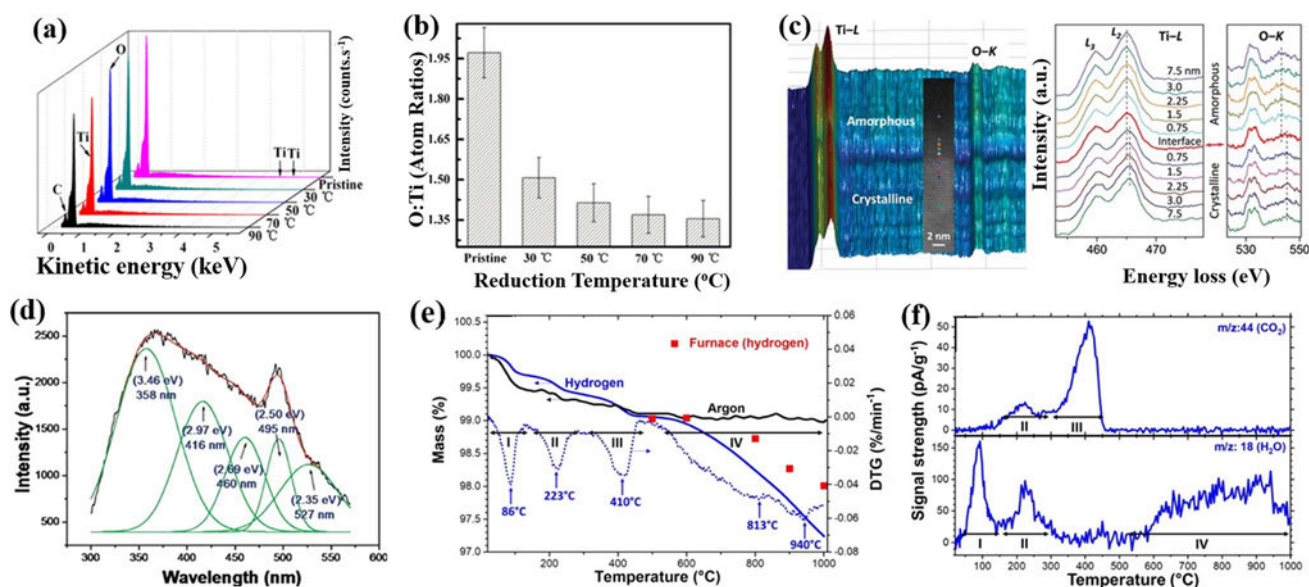


Fig. 27 **a** EDS spectra and **b** corresponding variations of O:Ti atom ratios for pristine and NaBH_4 -reduced TiO_2 nanotube arrays at different temperatures. Reprinted with permission from Ref. [161], copyright 2015, IOP Publishing. **c** 3D EELS spectra with the STEM image marked with positions in which EELS spectra were recorded in the left panel, and corresponding EELS spectra for Ti- $L_{2,3}$ and O-K edges were recorded at various positions in the right panel. Reprinted with permission from Ref. [183], copyright (2016) American Chemi-

cal Society. **d** Cathodoluminescence spectra and Gaussian fitting results for sputter-deposited TiO_2 nanowires. Reprinted with permission from Ref. [159], copyright (2010) American Chemical Society. **e** Thermal gravimetric analysis (TGA) and derivative thermogravimetry (DTG) of LTO nanoparticles under Ar or H_2 atmosphere and **f** mass spectra signals of CO_2 and H_2O during annealing under H_2 atmosphere. Reprinted with permissions from Ref. [186], copyright John Wiley and Sons

energy and see their paths slightly deflected. This deflection is related to the structure and chemical state of the sample atoms as well as their neighboring environment. As a result, these properties can be measured by an electron spectrometer and can be typically incorporated into TEM or STEM. Overall, electron energy loss spectroscopy (EELS) is a powerful technique to analyze changes in kinetic energy distribution with much higher sensitivity as compared with EDS, especially for elements with smaller atomic numbers. For example, Lü et al. [183] fabricated TiO₂ bilayer thin films with a crystalline core and an oxygen-deficient amorphous shell through pulsed laser deposition (PLD) and were able to simultaneously record Ti-*L*_{2,3} and O-*K* spectra using STEM-EELS (Fig. 27c). And based on previous studies [184, 185], Ti-*L* and O-*K* edges are sensitive to the existence of Ti³⁺ and OV_s, respectively, in which the obtained STEM-EELS in this study showed that the Ti-*L*₂ peak shifts by ~0.5 eV from the core up to the surface, revealing the presence of Ti³⁺ ions from the amorphous surface to the crystalline lattice within 3 nm including the interface. A similar shift was also observed in the amorphous layer and the interface in the O-*K* spectra. And because the spectra in the crystalline side do not change with depth, this confirms that areas with high crystallinity contain fewer OV_s. Furthermore, similar results were also observed in hydrogenated black TiO₂ [174].

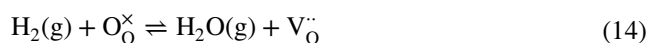
4.3.5 Cathodoluminescence (CL) Spectroscopy

Cathodoluminescence (CL) is the emission of photons of a characteristic wavelength from a material in response to electron radiation. In essence, this phenomenon is the radiative recombination of electron-hole pairs as induced by incident electrons. Compared with optical characterization techniques, CL spectroscopy possesses several advantages in terms of spatial resolution and the association of morphology and structure, such as size, shape, composition, crystallography, electronic properties and much more. These advantages make CL spectroscopy a powerful characterization technique to study OV_s. For example, Wu et al. [159] obtained the CL spectra and Gaussian fitting curves of sputter-deposited anatase TiO₂ nanowires (Fig. 27d) and found that the dominant peak centered at 358 nm originated from band-to-band emission, indicating a direct band gap of 3.46 eV. Here, these researchers attributed this blueshift as compared with the generally reported band gap of ~3.20 eV (387 nm) to the quantum confinement effect. These researchers also attributed the peak positioned at 416 nm (2.97 eV) to self-trapped excitons localized on the TiO₆ octahedra and the peaks centered at 460 nm (2.69 eV) and 527 nm (2.35 eV) to self-trapped excitons in F (an oxygen-ion vacancy occupied

by two electrons) and F⁺ (an oxygen-ion vacancy occupied by one electron) centers, respectively. Furthermore, the peak at 495 nm (2.50 eV) was attributed to surface defect states as induced by OV_s.

4.4 Thermal Analysis and Other Techniques

Thermal analysis includes a series of techniques in which the property of a sample (such as heat flow, weight loss and mechanical properties) is continuously measured as a function of temperature. And among these methods, thermal gravimetric analysis (TA) and differential scanning calorimetry (DSC) are the most widely used techniques. In addition, because the OV formation process can lead to changes in mass that can be quantitatively measured, thermal analysis can also be used to monitor the presence of OV_s under certain circumstances. For example, Widmaier et al. [186] used thermal analysis to study mass change in LTO during annealing under H₂ atmosphere (Fig. 27e) in which they attributed the observed peaks centered at 86 °C and 223 °C to water desorption [187, 188] and the third peak positioned at 410 °C to the decomposition of carboxylic groups on the LTO surface and/or the decomposition of impurities. These researchers also reported that at temperatures over 450 °C, no obvious changes were observed for the mass curve of LTO under Ar atmosphere but that continuous decreases for LTO under H₂ atmosphere at 450–1000 °C as well as simultaneous water desorption occurred (Fig. 27f). This phenomenon can only be explained by the reaction of H₂ with lattice oxygen producing OV_s and H₂O, which can be expressed with the Kröger–Vink notation:



And by analyzing the derivative thermogravimetry (DTG) curve (Fig. 27e), these researchers reported that oxygen atoms located in low-energy lattice sites were gradually removed at temperatures over 450 °C until temperatures reached 813 °C and that the removal of oxygen atoms located at high-energy lattice sites can be activated at temperatures over 813 °C before achieving a new balance at 940 °C.

As with thermal analysis, many other methods exist to detect the formation of oxygen defects and estimate the amount of oxygen deficiencies under specific conditions. These techniques including temperature-programmed desorption (TPD), temperature-programmed reduction (TPR) and oxidation (TPO) [189, 190]. Overall however, these methods do not directly detect OV_s or their characteristic properties, which limits application.

5 Theoretical Aspects of Defects in TiO₂ and LTO

Slight defects have little effect on crystal lattices but can greatly affect the electronic structure and electrochemical properties of materials (e.g., conductivity and ion transport). And although electronic structures can roughly be studied through experimental techniques, theoretical investigations by using computational techniques are necessary, especially for the understanding of mechanisms behind many phenomena and processes. In addition, electronic and ionic conductivities are two important performance parameters for electrode materials, and in this section, the theoretical analysis of defects in TiO₂ and LTO will be discussed with respect to these two parameters. Furthermore, electrical conductivity can be directly inferred from electronic structure in theoretical analysis, and therefore, the DOS and band structures for both pristine and defective TiO₂ and LTO will also be discussed in which by comparing the electronic structures of pristine and defective phases, the effects of defects on the electrical conductivity of TiO₂ and LTO can be understood. Moreover, because ionic conductivity is determined by intercalation energy and the activation energy barrier of diffusion pathways, intercalation and diffusion processes and the effects of defects on these processes will also be discussed in which detailed theoretical analyses concerning these processes usually involve different intercalation sites and diffusion pathways.

5.1 DOS and Band Gap

TiO₂ has been widely applied as an anode material for LIBs and other electrochemical devices due to its excellent ability for Li, Na and Mg ion storage. As a result, TiO₂ has been extensively investigated both experimentally and theoretically in which among four naturally existing TiO₂ polymorphs (anatase, rutile, TiO₂(B) and brookite [191]), anatase, rutile and TiO₂-B (bronze) have been reported to be promising candidates as electrode materials in Li-based rechargeable batteries [192–195]. In terms of electronic structure, researchers usually focus on the DOS and band structure, especially for theoretical analysis. While the DOS and the band gap of pristine TiO₂ have been calculated many times by using DFT, the results vary depending on the choice of exchange–correlation functionals. And although DFT is a powerful method to deal with quantum multi-body issues and allows for realistic ab initio calculations, improper descriptions of exchange–correlation functionals usually result in well-known underestimations of the band gap. To correct the band gap prediction of standard DFT [including local density approximation (LDA) and generalized gradient approximation (GGA) calculations], two

post-DFT methods can be used, including DFT + *U*, which includes the Hubbard *U* parameter (adding an on-site Hubbard *U* electron repulsion on selected localized orbitals), and hybrid density functionals, which contain a fraction of Hartree–Fock-type exchange functionals.

As an example, Dawson et al. [196] used GGA and screened exchange (sX) functionals to calculate the projected density of states (PDOS) of three pristine titania polymorphs (Fig. 28a, b) and found that the valence bands (VBs) of these polymorphs were all mainly composed of O-2p orbitals and that the CBs were mostly made up of Ti-3d orbitals in which the PDOS showed only one spin side because of its symmetric structure. These researchers also reported that for pristine TiO₂, the electrons were all found to be in pairs and consequently lacked spin polarization. These researchers also reported that the main difference between the PDOS calculated by GGA and that calculated by sX functionals is merely the distance between the VB and the CB, which is the band gap. Exact values of band gaps and lattice parameters are listed in Table 5 in which the values of GGA and sX correspond to those obtained from calculations (Fig. 28b) along with LDA, GGA + *U* and experimental (Exp.) values from other cited literature sources. Based on this, it is clear that LDA and GGA can severely underestimate the value of band gaps in comparison with experimental results, whereas GGA + *U* and sX functional results are much better.

Lithium titanate (Li₄Ti₅O₁₂, LTO) is another promising anode material for LIBs due to its well-known “zero strain” characteristic during charge/discharge [33, 198]. However, fewer theoretical studies of LTO exist as compared with TiO₂ due to the relatively complex structure of LTO which possesses a defective spinel structure with Li and Ti atoms randomly distributed among octahedral 16d sites. And based on the unit cell of LTO that can be denoted as (Li₈)^{8a}(Li_{8/3}Ti_{40/3})^{16d}(O₃₂)^{32e} (Fig. 28c), it can be seen that octahedral 32e sites and tetrahedral 8a sites are completely occupied by O and Li atoms, respectively, and that the ratio of Li/Ti in the 16d sites is 1/5 [197]. Here, to achieve correct stoichiometry, at least three unit cells are required to construct the atomic model for calculations, which results in a large supercell Li₃₂Ti₄₀O₉₆ containing 168 atoms. Furthermore, considering the numerous possible atomic arrangements of Ti and Li atoms in 16d sites because of their random distribution, it is necessary to find effective methods to determine the most likely specific structure with an exact Li/Ti distribution at the 16d sites, which is challenging, especially in such large supercells. To address this, Tsai et al. [197] systematically investigated the arrangements of Li and Ti atoms in 16d sites and proposed a proper method to effectively determine the atomic structure of LTO with the stablest Li/Ti distribution over the 16d sites by considering an appropriate distance between Li_{16d}–Li_{16d} pairs. And in the resulting calculated PDOS of the stablest structure

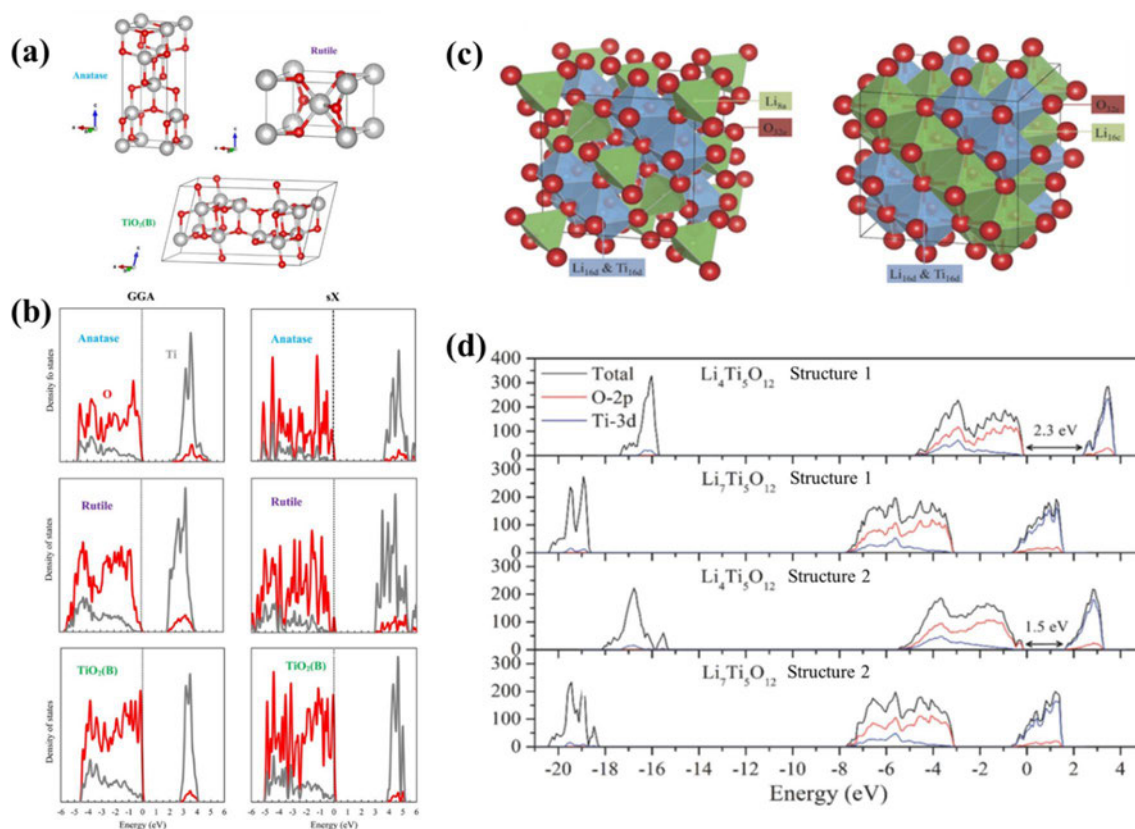


Fig. 28 **a** Crystal structure of TiO_2 . Red and silver spheres represent O and Ti atoms, respectively. **b** PDOS of pristine anatase, rutile and $\text{TiO}_2(\text{B})$ calculated by using GGA and screened exchange (sX) functionals (the vertical dotted line represents the top of the valence band and is set to zero). Reprinted with permission from Ref. [196],

copyright (2016) American Chemical Society. **c** Lattice structures of $\text{Li}_4\text{Ti}_5\text{O}_{12}$ and $\text{Li}_7\text{Ti}_5\text{O}_{12}$ with unit cells. **d** PDOS of $\text{Li}_4\text{Ti}_5\text{O}_{12}$ and $\text{Li}_7\text{Ti}_5\text{O}_{12}$ with two different structures from PBE results in which the Fermi level is aligned to 0 eV. Reprinted with permissions from Ref. [197] under Creative Commons

(Fig. 28d), these researchers reported that similar to TiO_2 , the VB and the CB of LTO are mainly composed of O-2p and Ti-3d states in which the band gap obtained from the PBE calculation was 2.3 eV, which was smaller than the experimentally reported result (3.8 eV [199–201]) and was not surprising for a result generated from PBE functionals (the GGA type) without Hubbard U correction. In general, however, not only do differences exist between theoretical and experimental results for estimations of LTO band gaps, large differences also exist between different theoretical results and even different experimental results (Table 5). One possible reason for this may be the different arrangements of Li/Ti in 16d sites, which is true for different calculated values ($\text{Li}_4\text{Ti}_5\text{O}_{12}$ structure 1 vs. $\text{Li}_4\text{Ti}_5\text{O}_{12}$ structure 2, Fig. 28d).

5.2 Theoretical Calculation of Defective Electronic Structures

Although TiO_2 and LTO have been experimentally confirmed to be promising anode materials with excellent Li

storage properties [195, 214, 215], they still possess drawbacks such as poor electrical conductivity and deficient diffusivity of Li-ions in lattices [155, 216–220]. Here, several strategies have been adopted to improve the electrochemical performance of TiO_2 and LTO in which the introduction of defects including intrinsic defects such as OV [113, 155, 221–224] and non-intrinsic defects such as doping [155, 220, 225–227] has shown experimental promise. As a result, theoretical analysis calculating defective electronic structures is important to understand such results.

5.2.1 Oxygen Vacancies

The introduction of OV into TiO_2 can enhance the electrical conductivity of corresponding electrodes and improve the rate performance, cycling stability and energy capacity of batteries [113, 219, 221, 223]. To further understand the mechanisms behind this effect, significant theoretical studies have been conducted [203, 228–230]. Here, to calculate the properties of TiO_2 with OV, the exact location of non-equivalent OV sites inside lattices needs to be first identified.

Table 5 Calculated lattice parameters and band gaps for three TiO₂ polymorphs, Li₄Ti₅O₁₂ and Li₇Ti₅O₁₂, together with experimental results for comparison

Structure	Method	Band gap		Lattice parameters		References
		E_g (eV)	a (Å)	b (Å)	c (Å)	
Anatase	LDA	2.00	3.69	–	9.47	[202]
	GGA	2.04	3.80	–	9.68	[196]
	GGA + U^a	3.18	3.79	–	9.77	[203]
	sX	3.51	3.75	–	9.59	[196]
	Exp.	3.20	–	–	–	[204]
	Exp.	–	3.79	–	9.51	[205]
Rutile	LDA	2.02	4.53	–	2.91	[206]
	GGA	1.77	4.63	–	2.96	[196]
	GGA + U^a	2.52	4.64	–	2.97	[203]
	sX	2.94	4.56	–	2.96	[196]
	Exp.	3.03	–	–	–	[204]
	Exp.	–	4.59	–	2.96	[205]
TiO ₂ (B)	LDA	–	12.14	3.73	6.49	[207]
	GGA	2.57	12.26	3.75	6.6	[196]
	GGA + U^a	3.28	12.28	3.76	6.62	[203]
	sX	3.71	12.15	3.72	6.48	[196]
	Exp.	3.22	–	–	–	[208]
	Exp.	–	12.18	3.74	6.53	[209]
Li ₄ Ti ₅ O ₁₂	GGA(PBE)	2.3	8.4257	–	–	[131, 197]
	GGA(PW91)	2	8.619	–	–	[210]
	Exp.	3.8	–	–	–	[199–201]
		3.1				[211]
		1.8				[212]
Li ₇ Ti ₅ O ₁₂	Exp.	–	8.3595	–	–	[213]
	GGA(PBE)	0 ^b	8.3609	–	–	[197]
	Exp.	–	8.3538	–	–	[213]

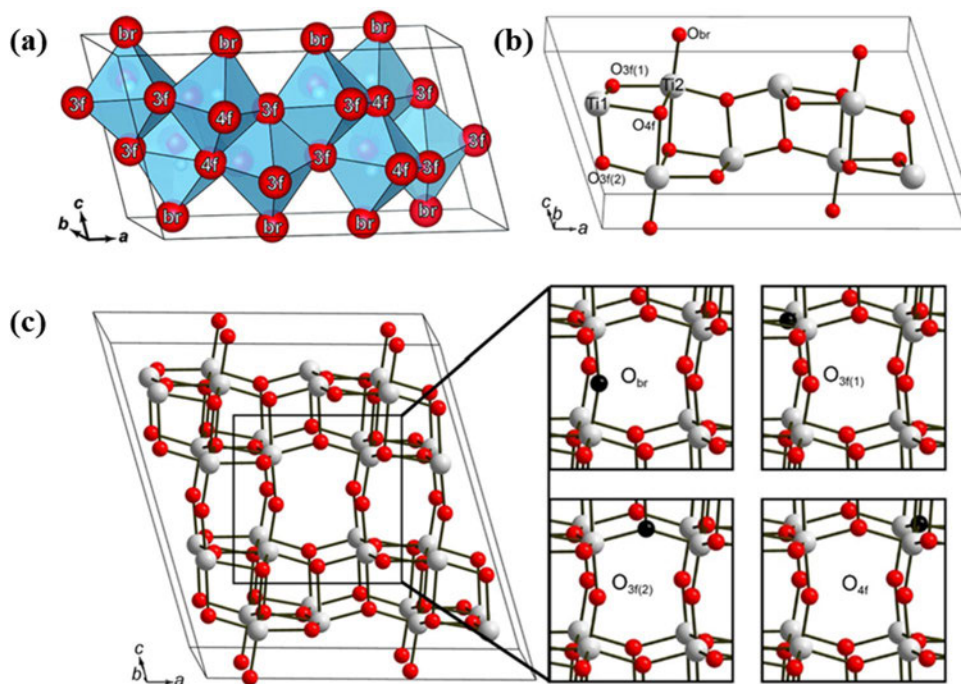
^aThe value of U used in this GGA + U calculation is 9.0 eV [203]^bLi₇Ti₅O₁₂ is a conductor with no band gaps [197, 210]

For anatase and rutile phases, there is only one type of OV sites [203] due to their relatively simple crystal structures in which the crystal structures of anatase (the space group $I4_1/amd$) and rutile (the space group $P4_2/mnm$) are both tetragonal (Fig. 28a). As for the TiO₂(B) (the space group $C2/m$) polymorph however, a monoclinic crystal structure exists (Fig. 29a) that is more complex in which Dalton et al. [231] showed that depending on different coordination numbers, two types of Ti atoms and three types of O atoms exist in TiO₂(B) and Arrouel et al. [232] denoted these atoms as Ti₁, Ti₂ and O_{br} (bridging oxygen), O_{3f} (threefold coordinated oxygen) and O_{4f} (fourfold coordinated oxygen) (Fig. 29a). Alternatively, Feist et al. [209] reported that based on the experimentally observed bulk crystal structure, four different O sites exist inside one unit of the TiO₂(B) lattice, including O atoms with nearly linear twofold coordination inside the ab-plane (001), O atoms with tetrahedral fourfold coordination, O atoms with planar threefold coordination parallel to the ac-plane (010) and O atoms with planar threefold coordination parallel to the ab-plane (001).

Based on this, Kong et al. [229] suggested that the label O_{3f} actually included two types of O atoms, which they labeled as O_{3f(1)} and O_{3f(2)} (Fig. 29b, c).

Finazzi et al. [228] also investigated OVs in bulk anatase using DFT calculations with GGA, GGA + U and hybrid functional methods performed on the CRYSTAL06 code in which the system with OVs used was a so-called triplet state, which possessed two extra electrons with each OV. Here, by using the equation $E_f = E(\text{TiO}_{2-x}) - E(\text{TiO}_2) + E(\frac{x}{2}\text{O}_2)$, these researchers calculated defect formation energies (E_f) for one OV in a supercell of 96 atoms (Ti₃₂O₆₄) with a OV concentration of 1.56% and obtained results that were in the range of 4.2–4.8 eV, varying based on the exchange–correlation functional used. In another study, Kong et al. [229] also calculated the OV formation energy of four types of O atoms in TiO₂(B) using VASP at the level of GGA + U ($U=4.0$ eV) and obtained results that were in the range of 5.67–6.2 eV with an OV concentration of 1.56%. These researchers also reported that the OV formation energy values follow the

Fig. 29 **a** Oxygen sites inside one unit of bulk crystal $\text{TiO}_2(\text{B})$ structure with the version of **a** br , 3f and 4f . Reprinted with permission from Ref. [231], copyright (2012) American Chemical Society. And **b** & **c** br , $3\text{f}(1)$, $3\text{f}(2)$ and 4f . Reprinted with permission from Ref. [229], copyright (2016) Elsevier



order: $\text{O}_{3\text{f}(1)} < \text{O}_{4\text{f}} < \text{O}_{3\text{f}(2)} < \text{O}_{\text{br}}$, suggesting that $\text{O}_{3\text{f}(1)}$ site O atoms were the easiest to remove from lattices. Furthermore, Zhang et al. [230] calculated the properties of OV in $\text{TiO}_2(\text{B})$ using the CASTEP code based on GGA and obtained OV formation energy values in the order of $\text{O}_{3\text{f}} < \text{O}_{\text{br}} < \text{O}_{4\text{f}}$ (only three types of oxygen sites were considered in this study in which the $\text{O}_{3\text{f}}$ site actually included $\text{O}_{3\text{f}(1)}$ and $\text{O}_{3\text{f}(2)}$ sites). And although the order of O_{br} and $\text{O}_{4\text{f}}$ was different in each study, the conclusion that OVs at the $\text{O}_{3\text{f}}$ site are the most energetically favorable is consistent. More recently, Yeh et al. [203] also calculated OV formation energy for anatase, rutile and $\text{TiO}_2(\text{B})$ and took into account all four non-equivalent O sites for $\text{TiO}_2(\text{B})$ using the CASTEP code with GGA + U ($U = 9.0$ eV). Here, the obtained results in this study for TiO_2 polymorphs were in the order of anatase (4.46 eV, 0.69% OV) < rutile (4.60 eV, 0.69% OV) < $\text{TiO}_2(\text{B})$ (in the range of 5.34–5.98 eV, 0.78% OV) and the results for the four non-equivalent O sites of $\text{TiO}_2(\text{B})$ were in the order: $\text{O}_{\text{br}} < \text{O}_{3\text{f}(1)} < \text{O}_{4\text{f}} < \text{O}_{3\text{f}(2)}$. However, although the order of $\text{O}_{3\text{f}(1)} < \text{O}_{4\text{f}} < \text{O}_{3\text{f}(2)}$ in this study was consistent with those reported by Kong et al. [229], these researchers concluded that O_{br} sites possessed the lowest OV formation energy, which conflicted with the two previously described studies [229, 230] that suggested O_{br} , $\text{O}_{3\text{f}}$ or $\text{O}_{3\text{f}(1)}$ sites possessed the lowest OV formation energy. Overall among the three polymorphs, OV formation energy data suggest that anatase can more easily form OVs than rutile or $\text{TiO}_2(\text{B})$.

Defect states introduced by OVs have profound influences on electronic structure, which can be clearly observed from

the calculated PDOS of anatase (Fig. 30) by Finazzi et al. [228]. And in contrast to pristine states (Fig. 28b), the existence of one OV can result in unpaired electrons and lead to asymmetry in the PDOS (Fig. 30), which possesses two sides, including a spin-up side and a spin-down side. These researchers also reported that the theoretical description of the electronic structure of one OV in bulk anatase TiO_2 is highly dependent on the computational method in which conventional DFT functionals such as PBE (the GGA type) present a completely delocalized electron (Fig. 30b) and no states in the gap (Fig. 30a, defect states are adjacent to the CB). In addition, the results of GGA + U calculations are strongly dependent on the value of U in which if U increases from 2 to 4 eV, electrons become more localized (Fig. 30d, f, h) and defect states move deeper inside the gap (Fig. 30c, e, g). And although hybrid functionals can fix the delocalization problem (Fig. 30j, l), the rationality of results depends on the proper percentage of Hartree–Fock exchange in which the H&HLYP (hybrid DFT with 50% HF exchange, H&H = half&half) yields a gap that is too large [6.82 eV [228] vs. 3.20 eV (an experimental value, Table 5)], leading to results without physical meaning. Furthermore, B3LYP (hybrid DFT with 20% HF exchange) can also overestimate the band gap (3.92 eV [228] vs. 3.20 eV) and a 13% [233] admixture of HF exchange is suggested to obtain a correct gap for TiO_2 .

The PDOS of OV-defective TiO_2 for all three polymorphs with different OV sites suggests that the existence of OVs can not only introduce defect states in band gaps, but also reduce gaps in which the position of gap states and the

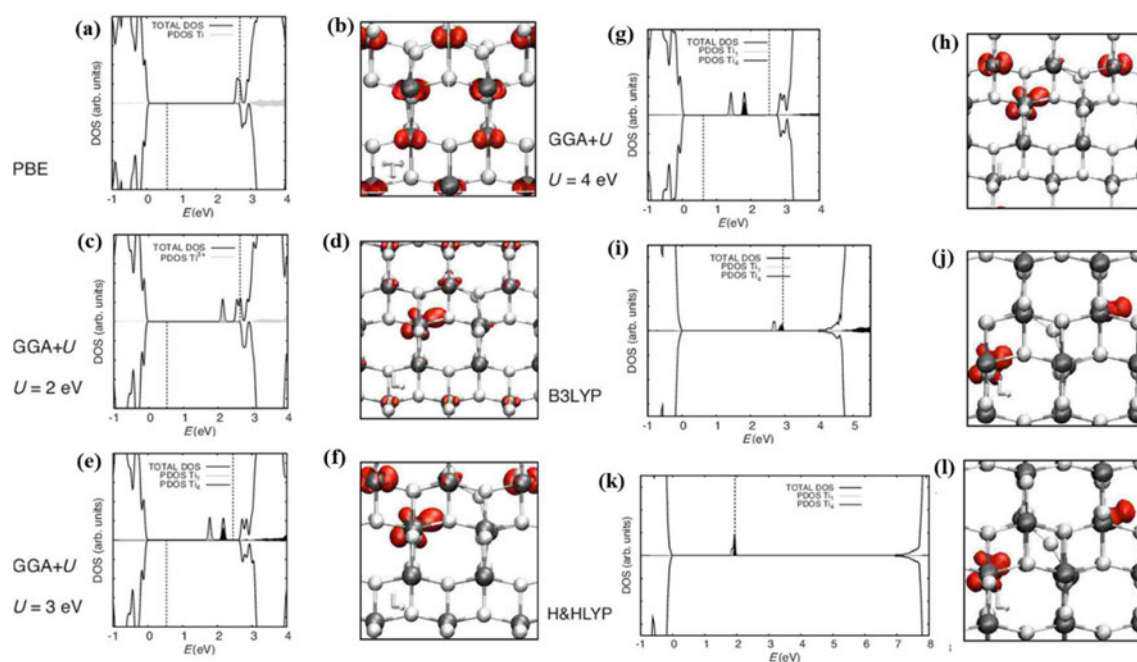


Fig. 30 Calculated PDOS for anatase with OV's (the left column, **a–e**) and corresponding spin distribution (**b–f**, Ti atoms: black spheres, O atoms: white spheres). **a, b** PBE (the GGA type), **c, d** GGA+ U ($U=2$ eV), **e, f** GGA+ U ($U=3$ eV), **g, h** GGA+ U ($U=4$ eV), **i, j**

B3LYP (hybrid DFT with 20% HF exchange) and **k, l** H&HLYP (hybrid DFT with 50% HF exchange, H&H=half&half). Reprinted with permission from Ref. [228], copyright (2008) AIP Publishing

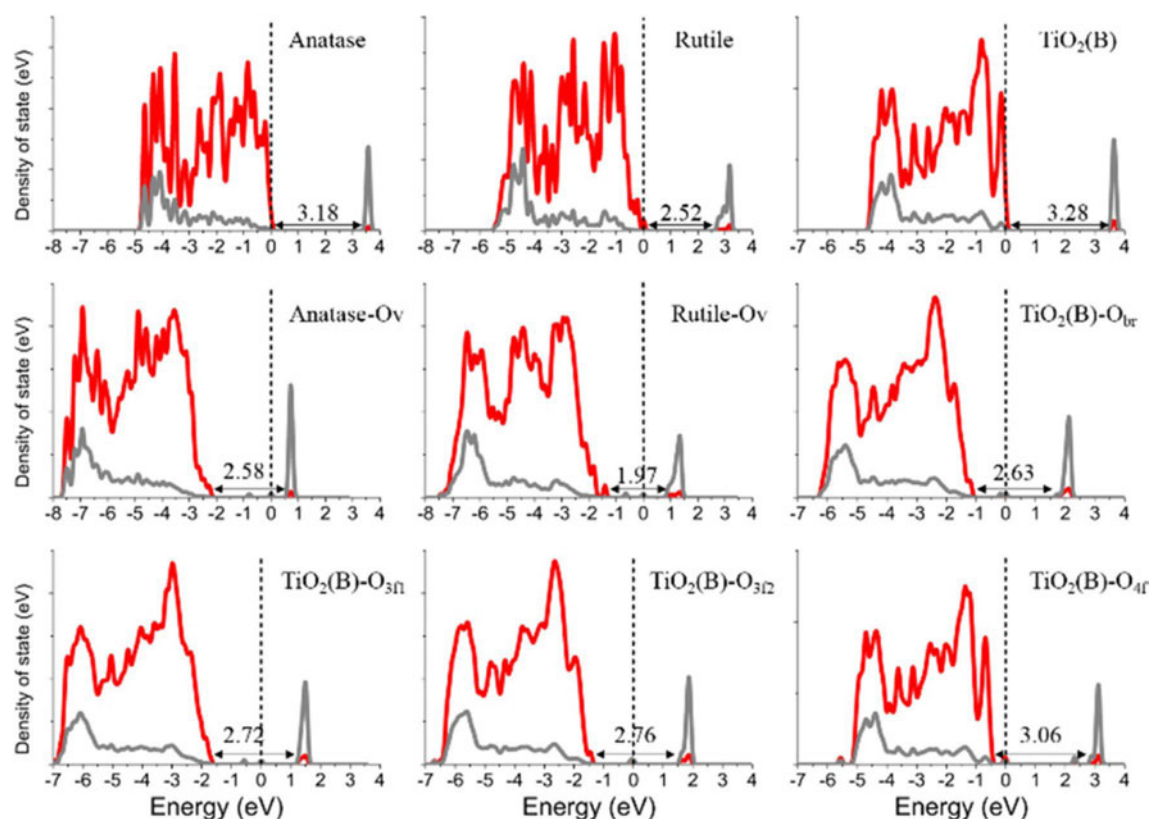


Fig. 31 PDOS of anatase, rutile, TiO_2 (B) and their OV-defective models. Red curves represent O-2p states, and gray curves represent Ti-3d states. Reprinted with permission from Ref. [203], copyright (2018) American Chemical Society

reduction of gaps vary from different OV sites (Fig. 31). Here, several theoretical calculations [203, 224, 229, 230] have demonstrated that the reason for enhanced electrochemical performance through the introduction of OVs in TiO_2 is the improvement of electrical conductivity by decreased band gaps and increased charge carrier concentrations. For example, Yeh et al. [203] in their calculations reported that after the introduction of OVs, band gaps were reduced by 0.66, 0.55 and 0.22–0.65 eV [depending on the different OV sites in $\text{TiO}_2(\text{B})$] for oxygen-defective anatase, rutile and $\text{TiO}_2(\text{B})$, respectively, and that for each polymorph, the Fermi level shifted toward the CB. Similarly, Finazzi et al. [228] reported that for anatase, the localized electrons calculated by GGA + U ($U = 3$ eV) and B3LYP gave rise to states within the gap at the position near ~ 1 eV below the CB (Fig. 30e, i), resulting in a decrease in the band gap. Furthermore, Zheng et al. [224] reported that as compared with the DOS of anatase with 1.56% oxygen deficiency, more DOS can be found below the Fermi level in 3.13% oxygen defective anatase, suggesting a higher charge carrier concentration with increased OVs.

As for LTO, researchers have experimentally [131, 155, 234] and theoretically [131, 235] reported that the existence of OVs can improve electrical conductivity. And to calculate OV-defective LTO, different oxygen sites do not need to be considered because there is only one type

of oxygen atoms that resides in the octahedral 32e sites of the spinel structure. For example, Nasara et al. [131] performed ab initio calculations on OV-defective LTO through VASP using a GGA functional parameterized by PBE in which the atomic models used were the cubic supercell $\text{Li}_{32}\text{Ti}_{40}\text{O}_{96}$ ($\text{Li}_4\text{Ti}_5\text{O}_{12}$) for the pristine phase and $\text{Li}_{32}\text{Ti}_{40}\text{O}_{95}$ ($\text{Li}_4\text{Ti}_5\text{O}_{11.875}$) for the OV-defective one, with an OV concentration of 1.04% (1/96 atoms) (Fig. 32a). In this study, the model used for the pristine LTO was the same as the stablest one reported by Tsai et al. [197]; therefore, the calculated PDOS and band gaps were also similar (Fig. 32b, 2.3 eV) under the same PBE functional. Nasara et al. also reported that the LTO lattice parameter can expand by 0.1519% (from 8.426 Å for the pristine material to 8.439 Å for the OV-defective one) in the presence of OVs and that the different charge distributions (Fig. 32c) revealed that the negative charge compensation as induced by OVs is localized around nearby Ti ions. Furthermore, these researchers also obtained the PDOS of OV-defective LTO (Fig. 32d) and reported that the Fermi level can shift to the CB due to the filling of charge compensated electrons in the CB in which the number of these electrons is two, corresponding to the model of one OV in a supercell. And based on this, OVs can increase charge carrier density and even allow LTO to behave like a metal, thus enhancing the electrical conductivity of OV-defective LTO. Samin et al. [235] also

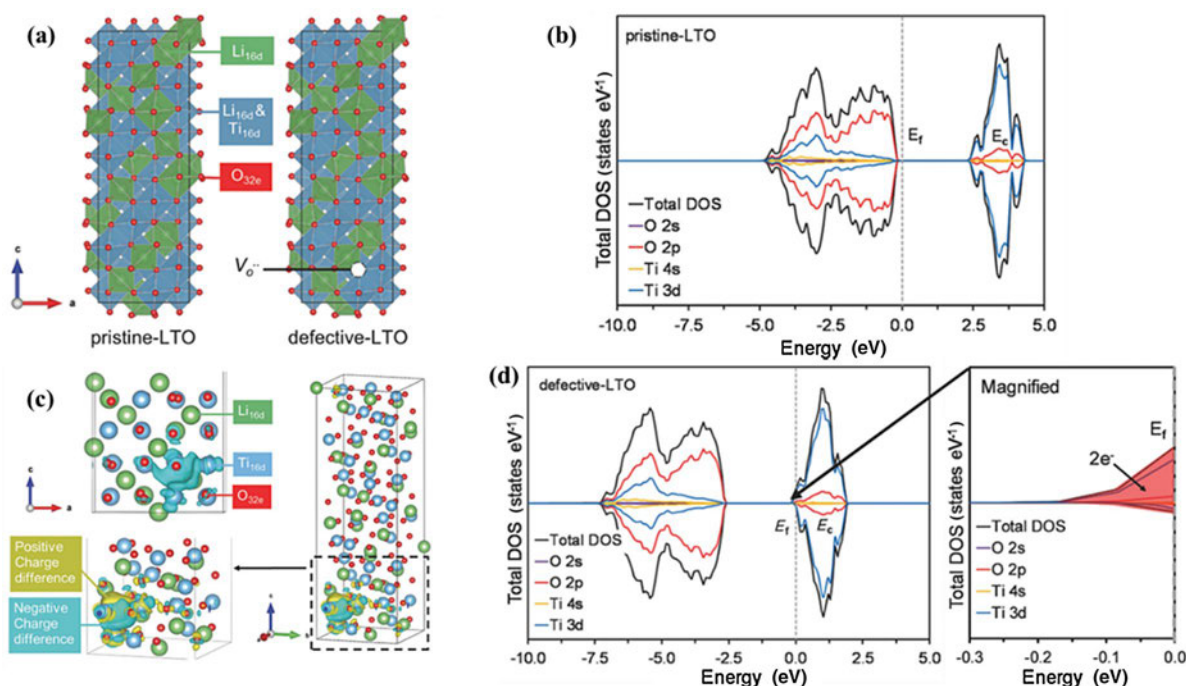


Fig. 32 **a** Supercell models for pristine and OV-defective LTO. **b** PDOS of pristine LTO. **c** Charge density difference schematic for OV-defective LTO. **d** PDOS of OV-defective LTO (the inset magnifies the

partially occupied CBM). Reprinted with permission from Ref. [131], copyright (2017) John Wiley and Sons

reported similar results for the insulator-to-metal transition of OV-defective LTO based on DFT calculations with the same atomic model and the same PBE functional in which their calculated formation energy for 1.04% OV was 7.45 eV.

Overall, OVs are essential defects in metal oxides due to their comprehensive influence. And according to theoretical analysis, OVs can act as shallow donors and increase the DOS to below the Fermi level and thus increase charge carrier concentration. In addition, OVs can introduce defective states into band gaps and reduce band gaps. Furthermore, the effects of OVs are not only limited to electrical conductivity and they can also have a significant impact on the intercalation and diffusion of Li-ions, which will be discussed in the following sections.

5.2.2 Li Doping

As electrode materials for rechargeable LIBs, the properties of Li-intercalated TiO_2 (Li-doped TiO_2) also need to be studied because the intercalation of Li atoms can also affect the electronic structure of host materials. For example, Dawson et al. [196] calculated the PDOS of Li-doped TiO_2 by using the hybrid sX functional and found that gap states

formed in the PDOS for all three polymorphs and that their positions were all at ~ 1 eV below the CB (Fig. 33a). Furthermore, these researchers also reported that these defect states all occupied the Ti-3d state, suggesting that excess charge from doped Li is localized at nearby Ti atoms, producing Ti^{3+} ions. Other calculations by using GGA + U [207, 236] and HSE [237] have also reported similar results, all of which are in agreement with experimental findings for anatase [238–241] and rutile [242]. Moreover, defect states generally do not appear within the band gap of Li-doped TiO_2 in GGA calculations [207, 236, 243] because excess charge is delocalized in GGA calculations, and GGA + U or hybrid functionals are necessary to correct the delocalization problem. However, Legrain et al. [244] reported that their calculations using GGA produced localized results with defect states appearing within the band gap and below the CB at ~ 1 eV for anatase and rutile and at 1.5 eV for $\text{TiO}_2(\text{B})$. These researchers also conducted a spin density difference analysis which showed that the occupied Ti-3d state was localized on single Ti atoms for all polymorphs, indicating the presence of Ti-3d species (Fig. 33b). Here, these researchers attributed this to the use of tuned, localized basis sets and norm-conserving pseudopotentials. Nevertheless, their findings will require further investigations to verify.

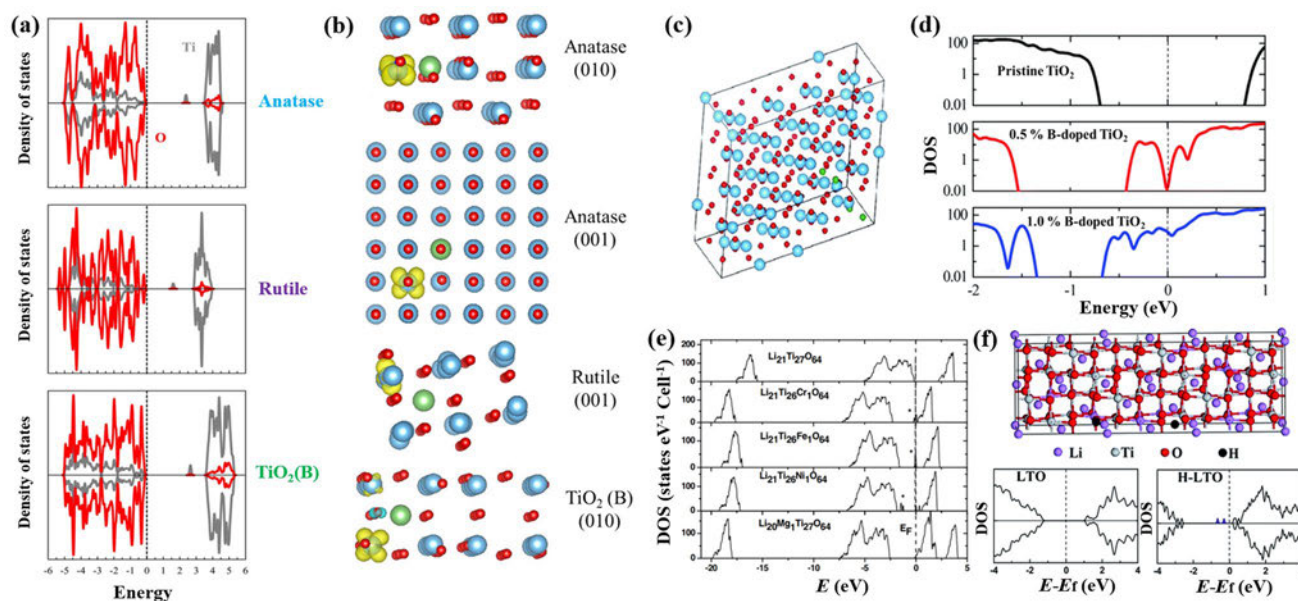


Fig. 33 **a** PDOS of Li-intercalated anatase, rutile and $\text{TiO}_2(\text{B})$ calculated by using sX functionals. The vertical dotted line represents the top of the valence band which is set to zero. Reprinted with permission from Ref. [196], copyright (2016) American Chemical Society. **b** Spin density differences $\rho_{\text{plotted}} = \rho_{\text{up}} - \rho_{\text{down}}$ in three Li-doped TiO_2 polymorphs (Ti atoms: blue spheres, O atoms: red spheres, Li atoms: green spheres). The projection plane is (001) and (010) for anatase, (001) for rutile and (010) for $\text{TiO}_2(\text{B})$. Reprinted with permission from Ref. [244], copyright (2015) Elsevier. **c** Supercell model of boron-doped rutile TiO_2 . **d** Calculated DOS of pristine and boron-

doped rutile TiO_2 with dopant concentrations of 0.5% and 1.0%. Reprinted with permission from Ref. [226], copyright (2014) Royal Society of Chemistry. **e** DOS of LTO and M-doped LTO (M = Cr, Fe, Ni and Mg) calculated with a $2 \times 1 \times 1$ supercell and GGA functional. Reprinted with permission from Ref. [245], copyright (2006) John Wiley and Sons. **f** $3 \times 1 \times 1$ supercell model for H-doped LTO and the calculated DOS for pristine and H-doped models from HSE06. Reprinted with permission from Ref. [110], copyright (2014) Royal Society of Chemistry

Similarities also exist between the electronic structures of Li-doped TiO_2 and OV-defective TiO_2 in which both contain defect states forming in the gap ~ 1 eV below the CB by affecting the Ti-3d states. For example, the PDOS of Li-doped anatase (Fig. 33a, top panel) is similar to the PDOS of OV-defective anatase (Fig. 30e) and the only difference is the shape of the defect states in which the former consists of one peak and the latter consists of two peaks. Here, the reasons for the similarities and differences in the electronic structures between these two defective systems are easy to understand and are based on the fact that one intercalating Li atom can bring one extra electron, whereas one OV can result in two extra electrons. And considering the similarity of electronic structures, the effects of these two types of defects are similar as well in which similar to OV-formation, Li doping can also reduce band gaps and increase charge carrier concentrations to improve electrical conductivity [236]. Furthermore, previously intercalated Li in TiO_2 can also affect the successive intercalation and transport of other Li-ions (discussed in Sect. 5.3).

The situation for Li-doped LTO is different from TiO_2 , however, because the intercalation of Li does not alter the phase structure of the TiO host, but will lead to phase transformations in LTO [33, 197, 210, 213, 246]. Overall, it is generally accepted that $\text{Li}_7\text{Ti}_5\text{O}_{12}$, a defective rock-salt structure (Fig. 28c), is the stablest phase for Li-doped LTO in which the unit cell of $\text{Li}_7\text{Ti}_5\text{O}_{12}$ can be denoted as $(\text{Li}_{16})^{16c}(\text{Li}_{8/3}\text{Ti}_{40/3})^{16d}(\text{O}_{32})^{32e}$ with octahedral 16c sites, 32e sites and 16d sites occupied by Li atoms, O atoms and a random distribution of 1/3 Li and 5/3 Ti, respectively. Similarly, a supercell $\text{Li}_{56}\text{Ti}_{40}\text{O}_{96}$ containing 192 atoms is composed of three unit cells to achieve correct stoichiometry. Here, Tsai et al. [197] calculated the PDOS of $\text{Li}_7\text{Ti}_5\text{O}_{12}$ with an optimized specific atomic structure (Fig. 28d) and reported that as compared with pristine LTO, the Fermi level shifted up into the conduction bands due to extra electrons from the ionization of intercalated Li atoms, making $\text{Li}_7\text{Ti}_5\text{O}_{12}$ a conductor. The metallic properties of $\text{Li}_7\text{Ti}_5\text{O}_{12}$ have also been reported in experimental studies [213].

5.2.3 Doping with Other Cations or Anions

To improve the electrochemical performance of TiO_2 as an anode in LIBs, the strategy of introducing non-intrinsic defects such as doping with cations or anions has also been adopted in which the effects of several different dopants for TiO_2 LIB anodes have been extensively investigated. These dopants include Fe^{3+} [247, 248], Mn [103, 104], Co [101], Ni [249], Cu [99], Zn [100], Nb [250], Mo^{6+} [251], Sn [252, 253], F^- [254], B [226], C [255], N [225, 256–259], P [227] and co-doping systems such as C–N [260, 261] and Cr–N

[262]. Despite the extensiveness of these dopants, aliovalent ion-doped TiO_2 electrodes have rarely been examined from a theoretical first-principle calculation perspective. However, computational studies of doped TiO_2 for photocatalysis or other applications are available and the doping effects of the same aliovalent elements in TiO_2 are constant regardless of application. Furthermore, although significant theoretical studies [226, 263–272] have demonstrated that doping with different elements can enhance electrical conductivity, the electronic structure of doped TiO_2 with different dopants differs significantly. And for the sake of conciseness, boron-doped TiO_2 will be used as an example in this review to discuss the electronic structure of doped systems and doping effects.

For example, Tian et al. [226] investigated rutile with B atoms substituting O atoms using GGA DFT calculations without the Hubbard U parameter and their calculated DOS for pristine and doped rutile with 0.5% and 1% dopants showed that B-doping can lead to Fermi levels moving toward the CB, indicating that the main carriers in this doped system are electrons (Fig. 33d). In addition, these researchers found that the defect states caused by B-doping started to appear in the gap but were adjacent to the CB. And to study the influence of B-doping on electrical conductivity (σ), these researchers also calculated the band structure and obtained the effective mass m^* of the CB minimum through $m^* = \hbar^2 / (\partial^2 E(k) / \partial k^2)$ in which \hbar is the reduced Planck constant. Here, based on the basic physical equation $\sigma = ne\mu$ (n , e , μ denotes carrier concentration, elementary charge and carrier mobility, respectively), the relationship between electrical conductivity, carrier concentration, defect concentration N and effective mass can be expressed as $\sigma \propto n/Nm^*$, in which μ is inversely proportional to N and m^* ($\mu \propto 1/Nm^*$) and the carrier concentration n can be calculated by integrating the DOS. Furthermore, because the defect concentration N is known, the value of electrical conductivity can also be obtained. And as a result, the calculated results obtained in this study revealed that B-doping at lower concentrations ($< 1\%$) can enhance carrier mobility μ and electrical conductivity σ by increasing carrier concentration n and decreasing effective mass m^* of the CB minimum. Similar results were also reported by Yang et al. [272] for Nb-doping and according to results from other studies [264–271], improved electrical conductivity caused by doping with various elements is a result of the reduction of band gaps. Overall, enhanced electrical conductivity is a positive effect of doping and is one of the reasons for improved electrochemical performance as seen in various experimental studies employing doping [99–101, 103, 104, 225–227, 247–259].

Similarly, significant experimental efforts have been undertaken to evaluate doping effects for LTO with various

aliovalent ions such as V [273], Cr [220, 274], Mn [274], Co [274], Ni [274], Zr [275, 276], Nb [277], Mo [155, 278], Ru [279], Gd [280], Na [281, 282], Mg [283], Ca [284], Sr [285], Br [286], H [110] and co-doping systems such as Mi–Mn [287], W–Br [288], Al–F [289] and Na–K [290], all of which have reported enhanced performances for LIBs. Despite this, there are few theoretical studies on aliovalent ion-doping for LTO in which theoretical studies on LTO doping with other cations or anions are limited to doping with Cr, Fe, Ni or Mg [245], Zr [276], H [110], Na [281], Zn [291], Br, Cl, F, N, P or S [292], W and Br [288], Gd [280] and Mg [293]. In this review, typical cases will be presented to illustrate defective electronic structures and doping effects associated with LTO. For example, Liu et al. [245] investigated the electronic properties of M-doped LTO (M = Cr, Fe, Ni and Mg) using DFT GGA calculations in which they considered a model with one Ti substituted by Cr, Fe or Ni and another model with one Li substituted by Mg in a $2 \times 1 \times 1$ supercell. Here, the calculated DOS showed that the new states consisting of 3d orbitals of dopants appeared in the gap for Cr-, Fe- and Ni-doped LTO (Fig. 33e) in which the Fe 3d states and Ni 3d states were localized and were far from the CB, making it difficult for electrons to hop to the CB. However, the Cr 3d states were also near the Ti 3d states (the main component of the CB), allowing the hopping of electrons between these 3d states to be feasible. As for Mg doping, these researchers reported that the Fermi level shifted toward the CBM due to the extra valence electron (Mg substituting Li), making the system an n-type semiconductor. As a result, these researchers reported that Cr- and Mg-doping can enhance the electrical conductivity of LTO by increasing the density of carriers, whereas Fe- and Ni-doping did not. The improved electrical conductivity of Mg-doping has also been reported by Cho et al. [293], who investigated Mg doping sites in LTO using first-principle calculations. Qiu et al. [110] also studied the electronic properties of H-doped LTO using DFT calculations based on HSE06, a hybrid functional. Here, the computational model (a $3 \times 1 \times 1$ supercell with two H atoms randomly distributed among interstitial sites) and the corresponding calculated DOS clearly revealed that H-doping can introduce mid-gap states that were below the Fermi level and thus were occupied with electrons that were easier to transport to the CB (Fig. 33f), meaning that the reduction of the band gap was the reason for enhancements in the electrical conductivity of H-doped LTO. Obvious changes in electronic structure and improved electrical conductivity for LTO have also been reported in doping with other elements such as Gd [280], Zn [291] and W–Br co-doping [288]. However, Kim et al. [276] also reported that in the case of Zr-doped LTO, little effects on electronic structure and electrical conductivity were found after Zr substituted Ti according to calculated results.

5.3 Li-Intercalation and Diffusion Processes and the Effects of Defects

In the study of TiO_2 anodes for LIBs, the processes of intercalation and diffusion of Li-ions are critically important, especially the theoretical aspects. In general, there are several different possible sites for intercalation and pathways for diffusion within the same structure, and in order to find the most probable ones, the usual technique is to calculate and analyze the intercalation energy for each site and the diffusion activation energy barrier for each pathway. Similarly, investigations into the influence of defects on these processes can also be achieved by calculating and comparing these two terms for pristine and defective structures.

5.3.1 Li-Intercalation and Diffusion Processes in Pristine Structures

5.3.1.1 Li-Intercalation The primary problem faced by the construction of a theoretical model for calculations is the defining of the precise location of Li-ions. In anatase and rutile structures, both the empty octahedral and tetrahedral sites are potential sites for Li-ions to intercalate [196, 243, 294], whereas for the $\text{TiO}_2(\text{B})$ structure, three possible intercalation sites exist [229, 232, 295] and can be referred to as C, A1 and A2 (Fig. 34a). Here, the C site is located in the middle of a distorted octahedron as the cavity of the *b*-axis channel and is also at the center of the square plane created by the arrangement of O_{br} atoms. Alternatively, the A1 site is fivefold coordinated to $\text{O}_{3\text{f}(2)}$ atoms in the (001) plane and the A2 site is also fivefold coordinated to O_{br} atoms within the (001) plane. Here, various experimental [296, 297] and theoretical [196, 232, 236, 243] studies have reported that intercalated Li atoms do not sit perfectly at the center of C sites in $\text{TiO}_2(\text{B})$ [196, 232, 296] or at the center of the O_6 octahedron in anatase [196, 236, 297] and rutile [196, 243] and according to the theoretical calculations by Dawson et al. [196], the off-center displacement of an intercalated Li atom is $\sim 0.3 \text{ \AA}$ along the *b*-axis in $\text{TiO}_2(\text{B})$ and $\sim 0.3 \text{ \AA}$ and 0.5 \AA along the *c*-axis in anatase and rutile, respectively.

The stability of Li-intercalated systems can also be analyzed by evaluating the defect formation energy of Li-doped TiO_2 or the intercalation energy of Li in TiO_2 , in which $E_{\text{intercalation}} = E_{\text{lithiated}} - E_{\text{TiO}_2} - E_{\text{Li}}$. Here, octahedral sites appear to be stabler for anatase and rutile [196, 244] because Li atoms positioned at the tetrahedral sites either provide higher energy or drift to octahedral sites [244]. For example, calculations conducted by Dawson et al. [196] showed that octahedral sites were more energetically favorable than tetrahedral sites by -0.39 and -0.61 eV in anatase [Li_xTiO_2 , $x(\text{Li}) = 0.028$] and rutile [Li_xTiO_2 , $x(\text{Li}) = 0.031$], respectively. Koudriachova et al. [294] reported similar results of -0.45 and -0.7 eV for anatase [$x(\text{Li}/\text{Ti}) = 0.5$] and rutile

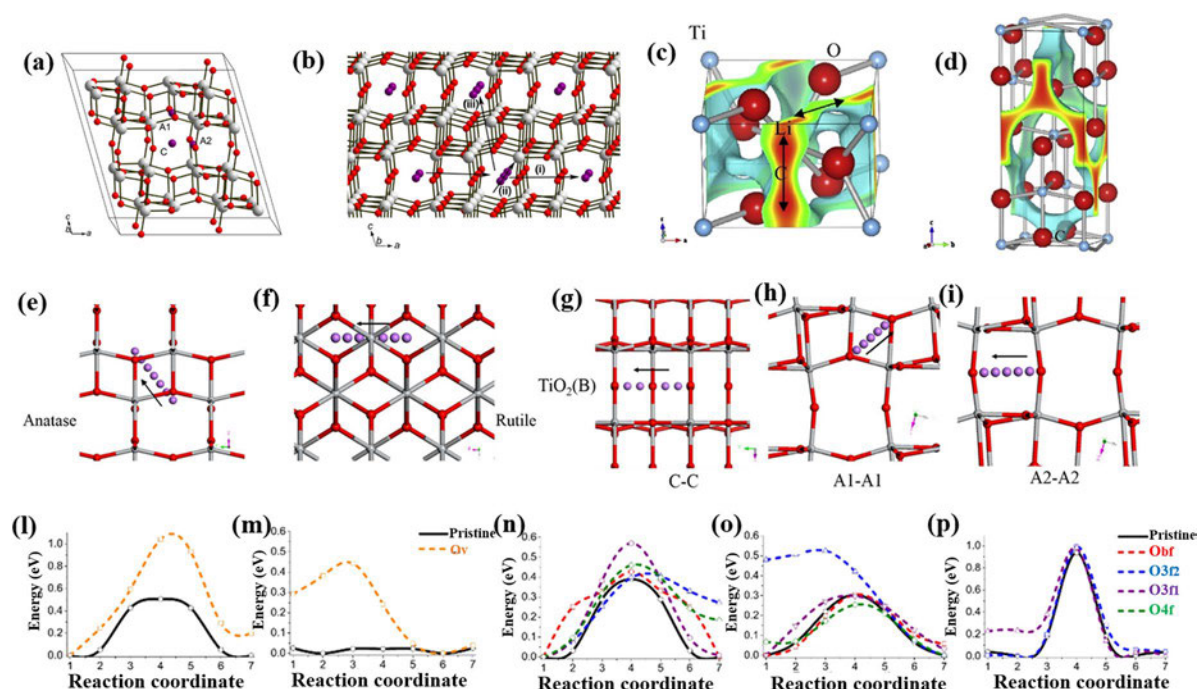


Fig. 34 **a** Three insertion sites in the structure of $\text{TiO}_2(\text{B})$. **b** Three possible diffusion pathways for Li-ions involving conventional hopping between two neighboring C sites in $\text{TiO}_2(\text{B})$. In **a** and **b**, white, red and purple spheres represent Ti, O and Li atoms, respectively. Reprinted with permission from Ref. [229], copyright (2016) Elsevier. **c** Diffusion pathway between two octahedral sites in rutile. **d** Diffusion pathway between two octahedral sites in anatase. In **c** and **d**, light blue and red spheres represent Ti and O atoms, respectively. Reprinted with permission from Ref. [298], copyright (2015) Else-

vier. Li diffusion pathways for **e** anatase and **f** rutile involving Li-ions hopping between two neighboring octahedral sites in each structure. Li diffusion pathways for $\text{TiO}_2(\text{B})$ with Li atoms hopping between **g** two adjacent C sites, **h** two neighboring A1 sites and **i** two neighboring A2 sites. **l–p** Calculated energy profiles for Li-ion diffusion pathways in pristine and OV-defective models of **l** anatase, **m** rutile and for $\text{TiO}_2(\text{B})$, **n** C–C, **o** A1–A1 and **p** A2–A2. Reprinted with permission from Ref. [203], copyright (2018) American Chemical Society

$[x(\text{Li}/\text{Ti})=0.5]$, respectively. As for $\text{TiO}_2(\text{B})$, disagreement exists concerning which of the potential three intercalation sites is the stablest in which many computational studies [196, 203, 229, 232] indicate that C sites are the lowest energy sites for Li-intercalation as confirmed with powder neutron diffraction experiments [296], whereas other calculations predict that A2 [207, 299] or A1 sites [231] are more energetically preferable.

And in the comparison of Li-intercalation energies among the three TiO_2 polymorphs, Yeh et al. [203] found the order of stability to be $\text{TiO}_2(\text{B})$ [C site, -1.4079 eV, $x(\text{Li}/\text{Ti})=0.016$] > anatase [octahedral site, -1.3616 eV, $x(\text{Li}/\text{Ti})=0.014$] > rutile [octahedral site, -0.1531 eV, $x(\text{Li}/\text{Ti})=0.014$]. Similar results were also reported by Legrain et al. [244]. Here, the negative values of the defect formation energy for Li-doped TiO_2 suggest that all three polymorphs can be good candidates for Li-intercalation. Despite this, Li-intercalation energy for rutile is much smaller than that for anatase and $\text{TiO}_2(\text{B})$, corresponding to lower theoretical capacity of rutile (168 mAh g^{-1} [300]) as compared with that of $\text{TiO}_2(\text{B})$ and anatase (both with capacities of 335 mAh g^{-1} [301]).

Li-ion intercalation in LTO is accompanied by phase transformation as induced by the location change of Li-ions in which in the spinel cubic unit cell $(\text{Li}_8)^{8a}(\text{Li}_{8/3}\text{Ti}_{40/3})^{16d}(\text{O}_{32})^{32e}$ of LTO, octahedral 16c sites are empty. Here, researchers have confirmed [197, 210, 246] that during the intercalation process, newly inserted Li-ions occupy empty octahedral 16c sites and Li-ions that originally resided in tetrahedral 8a sites transfer to octahedral 16c sites to form $(\text{Li}_{16})^{16c}(\text{Li}_{8/3}\text{Ti}_{40/3})^{16d}(\text{O}_{32})^{32e}$ ($\text{Li}_7\text{Ti}_5\text{O}_{12}$) and that this newly formed rock-salt phase of $\text{Li}_7\text{Ti}_5\text{O}_{12}$ can maintain the $(\text{Li}_{8/3}\text{Ti}_{40/3})^{16d}(\text{O}_{32})^{32e}$ framework, possibly being the reason for the “zero strain” characteristic. Researchers have also calculated the slight shrinkage in the lattice volume to be 0.2% [210] or 0.77% [197] for $\text{Li}_{4+x}\text{Ti}_5\text{O}_{12}$ if x changes from 0 to 3 and the average Li-intercalation voltage (from $x=0$ to $x=3$ for $\text{Li}_{4+x}\text{Ti}_5\text{O}_{12}$) was calculated to be 1.45 V [210] or 1.41 V [197], which is close to the experimental result of 1.55 V [198]. Overall, the reversible charge/discharge process of LTO is thought to occur between $\text{Li}_4\text{Ti}_5\text{O}_{12}$ and $\text{Li}_7\text{Ti}_5\text{O}_{12}$ phases [197, 210], corresponding to a reversible theoretical capacity of 175 mAh g^{-1} [33]. However, Zhong et al. [246] reported that

LTO can continue to be intercalated by Li-ions until reaching a $\text{Li}_{8.5}\text{Ti}_5\text{O}_{12}$ state during which the $(\text{Li}_{8/3}\text{Ti}_{40/3})^{16d}(\text{O}_{32})^{32c}$ framework can remain stable and that further intercalation of Li-ions can bring about clear structural distortion. Here, these researchers also reported based on calculations that the average intercalation voltage for $\text{Li}_{4+x}\text{Ti}_5\text{O}_{12}$ was 1.48 V (from $x=0$ to $x=3$) and 0.05 V (from $x=3$ to $x=4.5$) and that the total theoretical capacity was 260 mAh g^{-1} (with x from 0 to 4.5).

5.3.1.2 Li-Diffusion Process Based on the possible Li-ion diffusion pathways for the three polymorphs of TiO_2 (Fig. 34b–i) along with their corresponding energy profiles (Fig. 34l–p), the most probable Li-ion diffusion pathway is along the $\langle 201 \rangle$ direction for anatase (Fig. 34d) and along the c -axis direction for rutile (Fig. 34c) with the lowest activation energy being 0.42 eV and 0.04 eV for anatase and rutile, respectively [298], in which both pathways involve Li-ion hopping between two neighboring octahedral sites. As for Li hopping among tetrahedral sites, this leads to much higher energy barriers. For example, the activation energy of a zigzag path in the (001) plane with Li passing through tetrahedral sites in rutile is 0.8 eV [$x(\text{Li}/\text{Ti})=0.5$] [243], which is much higher than the activation energy of the c -axis directional path [0.04 eV from the same calculation [243] with the same $x(\text{Li}/\text{Ti})=0.5$]. Therefore, the diffusion of Li-ions in rutile is one dimensional (along the c -axis direction) and strongly anisotropic. The same diffusion direction and similar energy barriers as these two polymorphs of TiO_2 were also reported from other calculations such as the energy barrier for anatase (Li_xTiO_2) of 0.6 eV [$x(\text{Li}/\text{Ti})=0.03$] [302], 0.511 eV [$x(\text{Li}/\text{Ti})=0.028$] [236] and 0.5056 eV [$x(\text{Li}/\text{Ti})=0.014$] and for rutile (Li_xTiO_2) of 0.04 eV [$x(\text{Li}/\text{Ti})=0.5$] [243, 294] and 0.0254 [$x(\text{Li}/\text{Ti})=0.014$] [203]. As for $\text{TiO}_2(\text{B})$, three possible Li-ion diffusion pathways involving conventional hopping between two neighboring C sites (Fig. 34 b) exist, including migration along the a -axis direction with Li-ions following a zigzag path in the (001) plane through A2 sites (path i), migration along the b -axis channel (the b -axis direction) between two adjacent C sites (path ii) and migration along the c -axis direction between two b -axis channels through A1 sites (path iii) [229, 232]. Here, Arrouvel et al. [232] calculated the activation energy barriers of these three pathways and found that they were in the order of path (ii) (~ 0.3 eV) < path (iii) (~ 0.5 eV) < path (i) (~ 1 eV) [$x(\text{Li})=0.125$] and Kong et al. [229] reported similar results with an order of path (ii) (0.51 eV) < path (iii) (0.71 eV) < path (i) (1.16 eV) [$x(\text{Li}/\text{Ti})=0.031$]. And although the values from these different calculations were not exactly the same, the same order of pathways—path (ii) < path (iii) < path (i) in both studies suggested that the b -axis direction along the b -axis channel is the most energetically favorable pathway for Li-ion migration in $\text{TiO}_2(\text{B})$.

Despite this, these results only considered Li-ions hopping from one C site to another C site (the C–C path, Fig. 34g), and more recently, Yeh et al. [203] conducted a systematic investigation of the minimum energy pathways in $\text{TiO}_2(\text{B})$ for Li-ion hopping between two A1 sites (the A1–A1 path, Fig. 34h) and between two A2 sites (the A2–A2 path, Fig. 34i) and found that the energy barrier was the lowest for the A1–A1 pathway [0.3037 eV, Fig. 34o, $x(\text{Li})=0.016$] rather than for the C–C pathway [0.3894 eV, Fig. 34 n, $x(\text{Li})=0.016$] in which their C–C pathway was equivalent to path (ii) and that the energy barrier for the A2–A2 pathway [0.9381 eV, Fig. 34p, $x(\text{Li})=0.016$] was the highest.

Overall, activation energy barrier data suggest that Li-ion diffusion in rutile possesses the lowest energy barrier [e.g., 0.0254 eV [203], Fig. 34m, $x(\text{Li})=0.014$] and that diffusion in rutile is easier than in $\text{TiO}_2(\text{B})$ [the energy barrier = 0.3 eV [203], Fig. 34o, $x(\text{Li})=0.016$], with diffusion being least favorable in anatase [the energy barrier = 0.5 eV [203], Fig. 34l, $x(\text{Li})=0.014$]. However, the intercalation of Li in rutile is nonetheless significantly more difficult than that in the other two polymorphs, and considering both intercalation energy and activation energy, $\text{TiO}_2(\text{B})$ is the most promising of the three polymorphs as an anode material for LIBs.

Li-ion diffusion in LTO is usually considered in both the delithiated spinel phase $\text{Li}_4\text{Ti}_5\text{O}_{12}$ and the lithiated rock-salt phase $\text{Li}_7\text{Ti}_5\text{O}_{12}$, and Ziebarth et al. [303] systematically investigated this diffusion process with first principle calculations using a simplified model that considered the hopping of only one Li vacancy in a supercell lattice in which in the spinel phase $\text{Li}_4\text{Ti}_5\text{O}_{12}$, tetrahedral 8a sites are filled with Li-ions, whereas octahedral 16c sites are empty, meaning that the diffusion pathways mainly involved vacancy hopping between two 8a sites. Here, these researchers reported that based on their results, a traditional symmetric pathway ($8a \rightarrow 16c \rightarrow 8a'$) possessing activation energy of 0.48 eV existed for single vacancies and that the 16c site between two 8a sites that acted as the transition state was not observed and was the metastable state. However, these researchers also reported that considering the different local chemical environments caused by the random distribution of Li/Ti in 16d sites, other pathways still existed in which the other pathways ($8a \rightarrow 16c \rightarrow 8a'$) with lower energy barriers (0.30–0.36 eV) were all asymmetric and all showed a flat plateau near the middle passed 16c sites, indicating a metastable transition state. As for the rock-salt phase $\text{Li}_7\text{Ti}_5\text{O}_{12}$, these researchers reported that the 16c sites were occupied and 8a sites were empty, meaning that the main pathway was the one with vacancy hopping between two 16c sites in which the energy barrier of these diffusion pathways ($16c \rightarrow 8a \rightarrow 16c'$) was in the range of 0.2–0.51 eV and that the middle passed 8a sites for all of

these pathways were not observed and were metastable transition states. Moreover, the shapes of most of these pathways were asymmetric. In this study, these researchers also investigated the mobility of Li-ions at the stable 16d sites and reported that the diffusion of one single Li vacancy from the 16d site to the 8a site was difficult (with a high energy barrier of 0.92 eV) in the spinel phase, whereas the reverse direction was much easier (with much lower activation energy of 0.42 eV), indicating that vacancies can easily be trapped in stable 16d sites, which can slow down diffusion processes in lattices. Nevertheless, the situation in the rock-salt phase was different, suggesting that vacancies were not stable in 16d sites, and therefore, the diffusion of Li-ions in rock-salt phases is easier than in the spinel phase, which is in agreement with previous reported computational results from Chen et al. [304]. However, because Li-ion diffusion for composition between spinel and rock-salt phases is complex, it is rarely reported in theoretical studies.

5.3.2 The Effects of Defects on Li-Intercalation and Diffusion Processes

5.3.2.1 Effects of OV on Li-Intercalation OVs can have great influences on the intercalation and diffusion of Li atoms, and the effects of OVs on Li-intercalation can be evaluated by comparing the intercalation energy of Li inserting into pristine and OV-defective TiO_2 ($E_{\text{f,Li}}^{\text{OV}}$). Here, Li-intercalation in OV-defective TiO_2 can form systems with complex defects in which both OV sites and intercalation sites for Li atoms need to be considered. In addition, a combination of these two types of defect sites has many permutations, especially for $\text{TiO}_2(\text{B})$, because of the existence of four different OV sites (O_{br} , $\text{O}_{3\text{fl}}$, $\text{O}_{3\text{f2}}$ and $\text{O}_{4\text{f}}$, Fig. 29b, c) and three different Li-intercalation sites (C, A1 and A2, Fig. 34a). Based on this, Yeh et al. [203] took into account all permutations and combinations of these two different sites and reported that Li-intercalation at the A2 site in $\text{TiO}_2(\text{B})$ with an $\text{O}_{4\text{f}}$ OV site was unstable because it can either immigrate to a C site or possess higher energy. Furthermore, these researchers compared $E_{\text{f,Li}}^{\text{OV}}$ with $E_{\text{f,Li}}^{\text{P}}$ and found that OVs (0.69%) were detrimental for Li-intercalation in anatase and rutile but that the opposite was true for $\text{TiO}_2(\text{B})$ with the C- $\text{O}_{4\text{f}}$ site combination (with OV concentration at 0.78%). Similar results for $\text{TiO}_2(\text{B})$ were also reported by Kong et al. [229] who reported that the voltage for Li insertion at C sites in OV-defective $\text{TiO}_2(\text{B})$ (OV concentration of 1.56%) was higher than that in pristine $\text{TiO}_2(\text{B})$, suggesting that the existence of OVs is beneficial for Li-intercalation in $\text{TiO}_2(\text{B})$.

As for LTO, Samin et al. [235] reported that the calculated average intercalation potential between $\text{Li}_4\text{Ti}_5\text{O}_{12}$ and $\text{Li}_7\text{Ti}_5\text{O}_{12}$ reduced from 1.26 V in pristine LTO to 1.09 V in the OV-defective structure, which represented decreased

battery discharge capacities due to introduced OVs. Alternatively, Nasara et al. [131] concluded that the theoretical capacity of LTO between $\text{Li}_4\text{Ti}_5\text{O}_{12}$ and $\text{Li}_7\text{Ti}_5\text{O}_{12}$ can increase from 175 (pristine) to 180 mAh g^{-1} (6.5% OV defective) and also reported that the capacities observed from experimental results were 171.2 and 169.9 mAh g^{-1} for OV-defective and pristine LTO, respectively.

5.3.2.2 Effects of OVs on Li-Diffusion Activation energy is a good reference to evaluate the effects of OVs on Li-ion diffusion. For example, based on the energy profiles for Li-ion diffusion in OV-defective TiO_2 along with data for the pristine structure (Fig. 34l–p), Yeh et al. [203] demonstrated that compared with pristine structures, the diffusion energy barriers in OV-defective anatase and rutile [0.69% OV, $x(\text{Li}/\text{Ti})=0.014$] can increase by 0.5 and 0.4 eV, respectively (Fig. 34l, m), suggesting that OVs may hinder Li-ion diffusion in these polymorphs. Alternatively, these researchers also found that the energy barrier for the A1–A1 pathway decreased by 0.006 and 0.049 eV after the introduction of OVs (0.78%) at $\text{O}_{3\text{fl}}$ and $\text{O}_{4\text{f}}$ sites, respectively, for $\text{TiO}_2(\text{B})$ [$x(\text{Li}/\text{Ti})=0.016$] (Fig. 34o) but increased for the A1–A1 pathway with other OV sites (Fig. 34o) as well as other pathways with all types of OV sites (Fig. 34n, p). These researchers also reported that the A2–A2 pathway diffusion may not exist in $\text{TiO}_2(\text{B})$ with O_{br} and $\text{O}_{4\text{f}}$ OVs (Fig. 34p) because Li-ions initially on the A2–A2 pathway will move to adjacent C sites after full relaxation of the lattice. Overall, the decreased energy barriers for the A1–A1 pathway in $\text{TiO}_2(\text{B})$ - $\text{O}_{3\text{fl}}$ and $\text{TiO}_2(\text{B})$ - $\text{O}_{4\text{f}}$ suggest that the diffusion of Li-ions in $\text{TiO}_2(\text{B})$ can become more efficient in the presence of these two types of OVs. In a further study, Kong et al. [229] suggested that the effects of OVs on Li-ion diffusion may depend on OV concentration in which the diffusion energy barrier for the C–C pathway (path (ii) in Fig. 34b) in a 1.56% OV $\text{TiO}_2(\text{B})$ - $\text{O}_{3\text{fl}}$ or $\text{TiO}_2(\text{B})$ - $\text{O}_{4\text{f}}$ structure is slightly higher than that in the pristine $\text{TiO}_2(\text{B})$ structure, which is consistent with the 0.78% OV results from Yeh et al. [203]. Nevertheless, the energy barrier for the same pathway in the same structure is lower than that with 1.56% OV and even lower than that in pristine materials at 3.12% OV. As for the effects of OVs on Li-diffusion in LTO, Nasara et al. [131] reported that the calculated diffusion coefficient for OV-defective LTO was $1.53 \times 10^{-12} \text{ cm}^2 \text{ s}^{-1}$, which was almost 1.9 times that for pristine LTO ($8.06 \times 10^{-13} \text{ cm}^2 \text{ s}^{-1}$). Here, these researchers claimed that the enhanced diffusivity of Li-ions in OV-defective LTO can be attributed to wider channels created by OV-induced lattice expansion in which the expansion rate of the lattice parameter was calculated to be 0.1519%.

5.3.2.3 Effects of Li Concentration Li-intercalation and diffusion processes can also be affected by previously interca-

lated Li. For example, Ti–Li repulsion and the mutual repulsion of Li-ions in $\text{TiO}_2(\text{B})$ are two factors that can affect the stability of insertion sites [229, 232] in which the experimental and computational studies by Armstrong et al. [296] showed that C sites were the most energetically favorable for Li-ion intercalation but only with low concentrations of Li-ions [$x(\text{Li}/\text{Ti}) \leq 0.25$]. Here, these researchers reported that at $x(\text{Li}/\text{Ti}) = 0.25$, all C sites were occupied and at a higher concentration range of $0.25 < x(\text{Li}/\text{Ti}) \leq 0.5$, A1 sites become more favorable than C sites and all A1 sites become fully occupied at $x(\text{Li}/\text{Ti}) = 0.5$. In addition, if $x(\text{Li}/\text{Ti}) > 0.5$, A2 sites become more favorable than C or A1 sites and all C, A1 and A2 sites become fully occupied at $x(\text{Li}/\text{Ti}) = 1$, leading to maximum Li storage capacity. Researchers have also suggested that the reason why C sites are the stablest at low Li-ion concentrations is that Li–Ti distances are maximized at C sites, thus minimizing Li–Ti repulsion [229]. And with the increasing Li content, mutual repulsion of Li-ions becomes stronger in C sites than that in A1 sites as C sites become fully occupied with Li-ions, leading to changes in the most favorable site. Similar reasons underlie the transition from A1 to A2 sites. In another study, Arrouel et al. [232] reported that the intercalation voltage for pristine $\text{TiO}_2(\text{B})$ decreased from 1.64 to 1.29 V as Li content $x(\text{Li}/\text{Ti})$ increased from 0.031 to 0.125, indicating that Li-intercalation becomes more difficult as Li concentrations increase. Kong et al. [229] also reported similar results, showing that as $x(\text{Li}/\text{Ti})$ increases from 0.031 to 1, insertion voltages for pristine and OV-defective $\text{TiO}_2(\text{B})$ decrease from 1.29 to 0.72 V and from 1.35 to 0.69 V, respectively. Furthermore, these researchers found that the intercalation voltage of OV-defective $\text{TiO}_2(\text{B})$ was higher than that of pristine $\text{TiO}_2(\text{B})$ at lower Li concentrations [$x(\text{Li}/\text{Ti}) \leq 0.25$] but that the voltage was lower at high Li concentrations [$0.25 < x(\text{Li}/\text{Ti}) \leq 1$], suggesting that OVs are beneficial for both charge and discharge processes in $\text{TiO}_2(\text{B})$ anodes. These researchers attributed this effect to that fact that higher insertion voltages in the low Li content allow for easier lithiation in anodes during charging, whereas lower insertion voltages allow for easier delithiation in anodes during discharging.

As for Li diffusion, Olson et al. [302] showed that for anatase, activation energy decreased from 0.65 to 0.45 eV as Li content $x(\text{Li}/\text{Ti})$ increased from 0.03 to 0.1, suggesting that Li diffusion becomes easier with higher Li concentrations. Here, these researchers suggested that increased Li-intercalation will lead to greater amounts of charge compensated electrons, which can provide stronger coupling screening effects [302] for Li-ions, and as a result, a higher Li content is beneficial for Li-ion diffusion. Similar results for anatase have also been reported by Yildirim et al. [305], who found that energy barriers will increase with increasing the Li content only above a theoretical Li concentration limit in anatase whereas for rutile, the results were on the contrary

in which the energy barrier increased by 0.2 eV as $x(\text{Li}/\text{Ti})$ increased from 0.1 to 0.5. Here, these researchers suggested that the channels for Li diffusion can easily be blocked (energy preferable sites becoming unavailable) in rutile due to the one dimensional diffusion mechanism whereas the diffusion mechanism for anatase involves 3D hopping between octahedral sites, which can tolerate stronger Li–Li repulsive interactions. And because the different diffusion mechanisms are determined by different structures, concentration dependence of diffusivity is structure dependent.

5.3.2.4 Effects of Other Dopants Aliovalent elemental doping of TiO_2 LIB anodes has seldom being examined by theoretical studies. As a result, limited theoretical investigations of the effects of doping with other elements on Li-intercalation in TiO_2 exist. However, Kumar et al. [263] investigated the Li-intercalation energy of C- and N-doped anatase TiO_2 by DFT using a PBE functional (a GGA type) together with the Hubbard U parameter and considered a system of anatase with one O atom substituted by one C or N atom with one or two OVs created to maintain charge neutrality in which their doped system was denoted as $\text{TiO}_{2-2x}\text{C}_x$ or $\text{TiO}_{2-3x}\text{N}_{2x}$ for C- and N-doping. Here, these researchers reported that the Li-intercalation energy for C-doped anatase was lower than that of pristine anatase with a low Li content, indicating that C-doping is beneficial for Li-intercalation in anatase. These researchers also reported that opposite results were found for N-doped anatase in which N-doping led to higher Li-intercalation energy under low Li-loading. In addition, these researchers calculated the theoretical charge capacities of LIBs with doped TiO_2 anodes using Bader charge analysis [306–308] and obtained 310, 438 and 421 mA g^{-1} for pristine, C-doped and N-doped anatase TiO_2 , respectively. And to the best of our knowledge, other theoretical studies into the effects of other dopants on Li diffusion in TiO_2 have yet to be reported. As for LTO, Song et al. [281] reported that Na-doping is beneficial for Li diffusion in which based on their calculated results, the activation energy barrier for Li diffusion in Na-doped LTO (spinel $\text{NaLi}_{30}\text{Ti}_{40}\text{O}_{96}$) was ~ 0.25 eV, which was much lower than that in the undoped phase (spinel $\text{Li}_{31}\text{Ti}_{40}\text{O}_{96}$) at 0.38 eV and they attributed this effect to a lattice expansion from 8.427 to 8.443 Å.

6 Applications of TiO_2 and LTO

Ti-based oxides are frequently studied in electrochemical energy storage devices because of their promising potential for high energy density, working voltage and cycle lifes [12, 309, 310]. However, the further development of Ti-based oxides for energy storage is limited by slow kinetic behaviors during charge/discharge in which kinetics is slowed by limited active sites in TiO_2/LTO and large ionic radii (Li^+ ,

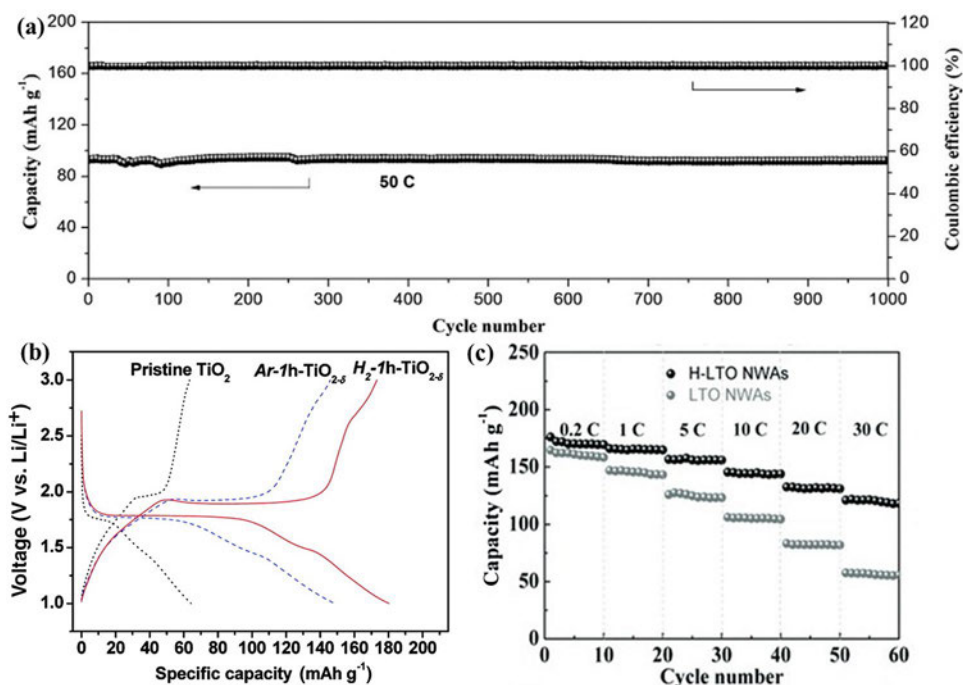
Na^+ , Mg^{2+} and Al^{3+}), which slow ion insertion/extraction in metal-ion batteries [311–313]. Here, sluggish ion diffusion can be addressed by introducing defects such as vacancies, lattice distortions, unpaired electrons and Ti^{3+} [314, 315]. In addition, defects can also cause corresponding charge redistribution to balance the insertion/extraction of Li^+ by enhancing electron diffusion. For example, extrinsic defects (ion doping) in TiO_2/LTO can generally reduce ion diffusion depth and improve intra-particle conductivity and these effects are particularly advantageous for LIBs in which ion diffusion is a rate-limiting factor. Moreover, extrinsically defective TiO_2/LTO can also be used for a range of different electrochemical energy storage devices, including SIBs, multivalent-ion batteries and supercapacitors. As for non-stoichiometric defects (vacancies), these are accompanied by disordered surface layers, accelerated ion desolvation in electrolytes and improved electron conductivity through corresponding charge compensation, all of which are advantageous for charge-transfer reactions in electrochemical energy storage devices. In summary, defective Ti-based oxides can be applied in LIBs, SIBs, multivalent-ion batteries and supercapacitors to achieve better electrochemical performance [316, 317] and in this section, defective TiO_2/LTO with vacancy-induced lattice relaxations and atom-doped lattice distortions is discussed for energy storage applications.

6.1 Lithium-Ion Batteries (LIBs)

TiO_2/LTO has widely been used as anode materials in LIBs because of rapid Li-ion insertion/extraction behaviors.

However, poor electronic and ionic conductivities of TiO_2/LTO greatly limit application in electrochemical energy storage devices [110, 143, 318]. To overcome these limitations, defect structures in Ti-based oxides can promote the migration of electrons and ions in bulk phases and improve dynamic performance [315, 316]. Recently, Ti-based oxides with Ti^{3+} or OV's have also shown promise for LIBs. For example, Chen et al. [77] prepared dark rutile TiO_2 nanorods through a simple solvent-thermal method (Fig. 35a) and reported that the dark TiO_2 exhibited a higher specific capacity (92.1 mAh g^{-1} , 50 C, $1 \text{ C} = 168 \text{ mA g}^{-1}$) and impressive capacity retention of 98.4% after 1000 cycles. Here, these researchers attributed the remarkable rate capability and extraordinary cycling stability to the optimized electronic structure resulting from Ti^{3+} and OV's. In another example, Shin et al. [219] used a hydrogen-thermal treatment method to prepare oxygen-deficient $\text{TiO}_{2-\delta}$ nanoparticles in which 1-h thermal treated TiO_2 under 5% $\text{H}_2/95\%$ Ar atmosphere (H_2 -1 h- $\text{TiO}_{2-\delta}$), 1-h thermal treated TiO_2 under Ar atmosphere (Ar-1 h- $\text{TiO}_{2-\delta}$) and pristine TiO_2 were all prepared and utilized as anodes in LIBs. And as a result, these researchers reported that the conductivity of H_2 -1 h- $\text{TiO}_{2-\delta}$ reached $1.5 \times 10^{-3} \text{ S cm}^{-1}$ and was much higher than Ar-1 h- $\text{TiO}_{2-\delta}$ and pristine TiO_2 . In addition, these researchers reported that the Li^+ storage for H_2 -1 h- $\text{TiO}_{2-\delta}$ and Ar-1 h- $\text{TiO}_{2-\delta}$ showed great enhancements as compared with pristine TiO_2 and that the discharge capacities of H_2 -1 h- $\text{TiO}_{2-\delta}$ and Ar-1 h- $\text{TiO}_{2-\delta}$ were 180 and 148 mAh g^{-1} at 0.2 C ($1 \text{ C} = 336 \text{ mA g}^{-1}$), respectively, whereas the pristine TiO_2 only produced 64 mAh g^{-1} (Fig. 35b).

Fig. 35 **a** Cycling performance of dark TiO_2 at a rate of 50 C expressed as extraction capacity and Coulombic efficiency versus the cycle number. Reprinted with permission from Ref. [77], copyright (2018) American Chemical Society. **b** Charge/discharge profiles (at the 20th cycle) for pristine TiO_2 (the dotted line), Ar-1 h- $\text{TiO}_{2-\delta}$ (the dashed line) and H_2 -1 h- $\text{TiO}_{2-\delta}$ (the solid line) cycled at 0.2 C. Reprinted with permission from Ref. [219], copyright (2012) American Chemical Society. **c** Specific discharge capacities at various C rates for LTO and H-LTO NWAs. Reprinted with permission from Ref. [318], copyright (2012) John Wiley and Sons



Furthermore, Deng et al. [319] fabricated an oxygen deficient H-TiO₂@C electrode through a hydrothermal process followed by a hydrogenation process and reported that the rich OV's induced by hydrogenation resulted in excellent pseudo-capacitive storage in which the resulting H-TiO₂@C electrode delivered a remarkable capacity of 310 mAh g⁻¹ at 0.1 A g⁻¹ and a higher rate performance of 126 mAh g⁻¹ at 1 A g⁻¹. Qiu et al. [113] also successfully prepared blue rutile TiO₂ nanoparticles through an enhanced high-pressure hydrogenation process and reported that the blue TiO₂ possessed remarkable discharge capacities and rate performances as compared with pristine rutile TiO₂ in which outstanding discharge specific capacities of 179.8 mAh g⁻¹ and 129.2 mAh g⁻¹ were achieved at rates of 0.1 C and 5 C (1 C = 336 mA g⁻¹), respectively. Moreover, Qiu et al. [110] also prepared hydrogenated Li titanate (H-LTO) through a similar process and reported much higher reversible capacities and better cycling stability (134.9 mAh g⁻¹ at 5 C after 100 cycles, 1 C = 175 mA g⁻¹). In another example, Shen et al. [318] used a hydrogenation process to successfully introduce Ti³⁺ in LTO nanowires (H-LTO NWAs) and

reported that as compared with pristine LTO nanowires (NWAs), the H-LTO NWAs delivered much higher Li⁺ storage capacities (173 mAh g⁻¹ at 0.2 C) and much better rate performances (121 mAh g⁻¹ at 30 C) (Fig. 35c). In addition, Chen et al. [85] used a solvothermal method with a subsequent annealing treatment to obtain defective mesoporous Li₄Ti₅O_{12-y} and reported that the resulting excellent rate performances (139 mAh g⁻¹ at 20 C) can be attributed to the unique defective mesoporous structure and the presence of OV's and Ti³⁺-O²⁻-Ti⁴⁺ pairs. Nasara et al. [131] also synthesized a highly oxygen-deficient LTO (the OV's content up to ~6.5%) from a one-pot thermal reduction process and reported that the high concentration of OV's greatly improved electronic and ionic conductivities of the LTO material as evidenced by the decreased impedance of the defective LTO electrode (Fig. 36a) as well as lowered polarization voltage and a much stronger peak current and peak symmetry (Fig. 36b), all of which can provide increased electrochemical activity and enhanced reaction kinetics as compared with pristine LTO.

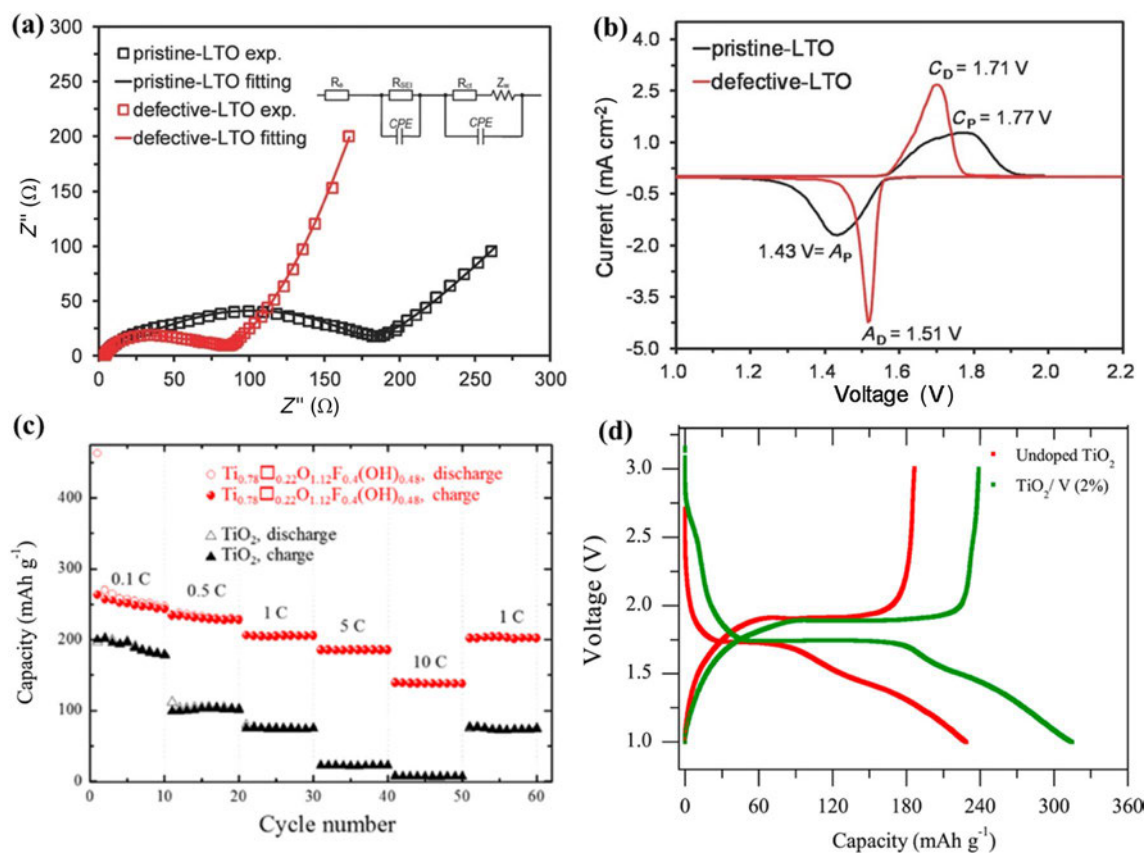


Fig. 36 **a** Electrochemical impedance spectroscopy for pristine and defective LTO. **b** Cyclic voltammetry for pristine and defective LTO. Reprinted with permission from Ref. [131], copyright (2017) John Wiley and Sons. **c** Rate capabilities of pure TiO₂ anatase and Ti_{0.78}O_{1.12}F_{0.4}(OH)_{0.48} electrodes. Reprinted with permission

from Ref. [320], copyright (2015) American Chemical Society. **d** Initial charge/discharge profiles of undoped and V⁵⁺-doped TiO₂ electrodes. Reprinted with permission from Ref. [322], copyright (2013) Elsevier

OVs in TiO_2/LTO lattices can also enhance electron and ion transport and thus promote better rate performances and cycling stability in LIBs. In addition, atom doping-induced lattice distortions in TiO_2/LTO structures are also considered to be an effective strategy to this end. For example, Li et al. [320] prepared monovalent F^-/OH^- -anion-doped TiO_2 ($\text{Ti}_{0.78}\square_{0.22}\text{O}_{1.12}\text{F}_{0.4}(\text{OH})_{0.48}$) through a mild solvothermal process and reported outstanding electrochemical performances as compared with pure TiO_2 in which the doping of monovalent F^-/OH^- anions can cause the replacement of O^{2-} divalent ions and the disruption of the crystalline atomic structure of TiO_2 . As a result, the as-synthesized $\text{Ti}_{0.78}\square_{0.22}\text{O}_{1.12}\text{F}_{0.4}(\text{OH})_{0.48}$ possessed a uniform distribution of cationic vacancies with a concentration up to 22% and was able to deliver reversible specific capacities of 204 mAh g^{-1} and 134 mAh g^{-1} at current densities of 1 C and 10 C, respectively (Fig. 36c). In addition, even at an extremely high current density of 50 C, the sample still delivered a specific capacity of 75 mAh g^{-1} after 300 cycles. Here, these researchers attributed the improved electrochemical Li storage properties to defect chemistry and cationic vacancies, which play an important role in providing additional Li^+ diffusion pathways and enhancing the transport of Li^+ . In another study, Ma et al. [321] synthesized F-doped carbon-encapsulated $\text{Li}_4\text{Ti}_5\text{O}_{12}$ composites (C-FLTOs) through a hydrothermal process and a controlled solid state lithiation reaction at high temperatures and reported that charge compensation in the lattice resulting from F-doping is beneficial to structural stability and electronic conductivity of C-FLTOs in which the optimized sample (C-FLTO with a carbon content of 2.03 wt%) delivered an outstanding charge capacity of $\sim 158 \text{ mAh g}^{-1}$ at 1 C and high rate performances up to 140 C.

In addition to anion doping, various types of cation doping have also been reported to improve the electrochemical performance of Ti-based materials. For example, Anh et al. [322] found that Vanadium (V^{5+})-doped TiO_2 synthesized through a solvothermal method following a calcination treatment gave rise to Ti^{4+} vacancies and increased ion and electronic conductivity, which enhanced the Li^+ storage performance of the V^{5+} -doped TiO_2 electrode. As a result, the optimized V^{5+} -doped TiO_2 (TiO_2/V 2%) exhibited decreased polarization voltages in initial charge/discharge profiles relative to undoped TiO_2 (Fig. 36d) in which as compared with undoped TiO_2 , the TiO_2/V 2% electrode delivered a higher reversible capacity of 232.6 mAh g^{-1} at 0.1 mA cm^{-2} . In another study, Thi et al. [251] investigated the effects of Mo^{6+} doping on the electrochemical properties of TiO_2 . Here, these researchers synthesized anatase-type Ti with different Mo^{6+} doping levels (1, 3, and 5 wt%) through a simple solvothermal method followed by an annealing process and reported that Mo^{6+} -doped TiO_2 with increasing numbers of Ti^{4+} vacancies showed higher conductivities and therefore

led to enhanced electrochemical performances in which TiO_2 nanoparticles doped at 1, 3 and 5 wt% delivered capacities of 165.3, 169.5 and 152.7 mAh g^{-1} , respectively, after 30 cycles at 0.8 mA cm^{-2} , whereas undoped TiO_2 only delivered a capacity of 127.7 mAh g^{-1} under the same conditions. Fehse et al. [323] also prepared Nb-doped TiO_2 nanofibers through a facile, single-step electrospinning method and reported that Nb doping had significant effects on electronic structure, increased the lattice disorder in doped samples and also reduced diffusion pathway lengths and improved intra-particle conductivity. And as a result, the Nb-doped TiO_2 nanofibers possessed higher rate capabilities than non-doped materials during the electrochemical cycling process. In addition, Bai et al. [324] fabricated Y-modified $\text{Li}_4\text{Ti}_5\text{O}_{12}$ with different Y-doping contents (Y_xLTO , $x=0-1.1$) through a coprecipitation method and reported that Y-doping led to an increased lattice constant and enhanced electronic and ionic conductivities, which resulted in outstanding rate capabilities and long cycle life spans, leading to the Y_xLTO ($x=0.06$) electrode maintaining a capacity of 156.8 mAh g^{-1} at 10 C after 1000 cycles. Furthermore, Song et al. [220] fabricated $\text{Li}_{4-x/3}\text{Ti}_{5-2x/3}\text{Cr}_x\text{O}_{12}$ with an unexpected structure through ball milling following by heat treatment. Here, although doping with heterogeneous elements normally increases structural disorder, in this study, the doping of Cr^{3+} in LTO resulted in an anomalous decrease in structural disorder due to the straightening of Ti–O–Ti bonds. This decreased disorder and enhanced electronic conductivity with the introduction of Cr^{3+} subsequently contributed to exceptional electrochemical performances in which at a rate of 10 C, the $\text{Li}_{4-x/3}\text{Ti}_{5-2x/3}\text{Cr}_x\text{O}_{12}$ displayed a high discharge capacity of 125 mAh g^{-1} . In summary, the excellent electrochemical performances of defective Ti-based oxides in LIBs can be ascribed to modified electronic structures (OVs, Ti^{3+} and ion doping), shortened Li^+ diffusion pathways and enhanced diffusion of Li^+ [315, 316, 321].

6.2 Sodium-Ion Batteries (SIBs)

Similar to LIBs, the optimized electronic structure and improved electronic and ionic transport imparted by introducing defects in Ti-based oxides have also been applied to SIBs. For example, Chen et al. [325] prepared nanostructured black anatase TiO_2 with OVs through a NaBH_4 high temperature reduction process and used it as a SIB anode, resulting in the black TiO_2 (B-TO) delivering a high capacity of 207.6 mAh g^{-1} at a current density of 0.2 C and 91.2 mAh g^{-1} at a high current density of 20 C (Fig. 37a), which were superior to white TiO_2 (W-TO) anodes. Here, these researchers attributed such remarkably high rate capabilities and long cycling life spans to the presence of OVs, which can improve both intrinsic electrical conductivity and kinetics of the Na ion uptake-release process. In another

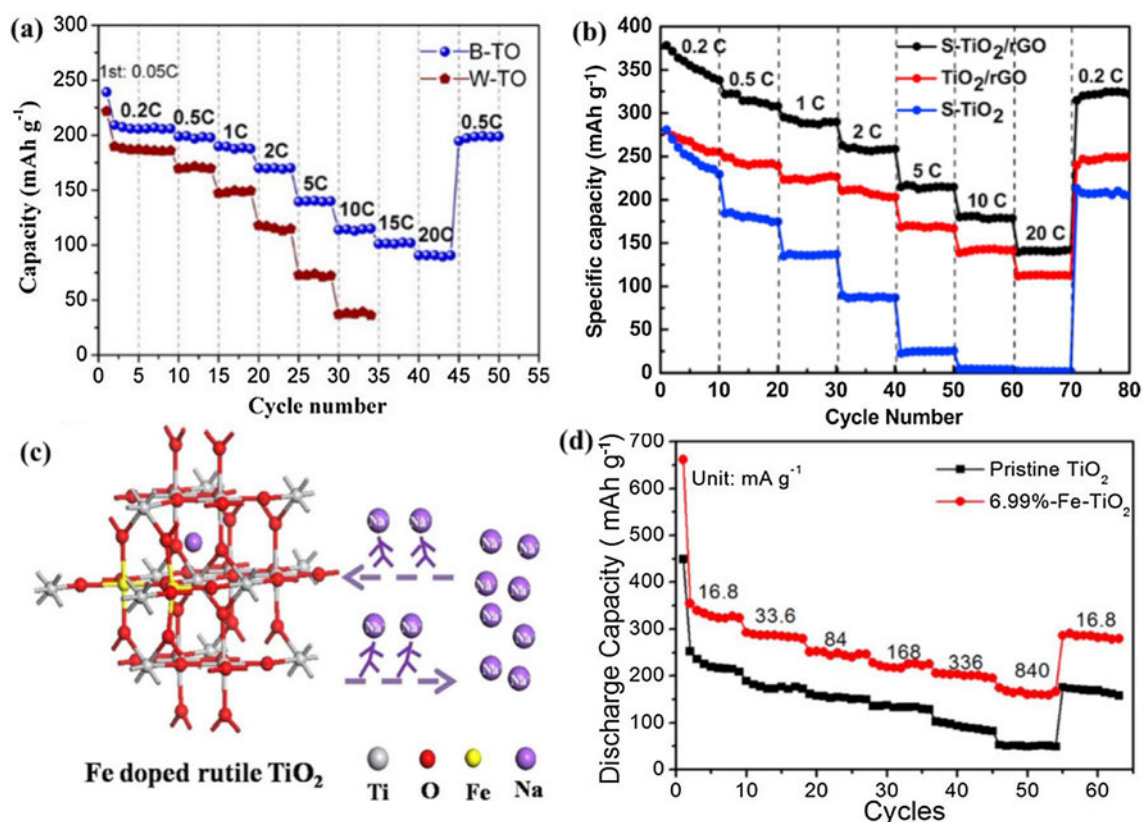


Fig. 37 **a** Rate performances of B-TiO₂ and W-TiO₂ at elevated rates expressed as Na⁺ extraction capacity versus the cycle number. Reprinted with permission from Ref. [325], copyright (2016) American Chemical Society. **b** Rate capabilities of S-TiO₂/rGO, TiO₂/rGO and S-TiO₂ electrodes at different current densities. Reprinted with

permission from Ref. [328], copyright (2018) Elsevier. **c** Structural models of Fe-doped-TiO₂. **d** Rate capabilities of pristine and Fe-doped TiO₂ at different currents. Reprinted (adapted) with permission from Ref. [329]. Copyright (2017) American Chemical Society

study, Zhang et al. [230] designed a blue-colored TiO₂(B) as a SIB anode and reported that the introduction of OV in the blue TiO₂(B) allowed for higher capacities as compared with pristine white TiO₂(B) electrodes in which the blue TiO₂(B) electrode delivered a capacity of 210.5 mAh g⁻¹ and 89.8 mAh g⁻¹ at 0.5 C and 15 C, respectively. And by using a controlled hydrothermal process followed by heat treatment, Zhao et al. [326] successfully synthesized carbon-bonded oxygen-deficient TiO₂ nanotubes (TiO_{2-x}/C) through a carbon reduction process and reported that as an anode for SIBs, the TiO_{2-x}/C displayed superior rate capabilities of 191 mAh g⁻¹ at 0.2 C and 141 mAh g⁻¹ at 10 C. Here, these researchers attributed this pseudocapacitance-dominant reversible charge/discharge process to the synergy between the ultrathin nanotube structure, the existence of OVs, Ti–C bonding at the TiO₂/C interface and coherent amorphous/TiO₂(B) heterojunctions. Xiong et al. [327] also found that cation-deficient 2D nanosheet Ti_{0.87}O₂ as a SIB electrode can exhibit outstanding reversible capacities (490 mAh g⁻¹, 0.1 A g⁻¹), ultra-long cycle life spans and superior low-temperature capabilities for Na storage

due to its unique structure which is composed of intimately hybridized Ti_{0.87}O₂ and N-doped graphene in which these Ti vacancies can not only promote ion transport, but also provide fully accessible sites for ion insertion.

In addition to the introduction of OVs, the production of defects through the introduction of different anions and cations is another effective strategy to improve the Na⁺ storage properties of Ti-based oxides. For example, He et al. [330] synthesized a surface-defect-rich and deep-cation-site-rich S-doped rutile TiO₂ (R-TiO_{2-x}-S) through a plasma-assisted method as a SIB anode and reported that the R-TiO_{2-x}-S delivered excellent capacities of 264.8 mAh g⁻¹ and 128.5 mAh g⁻¹ at current densities of 50 mA g⁻¹ and 10000 mA g⁻¹, respectively. Zhang et al. [328] also synthesized S-doped TiO₂ nanosheets encapsulated in graphene nanosheets (S-TiO₂/rGO) for SIBs in which calcination in a mixed gas of sulfur vapor and hydrogen at 600 °C endowed the S-TiO₂/rGO composite with rich Ti³⁺/OV defects. And as a result, the S-TiO₂/rGO electrode exhibited outstanding rate performances (153 mAh g⁻¹ at 20 C) as compared with the two control electrodes of TiO₂/rGO and S-TiO₂ (Fig. 37b).

These researchers also reported that the pseudocapacitance imparted by the 2D morphology and vacancy-rich TiO_2 nanosheets was able to deliver ultra-stable cycle performances with limited losses even after 8000 cycles. In addition, Wu et al. [331] prepared N-doped white mesoporous TiO_2 (N-MTO) nanofibers through an electrospinning method followed by annealing in which the as-spun nanofibers were first annealed in air to remove organic components and subsequently calcined under 5% NH_3/Ar atmosphere at 550 °C to introduce OV and partial reduce Ti^{4+} to Ti^{3+} . And as a result, the N-MTO delivered a much better Na^+ storage capability of 110 mAh g^{-1} at 10 C as compared with white mesoporous TiO_2 (MTO) nanofibers and no noticeable capacity loss even after 500 cycles. Here, these researchers attributed these improved electrochemical properties to the existence of Ti^{3+} and OV as caused by the introduction of N. Furthermore, Usui et al. [332] successfully prepared Nb-doped rutile TiO_2 ($\text{Ti}_{1-x}\text{Nb}_x\text{O}_2$, $x = 0\text{--}0.18$) through a sol-gel method followed by gas deposition and the resulting $\text{Ti}_{0.94}\text{Nb}_{0.06}\text{O}_2$ electrode exhibited a high Na^+ extraction capacity of 160 mAh g^{-1} at 50 mA g^{-1} after 50 cycles. Moreover, He et al. [329] synthesized Fe-doped 3D

cauliflower-like rutile TiO_2 as a SIB anode in the calcination process, and Fe ions replaced Ti^{4+} at some sites and created corresponding OV in the TiO_2 crystal structure (Fig. 37c) with the prepared TiO_2 with 6.99% Fe doping possessing higher concentrations of OV on the surface. And as a result, the Fe-doped TiO_2 delivered a discharge capacity of 327.1 mAh g^{-1} at 16.8 mA g^{-1} and a high rate performance of 160.5 mAh g^{-1} at 840 mA g^{-1} (Fig. 37d). Here, these improved performances were attributed to the OV produced from Fe doping in the TiO_2 structure. In summary, the improved capacity and cycle stability of defective TiO_2/LTO for SIBs can be attributed to the introduction of OV and non-intrinsic defects such as doping, thus enabling enhanced intrinsic electronic conductivity and fast Na-ion diffusion kinetics [79, 333–335].

6.3 Other Metal-Ion Batteries

Multivalent ion batteries such as reversible Mg- and Al-ion batteries are particularly attractive for large-scale energy storage applications due to superior theoretical volumetric energy densities. However, the development of multivalent

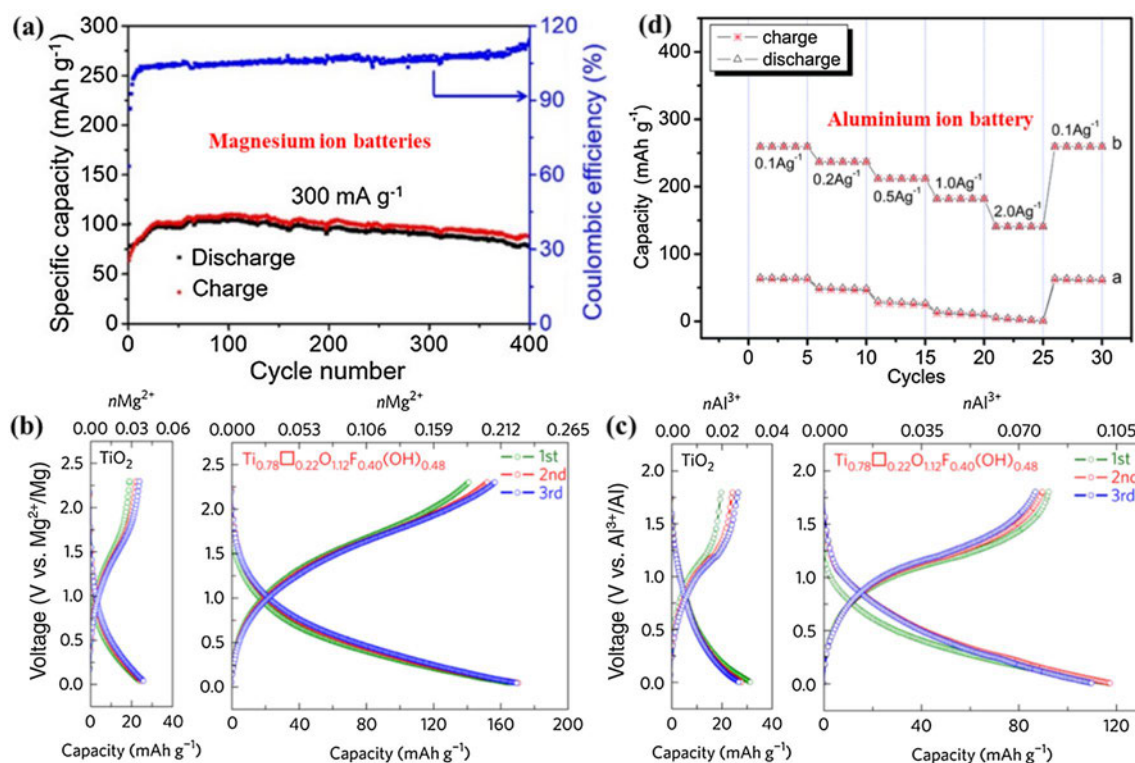


Fig. 38 **a** Electrochemical performance of porous B-TiO_{2-x} at 300 mA g^{-1} (Mg^{2+} extraction capacity vs. the cycle number). Reprinted with permission from Ref. [339], copyright (2018) American Chemical Society. **b** Galvanostatic discharge-charge curves for TiO_2 and $\text{Ti}_{0.78}\square_{0.22}\text{O}_{1.12}\text{F}_{0.40}(\text{OH})_{0.48}$ versus Mg. Cells were cycled at 20 mA g^{-1} in the potential range 0.05–2.3 V versus Mg^{2+}/Mg . **c** Galvanostatic discharge-charge curves for TiO_2

and $\text{Ti}_{0.78}\square_{0.22}\text{O}_{1.12}\text{F}_{0.40}(\text{OH})_{0.48}$ versus Al. Cells were cycled at 20 mA g^{-1} in the potential range 0.01–1.8 V versus Al^{3+}/Al . Reprinted with permission from Ref. [340], copyright (2017) Springer Nature. **d** Rate performances of commercial white anatase TiO_2 and black anatase TiO_2 nanoleaves electrodes at different current rates. Reprinted with permission from Ref. [341], copyright (2014) Royal Society of Chemistry

batteries still faces challenges related to inherent limited ion mobility, strong kinetic barriers and lack of suitable electrode materials [336–338]. Here, the presence of OV's can play a vital role in improving the development of rechargeable Mg and Al batteries because they can enhance Mg^{2+} and Al^{3+} ion diffusion kinetics. For example, Wang et al. [339] synthesized vacancy-rich, 2D black TiO_{2-x} (B- TiO_{2-x}) nanoflakes through an efficient atomic substitution strategy and reported that the unique structure of the ultrathin porous nanoflakes can play a crucial role in the reversible Mg^{2+} storage process with discharge capacities of 150, 126, 114 and 106 mAh g^{-1} at current densities of 50, 100, 200 and 300 mA g^{-1} , respectively. These researchers also reported that even after 400 cycles at 300 mA g^{-1} , the B- TiO_{2-x} was still able to deliver a capacity of 77 mAh g^{-1} (76% retention) and demonstrated good cycling stability (Fig. 38a). In addition, both experimental results and DFT calculations have demonstrated that OV's can enhance electrical conductivity and ion diffusion kinetics and provide more active sites for multivalent ion insertion. Koketsu et al. [340] also found that prepared $\text{Ti}_{0.78}\square_{0.22}\text{O}_{1.12}\text{F}_{0.40}(\text{OH})_{0.48}$ can present good reversible electrochemical performances for both Mg and Al ion storage in which the Mg^{2+} extraction capacity of $\text{Ti}_{0.78}\square_{0.22}\text{O}_{1.12}\text{F}_{0.40}(\text{OH})_{0.48}$ (165 mAh g^{-1} at 20 mA g^{-1}) was much higher than that of TiO_2 (only 25 mAh g^{-1} at 20 mA g^{-1}) (Fig. 38b). Furthermore the detailed analysis of Al storage properties (Fig. 38c) showed that $\text{Ti}_{0.78}\square_{0.22}\text{O}_{1.12}\text{F}_{0.40}(\text{OH})_{0.48}$ can deliver a discharge capacity up to 120 mAh g^{-1} at the initial cycle and further stabilized at 90 mAh g^{-1} at 20 mA g^{-1} , whereas pure TiO_2 exhibited poor intercalation properties for Al^{3+} . In another study, He et al. [341] synthesized black, well-defined nanostructured anatase TiO_2 for Al^{3+} ion storage and reported that the black anatase TiO_2 containing electro-conducting Ti^{3+} can exhibit a sustained rate capability of 141.3 mAh g^{-1} at a current density of 2.0 A g^{-1} that was much better than that of white anatase TiO_2 (Fig. 38d).

6.4 Supercapacitors

Because of its remarkably high stability, low toxicity and low costs, TiO_2 has also been considered as a potential material in electrochemical capacitors. For example, Li et al. [342] reported a facile electrochemical method to prepare Ti^{3+} self-doped anatase TiO_2 with OV's in an ethylene glycol electrolyte in which in a three-electrode system, the capacitance of the self-doped, black TiO_2 produced a significant 42-fold improvement over pristine TiO_2 . In addition, the self-doping in black TiO_2 possessed significantly narrower band gaps and lower resistivities, which can greatly contribute to supercapacitor properties. In another example, Lu et al. [343] synthesized hydrogenated TiO_2 (H- TiO_2) through the calcination of anodized TiO_2 nanotube arrays (NTAs) in hydrogen

atmosphere and reported that the H- TiO_2 NTAs prepared at 400 °C achieved a 40 times higher specific capacitance (3.24 mF cm^{-2} , 100 mV s^{-1}) as compared with air-annealed TiO_2 synthesized under the same conditions. In addition, Zhou et al. [344] prepared self-doped TiO_2 nanotube arrays through a simple cathodic polarization treatment of pristine TiO_2 nanotube arrays and reported that as an electrode material for supercapacitors, the self-doped TiO_2 nanotube arrays exhibited 39 times higher capacitance than pristine TiO_2 . Kim et al. [345] also used an electrochemical self-doping method to fabricate blue and black colored TiO_2 nanotube arrays and reported that the black-colored TiO_2 nanotube arrays exhibited better capacitance than the blue TiO_2 . Furthermore, Salari et al. [346] used a facile method to fabricate highly ordered OV-defective Ti nanotubes that delivered a high and stable capacitance with approximately 98% capacitance retention after 500 cycles and Wu et al. [122] prepared 1D anodic Ti oxide (ATO) nanotube arrays through a plasma-assisted hydrogenation method and investigated its electrochemical performance in supercapacitors. Here, the hydrogenated ATO delivered a higher capacity of 7.4 times (7.22 mF cm^{-2}) at a current density of 0.05 mA cm^{-2} as compared with pristine ATO and these researchers attributed the excellent rate capability and cycling stability of the prepared ATO nanotubes to the outstanding conductivity and larger specific surface areas. Overall, the introduction of OV's can enhance the capacitance in supercapacitors because they can serve as active sites to enhance adsorption properties, promote electron and ion migration and increase the density of charge carriers [317, 347, 348].

7 Summary and Outlook

Overall, this review has summarized the mechanisms of defect formation, the types of structural defects, defect-induced modifications of structural and chemical properties in TiO_2/LTO and the application of defective Ti oxides in electrochemical energy storage devices. Over the years, an array of physical, chemical and doping methods has been developed to partially reduce Ti^{4+} to Ti^{3+} or introduce OV's in lattices to improve electronic and ionic conductivities of Ti-based oxides, resulting in corresponding charge compensation and optimizations to charge carrier transportation kinetics, allowing for enhanced electronic, optical and chemical properties for defective TiO_2/LTO as compared with pristine TiO_2/LTO lattices. For example, extra mid-gap states or narrowed band gaps introduced by defects can increase the absorption of visible light, and OV's and Ti^{3+} centers can serve as shallow donors to accelerate electron mobility, and highly active surface amorphous layers can facilitate the adsorption and dissociation of reactants. And based on these improvements, defective TiO_2/LTO

nanomaterials can be used in a wide range of promising energy storage applications. Furthermore, the future development of TiO₂/LTO nanomaterials for practical application in electrochemical storage applications should focus on several key areas. First, the existing technologies and methods to tune defects are relatively complex or resource intensive and it is necessary to develop effective, facile and large-scale synthetic methods to prepare and control defect structures. Second, generated OV_s and Ti³⁺ are unstable in TiO₂/LTO lattices in which Ti³⁺ is prone to oxidization to Ti⁴⁺ by air and OV_s are easily filled by dissociated oxygen in air or water, meaning further research should focus on the preservation of oxygen defects and Ti³⁺ in TiO₂/LTO lattices. Third, because defect concentrations are usually not controllable during defect formation, the quantitative control of defects can allow for more precise understanding of the effects of defects on the electronic structure and physical and on chemical properties of materials.

Overall, the creation of defects is a promising route to resolve poor electronic and ionic conductivities caused by empty Ti⁴⁺ 3d orbitals in Ti-based oxides and TiO₂/LTO defect structures possess many promising applications in the field of electrochemical energy generation and storage. However, further research efforts are still required, from theoretical calculations to synthetic methods, in order to improve our understanding of defective TiO₂/LTO materials and their practical application in clean energy devices.

Acknowledgements We are grateful for the financial support from the Australia Research Council Discovery Projects DP170103721 and DP180102003, the National Key R&D Program of China (2016YFB0700600), the Soft Science Research Project of Guangdong Province (No. 2017B030301013) and the Shenzhen Science and Technology Research Grant (ZDSYS201707281026184). We would also like to thank Dr. Sean E. Lowe (Griffith University) for his contributions in polishing our manuscript.

References

- Forster, B.A.: Optimal energy use in a polluted environment. *J. Environ. Econ. Manag.* **7**, 321–333 (1980). [https://doi.org/10.1016/0095-0696\(80\)90025-x](https://doi.org/10.1016/0095-0696(80)90025-x)
- Chen, X., He, W., Ding, L.X., et al.: Enhancing interfacial contact in all solid state batteries with a cathode-supported solid electrolyte membrane framework. *Energy Environ. Sci.* **12**, 938–944 (2019). <https://doi.org/10.1039/c8ee02617c>
- Chen, H., Cong, T.N., Yang, W., et al.: Progress in electrical energy storage system: a critical review. *Prog. Nat. Sci.* **19**, 291–312 (2009). <https://doi.org/10.1016/j.pnsc.2008.07.014>
- Wang, P.J., Huang, S.M., Wu, W.C.: Electrical energy storage device. United States Patent US6373152B1, Apr. 16, 2002
- Goodenough, J.B., Park, K.S.: The Li-ion rechargeable battery: a perspective. *J. Am. Chem. Soc.* **135**, 1167–1176 (2013). <https://doi.org/10.1021/ja3091438>
- Xiang, H., Chen, J., Li, Z., et al.: An inorganic membrane as a separator for lithium-ion battery. *J. Power Sources* **196**, 8651–8655 (2011). <https://doi.org/10.1016/j.jpowsour.2011.06.055>
- Jiang, Z., Xie, H., Wang, S., et al.: Perovskite membranes with vertically aligned microchannels for all-solid-state lithium batteries. *Adv. Energy Mater.* **8**, 1801433 (2018). <https://doi.org/10.1002/aenm.201801433>
- Van Schalkwijk, W., Scrosati, B.: Advances in lithium ion batteries introduction. In: Van Schalkwijk, W.A., Scrosati, B. (eds.) *Advances in Lithium-Ion Batteries*, pp. 1–5. Springer, US, Boston, MA (2002)
- Yabuuchi, N., Kubota, K., Dahbi, M., et al.: Research development on sodium-ion batteries. *Chem. Rev.* **114**, 11636–11682 (2014). <https://doi.org/10.1021/cr500192f>
- Wang, G., Zhang, L., Zhang, J.: A review of electrode materials for electrochemical supercapacitors. *Chem. Soc. Rev.* **41**, 797–828 (2012). <https://doi.org/10.1039/C1CS15060J>
- González, A., Goikolea, E., Barrena, J.A., et al.: Review on supercapacitors: technologies and materials. *Renew. Sustain. Energy Rev.* **58**, 1189–1206 (2016). <https://doi.org/10.1016/j.rser.2015.12.249>
- Zhu, G.N., Wang, Y.G., Xia, Y.Y.: Ti-based compounds as anode materials for Li-ion batteries. *Energy Environ. Sci.* **5**, 6652–6667 (2012). <https://doi.org/10.1039/C2EE03410G>
- Lan, T.B., Tu, J.X., Zou, Q.M., et al.: Synthesis of anatase TiO₂ mesocrystals with highly exposed low-index facets for enhanced electrochemical performance. *Electrochim. Acta* **319**, 101–109 (2019). <https://doi.org/10.1016/j.electacta.2019.06.152>
- Zaleska, A.: Doped-TiO₂: a review. *Recent Patents Eng.* **2**, 157–164 (2008). <https://doi.org/10.2174/187221208786306289>
- Mor, G.K., Varghese, O.K., Paulose, M., et al.: A review on highly ordered, vertically oriented TiO₂ nanotube arrays: fabrication, material properties, and solar energy applications. *Sol. Energy Mater. Sol. Cells* **90**, 2011–2075 (2006). <https://doi.org/10.1016/j.solmat.2006.04.007>
- Paramasivam, I., Jha, H., Liu, N., et al.: A review of photocatalysis using self-organized TiO₂ nanotubes and other ordered oxide nanostructures. *Small* **8**, 3073–3103 (2012). <https://doi.org/10.1002/smll.201200564>
- Xiong, H., Slater, M.D., Balasubramanian, M., et al.: Amorphous TiO₂ nanotube anode for rechargeable sodium ion batteries. *J. Phys. Chem. Lett.* **2**, 2560–2565 (2011). <https://doi.org/10.1021/jz2012066>
- Fujishima, A., Honda, K.: Electrochemical photolysis of water at a semiconductor electrode. *Nature* **238**, 37–38 (1972). <https://doi.org/10.1038/238037a0>
- Zhang, W., Zhang, Y., Yu, L., et al.: TiO₂-B nanowires via topological conversion with enhanced lithium-ion intercalation properties. *J. Mater. Chem. A* **7**, 3842–3847 (2019). <https://doi.org/10.1039/C8TA10709B>
- Liu, Y., Chen, W., Yang, C., et al.: Hierarchical TiO₂-B composed of nanosheets with exposed 010 facets as a high-performance anode for lithium ion batteries. *J. Power Sources* **392**, 226–231 (2018). <https://doi.org/10.1016/j.jpowsour.2018.04.110>
- Ding, T., Wu, J., Chen, Z., et al.: Synthesis of hierarchically mesoporous TiO₂ spheres via a emulsion polymerization route for superior lithium-ion batteries. *J. Electroanal. Chem.* **818**, 1–9 (2018). <https://doi.org/10.1016/j.jelechem.2018.04.023>
- Liu, Y., Guo, M., Liu, Z., et al.: Rapid and facile synthesis of hierarchically mesoporous TiO₂-B with enhanced reversible capacity and rate capability. *J. Mater. Chem. A* **6**, 1196–1200 (2018). <https://doi.org/10.1039/C7TA09264D>
- Zhang, W., Xu, T., Liu, Z., et al.: Hierarchical TiO_{2-x} imbedded with graphene quantum dots for high-performance lithium storage. *Chem. Commun.* **54**, 1413–1416 (2018). <https://doi.org/10.1039/C7CC09406J>

24. Zhang, W., Lan, T., Ding, T., et al.: Carbon coated anatase TiO₂ mesocrystals enabling ultrastable and robust sodium storage. *J. Power Sources* **359**, 64–70 (2017). <https://doi.org/10.1016/j.jpowsour.2017.05.040>
25. Liu, S., Yu, J., Jaroniec, M.: Anatase TiO₂ with dominant high-energy 001 facets: synthesis, properties, and applications. *Chem. Mater.* **23**, 4085–4093 (2011). <https://doi.org/10.1021/cm200597m>
26. Dylla, A.G., Henkelman, G., Stevenson, K.J.: Lithium insertion in nanostructured TiO₂ (B) architectures. *Acc. Chem. Res.* **46**, 1104–1112 (2013). <https://doi.org/10.1021/ar300176y>
27. Li, J., Wan, W., Zhou, H., et al.: Hydrothermal synthesis of TiO₂(B) nanowires with ultrahigh surface area and their fast charging and discharging properties in Li-ion batteries. *Chem. Commun.* **47**, 3439–3441 (2011). <https://doi.org/10.1039/c0cc04634e>
28. Rai, A.K., Anh, L.T., Gim, J., et al.: Simple synthesis and particle size effects of TiO₂ nanoparticle anodes for rechargeable lithium ion batteries. *Electrochim. Acta* **90**, 112–118 (2013). <https://doi.org/10.1016/j.electacta.2012.11.104>
29. Tian, J., Zhao, Z., Kumar, A., et al.: Recent progress in design, synthesis, and applications of one-dimensional TiO₂ nanostructured surface heterostructures: a review. *Chem. Soc. Rev.* **43**, 6920–6937 (2014). <https://doi.org/10.1039/C4CS00180J>
30. Chen, X., Selloni, A.: Introduction: titanium dioxide (TiO₂) nanomaterials. *Chem. Rev.* **114**, 9281–9282 (2014). <https://doi.org/10.1021/cr500422r>
31. Ge, M.Z., Cai, J.S., Iocozzia, J., et al.: A review of TiO₂ nanostructured catalysts for sustainable H₂ generation. *Int. J. Hydrogen Energy* **42**, 8418–8449 (2017). <https://doi.org/10.1016/j.ijhydene.2016.12.052>
32. Reddy, K.M., Manorama, S.V., Reddy, A.R.: Bandgap studies on anatase titanium dioxide nanoparticles. *Mater. Chem. Phys.* **78**, 239–245 (2003). [https://doi.org/10.1016/S0254-0584\(02\)00343-7](https://doi.org/10.1016/S0254-0584(02)00343-7)
33. Zhao, B., Ran, R., Liu, M.L., et al.: A comprehensive review of Li₄Ti₅O₁₂-based electrodes for lithium-ion batteries: the latest advancements and future perspectives. *Mater. Sci. Eng. R Rep.* **98**, 1–71 (2015). <https://doi.org/10.1016/j.mser.2015.10.001>
34. Zhang, Y.L., Hu, X.B., Xu, Y.L., et al.: Recent progress of Li₄Ti₅O₁₂ with different morphologies as anode material. *Acta Chim. Sin.* **71**, 1341–1353 (2013). <https://doi.org/10.6023/A13040423>
35. Lin, X., Pan, F., Wang, H.: Progress of Li₄Ti₅O₁₂ anode material for lithium ion batteries. *Mater. Technol.* **29**, A82–A87 (2014). <https://doi.org/10.1179/1753555714Y.0000000170>
36. Yu, L., Wu, H.B., Lou, X.W.: Mesoporous Li₄Ti₅O₁₂ hollow spheres with enhanced lithium storage capability. *Adv. Mater.* **25**, 2296–2300 (2013). <https://doi.org/10.1002/adma.201204912>
37. Zhao, L., Hu, Y.S., Li, H., et al.: Porous Li₄Ti₅O₁₂ coated with N-doped carbon from ionic liquids for Li-ion batteries. *Adv. Mater.* **23**, 1385–1388 (2011). <https://doi.org/10.1002/adma.201003294>
38. Shi, Y., Gao, J., Abruna, H.D., et al.: Rapid synthesis of Li₄Ti₅O₁₂/graphene composite with superior rate capability by a microwave-assisted hydrothermal method. *Nano Energy* **8**, 297–304 (2014). <https://doi.org/10.1016/j.nanoen.2014.06.009>
39. He, Y., Muhetaer, A., Li, J., et al.: Ultrathin Li₄Ti₅O₁₂ nanosheet based hierarchical microspheres for high-rate and long-cycle life Li-ion batteries. *Adv. Energy Mater.* **7**, 1700950 (2017). <https://doi.org/10.1002/aenm.201700950>
40. Shen, L., Zhang, X., Uchaker, E., et al.: Li₄Ti₅O₁₂ nanoparticles embedded in a mesoporous carbon matrix as a superior anode material for high rate lithium ion batteries. *Adv. Energy Mater.* **2**, 691–698 (2012). <https://doi.org/10.1002/aenm.201100720>
41. Wang, Y.-Q., Gu, L., Guo, Y.-G., et al.: Rutile-TiO₂ nanocoating for a high-rate Li₄Ti₅O₁₂ anode of a lithium-ion battery. *J. Am. Chem. Soc.* **134**, 7874–7879 (2012). <https://doi.org/10.1021/ja301266w>
42. Naldoni, A., Allieta, M., Santangelo, S., et al.: Effect of nature and location of defects on bandgap narrowing in black TiO₂ nanoparticles. *J. Am. Chem. Soc.* **134**, 7600–7603 (2012). <https://doi.org/10.1021/ja3012676>
43. Cho, E., Han, S., Ahn, H.S., et al.: First-principles study of point defects in rutile TiO_{2-x}. *Phys. Rev. B* **73**, 193202 (2006). <https://doi.org/10.1103/PhysRevB.73.193202>
44. Yu, X., Kim, B., Kim, Y.K.: Highly enhanced photoactivity of anatase TiO₂ nanocrystals by controlled hydrogenation-induced surface defects. *ACS Catal.* **3**, 2479–2486 (2013). <https://doi.org/10.1021/cs4005776>
45. Xu, H., Chen, J., Li, Y., et al.: Fabrication of Li₄Ti₅O₁₂-TiO₂ nanosheets with structural defects as high-rate and long-life anodes for lithium-ion batteries. *Sci. Rep.* **7**, 2960 (2017). <https://doi.org/10.1038/s41598-017-03149-2>
46. Fischer, S., Munz, A.W., Schierbaum, K.-D., et al.: The geometric structure of intrinsic defects at TiO₂ (110) surfaces: an STM study. *Surf. Sci.* **337**, 17–30 (1995). [https://doi.org/10.1016/0039-6028\(95\)00572-2](https://doi.org/10.1016/0039-6028(95)00572-2)
47. Göpel, W., Anderson, J.A., Frankel, D., et al.: Surface defects of TiO₂(110): a combined XPS, XAES and ELS study. *Surf. Sci.* **139**, 333–346 (1984). [https://doi.org/10.1016/0039-6028\(84\)90054-2](https://doi.org/10.1016/0039-6028(84)90054-2)
48. Morgan, B.J., Watson, G.W.: Intrinsic n-type defect formation in TiO₂: a comparison of rutile and anatase from GGA + *U* calculations. *J. Phys. Chem. C* **114**, 2321–2328 (2010). <https://doi.org/10.1021/jp9088047>
49. Czoska, A., Livraghi, S., Chiesa, M., et al.: The nature of defects in fluorine-doped TiO₂. *J. Phys. Chem. C* **112**, 8951–8956 (2008). <https://doi.org/10.1021/jp8004184>
50. Di Valentin, C., Pacchioni, G., Selloni, A.: Reduced and n-type doped TiO₂: nature of Ti³⁺ species. *J. Phys. Chem. C* **113**, 20543–20552 (2009). <https://doi.org/10.1021/jp9061797>
51. Tachikawa, T., Ishigaki, T., Li, J.G., et al.: Defect-mediated photoluminescence dynamics of Eu³⁺-doped TiO₂ nanocrystals revealed at the single-particle or single-aggregate level. *Angew. Chem. Int. Ed.* **47**, 5348–5352 (2008). <https://doi.org/10.1002/anie.200800528>
52. Kong, L., Wang, C., Zheng, H., et al.: Defect-induced yellow color in Nb-doped TiO₂ and its impact on visible-light photocatalysis. *J. Phys. Chem. C* **119**, 16623–16632 (2015). <https://doi.org/10.1021/acs.jpcc.5b03448>
53. Kofstad, P.: Thermogravimetric studies of the defect structure of rutile (TiO₂). *J. Phys. Chem. Solids* **23**, 1579–1586 (1962). [https://doi.org/10.1016/0022-3697\(62\)90240-8](https://doi.org/10.1016/0022-3697(62)90240-8)
54. Marucco, J.-F., Gautron, J., Lemasson, P.: Thermogravimetric and electrical study of non-stoichiometric titanium dioxide TiO_{2-x}, between 800 and 1100°C. *J. Phys. Chem. Solids* **42**, 363–367 (1981). [https://doi.org/10.1016/0022-3697\(81\)90043-3](https://doi.org/10.1016/0022-3697(81)90043-3)
55. Millot, F., Picard, C.: Oxygen self-diffusion in non-stoichiometric rutile TiO_{2-x} at high temperature. *Solid State Ionics* **28**, 1344–1348 (1988). [https://doi.org/10.1016/0167-2738\(88\)90384-0](https://doi.org/10.1016/0167-2738(88)90384-0)
56. Catlow, C.R.A., James, R.: Disorder in TiO_{2-x}. *Proc. R. Soc. Lond. Ser. A Math. Phys. Eng. Sci.* **384**, 157–173 (1982). <https://doi.org/10.1098/rspa.1982.0152>
57. Menetrey, M., Markovits, A., Minot, C., et al.: Formation of Schottky defects at the surface of MgO, TiO₂, and SnO₂: a comparative density functional theoretical study. *J. Phys. Chem. B* **108**, 12858–12864 (2004). <https://doi.org/10.1021/jp048497c>
58. Weibel, A., Bouchet, R., Knauth, P.: Electrical properties and defect chemistry of anatase (TiO₂). *Solid State Ionics* **177**, 229–236 (2006). <https://doi.org/10.1016/j.ssi.2005.11.002>

59. Bak, T., Nowotny, J., Sucher, N.J., et al.: Effect of crystal imperfections on reactivity and photoreactivity of TiO₂ (rutile) with oxygen, water, and bacteria. *J. Phys. Chem. C* **115**, 15711–15738 (2011). <https://doi.org/10.1021/jp2027862>
60. Batzill, M., Katsiev, K., Gaspar, D.J., et al.: Variations of the local electronic surface properties of TiO₂ (110) induced by intrinsic and extrinsic defects. *Phys. Rev. B* **66**, 235401 (2002). <https://doi.org/10.1103/PhysRevB.66.235401>
61. Nowotny, J., Bak, T., Nowotny, M.K., et al.: Defect chemistry and electrical properties of titanium dioxide. I. Defect diagrams. *J. Phys. Chem. C* **112**, 590–601 (2008). <https://doi.org/10.1021/jp074565u>
62. Hoshino, K., Peterson, N.L., et al.: Diffusion and point-defects in TiO_{2-x}. *J. Phys. Chem. Solids* **46**, 1397–1411 (1985). [https://doi.org/10.1016/0022-3697\(85\)90079-4](https://doi.org/10.1016/0022-3697(85)90079-4)
63. Carneiro, J., Azevedo, S., Fernandes, F., et al.: Synthesis of iron-doped TiO₂ nanoparticles by ball-milling process: the influence of process parameters on the structural, optical, magnetic, and photocatalytic properties. *J. Mater. Sci.* **49**, 7476–7488 (2014). <https://doi.org/10.1007/s10853-014-8453-3>
64. Serpone, N.: Is the band gap of pristine TiO₂ narrowed by anion- and cation-doping of titanium dioxide in second-generation photocatalysts? *J. Phys. Chem. B* **110**, 24287–24293 (2006). <https://doi.org/10.1021/jp065659r>
65. Wang, J., Tafen, D.N., Lewis, J.P., et al.: Origin of photocatalytic activity of nitrogen-doped TiO₂ nanobelts. *J. Am. Chem. Soc.* **131**, 12290–12297 (2009). <https://doi.org/10.1021/ja903781h>
66. Huang, H., Li, X., Wang, J., et al.: Anionic group self-doping as a promising strategy: band-gap engineering and multifunctional applications of high-performance CO₃²⁻-doped Bi₂O₂CO₃. *ACS Catal.* **5**, 4094–4103 (2015). <https://doi.org/10.1021/acscatal.5b00444>
67. Sathish, M., Viswanathan, B., Viswanath, R., et al.: Synthesis, characterization, electronic structure, and photocatalytic activity of nitrogen-doped TiO₂ nanocatalyst. *Chem. Mater.* **17**, 6349–6353 (2005). <https://doi.org/10.1021/cm052047v>
68. Chen, X., Burda, C.: The electronic origin of the visible-light absorption properties of C-, N- and S-doped TiO₂ nanomaterials. *J. Am. Chem. Soc.* **130**, 5018–5019 (2008). <https://doi.org/10.1021/ja711023z>
69. Luo, N.J., Jiang, Z., Shi, H.H., et al.: Photo-catalytic conversion of oxygenated hydrocarbons to hydrogen over heteroatom-doped TiO₂ catalysts. *Int. J. Hydrogen Energy* **34**, 125–129 (2009). <https://doi.org/10.1016/j.ijhydene.2008.09.097>
70. Sathish, M., Viswanath, R.P., Gopinath, C.S.: N,S-co-doped TiO₂ nanophotocatalyst: synthesis, electronic structure and photocatalysis. *J. Nanosci. Nanotechnol.* **9**, 423–432 (2009). <https://doi.org/10.1166/jnn.2009.j095>
71. Zhen, C., Wang, L., Liu, L., et al.: Nonstoichiometric rutile TiO₂ photoelectrodes for improved photoelectrochemical water splitting. *Chem. Commun.* **49**, 6191–6193 (2013). <https://doi.org/10.1039/c3cc42458h>
72. He, J., Behera, R., Finnis, M., et al.: Prediction of high-temperature point defect formation in TiO₂ from combined ab initio and thermodynamic calculations. *Acta Mater.* **55**, 4325–4337 (2007). <https://doi.org/10.1016/j.actamat.2007.04.005>
73. Amade, R., Heitjans, P., Indris, S., et al.: Defect formation during high-energy ball milling in TiO₂ and its relation to the photocatalytic activity. *J. Photochem. Photobiol. A Chem.* **207**, 231–235 (2009). <https://doi.org/10.1016/j.jphotochem.2009.07.015>
74. Wu, Q., Zheng, Q., van de Krol, R.: Creating oxygen vacancies as a novel strategy to form tetrahedrally coordinated Ti⁴⁺ in Fe/TiO₂ nanoparticles. *J. Phys. Chem. C* **116**, 7219–7226 (2012). <https://doi.org/10.1021/jp212577g>
75. Chen, X., Liu, L., Peter, Y.Y., et al.: Increasing solar absorption for photocatalysis with black hydrogenated titanium dioxide nanocrystals. *Science* **331**, 746–750 (2011). <https://doi.org/10.1126/science.1200448>
76. Xin, X., Xu, T., Yin, J., et al.: Management on the location and concentration of Ti³⁺ in anatase TiO₂ for defects-induced visible-light photocatalysis. *Appl. Catal. B* **176**, 354–362 (2015). <https://doi.org/10.1016/j.apcatb.2015.04.016>
77. Chen, J., Song, W., Hou, H., et al.: Ti³⁺ self-doped dark rutile TiO₂ ultrafine nanorods with durable high-rate capability for lithium-ion batteries. *Adv. Funct. Mater.* **25**, 6793–6801 (2015). <https://doi.org/10.1002/adfm.201502978>
78. Kirner, U., Schierbaum, K., Göpel, W., et al.: Low and high temperature TiO₂ oxygen sensors. *Sensors Actuators B Chem.* **1**, 103–107 (1990). [https://doi.org/10.1016/0925-4005\(90\)80181-X](https://doi.org/10.1016/0925-4005(90)80181-X)
79. Ou, G., Xu, Y., Wen, B., et al.: Tuning defects in oxides at room temperature by lithium reduction. *Nat. Commun.* **9**, 1302 (2018). <https://doi.org/10.1038/s41467-018-03765-0>
80. Feng, H., Xu, Z., Ren, L., et al.: Activating titania for efficient electrocatalysis by vacancy engineering. *ACS Catal.* **8**, 4288–4293 (2018). <https://doi.org/10.1021/acscatal.8b00719>
81. Ghosh, S., Khan, G.G., Mandal, K., et al.: Evolution of vacancy-type defects, phase transition, and intrinsic ferromagnetism during annealing of nanocrystalline TiO₂ studied by positron annihilation spectroscopy. *J. Phys. Chem. C* **117**, 8458–8467 (2013). <https://doi.org/10.1021/jp3115836>
82. Xia, T., Zhang, Y., Murowchick, J., et al.: Vacuum-treated titanium dioxide nanocrystals: optical properties, surface disorder, oxygen vacancy, and photocatalytic activities. *Catal. Today* **225**, 2–9 (2014). <https://doi.org/10.1016/j.cattod.2013.08.026>
83. Xia, T., Zhang, W., Murowchick, J.B., et al.: A facile method to improve the photocatalytic and lithium-ion rechargeable battery performance of TiO₂ nanocrystals. *Adv. Energy Mater.* **3**, 1516–1523 (2013). <https://doi.org/10.1002/aenm.201300294>
84. Guillemot, F., Porte, M., Labrugère, C., et al.: Ti⁴⁺ to Ti³⁺ conversion of TiO₂ uppermost layer by low-temperature vacuum annealing: interest for titanium biomedical applications. *J. Colloid Interface Sci.* **255**, 75–78 (2002). <https://doi.org/10.1006/jcis.2002.8623>
85. Chen, X., Guan, X., Li, L., et al.: Defective mesoporous Li₄Ti₅O_{12-y}: an advanced anode material with anomalous capacity and cycling stability at a high rate of 20 C. *J. Power Sources* **210**, 297–302 (2012). <https://doi.org/10.1016/j.jpowsour.2012.03.014>
86. Pan, X., Ma, X.: Study on the milling-induced transformation in TiO₂ powder with different grain sizes. *Mater. Lett.* **58**, 513–515 (2004). [https://doi.org/10.1016/S0167-577X\(03\)00536-6](https://doi.org/10.1016/S0167-577X(03)00536-6)
87. Pan, X., Ma, X.: Phase transformations in nanocrystalline TiO₂ milled in different milling atmospheres. *J. Solid State Chem.* **177**, 4098–4103 (2004). <https://doi.org/10.1016/j.jssc.2004.08.017>
88. Sepelak, V., Begin-Colin, S., Le Caer, G.: Transformations in oxides induced by high-energy ball-milling. *Dalton Trans.* **41**, 11927–11948 (2012). <https://doi.org/10.1039/c2dt30349c>
89. Indris, S., Amade, R., Heitjans, P., et al.: Preparation by high-energy milling, characterization, and catalytic properties of nanocrystalline TiO₂. *J. Phys. Chem. B* **109**, 23274–23278 (2005). <https://doi.org/10.1021/jp054586t>
90. Ren, R.M., Yang, Z.G., Shaw, L.L.: Polymorphic transformation and powder characteristics of TiO₂ during high energy milling. *J. Mater. Sci.* **35**, 6015–6026 (2000). <https://doi.org/10.1023/A:1026751017284>
91. Marinell, S., Choi, D.H., Heuguet, R., et al.: Broadband dielectric characterization of TiO₂ ceramics sintered through microwave and conventional processes. *Ceram. Int.* **39**, 299–306 (2013). <https://doi.org/10.1016/j.ceramint.2012.06.025>

92. Chen, Y., Li, W., Wang, J., et al.: Microwave-assisted ionic liquid synthesis of Ti^{3+} self-doped TiO_2 hollow nanocrystals with enhanced visible-light photoactivity. *Appl. Catal. B* **191**, 94–105 (2016). <https://doi.org/10.1016/j.apcatb.2016.03.021>
93. Ishida, Y., Doshin, W., Tsukamoto, H., et al.: Black TiO_2 nanoparticles by a microwave-induced plasma over titanium complex aqueous solution. *Chem. Lett.* **44**, 1327–1329 (2015). <https://doi.org/10.1246/cl.150531>
94. Choi, J., Park, H., Hoffmann, M.R., et al.: Effects of single metal-ion doping on the visible-light photoreactivity of TiO_2 . *J. Phys. Chem. C* **114**, 783–792 (2009). <https://doi.org/10.1021/jp908088x>
95. Di Valentin, C., Pacchioni, G.: Trends in non-metal doping of anatase TiO_2 : B, C, N and F. *Catal. Today* **206**, 12–18 (2013). <https://doi.org/10.1016/j.cattod.2011.11.030>
96. Yang, X., Zhang, M.J., Min, Y., et al.: Controllable formation of (004)-orientated Nb: TiO_2 for High-Performance transparent conductive oxide thin films with tunable near-infrared transmittance. *ACS Appl. Mater. Interfaces*. **9**, 29021–29029 (2017). <https://doi.org/10.1021/acsami.7b06792>
97. Lan, T., Zhang, W., Wu, N.L., et al.: Nb-doped rutile TiO_2 mesocrystals with enhanced lithium storage properties for lithium ion battery. *Chem. A Eur. J.* **23**, 5059–5065 (2017). <https://doi.org/10.1002/chem.201605115>
98. Pathak, S.K., Abate, A., Ruckdeschel, P., et al.: Performance and stability enhancement of dye-sensitized and perovskite solar cells by Al doping of TiO_2 . *Adv. Funct. Mater.* **24**, 6046–6055 (2014). <https://doi.org/10.1002/adfm.201401658>
99. Zhang, Y., Meng, Y., Zhu, K., et al.: Copper-doped titanium dioxide bronze nanowires with superior high rate capability for lithium ion batteries. *ACS Appl. Mater. Interfaces*. **8**, 7957–7965 (2016). <https://doi.org/10.1021/acsami.5b10766>
100. Ali, Z., Cha, S.N., Sohn, J.I., et al.: Design and evaluation of novel Zn doped mesoporous TiO_2 based anode material for advanced lithium ion batteries. *J. Mater. Chem.* **22**, 17625–17629 (2012). <https://doi.org/10.1039/C2JM33315E>
101. Kashale, A.A., Rasal, A.S., Kamble, G.P., et al.: Biosynthesized Co-doped TiO_2 nanoparticles based anode for lithium-ion battery application and investigating the influence of dopant concentrations on its performance. *Compos. Part B Eng.* **167**, 44–50 (2019). <https://doi.org/10.1016/j.compositesb.2018.12.001>
102. Hong, Z., Kang, M., Chen, X., et al.: Synthesis of mesoporous Co^{2+} -doped TiO_2 nanodisks derived from metal organic frameworks with improved sodium storage performance. *ACS Appl. Mater. Interfaces* **9**, 32071–32079 (2017). <https://doi.org/10.1021/acsami.7b06290>
103. Zhang, W., Zhou, W., Wright, J.H., et al.: Mn-doped TiO_2 nanosheet-based spheres as anode materials for lithium-ion batteries with high performance at elevated temperatures. *ACS Appl. Mater. Interfaces*. **6**, 7292–7300 (2014). <https://doi.org/10.1021/am500604p>
104. Wang, J., Yang, G., Wang, L., et al.: In-situ fabrication of transition-metal-doped TiO_2 nanofiber/nanosheet structure for high-performance Li storage. *J. Alloys Compd.* **787**, 1110–1119 (2019). <https://doi.org/10.1016/j.jallcom.2019.02.152>
105. Serpone, N., Lawless, D., Disdier, J., et al.: Spectroscopic, photoconductivity, and photocatalytic studies of TiO_2 colloids: naked and with the lattice doped with Cr^{3+} , Fe^{3+} , and V^{5+} cations. *Langmuir* **10**, 643–652 (1994). <https://doi.org/10.1021/la00015a010>
106. Yang, K., Dai, Y., Huang, B.: Understanding photocatalytic activity of S- and P-doped TiO_2 under visible light from first-principles. *J. Phys. Chem. C* **111**, 18985–18994 (2007). <https://doi.org/10.1021/jp0756350>
107. Feng, N., Liu, F., Huang, M., et al.: Unravelling the efficient photocatalytic activity of boron-induced $\text{Ti}(3+)$ species in the surface layer of TiO_2 . *Sci. Rep.* **6**, 34765 (2016). <https://doi.org/10.1038/srep34765>
108. Irie, H., Watanabe, Y., Hashimoto, K.: Nitrogen-concentration dependence on photocatalytic activity of $\text{TiO}_2\text{-N}_x$ powders. *J. Phys. Chem. B* **107**, 5483–5486 (2003). <https://doi.org/10.1021/jp030133h>
109. Qi, Y., Huang, Y., Jia, D., et al.: Preparation and characterization of novel spinel $\text{Li}_4\text{Ti}_5\text{O}_{12-x}\text{Br}_x$ anode materials. *Electrochim. Acta* **54**(21), 4772–4776 (2009). <https://doi.org/10.1016/j.electacta.2009.04.010>
110. Qiu, J., Lai, C., Gray, E., et al.: Blue hydrogenated lithium titanate as a high-rate anode material for lithium-ion batteries. *J. Mater. Chem. A* **2**, 6353–6358 (2014). <https://doi.org/10.1039/C4TA00556B>
111. Jiang, X., Zhang, Y., Jiang, J., et al.: Characterization of oxygen vacancy associates within hydrogenated TiO_2 : a positron annihilation study. *J. Phys. Chem. C* **116**, 22619–22624 (2012). <https://doi.org/10.1021/jp307573c>
112. Wang, G., Wang, H., Ling, Y., et al.: Hydrogen-treated TiO_2 nanowire arrays for photoelectrochemical water splitting. *Nano Lett.* **11**, 3026–3033 (2011). <https://doi.org/10.1021/nl201766h>
113. Qiu, J., Li, S., Gray, E., et al.: Hydrogenation synthesis of blue TiO_2 for high-performance lithium-ion batteries. *J. Phys. Chem. C* **118**, 8824–8830 (2014). <https://doi.org/10.1021/jp501819p>
114. Lu, H.Q., Zhao, B.B., Pan, R.L., et al.: Safe and facile hydrogenation of commercial Degussa P25 at room temperature with enhanced photocatalytic activity. *RSC Adv.* **4**, 1128–1132 (2014). <https://doi.org/10.1039/c3ra44493g>
115. Cai, J., Wang, Y., Zhu, Y., et al.: In situ formation of disorder-engineered TiO_2 (B)-anatase heterophase junction for enhanced photocatalytic hydrogen evolution. *ACS Appl. Mater. Interfaces*. **7**, 24987–24992 (2015). <https://doi.org/10.1021/acsami.5b07318>
116. Su, T., Yang, Y., Na, Y., et al.: An insight into the role of oxygen vacancy in hydrogenated TiO_2 nanocrystals in the performance of dye-sensitized solar cells. *ACS Appl. Mater. Interfaces*. **7**, 3754–3763 (2015). <https://doi.org/10.1021/am5085447>
117. Wu, M.C., Chang, I.C., Hsiao, K.C., et al.: Highly visible-light absorbing black TiO_2 nanocrystals synthesized by sol-gel method and subsequent heat treatment in low partial pressure H_2 . *J. Taiwan Inst. Chem. Eng.* **63**, 430–435 (2016). <https://doi.org/10.1016/j.jtice.2016.02.026>
118. Liu, N., Schneider, C., Freitag, D., et al.: Black TiO_2 nanotubes: cocatalyst-free open-circuit hydrogen generation. *Nano Lett.* **14**, 3309–3313 (2014). <https://doi.org/10.1021/nl500710j>
119. Wang, W., Lu, C., Ni, Y., et al.: A new sight on hydrogenation of F and NF doped 0 0 1 facets dominated anatase TiO_2 for efficient visible light photocatalyst. *Appl. Catal. B* **127**, 28–35 (2012). <https://doi.org/10.1016/j.apcatb.2012.08.002>
120. Hoang, S., Berglund, S.P., Hahn, N.T., et al.: Enhancing visible light photo-oxidation of water with TiO_2 nanowire arrays via cotreatment with H_2 and NH_3 : synergistic effects between Ti^{3+} and N. *J. Am. Chem. Soc.* **134**, 3659–3662 (2012). <https://doi.org/10.1021/ja211369s>
121. Yan, Y., Han, M., Konkin, A., et al.: Slightly hydrogenated TiO_2 with enhanced photocatalytic performance. *J. Mater. Chem. A* **2**, 12708–12716 (2014). <https://doi.org/10.1039/c4ta02192d>
122. Wu, H., Xu, C., Xu, J., et al.: Enhanced supercapacitance in anodic TiO_2 nanotube films by hydrogen plasma treatment. *Nanotechnology* **24**, 455401 (2013). <https://doi.org/10.1088/0957-4484/24/45/455401>
123. Yang, C., Wang, Z., Lin, T., et al.: Core-shell nanostructured “black” rutile titania as excellent catalyst for hydrogen production enhanced by sulfur doping. *J. Am. Chem. Soc.* **135**, 17831–17838 (2013). <https://doi.org/10.1021/ja4076748>
124. Lin, T., Yang, C., Wang, Z., et al.: Effective nonmetal incorporation in black titania with enhanced solar energy utilization.

- Energy Environ. Sci. **7**, 967–972 (2014). <https://doi.org/10.1039/C3EE42708K>
125. Ye, M., Jia, J., Wu, Z., et al.: Synthesis of black TiO₂ nanoparticles by Mg reduction of TiO₂ nanocrystals and their application for solar water evaporation. *Adv. Energy Mater.* **7**, 1601811 (2017). <https://doi.org/10.1002/aenm.201601811>
 126. Zheng, Z., Huang, B., Meng, X., et al.: Metallic zinc-assisted synthesis of Ti³⁺ self-doped TiO₂ with tunable phase composition and visible-light photocatalytic activity. *Chem. Commun.* **49**, 868–870 (2013). <https://doi.org/10.1039/c3cc37976g>
 127. Sinhamahapatra, A., Jeon, J.-P., Yu, J.-S.: A new approach to prepare highly active and stable black titania for visible light-assisted hydrogen production. *Energy Environ. Sci.* **8**, 3539–3544 (2015). <https://doi.org/10.1039/C5EE02443A>
 128. Ariyanti, D., Mills, L., Dong, J., et al.: NaBH₄ modified TiO₂: defect site enhancement related to its photocatalytic activity. *Mater. Chem. Phys.* **199**, 571–576 (2017). <https://doi.org/10.1016/j.matchemphys.2017.07.054>
 129. Xu, J., Qi, X., Luo, C., et al.: Synthesis and enhanced microwave absorption properties: a strongly hydrogenated TiO₂ nanomaterial. *Nanotechnology* **28**, 425701 (2017). <https://doi.org/10.1088/1361-6528/aa81ba>
 130. Chen, S., Xiao, Y., Wang, Y., et al.: A facile approach to prepare black TiO₂ with oxygen vacancy for enhancing photocatalytic activity. *Nanomaterials* **8**, 245 (2018). <https://doi.org/10.3390/nano8040245>
 131. Nasara, R.N., Tsai, P.C., Lin, S.K.: One-step synthesis of highly oxygen-deficient lithium titanate oxide with conformal amorphous carbon coating as anode material for lithium ion batteries. *Adv. Mater. Interfaces* **4**, 1700329 (2017). <https://doi.org/10.1002/admi.201700329>
 132. Tominaka, S., Tsujimoto, Y., Matsushita, Y., et al.: Synthesis of nanostructured reduced titanium oxide: crystal structure transformation maintaining nanomorphology. *Angew. Chem. Int. Ed.* **50**, 7418–7421 (2011). <https://doi.org/10.1002/anie.201101432>
 133. Mao, C., Zuo, F., Hou, Y., et al.: In situ preparation of a Ti³⁺ self-doped TiO₂ film with enhanced activity as photoanode by N₂H₄ reduction. *Angew. Chem. Int. Ed.* **53**, 10485–10489 (2014). <https://doi.org/10.1002/anie.201406017>
 134. Ullattil, S.G., Periyat, P.: A ‘one pot’ gel combustion strategy towards Ti³⁺ self-doped ‘black’ anatase TiO_{2-x} solar photocatalyst. *J. Mater. Chem. A* **4**, 5854–5858 (2016). <https://doi.org/10.1039/C6TA01993E>
 135. Zou, X., Liu, J., Su, J., et al.: Facile synthesis of thermal-and photostable titania with paramagnetic oxygen vacancies for visible-light photocatalysis. *Chem. A Eur. J.* **19**, 2866–2873 (2013). <https://doi.org/10.1002/chem.201202833>
 136. Zhang, Z., Hedhili, M.N., Zhu, H., et al.: Electrochemical reduction induced self-doping of Ti³⁺ for efficient water splitting performance on TiO₂ based photoelectrodes. *Phys. Chem. Chem. Phys.* **15**, 15637–15644 (2013). <https://doi.org/10.1039/c3cp52759j>
 137. Dong, J., Han, J., Liu, Y., et al.: Defective black TiO₂ synthesized via anodization for visible-light photocatalysis. *ACS Appl. Mater. Interfaces* **6**, 1385–1388 (2014). <https://doi.org/10.1021/am405549p>
 138. Grabstanowicz, L.R., Gao, S., Li, T., et al.: Facile oxidative conversion of TiH₂ to high-concentration Ti³⁺-self-doped rutile TiO₂ with visible-light photoactivity. *Inorg. Chem.* **52**, 3884–3890 (2013). <https://doi.org/10.1021/ic3026182>
 139. Liu, X., Xu, H., Grabstanowicz, L.R., et al.: Ti³⁺ self-doped TiO_{2-x} anatase nanoparticles via oxidation of TiH₂ in H₂O₂. *Catal. Today* **225**, 80–89 (2014). <https://doi.org/10.1016/j.catto.2013.08.025>
 140. Zhu, Q., Peng, Y., Lin, L., et al.: Stable blue TiO_{2-x} nanoparticles for efficient visible light photocatalysts. *J. Mater. Chem. A* **2**, 4429–4437 (2014). <https://doi.org/10.1039/c3ta14484d>
 141. Zhao, Z., Tan, H., Zhao, H., et al.: Reduced TiO₂ rutile nanorods with well-defined facets and their visible-light photocatalytic activity. *Chem. Commun.* **50**, 2755–2757 (2014). <https://doi.org/10.1039/c3cc49182j>
 142. Pei, Z., Ding, L., Lin, H., et al.: Facile synthesis of defect-mediated TiO_{2-x} with enhanced visible light photocatalytic activity. *J. Mater. Chem. A* **1**, 10099–10102 (2013). <https://doi.org/10.1039/c3ta12062g>
 143. Dong, S., Wang, X., Shen, L., et al.: Trivalent Ti self-doped Li₄Ti₅O₁₂: a high performance anode material for lithium-ion capacitors. *J. Electroanal. Chem.* **757**, 1–7 (2015). <https://doi.org/10.1016/j.jelechem.2015.09.002>
 144. Schaub, R., Wahlström, E., Rønnau, A., et al.: Oxygen-mediated diffusion of oxygen vacancies on the TiO₂ (110) surface. *Science* **299**, 377–379 (2003). <https://doi.org/10.1126/science.1078962>
 145. Choudhury, B., Choudhury, A.: Luminescence characteristics of cobalt doped TiO₂ nanoparticles. *J. Lumin.* **132**, 178–184 (2012). <https://doi.org/10.1016/j.jlumin.2011.08.020>
 146. Yun, H.J., Lee, D.M., Yu, S., et al.: Effect of valence band energy on the photocatalytic performance of N-doped TiO₂ for the production of O₂ via the oxidation of water by visible light. *J. Mol. Catal. A: Chem.* **378**, 221–226 (2013). <https://doi.org/10.1016/j.molcata.2013.06.016>
 147. Sarkar, A., Khan, G.G., Chaudhuri, A., et al.: Multifunctional BiFeO₃/TiO₂ nano-heterostructure: photo-ferroelectricity, rectifying transport, and nonvolatile resistive switching property. *Appl. Phys. Lett.* **108**, 033112 (2016). <https://doi.org/10.1063/1.4940118>
 148. Samsudin, E.M., Hamid, S.B.A., Juan, J.C., et al.: Effective role of trifluoroacetic acid (TFA) to enhance the photocatalytic activity of F-doped TiO₂ prepared by modified sol–gel method. *Appl. Surf. Sci.* **365**, 57–68 (2016). <https://doi.org/10.1016/j.apsusc.2016.01.016>
 149. Shrivastava, B.D.: X-ray absorption fine structure (XAFS) spectroscopy using synchrotron radiation. *J. Phys. Conf. Ser.* **365**, 012002 (2012). <https://doi.org/10.1088/1742-6596/365/1/012002>
 150. Yamashita, H., Ichihashi, Y., Anpo, M., et al.: Photocatalytic decomposition of NO at 275 K on titanium oxides included within y-zeolite cavities: the structure and role of the active sites. *J. Phys. Chem.* **100**, 16041–16044 (1996). <https://doi.org/10.1021/jp9615969>
 151. Chen, L.X., Rajh, T., Jager, W., et al.: X-ray absorption reveals surface structure of titanium dioxide nanoparticles. *J. Synchrotron Radiat.* **6**, 445–447 (1999). <https://doi.org/10.1107/S090904959801591X>
 152. Graetz, J., Reilly, J.J., Johnson, J., et al.: X-ray absorption study of Ti-activated sodium aluminum hydride. *Appl. Phys. Lett.* **85**, 500–502 (2004). <https://doi.org/10.1063/1.1773614>
 153. Wagemaker, M., Lützenkirchen-Hecht, D., Keil, P., et al.: Quasi-in situ reflection mode XANES at the Ti K-edge of lithium intercalated TiO₂ rutile and anatase. *Phys. B* **336**, 118–123 (2003). [https://doi.org/10.1016/S0921-4526\(03\)00279-5](https://doi.org/10.1016/S0921-4526(03)00279-5)
 154. Liu, Z.F., Davis, R.J.: Investigation of the structure of microporous Ti–Si mixed oxides by X-Ray, Uv reflectance, Ft-Raman, and Ft-IR spectroscopies. *J. Phys. Chem.* **98**, 1253–1261 (1994). <https://doi.org/10.1021/j100055a035>
 155. Song, H., Jeong, T.G., Moon, Y.H., et al.: Stabilization of oxygen-deficient structure for conducting Li₄Ti₅O₁₂-delta by molybdenum doping in a reducing atmosphere. *Sci. Rep.* **4**, 4350 (2014). <https://doi.org/10.1038/srep04350>
 156. Konno, H.: Chapter 8—X-ray photoelectron spectroscopy. In: Inagaki, M., Kang, F. (eds.) *Materials Science and Engineering of Carbon*, pp. 153–171. Butterworth-Heinemann, Oxford (2016)

157. Kang, Q., Cao, J., Zhang, Y., et al.: Reduced TiO₂ nanotube arrays for photoelectrochemical water splitting. *J. Mater. Chem. A* **1**, 5766–5774 (2013). <https://doi.org/10.1039/C3TA10689F>
158. Guo, Q., Cheng, X., Shi, Y., et al.: Bluish Li₄Ti₅O₁₂ with enhanced rate performance. *J. Alloys Compd.* **710**, 383–392 (2017). <https://doi.org/10.1016/j.jallcom.2017.03.296>
159. Wu, W.Y., Chang, Y.M., Ting, J.M.: Room-temperature synthesis of single-crystalline anatase TiO₂ nanowires. *Cryst. Growth Des.* **10**, 1646–1651 (2010). <https://doi.org/10.1021/cg901210c>
160. Ferraro, J.R., Nakamoto, K., Brown, C.W.: Chapter 1—basic theory. In: Ferraro, J.R., Nakamoto, K., Brown, C.W. (eds.) *Introductory Raman spectroscopy*, 2nd edn, pp. 1–94. Academic Press, San Diego (2003)
161. Zhang, X.Q., Chen, J.B., Wang, C.W., et al.: Low-temperature liquid phase reduced TiO₂ nanotube arrays: synergy of morphology manipulation and oxygen vacancy doping for enhancement of field emission. *Nanotechnology* **26**, 175705 (2015). <https://doi.org/10.1088/0957-4484/26/17/175705>
162. Yi, T.F., Jiang, L.J., Liu, J., et al.: Structure and physical properties of Li₄Ti₅O₁₂ synthesized at deoxidization atmosphere. *Ionics* **17**, 799–803 (2011). <https://doi.org/10.1007/s11581-011-0581-z>
163. Parker, J.C., Siegel, R.W.: Calibration of the Raman spectrum to the oxygen stoichiometry of nanophase TiO₂. *Appl. Phys. Lett.* **57**, 943–945 (1990). <https://doi.org/10.1063/1.104274>
164. Zhang, W.F., He, Y.L., Zhang, M.S., et al.: Raman scattering study on anatase TiO₂ nanocrystals. *J. Phys. D Appl. Phys.* **33**, 912–916 (2000). <https://doi.org/10.1088/0022-3727/33/8/305>
165. Choudhury, B., Dey, M., Choudhury, A.: Defect generation, d-d transition, and band gap reduction in Cu-doped TiO₂ nanoparticles. *Int. Nano Lett.* **3**, 25 (2013). <https://doi.org/10.1186/2228-5326-3-25>
166. Sarkar, A., Karmakar, K., Khan, G.G.: Designing Co–Pi modified one-dimensional N–P TiO₂/ZnCo₂O₄ nanoheterostructure photoanode with reduced electron–hole pair recombination and excellent photoconversion efficiency (> 3%). *J. Phys. Chem. C* **121**, 25705–25717 (2017). <https://doi.org/10.1021/acs.jpcc.7b08213>
167. Wajid Shah, M., Zhu, Y., Fan, X., et al.: Facile synthesis of defective TiO_{2-x} nanocrystals with high surface area and tailoring bandgap for visible-light photocatalysis. *Sci. Rep.* **5**, 15804 (2015). <https://doi.org/10.1038/srep15804>
168. McDevitt, N.T., Baun, W.L.: Infrared absorption study of metal oxides in the low frequency region (700–240 cm⁻¹). *Spectrochim. Acta* **20**, 799–808 (1964). [https://doi.org/10.1016/0371-1951\(64\)80079-5](https://doi.org/10.1016/0371-1951(64)80079-5)
169. Wang, P., Qi, C., Wen, P., et al.: Synthesis of Si, N co-doped nano-sized TiO₂ with high thermal stability and photocatalytic activity by mechanochemical method. *Nanomaterials* (2018). <https://doi.org/10.3390/nano8050294>
170. Benjwal, P., Kar, K.K.: Removal of methylene blue from wastewater under a low power irradiation source by Zn, Mn co-doped TiO₂ photocatalysts. *RSC Adv.* **5**, 98166–98176 (2015). <https://doi.org/10.1039/C5RA19353B>
171. Yu, D., Goh, K., Wang, H., et al.: Scalable synthesis of hierarchically structured carbon nanotube–graphene fibres for capacitive energy storage. *Nat. Nanotechnol.* **9**, 555 (2014). <https://doi.org/10.1038/NNANO.2014.93>
172. Li, J., Zhang, M., Guan, Z., et al.: Synergistic effect of surface and bulk single-electron-trapped oxygen vacancy of TiO₂ in the photocatalytic reduction of CO₂. *Appl. Catal. B* **206**, 300–307 (2017). <https://doi.org/10.1016/j.apcatb.2017.01.025>
173. Sun, Y., Egawa, T., Shao, C., et al.: Quantitative study of F center in high-surface-area anatase titania nanoparticles prepared by MOCVD. *J. Phys. Chem. Solids* **65**, 1793–1797 (2004). <https://doi.org/10.1016/j.jpcs.2004.05.006>
174. Guo, Y., Chen, S., Yu, Y., et al.: Hydrogen-location-sensitive modulation of the redox reactivity for oxygen-deficient TiO₂. *J. Am. Chem. Soc.* (2019). <https://doi.org/10.1021/jacs.9b01836>
175. Meng, W.-W., Yan, B.-L., Xu, Y.-J.: A facile electrochemical modification route in molten salt for Ti³⁺ self-doped spinel lithium titanate. *Electrochim. Acta* **279**, 128–135 (2018). <https://doi.org/10.1016/j.electacta.2018.05.070>
176. Liu, H., Ma, H.T., Li, X.Z., et al.: The enhancement of TiO₂ photocatalytic activity by hydrogen thermal treatment. *Chemosphere* **50**, 39–46 (2003). [https://doi.org/10.1016/S0045-6535\(02\)00486-1](https://doi.org/10.1016/S0045-6535(02)00486-1)
177. Kaftelen, H., Tuncer, M., Tu, S., et al.: Mn-substituted spinel Li₄Ti₅O₁₂ materials studied by multifrequency EPR spectroscopy. *J. Mater. Chem. A* **1**, 9973–9982 (2013). <https://doi.org/10.1039/C3TA11590A>
178. Yoshida, K., Kawai, T., Nambara, T., et al.: Direct observation of oxygen atoms in rutile titanium dioxide by spherical aberration corrected high-resolution transmission electron microscopy. *Nanotechnology* **17**, 3944–3950 (2006). <https://doi.org/10.1088/0957-4484/17/15/056>
179. Lu, X., Zhao, L., He, X., et al.: Lithium storage in Li₄Ti₅O₁₂ spinel: the full static picture from electron microscopy. *Adv. Mater.* **24**, 3233–3238 (2012). <https://doi.org/10.1002/adma.201200450>
180. Gomathi Devi, L., Narasimha Murthy, B.: Characterization of Mo Doped TiO₂ and its enhanced photo catalytic activity under visible light. *Catal. Lett.* **125**, 320–330 (2008). <https://doi.org/10.1007/s10562-008-9568-4>
181. Ho, W., Yu, J.C., Lee, S.: Synthesis of hierarchical nanoporous F-doped TiO₂ spheres with visible light photocatalytic activity. *Chem. Commun.* **10**, 1115–1117 (2006). <https://doi.org/10.1039/B515513D>
182. Samsudin, E.M., Abd Hamid, S.B., Juan, J.C., et al.: Controlled nitrogen insertion in titanium dioxide for optimal photocatalytic degradation of atrazine. *RSC Adv.* **5**, 44041–44052 (2015). <https://doi.org/10.1039/C5RA00890E>
183. Lü, X., Chen, A., Luo, Y., et al.: Conducting Interface in oxide homojunction: understanding of superior properties in black TiO₂. *Nano Lett.* **16**, 5751–5755 (2016). <https://doi.org/10.1021/acs.nanolett.6b02454>
184. Muller, D.A., Nakagawa, N., Ohtomo, A., et al.: Atomic-scale imaging of nanoengineered oxygen vacancy profiles in SrTiO₃. *Nature* **430**, 657–661 (2004). <https://doi.org/10.1038/nature02756>
185. Nakagawa, N., Hwang, H.Y., Muller, D.A.: Why some interfaces cannot be sharp. *Nat. Mater.* **5**, 204–209 (2006). <https://doi.org/10.1038/nmat1569>
186. Widmaier, M., Pfeifer, K., Bommer, L., et al.: Valence-tuned lithium titanate nanopowder for high-rate electrochemical energy storage. *Batter. Supercaps* **1**, 11–26 (2018). <https://doi.org/10.1002/batt.201700007>
187. Hugenschmidt, M.B., Gamble, L., Campbell, C.T.: The interaction of H₂O with a TiO₂(110) surface. *Surf. Sci.* **302**, 329–340 (1994). [https://doi.org/10.1016/0039-6028\(94\)90837-0](https://doi.org/10.1016/0039-6028(94)90837-0)
188. Henderson, M.A.: Evidence for bicarbonate formation on vacuum annealed TiO₂(110) resulting from a precursor-mediated interaction between CO₂ and H₂O. *Surf. Sci.* **400**, 203–219 (1998). [https://doi.org/10.1016/S0039-6028\(97\)00863-7](https://doi.org/10.1016/S0039-6028(97)00863-7)
189. Besselmann, S., Freitag, C., Hinrichsen, O., et al.: Temperature-programmed reduction and oxidation experiments with V₂O₅/TiO₂ catalysts. *Phys. Chem. Chem. Phys.* **3**, 4633–4638 (2001). <https://doi.org/10.1039/B105466J>
190. Setvin, M., Hulva, J., Parkinson, G.S., et al.: Electron transfer between anatase TiO₂ and an O₂ molecule directly observed by atomic force microscopy. *Proc. Natl. Acad. Sci. USA* **114**, E2556–E2562 (2017). <https://doi.org/10.1073/pnas.1618723114>

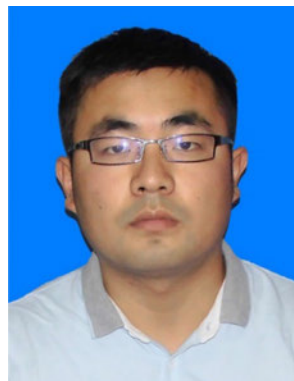
191. Ma, Y., Wang, X., Jia, Y., et al.: Titanium dioxide-based nano-materials for photocatalytic fuel generations. *Chem. Rev.* **114**, 9987–10043 (2014). <https://doi.org/10.1021/cr500008u>
192. Huang, S.Y., Kavan, L., Exnar, I., et al.: Rocking chair lithium battery based on nanocrystalline TiO_2 (anatase). *J. Electrochem. Soc.* **142**, L142–L144 (1995). <https://doi.org/10.1149/1.2048726>
193. Jiang, C., Wei, M., Qi, Z., et al.: Particle size dependence of the lithium storage capability and high rate performance of nanocrystalline anatase TiO_2 electrode. *J. Power Sources* **166**, 239–243 (2007). <https://doi.org/10.1016/j.jpowsour.2007.01.004>
194. Yang, Z.G., Choi, D., Kerisit, S., et al.: Nanostructures and lithium electrochemical reactivity of lithium titanites and titanium oxides: a review. *J. Power Sources* **192**, 588–598 (2009). <https://doi.org/10.1016/j.jpowsour.2009.02.038>
195. Deng, D., Kim, M.G., Lee, J.Y., et al.: Green energy storage materials: nanostructured TiO_2 and Sn-based anodes for lithium-ion batteries. *Energy Environ. Sci.* **2**, 818–837 (2009). <https://doi.org/10.1039/B823474D>
196. Dawson, J.A., Robertson, J.: Improved calculation of Li and Na intercalation properties in anatase, rutile, and $\text{TiO}_2(\text{B})$. *J. Phys. Chem. C* **120**, 22910–22917 (2016). <https://doi.org/10.1021/acs.jpcc.6b08842>
197. Tsai, P.-C., Hsu, W.-D., Lin, S.-K.: Atomistic structure and Ab initio electrochemical properties of $\text{Li}_4\text{Ti}_5\text{O}_{12}$ defect spinel for Li ion batteries. *J. Electrochem. Soc.* **161**, A439–A444 (2014). <https://doi.org/10.1149/2.095403jes>
198. Ohzuku, T., Ueda, A., Yamamoto, N.: Zero-strain insertion material of $\text{Li}[\text{Li}_{1/3}\text{Ti}_{5/3}]\text{O}_4$ for rechargeable lithium cells. *J. Electrochem. Soc.* **142**, 1431–1435 (1995). <https://doi.org/10.1149/1.2048592>
199. Kostlánová, T., Dědeček, J., Krtil, P.: The effect of the inner particle structure on the electronic structure of the nano-crystalline Li–Ti–O spinels. *Electrochim. Acta* **52**, 1847–1856 (2007). <https://doi.org/10.1016/j.electacta.2006.07.048>
200. Jhan, Y.R., Duh, J.G.: Electrochemical performance and low discharge cut-off voltage behavior of ruthenium doped $\text{Li}_4\text{Ti}_5\text{O}_{12}$ with improved energy density. *Electrochim. Acta* **63**, 9–15 (2012). <https://doi.org/10.1016/j.electacta.2011.12.014>
201. Kim, C., Norberg, N.S., Alexander, C.T., et al.: Mechanism of phase propagation during lithiation in carbon-free $\text{Li}_4\text{Ti}_5\text{O}_{12}$ battery electrodes. *Adv. Funct. Mater.* **23**, 1214–1222 (2013). <https://doi.org/10.1002/adfm.201201684>
202. Asahi, R., Taga, Y., Mannstadt, W., et al.: Electronic and optical properties of anatase TiO_2 . *Phys. Rev. B* **61**, 7459–7465 (2000). <https://doi.org/10.1103/PhysRevB.61.7459>
203. Yeh, H.L., Tai, S.H., Hsieh, C.M., et al.: First-principles study of lithium intercalation and diffusion in oxygen-defective titanium dioxide. *J. Phys. Chem. C* **122**, 19447–19454 (2018). <https://doi.org/10.1021/acs.jpcc.8b06540>
204. Scanlon, D.O., Dunnill, C.W., Buckeridge, J., et al.: Band alignment of rutile and anatase TiO_2 . *Nat. Mater.* **12**, 798–801 (2013). <https://doi.org/10.1038/nmat3697>
205. Burdett, J.K., Hughbanks, T., Miller, G.J., et al.: Structural-electronic relationships in inorganic solids: powder neutron diffraction studies of the rutile and anatase polymorphs of titanium dioxide at 15 and 295 K. *J. Am. Chem. Soc.* **109**, 3639–3646 (1987). <https://doi.org/10.1021/ja00246a021>
206. Shi, L.-B., Wang, Y.P.: A study on native defects and magnetic properties in undoped rutile TiO_2 using LDA and LDA + $U_{\text{Op}} + U_{\text{Tid}}$ methods. *J. Magn. Magn. Mater.* **405**, 1–8 (2016). <https://doi.org/10.1016/j.jmmm.2015.12.045>
207. Morgan, B.J., Madden, P.A.: Lithium intercalation into $\text{TiO}_2(\text{B})$: a comparison of LDA, GGA, and GGA + U density functional calculations. *Phys. Rev. B* **86**, 035147 (2012). <https://doi.org/10.1103/PhysRevB.86.035147>
208. D'Elia, D.: Elaboration and study of TiO_2 nanostructures for hydrogen generation via photolysis of water. *École Nationale Supérieure des Mines de Paris* (2011)
209. Feist, T.P., Davies, P.K.: The soft chemical synthesis of TiO_2 (B) from layered titanates. *J. Solid State Chem.* **101**, 275–295 (1992). [https://doi.org/10.1016/0022-4596\(92\)90184-W](https://doi.org/10.1016/0022-4596(92)90184-W)
210. Ouyang, C.Y., Zhong, Z.Y., Lei, M.S.: Ab initio studies of structural and electronic properties of $\text{Li}_4\text{Ti}_5\text{O}_{12}$ spinel. *Electrochem. Commun.* **9**, 1107–1112 (2007). <https://doi.org/10.1016/j.elecom.2007.01.013>
211. Kellerman, D.G., Mukhina, N.A., Zhuravlev, N.A., et al.: Optical absorption and nuclear magnetic resonance in lithium titanium spinel doped by chromium. *Phys. Solid State* **52**, 459–464 (2010). <https://doi.org/10.1134/s1063783410030030>
212. Raja, M.W., Mahanty, S., Kundu, M., et al.: Synthesis of nanocrystalline $\text{Li}_4\text{Ti}_5\text{O}_{12}$ by a novel aqueous combustion technique. *J. Alloys Compd.* **468**, 258–262 (2009). <https://doi.org/10.1016/j.jallcom.2007.12.072>
213. Scharner, S., Weppner, W., Schmid-Beurmann, P.: Evidence of two-phase formation upon lithium insertion into the $\text{Li}_{1.33}\text{Ti}_{1.67}\text{O}_4$ spinel. *J. Electrochem. Soc.* **146**, 857–861 (1999). <https://doi.org/10.1149/1.1391692>
214. Wagemaker, M., Borghols, W.J.H., Mulder, F.M.: Large impact of particle size on insertion reactions. A case for anatase Li_xTiO_2 . *J. Am. Chem. Soc.* **129**, 4323–4327 (2007). <https://doi.org/10.1021/ja067733p>
215. Armstrong, A.R., Armstrong, G., Canales, J., et al.: Lithium-ion intercalation into TiO_2 -B nanowires. *Adv. Mater.* **17**, 862–865 (2005). <https://doi.org/10.1002/adma.200400795>
216. Shin, J.-Y., Samuelis, D., Maier, J.: Sustained lithium-storage performance of hierarchical, nanoporous anatase TiO_2 at high rates: emphasis on interfacial storage phenomena. *Adv. Funct. Mater.* **21**, 3464–3472 (2011). <https://doi.org/10.1002/adfm.201002527>
217. Rahman, M.A., Wang, X., Wen, C.: Enhanced electrochemical performance of Li-ion batteries with nanoporous titania as negative electrodes. *J. Energy Chem.* **24**, 157–170 (2015). [https://doi.org/10.1016/S2095-4956\(15\)60296-0](https://doi.org/10.1016/S2095-4956(15)60296-0)
218. Dambournet, D., Belharouak, I., Amine, K.: Tailored preparation methods of TiO_2 anatase, Rutile, Brookite: mechanism of formation and electrochemical properties. *Chem. Mater.* **22**, 1173–1179 (2010). <https://doi.org/10.1021/cm902613h>
219. Shin, J.Y., Joo, J.H., Samuelis, D., et al.: Oxygen-deficient $\text{TiO}_{2-\delta}$ nanoparticles via hydrogen reduction for high rate capability lithium batteries. *Chem. Mater.* **24**, 543–551 (2012). <https://doi.org/10.1021/cm2031009>
220. Song, H., Yun, S.W., Chun, H.H., et al.: Anomalous decrease in structural disorder due to charge redistribution in Cr-doped $\text{Li}_4\text{Ti}_5\text{O}_{12}$ negative-electrode materials for high-rate Li-ion batteries. *Energy Environ. Sci.* **5**, 9903–9913 (2012). <https://doi.org/10.1039/C2EE22734G>
221. Lu, Z., Yip, C.T., Wang, L., et al.: Hydrogenated TiO_2 nanotube arrays as high-rate anodes for lithium-ion microbatteries. *ChemPlusChem* **77**, 991–1000 (2012). <https://doi.org/10.1002/cplu.201200104>
222. Ventosa, E., Tymoczko, A., Xie, K., et al.: Low temperature hydrogen reduction of high surface area anatase and anatase/ β - TiO_2 for high-charging-rate batteries. *Chemosuschem* **7**, 2584–2589 (2014). <https://doi.org/10.1002/cssc.201402279>
223. Zhang, Z., Zhou, Z., Nie, S., et al.: Flower-like hydrogenated $\text{TiO}_2(\text{B})$ nanostructures as anode materials for high-performance lithium ion batteries. *J. Power Sources* **267**, 388–393 (2014). <https://doi.org/10.1016/j.jpowsour.2014.05.121>
224. Zheng, J., Liu, Y., Ji, G., et al.: Hydrogenated oxygen-deficient blue anatase as anode for high-performance lithium batteries. *ACS Appl. Mater. Interfaces* **7**, 23431–23438 (2015). <https://doi.org/10.1021/acsami.5b07000>

225. Kim, J.G., Shi, D., Kong, K.J., et al.: Structurally and electronically designed TiO_2N_x nanofibers for lithium rechargeable batteries. *ACS Appl. Mater. Interfaces*. **5**, 691–696 (2013). <https://doi.org/10.1021/am302197y>
226. Tian, H., Xin, F., Tan, X., et al.: High lithium electroactivity of boron-doped hierarchical rutile submicrosphere TiO_2 . *J. Mater. Chem. A*. **2**, 10599–10606 (2014). <https://doi.org/10.1039/C4TA01438C>
227. Cao, M., Tao, L., Lv, X., et al.: Phosphorus-doped TiO_2 -B nanowire arrays boosting robust pseudocapacitive properties for lithium storage. *J. Power Sources*. **396**, 327–334 (2018). <https://doi.org/10.1016/j.jpowsour.2018.06.012>
228. Finazzi, E., Di Valentin, C., Pacchioni, G., et al.: Excess electron states in reduced bulk anatase TiO_2 : comparison of standard GGA, GGA + U , and hybrid DFT calculations. *J. Chem. Phys.* **129**, 154113 (2008). <https://doi.org/10.1063/1.2996362>
229. Kong, L.M., Zhu, B.L., Pang, X.Y., et al.: First-principles study on TiO_2 -B with oxygen vacancies as a negative material of rechargeable lithium-ion batteries. *Acta Phys. Chim. Sin.* **32**, 656–664 (2016). <https://doi.org/10.3866/pku.whxb201512292>
230. Zhang, Y., Ding, Z.Y., Foster, C.W., et al.: Oxygen vacancies evoked blue $\text{TiO}_2(\text{B})$ nanobelts with efficiency enhancement in sodium storage behaviors. *Adv. Funct. Mater.* (2017). <https://doi.org/10.1002/adfm.201700856>
231. Dalton, A.S., Belak, A.A., Van der Ven, A.: Thermodynamics of lithium in $\text{TiO}_2(\text{B})$ from first principles. *Chem. Mater.* **24**, 1568–1574 (2012). <https://doi.org/10.1021/cm203283v>
232. Arrouvel, C., Parker, S.C., Islam, M.S.: Lithium insertion and transport in the TiO_2 -B anode material: a computational study. *Chem. Mater.* **21**, 4778–4783 (2009). <https://doi.org/10.1021/cm900373u>
233. Zhang, Y.F., Lin, W., Li, Y., et al.: A theoretical study on the electronic structures of TiO_2 : effect of hartree–fock exchange. *J. Phys. Chem. B* **109**, 19270–19277 (2005). <https://doi.org/10.1021/jp0523625>
234. Yuan, T., Cai, R., Shao, Z.P.: Different effect of the atmospheres on the phase formation and performance of $\text{Li}_4\text{Ti}_5\text{O}_{12}$ prepared from ball-milling-assisted solid-phase reaction with pristine and carbon-precoated TiO_2 as starting materials. *J. Phys. Chem. C* **115**, 4943–4952 (2011). <https://doi.org/10.1021/jp111353e>
235. Samin, A., Kurth, M., Cao, L.: Ab initio study of radiation effects on the $\text{Li}_4\text{Ti}_5\text{O}_{12}$ electrode used in lithium-ion batteries. *AIP Adv.* (2015). <https://doi.org/10.1063/1.4917308>
236. Morgan, B.J., Watson, G.W.: GGA + U description of lithium intercalation into anatase TiO_2 . *Phys. Rev. B* **82**, 144119 (2010). <https://doi.org/10.1103/PhysRevB.82.144119>
237. Spreafico, C., VandeVondele, J.: Excess electrons and interstitial Li atoms in TiO_2 anatase: properties of the (101) interface. *J. Phys. Chem. C* **119**, 15009–15018 (2015). <https://doi.org/10.1021/acs.jpcc.5b04103>
238. Södergren, S., Siegbahn, H., Rensmo, H., et al.: Lithium intercalation in nanoporous anatase TiO_2 studied with XPS. *J. Phys. Chem. B* **101**, 3087–3090 (1997). <https://doi.org/10.1021/jp9639399>
239. Augustsson, A., Henningsson, A., Butorin, S.M., et al.: Lithium ion insertion in nanoporous anatase TiO_2 studied with RIXS. *J. Chem. Phys.* **119**, 3983–3987 (2003). <https://doi.org/10.1063/1.1591735>
240. Henningsson, A., Rensmo, H., Sandell, A., et al.: Electronic structure of electrochemically Li-inserted TiO_2 studied with synchrotron radiation electron spectroscopies. *J. Chem. Phys.* **118**, 5607–5612 (2003). <https://doi.org/10.1063/1.1545086>
241. Richter, J.H., Henningsson, A., Karlsson, P.G., et al.: Electronic structure of lithium-doped anatase TiO_2 prepared in ultrahigh vacuum. *Phys. Rev. B* **71**, 235418 (2005). <https://doi.org/10.1103/PhysRevB.71.235418>
242. Brant, A.T., Giles, N.C., Halliburton, L.E.: Insertion of lithium ions into TiO_2 (rutile) crystals: an electron paramagnetic resonance study of the Li-associated Ti^{3+} small polaron. *J. Appl. Phys.* **113**, 053712 (2013). <https://doi.org/10.1063/1.4790366>
243. Koudriachova, M.V., Harrison, N.M., de Leeuw, S.W., et al.: Density-functional simulations of lithium intercalation in rutile. *Phys. Rev. B* **65**, 235423 (2002). <https://doi.org/10.1103/physrevb.65.235423>
244. Legrain, F., Malyi, O., Manzhos, S.: Insertion energetics of lithium, sodium, and magnesium in crystalline and amorphous titanium dioxide: a comparative first-principles study. *J. Power Sources* **278**, 197–202 (2015). <https://doi.org/10.1016/j.jpowsour.2014.12.058>
245. Liu, D.T., Ouyang, C.Y., Shu, J., et al.: Theoretical study of cation doping effect on the electronic conductivity of $\text{Li}_4\text{Ti}_5\text{O}_{12}$. *Phys. Status Solidi B Basic Solid State Phys.* **243**, 1835–1841 (2006). <https://doi.org/10.1002/pssb.200541404>
246. Zhong, Z., Ouyang, C., Shi, S., et al.: Ab initio studies on $\text{Li}_{4+x}\text{Ti}_5\text{O}_{12}$ compounds as anode materials for lithium-ion batteries. *ChemPhysChem* **9**, 2104–2108 (2008). <https://doi.org/10.1002/cphc.200800333>
247. Das, S.K., Gnanavel, M., Patel, M.U.M., et al.: Anomolously high lithium storage in mesoporous nanoparticulate aggregation of Fe^{3+} doped anatase titania. *J. Electrochem. Soc.* **158**, A1290–A1297 (2011). <https://doi.org/10.1149/2.029112jes>
248. Grosjean, R., Fehse, M., Pigeot-Remy, S., et al.: Facile synthetic route towards nanostructured $\text{Fe-TiO}_2(\text{B})$, used as negative electrode for Li-ion batteries. *J. Power Sources* **278**, 1–8 (2015). <https://doi.org/10.1016/j.jpowsour.2014.12.032>
249. Zhang, W., Gong, Y., Mellott, N.P., et al.: Synthesis of nickel doped anatase titanate as high performance anode materials for lithium ion batteries. *J. Power Sources* **276**, 39–45 (2015). <https://doi.org/10.1016/j.jpowsour.2014.11.098>
250. Luebke, M., Shin, J., Marchand, P., et al.: Highly pseudocapacitive Nb-doped TiO_2 high power anodes for lithium-ion batteries. *J. Mater. Chem. A* **3**, 22908–22914 (2015). <https://doi.org/10.1039/c5ta07554h>
251. Thi, T.V., Rai, A.K., Gim, J., et al.: Effect of Mo^{6+} doping on electrochemical performance of anatase TiO_2 as a high performance anode material for secondary lithium-ion batteries. *J. Alloys Compd.* **598**, 16–22 (2014). <https://doi.org/10.1016/j.jallcom.2014.02.019>
252. Wang, Y., Xu, M., Peng, Z., et al.: Direct growth of mesoporous Sn-doped TiO_2 thin films on conducting substrates for lithium-ion battery anodes. *J. Mater. Chem. A* **1**, 13222–13226 (2013). <https://doi.org/10.1039/c3ta13198j>
253. Wang, H., Xi, L., Tucek, J., et al.: Synthesis and characterization of tin titanate nanotubes: precursors for nanoparticulate Sn-doped TiO_2 anodes with synergistically improved electrochemical performance. *Chemelectrochem* **1**, 1563–1569 (2014). <https://doi.org/10.1002/celc.201402188>
254. Jung, H.G., Yoon, C.S., Prakash, J., et al.: Mesoporous anatase TiO_2 with high surface area and controllable pore size by F-Ion doping: applications for high-power Li-Ion battery anode. *J. Phys. Chem. C* **113**, 21258–21263 (2009). <https://doi.org/10.1021/jp908719k>
255. Goriparti, S., Miele, E., Prato, M., et al.: Direct synthesis of carbon-doped TiO_2 -bronze nanowires as anode materials for high performance lithium-ion batteries. *ACS Appl. Mater. Interfaces*. **7**, 25139–25146 (2015). <https://doi.org/10.1021/acsami.5b06426>
256. Xiao, Y., Hu, C., Cao, M.: Compositing amorphous TiO_2 with N-doped carbon as high-rate anode materials for lithium-ion batteries. *Chem. Asian J.* **9**, 351–356 (2014). <https://doi.org/10.1002/asia.201301183>

257. Yang, Y., Ji, X., Jing, M., et al.: Carbon dots supported upon N-doped TiO₂ nanorods applied into sodium and lithium ion batteries. *J. Mater. Chem. A* **3**, 5648–5655 (2015). <https://doi.org/10.1039/c4ta05611f>
258. Zhang, Y., Fu, Q., Xu, Q., et al.: Improved electrochemical performance of nitrogen doped TiO₂-B nanowires as anode materials for Li-ion batteries. *Nanoscale* **7**, 12215–12224 (2015). <https://doi.org/10.1039/c5nr02457a>
259. Chen, C., Zhang, B., Miao, L., et al.: Binding TiO₂-B nanosheets with N-doped carbon enables highly durable anodes for lithium-ion batteries. *J. Mater. Chem. A* **4**, 8172–8179 (2016). <https://doi.org/10.1039/c6ta01955b>
260. Lai, C., Yuan, X.C., Cao, X.L., et al.: Enhanced high-rate capability of the C-N-doped TiO₂ as anode material for lithium-ion battery. *Electrochim. Solid State Lett.* **15**, A65–A67 (2012). <https://doi.org/10.1149/2.023205esl>
261. Gao, Y., Wang, C., Hu, P., et al.: Carbon-incorporated, nitrogen-doped branch-like TiO₂ nanostructure towards superior lithium storage performance. *J. Alloys Compd.* **787**, 944–951 (2019). <https://doi.org/10.1016/j.jallcom.2019.02.169>
262. Bi, Z., Paranthaman, M.P., Guo, B., et al.: High performance Cr, N-codoped mesoporous TiO₂ microspheres for lithium-ion batteries. *J. Mater. Chem. A* **2**, 1818–1824 (2014). <https://doi.org/10.1039/c3ta14535b>
263. Kumar, V.S.P., Deshpande, P.A.: DFT reveals concentration-dependent cathodic/anodic behaviour of lithiated titania. *Mater. Res. Express* (2018). <https://doi.org/10.1088/2053-1591/aad5bc>
264. Liu, X.D., Jiang, E.Y., Li, Z.Q., et al.: Electronic structure and optical properties of Nb-doped anatase TiO₂. *Appl. Phys. Lett.* (2008). <https://doi.org/10.1063/1.2949070>
265. Peng, H.W., Li, J.B., Li, S.S., et al.: First-principles study of the electronic structures and magnetic properties of 3d transition metal-doped anatase TiO₂. *J. Phys. Condens. Matter* (2008). <https://doi.org/10.1088/0953-8984/20/12/125207>
266. Shirley, R., Kraft, M., Inderwildi, O.R.: Electronic and optical properties of aluminium-doped anatase and rutile TiO₂ from ab initio calculations. *Phys. Rev. B* (2010). <https://doi.org/10.1103/physrevb.81.075111>
267. Yu, Q.H., Jin, L., Zhou, C.G.: Ab initio study of electronic structures and absorption properties of pure and Fe³⁺ doped anatase TiO₂. *Sol. Energy Mater. Sol. Cells* **95**, 2322–2326 (2011). <https://doi.org/10.1016/j.solmat.2011.03.048>
268. Zhang, R.S., Liu, Y., Gao, Q., et al.: First-principles study on the electronic and optical properties of F- and Nb-doped anatase TiO₂. *J. Alloys Compd.* **509**, 9178–9182 (2011). <https://doi.org/10.1016/j.jallcom.2011.06.105>
269. Li, C., Zhao, Y.F., Gong, Y.Y., et al.: Band gap engineering of early transition-metal-doped anatase TiO₂: first principles calculations. *Phys. Chem. Chem. Phys.* **16**, 21446–21451 (2014). <https://doi.org/10.1039/c4cp03587a>
270. Han, Y.X., Yang, C.L., Wang, M.S., et al.: Enhancing the visible-light absorption of TiO₂ with the use of key N Co, and Na dopant concentrations. *Sol. Energy Mater. Sol. Cells* **132**, 94–100 (2015). <https://doi.org/10.1016/j.solmat.2014.08.027>
271. Pan, J.W., Li, C., Zhao, Y.F., et al.: Electronic properties of TiO₂ doped with Sc, Y, La, Zr, Hf, V, Nb and Ta. *Chem. Phys. Lett.* **628**, 43–48 (2015). <https://doi.org/10.1016/j.cplett.2015.03.056>
272. Yang, X.Y., Min, Y.X., Li, S.B., et al.: Conductive Nb-doped TiO₂ thin films with whole visible absorption to degrade pollutants. *Catal. Sci. Technol.* **8**, 1357–1365 (2018). <https://doi.org/10.1039/c7cy02614e>
273. Yu, Z.J., Zhang, X.F., Yang, G.L., et al.: High rate capability and long-term cyclability of Li₄Ti_{4.9}V_{0.1}O₁₂ as anode material in lithium ion battery. *Electrochim. Acta* **56**, 8611–8617 (2011). <https://doi.org/10.1016/j.electacta.2011.07.051>
274. Hao, Y.J., Lai, Q.Y., Lu, J.Z., et al.: Effects of dopant on the electrochemical properties of Li₄Ti₅O₁₂ anode materials. *Ionics* **13**, 369–373 (2007). <https://doi.org/10.1007/s11581-007-0111-1>
275. Li, X., Qu, M.Z., Yu, Z.L.: Structural and electrochemical performances of Li₄Ti_{5-x}Zr_xO₁₂ as anode material for lithium-ion batteries. *J. Alloys Compd.* **487**, L12–L17 (2009). <https://doi.org/10.1016/j.jallcom.2009.07.176>
276. Kim, J.G., Park, M.S., Hwang, S.M., et al.: Zr⁴⁺ doping in Li₄Ti₅O₁₂ anode for lithium-ion batteries: open Li⁺ diffusion paths through structural imperfection. *Chemsuschem* **7**, 1451–1457 (2014). <https://doi.org/10.1002/cssc.201301393>
277. Tian, B.B., Xiang, H.F., Zhang, L., et al.: Niobium doped lithium titanate as a high rate anode material for Li-ion batteries. *Electrochim. Acta* **55**, 5453–5458 (2010). <https://doi.org/10.1016/j.electacta.2010.04.068>
278. Zhong, Z.: Synthesis of Mo⁴⁺ substituted spinel Li₄Ti_{5-x}Mo_xO₁₂. *Electrochim. Solid-State Lett.* **10**, A267–A269 (2007). <https://doi.org/10.1149/1.2784142>
279. Jhan, Y.R., Lin, C.Y., Duh, J.G.: Preparation and characterization of ruthenium doped Li₄Ti₅O₁₂ anode material for the enhancement of rate capability and cyclic stability. *Mater. Lett.* **65**, 2502–2505 (2011). <https://doi.org/10.1016/j.matlet.2011.04.060>
280. Zhang, Q.Y., Verde, M.G., Seo, J.K., et al.: Structural and electrochemical properties of Gd-doped Li₄Ti₅O₁₂ as anode material with improved rate capability for lithium-ion batteries. *J. Power Sources* **280**, 355–362 (2015). <https://doi.org/10.1016/j.jpowsour.2015.01.124>
281. Song, K., Seo, D.-H., Jo, M.R., et al.: Tailored oxygen framework of Li₄Ti₅O₁₂ nanorods for high-power Li ion battery. *J. Phys. Chem. Lett.* **5**, 1368–1373 (2014). <https://doi.org/10.1021/jz5002924>
282. Yi, T.F., Yang, S.Y., Li, X.Y., et al.: Sub-micrometric Li_{4-x}Na_xTi₅O₁₂ (0 ≤ x ≤ 0.2) spinel as anode material exhibiting high rate capability. *J. Power Sources* **246**, 505–511 (2014). <https://doi.org/10.1016/j.jpowsour.2013.08.005>
283. Chen, C.H., Vaughey, J.T., Jansen, A.N., et al.: Studies of Mg-substituted Li_{4-x}Mg_xTi₅O₁₂ spinel Electrodes (0 ≤ x ≤ 1) for Lithium Batteries. *J. Electrochem. Soc.* **148**, A102–A104 (2001). <https://doi.org/10.1149/1.1344523>
284. Zhang, Q.Y., Zhang, C.L., Li, B., et al.: Preparation and electrochemical properties of Ca-doped Li₄Ti₅O₁₂ as anode materials in lithium-ion battery. *Electrochim. Acta* **98**, 146–152 (2013). <https://doi.org/10.1016/j.electacta.2013.03.006>
285. Wu, H.B., Chang, S., Liu, X.L., et al.: Sr-doped Li₄Ti₅O₁₂ as the anode material for lithium-ion batteries. *Solid State Ionics* **232**, 13–18 (2013). <https://doi.org/10.1016/j.ssi.2012.10.027>
286. Du, G.D., Sharma, N., Peterson, V.K., et al.: Br-doped Li₄Ti₅O₁₂ and composite TiO₂ anodes for Li-ion batteries: synchrotron X-ray and in situ neutron diffraction studies. *Adv. Funct. Mater.* **21**, 3990–3997 (2011). <https://doi.org/10.1002/adfm.201100846>
287. Long, W.M., Wang, X.Y., Yang, S.Y., et al.: Electrochemical properties of Li₄Ti_{5-2x}Ni_xMn_xO₁₂ compounds synthesized by sol-gel process. *Mater. Chem. Phys.* **131**, 431–435 (2011). <https://doi.org/10.1016/j.matchemphys.2011.09.071>
288. Zhang, Q., Lu, H., Zhong, H., et al.: W⁶⁺ & Br⁻ codoped Li₄Ti₅O₁₂ anode with super rate performance for Li-ion batteries. *J. Mater. Chem. A* **3**, 13706–13716 (2015). <https://doi.org/10.1039/C5TA02784E>
289. Huang, S.H., Wen, Z.Y., Gu, Z.H., et al.: Preparation and cycling performance of Al³⁺ and F⁻ co-substituted compounds Li₄Al_xTi_{5-x}F_yO_{12-y}. *Electrochim. Acta* **50**, 4057–4062 (2005). <https://doi.org/10.1016/j.electacta.2004.12.036>
290. Liu, Z.X., Sun, L.M., Yang, W.Y., et al.: The synergic effects of Na and K co-doping on the crystal structure and electrochemical properties of Li₄Ti₅O₁₂ as anode material for lithium ion battery.

- Solid State Sci. **44**, 39–44 (2015). <https://doi.org/10.1016/j.solidstatesciences.2015.04.002>
291. Duan, H., Li, J., Du, H.D., et al.: Tailoring native defects and zinc impurities in $\text{Li}_4\text{Ti}_5\text{O}_{12}$: insights from first-principles study. *J. Phys. Chem. C* **119**, 5238–5245 (2015). <https://doi.org/10.1021/acs.jpcc.5b00829>
 292. Yang, Z., Wang, J., Zhang, Q., et al.: Doping the $\text{Li}_4\text{Ti}_5\text{O}_{12}$ lattice with extra-large anions. *Mater. Express* **5**, 457–462 (2015). <https://doi.org/10.1166/mex.2015.1259>
 293. Cho, H., Son, H., Kim, D., et al.: Impact of Mg-doping site control in the performance of $\text{Li}_4\text{Ti}_5\text{O}_{12}$ Li-ion battery anode: first-principles predictions and experimental verifications. *J. Phys. Chem. C* **121**, 14994–15001 (2017). <https://doi.org/10.1021/acs.jpcc.7b01475>
 294. Koudriachova, M.V., Harrison, N.M., de Leeuw, S.W.: Effect of diffusion on lithium intercalation in titanium dioxide. *Phys. Rev. Lett.* **86**, 1275–1278 (2001). <https://doi.org/10.1103/PhysRevLett.86.1275>
 295. Brohan, L., Marchand, R.: Properties physiques des bronzes MxTiO_2 (B). *Solid State Ionics* **9–10**, 419–424 (1983). [https://doi.org/10.1016/0167-2738\(83\)90269-2](https://doi.org/10.1016/0167-2738(83)90269-2)
 296. Armstrong, A.R., Arrouvel, C., Gentili, V., et al.: Lithium coordination sites in Li_xTiO_2 (B): a structural and computational study. *Chem. Mater.* **22**, 6426–6432 (2010). <https://doi.org/10.1021/cm102589x>
 297. Wagemaker, M., Kearley, G.J., van Well, A.A., et al.: Multiple Li positions inside oxygen octahedra in lithiated TiO_2 anatase. *J. Am. Chem. Soc.* **125**, 840–848 (2003). <https://doi.org/10.1021/ja028165q>
 298. Arrouvel, C., Peixoto, T.C., Valerio, M.E.G., et al.: Lithium migration at low concentration in TiO_2 polymorphs. *Comput. Theor. Chem.* **1072**, 43–51 (2015). <https://doi.org/10.1016/j.comptc.2015.09.002>
 299. Panduwinata, D., Gale, J.D.: A first principles investigation of lithium intercalation in TiO_2 -B. *J. Mater. Chem.* **19**, 3931–3940 (2009). <https://doi.org/10.1039/B902683E>
 300. Zeng, T., Ji, P., Hu, X., et al.: Nano-Sn doped carbon-coated rutile TiO_2 spheres as a high capacity anode for Li-ion battery. *RSC Adv.* **6**, 48530–48536 (2016). <https://doi.org/10.1039/C6RA04672J>
 301. Liang, K., Chen, X., Guo, Z., et al.: Lithium intercalation and diffusion in TiO_2 nanotubes: a first-principles investigation. *Phys. Chem. Chem. Phys.* **18**, 24370–24376 (2016). <https://doi.org/10.1039/c6cp03830a>
 302. Olson, C.L., Nelson, J., Islam, M.S.: Defect chemistry, surface structures, and lithium insertion in anatase TiO_2 . *J. Phys. Chem. B* **110**, 9995–10001 (2006). <https://doi.org/10.1021/jp057261l>
 303. Ziebarth, B., Klinsmann, M., Eckl, T., et al.: Lithium diffusion in the spinel phase $\text{Li}_4\text{Ti}_5\text{O}_{12}$ and in the rocksalt phase $\text{Li}_7\text{Ti}_5\text{O}_{12}$ of lithium titanate from first principles. *Phys. Rev. B* **89**, 174301–174307 (2014). <https://doi.org/10.1103/PhysRevB.89.174301>
 304. Chen, Y.C., Ouyang, C.Y., Song, L.J., et al.: Lithium ion diffusion in $\text{Li}_{4+x}\text{Ti}_5\text{O}_{12}$: from ab initio studies. *Electrochim. Acta* **56**, 6084–6088 (2011). <https://doi.org/10.1016/j.electacta.2011.04.077>
 305. Yildirim, H., Greeley, J.P., Sankaranarayanan, S.K.: The effect of concentration on Li diffusivity and conductivity in rutile TiO_2 . *Phys. Chem. Chem. Phys.* **14**, 4565–4576 (2012). <https://doi.org/10.1039/c2cp22731b>
 306. Henkelman, G., Arnaldsson, A., Jonsson, H.: A fast and robust algorithm for Bader decomposition of charge density. *Comput. Mater. Sci.* **36**, 354–360 (2006). <https://doi.org/10.1016/j.commattsci.2005.04.010>
 307. Sanville, E., Kenny, S.D., Smith, R., et al.: Improved grid-based algorithm for Bader charge allocation. *J. Comput. Chem.* **28**, 899–908 (2007). <https://doi.org/10.1002/jcc.20575>
 308. Tang, W., Sanville, E., Henkelman, G.: A grid-based Bader analysis algorithm without lattice bias. *J. Phys.: Condens. Matter* **21**, 084204 (2009). <https://doi.org/10.1088/0953-8984/21/8/084204>
 309. Pazhamalai, P., Krishnamoorthy, K., Mariappan, V.K., et al.: Blue TiO_2 nanosheets as a high-performance electrode material for supercapacitors. *J. Colloid Interface Sci.* **536**, 62–70 (2019). <https://doi.org/10.1016/j.jcis.2018.10.031>
 310. Armstrong, A.R., Armstrong, G., Canales, J., et al.: TiO_2 (2)-B nanowires. *Angew. Chem. Int. Ed. Engl.* **43**, 2286–2288 (2004). <https://doi.org/10.1002/anie.200353571>
 311. Pérez-Flores, J.C., Baetz, C., Kuhn, A., et al.: Hollandite-type TiO_2 : a new negative electrode material for sodium-ion batteries. *J. Mater. Chem. A* **2**, 1825–1833 (2014). <https://doi.org/10.1039/c3ta13394j>
 312. Zhang, M., MacRae, A.C., Liu, H., et al.: Communication–investigation of anatase- TiO_2 as an efficient electrode material for magnesium-ion batteries. *J. Electrochem. Soc.* **163**, A2368–A2370 (2016). <https://doi.org/10.1149/2.1091610jes>
 313. Saha, P., Datta, M.K., Velikokhatnyi, O.I., et al.: Rechargeable magnesium battery: current status and key challenges for the future. *Prog. Mater. Sci.* **66**, 1–86 (2014). <https://doi.org/10.1016/j.pmatsci.2014.04.001>
 314. Gan, Q., He, H., Zhao, K., et al.: Plasma-induced oxygen vacancies in urchin-like anatase titania coated by carbon for excellent sodium-ion battery anodes. *ACS Appl. Mater. Interfaces* **10**, 7031–7042 (2018). <https://doi.org/10.1021/acsami.7b13760>
 315. Chen, X., Liu, L., Huang, F.: Black titanium dioxide (TiO_2) nanomaterials. *Chem. Soc. Rev.* **44**, 1861–1885 (2015). <https://doi.org/10.1039/c4cs00330f>
 316. Fan, L.Z., Chi, S.S., Wang, L.N., et al.: Synthesis of TiO_x nanotubular arrays with oxygen defects as high-performance anodes for lithium-ion batteries. *ChemElectroChem* **2**, 421–426 (2015). <https://doi.org/10.1002/celec.201402331>
 317. Zhang, J., Wang, Y., Wu, J., et al.: Remarkable supercapacitive performance of TiO_2 nanotube arrays by introduction of oxygen vacancies. *Chem. Eng. J.* **313**, 1071–1081 (2017). <https://doi.org/10.1016/j.cej.2016.11.004>
 318. Shen, L., Uchaker, E., Zhang, X., et al.: Hydrogenated $\text{Li}_4\text{Ti}_5\text{O}_{12}$ nanowire arrays for high rate lithium ion batteries. *Adv. Mater.* **24**, 6502–6506 (2012). <https://doi.org/10.1002/adma.201203151>
 319. Deng, X., Wei, Z., Cui, C., et al.: Oxygen-deficient anatase TiO_2 @C nanospindles with pseudocapacitive contribution for enhancing lithium storage. *J. Mater. Chem. A* **6**, 4013–4022 (2018). <https://doi.org/10.1039/c7ta11301c>
 320. Li, W., Corradini, D., Body, M., et al.: High substitution rate in TiO_2 anatase nanoparticles with cationic vacancies for fast lithium storage. *Chem. Mater.* **27**, 5014–5019 (2015). <https://doi.org/10.1021/acs.chemmater.5b01407>
 321. Ma, Y., Ding, B., Ji, G., et al.: Carbon-encapsulated F-doped $\text{Li}_4\text{Ti}_5\text{O}_{12}$ as a high rate anode material for Li^+ batteries. *ACS Nano* **7**, 10870–10878 (2013). <https://doi.org/10.1021/nn404311x>
 322. Anh, L.T., Rai, A.K., Thi, T.V., et al.: Improving the electrochemical performance of anatase titanium dioxide by vanadium doping as an anode material for lithium-ion batteries. *J. Power Sources* **243**, 891–898 (2013). <https://doi.org/10.1016/j.jpowsour.2013.06.080>
 323. Fehse, M., Cavaliere, S., Lippens, P.E., et al.: Nb-doped TiO_2 nanofibers for lithium ion batteries. *J. Phys. Chem. C* **117**, 13827–13835 (2013). <https://doi.org/10.1021/jp402498p>
 324. Bai, Y.J., Gong, C., Lun, N., et al.: Yttrium-modified $\text{Li}_4\text{Ti}_5\text{O}_{12}$ as an effective anode material for lithium ion batteries with

- outstanding long-term cyclability and rate capabilities. *J. Mater. Chem. A* **1**, 89–96 (2013). <https://doi.org/10.1039/C2TA00048B>
325. Chen, J., Ding, Z., Wang, C., et al.: Black anatase titania with ultrafast sodium-storage performances stimulated by oxygen vacancies. *ACS Appl. Mater. Interfaces* **8**, 9142–9151 (2016). <https://doi.org/10.1021/acsami.6b01183>
 326. Zhao, C., Cai, Y., Yin, K., et al.: Carbon-bonded, oxygen-deficient TiO₂ nanotubes with hybridized phases for superior Na-ion storage. *Chem. Eng. J.* **350**, 201–208 (2018). <https://doi.org/10.1016/j.cej.2018.05.194>
 327. Xiong, P., Zhang, X., Zhang, F., et al.: Two-dimensional unilamellar cation-deficient metal oxide nanosheet superlattices for high-rate sodium ion energy storage. *ACS Nano* **12**, 12337–12346 (2018). <https://doi.org/10.1021/acsnano.8b06206>
 328. Zhang, H., Jiang, Y., Qi, Z., et al.: Sulfur doped ultra-thin anatase TiO₂ nanosheets/graphene nanocomposite for high-performance pseudocapacitive sodium storage. *Energy Storage Mater.* **12**, 37–43 (2018). <https://doi.org/10.1016/j.ensm.2017.11.008>
 329. He, H., Sun, D., Zhang, Q., et al.: Iron-doped cauliflower-like rutile TiO₂ with superior sodium storage properties. *ACS Appl. Mater. Interfaces* **9**, 6093–6103 (2017). <https://doi.org/10.1021/acsami.6b15516>
 330. He, H., Huang, D., Pang, W., et al.: Plasma-induced amorphous shell and deep cation-site S doping endow TiO₂ with extraordinary sodium storage performance. *Adv. Mater.* **30**, e1801013 (2018). <https://doi.org/10.1002/adma.201801013>
 331. Wu, Y., Liu, X., Yang, Z., et al.: Nitrogen-doped ordered mesoporous anatase TiO₂ nanofibers as anode materials for high performance sodium-ion batteries. *Small* **12**, 3522–3529 (2016). <https://doi.org/10.1002/sml.201600606>
 332. Usui, H., Yoshioka, S., Wasada, K., et al.: Nb-doped rutile TiO₂: a potential anode material for Na-ion battery. *ACS Appl. Mater. Interfaces* **7**, 6567–6573 (2015). <https://doi.org/10.1021/am508670z>
 333. He, H., Zhang, Q., Wang, H., et al.: Defect-rich TiO_{2-δ} nanocrystals confined in a mooncake-shaped porous carbon matrix as an advanced Na ion battery anode. *J. Power Sources* **354**, 179–188 (2017). <https://doi.org/10.1016/j.jpowsour.2017.04.035>
 334. Wu, Y., Jiang, Y., Shi, J., et al.: Multichannel porous TiO₂ hollow nanofibers with rich oxygen vacancies and high grain boundary density enabling superior sodium storage performance. *Small* (2017). <https://doi.org/10.1002/sml.201700129>
 335. Xu, Y., Zhou, M., Wang, X., et al.: Enhancement of sodium ion battery performance enabled by oxygen vacancies. *Angew. Chem. Int. Ed. Engl.* **54**, 8768–8771 (2015). <https://doi.org/10.1002/anie.201503477>
 336. Er, D., Detsi, E., Kumar, H., et al.: Defective graphene and graphene allotropes as high-capacity anode materials for Mg ion batteries. *ACS Energy Lett.* **1**, 638–645 (2016). <https://doi.org/10.1021/acsenenergylett.6b00308>
 337. Bo, S.-H., Grey, C.P., Khalifah, P.G.: Defect-tolerant diffusion channels for Mg²⁺ ions in ribbon-type borates: structural insights into potential battery cathodes MgVBO₄ and Mg_xFe_{2-x}B₂O₅. *Chem. Mater.* **27**, 4630–4639 (2015). <https://doi.org/10.1021/acs.chemmater.5b01040>
 338. Shan, P., Gu, Y., Yang, L., et al.: Olivine FePO₄ cathode material for rechargeable Mg-ion batteries. *Inorg. Chem.* **56**, 13411–13416 (2017). <https://doi.org/10.1021/acs.inorgchem.7b02150>
 339. Wang, Y., Xue, X., Liu, P., et al.: Atomic substitution enabled synthesis of vacancy-rich two-dimensional black TiO_{2-x} nanoflakes for high-performance rechargeable magnesium batteries. *ACS Nano* **12**, 12492–12502 (2018). <https://doi.org/10.1021/acsnano.8b06917>
 340. Koketsu, T., Ma, J., Morgan, B.J., et al.: Reversible magnesium and aluminium ions insertion in cation-deficient anatase TiO₂. *Nat. Mater.* **16**, 1142–1148 (2017). <https://doi.org/10.1038/nmat4976>
 341. He, Y.J., Peng, J.F., Chu, W., et al.: Black mesoporous anatase TiO₂ nanoleaves: a high capacity and high rate anode for aqueous Al-ion batteries. *J. Mater. Chem. A* **2**, 1721–1731 (2014). <https://doi.org/10.1039/c3ta13906a>
 342. Li, H., Chen, Z., Tsang, C.K., et al.: Electrochemical doping of anatase TiO₂ in organic electrolytes for high-performance supercapacitors and photocatalysts. *J. Mater. Chem. A* **2**, 229–236 (2014). <https://doi.org/10.1039/C3TA13963H>
 343. Lu, X., Wang, G., Zhai, T., et al.: Hydrogenated TiO₂ nanotube arrays for supercapacitors. *Nano Lett.* **12**, 1690–1696 (2012). <https://doi.org/10.1021/nl300173j>
 344. Zhou, H., Zhang, Y.: Electrochemically self-doped TiO₂ nanotube arrays for supercapacitors. *J. Phys. Chem. C* **118**, 5626–5636 (2014). <https://doi.org/10.1021/jp4082883>
 345. Kim, C., Kim, S., Hong, S.P., et al.: Effect of doping level of colored TiO₂ nanotube arrays fabricated by electrochemical self-doping on electrochemical properties. *Phys. Chem. Chem. Phys.* **18**, 14370–14375 (2016). <https://doi.org/10.1039/c6cp01799a>
 346. Salari, M., Konstantinov, K., Liu, H.K.: Enhancement of the capacitance in TiO₂ nanotubes through controlled introduction of oxygen vacancies. *J. Mater. Chem.* **21**, 5128 (2011). <https://doi.org/10.1039/c0jm04085a>
 347. Lu, X., Zeng, Y., Yu, M., et al.: Oxygen-deficient hematite nanorods as high-performance and novel negative electrodes for flexible asymmetric supercapacitors. *Adv. Mater.* **26**, 3148–3155 (2014). <https://doi.org/10.1002/adma.201305851>
 348. Zhou, H., Zhang, Y.: Enhancing the capacitance of TiO₂ nanotube arrays by a facile cathodic reduction process. *J. Power Sources* **239**, 128–131 (2013). <https://doi.org/10.1016/j.jpowsour.2013.03.114>



Zhong Su is a Ph.D. candidate in the Centre for Clean Environment and Energy, the School of Environment and Science at Griffith University, Australia. Zhong was awarded his master degree and bachelor degree from Jiangsu Normal University, China in 2017 and 2014, respectively. In 2016, Zhong conducted one-year research on lithium-ion batteries as a visiting scholar at Griffith University. His research interests focus on high-energy-density Li-S batteries, high-power-density Li-I₂ batteries

and design of defective oxide electrode materials.



Jiahua Liu received his Bachelor's degree in 2017 from the School of Materials Science and Engineering, Nanchang University, China. He is now a graduate student in the School of Advanced Materials (SAM), Shenzhen Graduate School, Peking University, China, under supervision of Prof. Jiaxin Zheng and Prof. Feng Pan. His research focuses on computational materials and energy materials (battery materials, photoelectric materials).



Mouyi Weng is currently a Ph.D. candidate in Prof. Feng Pan's group at Shenzhen Graduate School, Peking University, China. He received his B.S. degree from Tsinghua University in 2015. His research interests include computational materials, materials simulation algorithms and electronic structure calculation in materials.



Meng Li obtained his Bachelor's degree from Beihang University in 2011 and his Master's degree in Engineering from China University of Mining and Technology in 2015. Since 2018, he has been studied theoretical and computational aspects of energy storage materials and devices as a Ph.D. candidate at Griffith University, Australia. His research interest lies in the study of electrode materials for Li and Na rechargeable batteries using computational tools.



Prof. Jiaxin Zheng received his B.Sc. degree in Physics in 2008 and Ph.D. degree in Condensed Matter Physics in 2013 from Peking University, China. Then, he joined the group of Prof. Feng Pan at the School of Advanced Materials (SAM), Shenzhen Graduate School, Peking University, China, as a postdoctoral fellow from October 2013 to October 2015. His research interests include computational materials, energy materials (battery materials, solar energy, thermoelectric materials), nanomaterials and nanoelectronics. Dr. Zheng has authored and co-authored more than 80 peer-reviewed research articles.



Yuxuan Zhu received her master degree in Chemistry from Jiangsu Normal University in 2017. She is currently a Ph.D. candidate at the School of Environment and Science, Griffith University, Australia. Her research focuses on ultrahigh-resolution 3D printing technology for rechargeable batteries.



Dr. Yulin Zhong completed his Ph.D. in Chemistry (2010) at the National University of Singapore (NUS) and did his postdoctoral trainings at Princeton University, Massachusetts Institute of Technology and Monash University. He was awarded an ARC DECRA Fellowship in 2014 and joined Griffith University as a Senior Lecturer since 2016. His research interests include electrochemical production of 2D nanomaterials, 3D printing, smart windows and wearable devices.



Shangshu Qian received his Bachelor and Master degrees in Chemistry from Ningbo University in 2015 and 2018, respectively. The work includes the development of new anode materials for lithium-ion batteries and the exploration of the mechanism of lithiation/delithiation. He obtained a Ph.D. scholarship from Griffith University in 2019. His main research interests are developing novel polymer-based electrolytes and their composites with ceramic-based electrolytes for solid-state batteries.



Prof. Feng Pan National 1000-plan Professor, Founding Dean of School of Advanced Materials, Peking University Shenzhen Graduate School, Director of National Center of Electric Vehicle Power Battery and Materials for International Research, got B.S. from Dept. Chemistry, Peking University in 1985 and Ph.D. from Department of P&A Chemistry, University of Strathclyde, Glasgow, UK, with “Patrick D. Ritchie Prize” for the best Ph.D. in 1994. With more than a decade experience in large

international incorporations, Prof. Pan has been engaged in fundamental research and product development of novel optoelectronic and energy storage materials and devices. As Chief Scientist, Prof. Pan led 8 entities in Shenzhen to win the 150 million RMB grant for the national new energy vehicles (power batteries) innovation project from 2013 to end of 2015. As Chief Scientist, Prof. Pan led 12 entities to win the national key project of material genomic engineering for solid state Li-ion batteries in China in 2016.



Prof. Shanqing Zhang obtained his Ph.D. degree in Electrochemistry in 2001 at Griffith University, Australia. Since then, he has been working on the synthesis, modification and characterization of nanostructured materials for sensing, energy conversion and energy storage devices. He has developed a series of patented and commercialized nanotechnologies for environmental monitoring based on functional nanomaterials. He was awarded as an Australia Research Council Future Fellow for the period of

2009–2013. Currently, he is leading his group conducting research on the synthesis of functional nanomaterials and functional polymers for lithium-ion batteries, sodium-ion batteries, supercapacitors and all solid-state lithium-ion batteries.

CHAPTER 3

OUTPERFORMING CAPACITY LIMIT OF LITHIUM TITANATE ANODE VIA QUENCHING-INDUCED OXYGEN VACANCIES AND CATION REDISTRIBUTION

To be Submitted to *Nature Energy* (2021)

3.1. INTRODUCTORY REMARKS

This chapter is written in an article form for submission to *Nature Energy* in 2021.

The chapter presents a simple defect preparation strategy to retain the defects induced at high temperatures in the LTO crystal lattice phase through a rapid quenching process. DFT calculation shows that the retained defects in the bulk crystal lattice provide abundant additional lithium storage sites. The as-prepared defect LTO anode showed an incredible capacity of 201.7 mAh g⁻¹ at a rate of 1 C where the theoretical capacity of LTO is only 175 mAh g⁻¹. Such a simple quenching strategy is a breakthrough technology for ultra-high lithium storage capacity in defective LTO, and demonstrates a wide range of commercial application prospects in comparison to the lower capacity of the current commercial LTO anode.

3.2 STATEMENT OF CONTRIBUTION

This chapter includes one first-authored paper. The bibliographic details of the co-authored paper, including all authors, are:

Zhong Su, Meng Li, Shangshu Qian, Lu Ma, Shunning Li, Tao Zhang, Jun Lu, Feng Pan, Shanqing Zhang*

Outperforming capacity limit of lithium titanate anode via quenching-induced oxygen vacancies and cation redistribution.

To be submitted to *Nature Energy*, 2021

My contribution to the paper included:

Conducting experiments, data collection and analysis, writing of manuscript.

(Signed) _____ (Date) 15/04/2021

Name of Student: Zhong Su

(Countersigned) _____ (Date) 15/04/2021

Corresponding author of paper: Shanqing Zhang

(Countersigned) _____ (Date) 15/04/2021

Supervisor: Shanqing Zhang

3.3 ARTICLE 2

Outperforming the capacity limit of lithium titanate anode via quenching-induced oxygen vacancies and cation redistribution

Zhong Su¹, Meng Li^{1,2}, Shunning Li², Lu Ma³, Shangshu Qian¹, Tao Zhang³, Cheng Dong², Jun Lu³✉, Feng Pan²✉, Shanqing Zhang¹✉

¹ Centre for Clean Environment and Energy, School of Environment and Science, Griffith University, Gold Coast Campus, Gold Coast, Queensland 4222, Australia. ² School of Advanced Materials, Peking University, Shenzhen Graduate School, Shenzhen, 518055, China. ³Chemical Sciences and Engineering Division, Argonne National Laboratory, Lemont, IL, USA.

✉ e-mail: junlu@anl.gov; panfeng@pkusz.edu.cn; s.zhang@griffith.edu.au.

Abstract

The analysis and control of point defects are now an integral part of materials research in the field of energy storage. However, the engineering of intrinsic defects by design remains elusive due to their instability and the lack of effective manipulation methods. Here, we present a strategy of rapid quenching to produce and harvest excessive intrinsic defects in lithium titanate ($\text{Li}_4\text{Ti}_5\text{O}_{12}$, LTO) for the pursuit of high-capacity electrodes. In-situ Synchrotron X-ray analysis and theoretical investigation suggest that oxygen off-stoichiometry is induced upon heating and preserved upon successive quenching in ice water, with intensive cation (i.e., Li^+/Ti^+) redistribution concurrently. The as-prepared LTO electrode delivers an extraordinary capacity of 202 mAh/g in the 1.0-2.5 V charge/discharge range, surpassing the theoretical and experimental values of pristine LTO by 15% and 33%, respectively, with excellent retention even at high rates. The oxygen vacancies and cation redistribution could facilitate the native Li ions in the bulk of the quenched LTO to participate in the charge/discharge processes; in contrast, these ions in the pristine LTO are essentially restricted and unextractable. Furthermore, we demonstrate the feasibility of tuning the degree of structural defectiveness via the choice of quenching agents. This work opens up an intriguing avenue of research to harness the intrinsic defects for the development of advanced electrodes in rechargeable batteries.

Defects are ubiquitous and so much a part of the physics and chemistry of solids that nearly the whole of the scientific revolution in the realms of semiconductors, superconductors, structural materials and battery electrodes, is inseparable from our understanding of defect properties and the remedies to defect-related issues^{1, 2, 3}. Among the structural defects in crystal lattices, the most prominent type is point defects, i.e., vacancies, interstitials, antisites and dopants, all of which can result in the breakdown of crystal symmetry and even local rearrangement of atoms, thus giving rise to unusual properties that are absent in pristine materials. So far, the possibility of tuning electronic and ionic conductivities via defect manipulation has already been well recognized, as exemplified by the modern silicon-based devices and solid oxide fuel cells^{4, 5, 6}. In the past decades, defect engineering via the introduction of impurities has conspicuously proven its importance as a tool for boosting the energy density of electrodes in lithium ion batteries (LIBs)^{7, 8}. Tantalizing indications of capacity enhancement by dopants could be evidenced in LiCoO_2 , the most widely used cathode for LIBs, where even the trace amount of selected dopants could contribute to a significant change of surface microstructures and hence endow the cathode with excellent stability against deterioration at high voltages^{9, 10, 11}. Besides the promising benefits provided by extrinsic dopants, there are also opportunities to promote the performance of electrodes via the intentional incorporation and control of intrinsic defects. In this work, we demonstrate the successful enrichment of oxygen vacancies (V_O) in lithium titanate ($\text{Li}_4\text{Ti}_5\text{O}_{12}$, LTO) anode via simple heat treatment, which can trigger Li/Ti redistribution and allow access to a specific capacity surpassing the theoretical value.

LTO crystallizes in spinel structure, with tetrahedral 8a sites occupied by Li and octahedral 16d sites occupied by randomly mixed Li and Ti ions in a ratio of 1:5. During Li intercalation, the spinel LTO undergoes a first-order phase transformation into rocksalt $\text{Li}_7\text{Ti}_5\text{O}_{12}$, accompanied by negligible

volume change (0.2%)^{12, 13, 14, 15}. This makes LTO well-known as a “zero-strain” anode, which guarantees an ultralong cycle life. Moreover, LTO exhibits a flat operating potential plateau of about 1.5 V versus Li/Li⁺, thus circumventing the issue of lithium dendrite formation. However, these advantages are compromised by the low energy density of LTO-based batteries due to such a high voltage plateau. One intuitive way to improve the energy density is to promote excess Li intercalation into the bulk of LTO, but most of the attempts ended in vain in the past because the rocksalt Li₇Ti₅O₁₂ possesses a close-packed cation and anion lattice, which restricts the accommodation of extra Li ions at the interstitial sites. Although there are some observations of lithium compositions exceeding Li₇Ti₅O₁₂, it is only accessible in the subsurface regions and in the first few cycles¹⁶. Unlocking the capacity limitations of LTO anodes still poses a great challenge, especially when the long-term cycling stability and the cost-effectiveness of treatments are simultaneously taken into account.

Herein, we manage to alter the delithiated limit at the Li₄Ti₅O₁₂ composition by modulating the V_O concentration and the Li/Ti ratio at 16d sites. For the first time, we report a defect-enriched LTO anode that is able to break the capacity limit of traditional LTO while preserving high rate capability and cycling stability. This striking feature is realized via a straightforward heating-quenching procedure from commercial LTO samples. Oxygen off-stoichiometry generated at high temperature is thus retained¹⁷, whereas Li/Ti redistribution occurs spontaneously due to the thermodynamic driving force to resist the accumulation of V_O. The highly defective LTO anode can reversibly extract/intercalate the native Li ions at 8a and 16d sites, which leads to a remarkable increase in capacity. It is envisaged that this efficient and low-cost rapid-quenching technique can greatly expedite the development and commercialization of LTO anodes, and that the underlying mechanism will cast new light on the design paradigm of energy-storage materials from a defect chemistry perspective.

Mechanistic pathways for increased capacity

We propose two mechanisms involving V_O that can allow for a capacity beyond the theoretical value of pristine LTO, as schematically illustrated in Fig. 1. Here, the structures of $Li_4Ti_5O_{12}$ and $Li_7Ti_5O_{12}$ are represented as $[Li_3]^{8a}[Li_1Ti_5]^{16d}[O_{12}]^{32e}$ (spinel) and $[Li_6]^{16c}[Li_1Ti_5]^{16d}[O_{12}]^{32e}$ (rocksalt), respectively. In the discharge process of $Li_4Ti_5O_{12}$, Li ions are inserted into one-half of the octahedral 16c sites, with the remaining half occupied by the existing Li migrating from the 8a sites. This is a two-phase transition reaction corresponding to a capacity of 3 Li per formula unit (f.u.). The defective $[Li_3]^{8a}[Li_1Ti_5]^{16d}[O_{12-x}]^{32e}$ yields the same amount of capacity in the first discharge process (Mechanism 1 in Fig. 1). However, there are a larger number of Ti^{3+} ions in the discharged product, $[Li_6]^{16c}[Li_1Ti_5]^{16d}[O_{12-x}]^{32e}$, than the defect-free $Li_7Ti_5O_{12}$, owing to the extra electrons introduced by V_O . If all the Ti ions are oxidized to Ti^{4+} in the subsequent charge process, a total of $3+2x$ Li/f.u. will be deintercalated, and thereby the specific capacity in the following cycles would exceed that of pristine LTO (3 Li/f.u.). According to density functional theory (DFT) calculations, the charged product is $[Li_{3-x}]^{8a}[Li_{1-x}Ti_5]^{16d}[O_{12-x}]^{32e}$ (Supplementary Fig. 1 and 2). In this scenario, a concentration of 1 at.% V_O could contribute to $((2x/3)/(x/12) \times 1\% =) 8\%$ increase in the capacity of the anode. DFT calculations predict an average Li (de)intercalation potential of 1.56 V for a structure with about 3 at.% V_O , which is slightly higher than that of the pristine LTO anode (1.45 V).

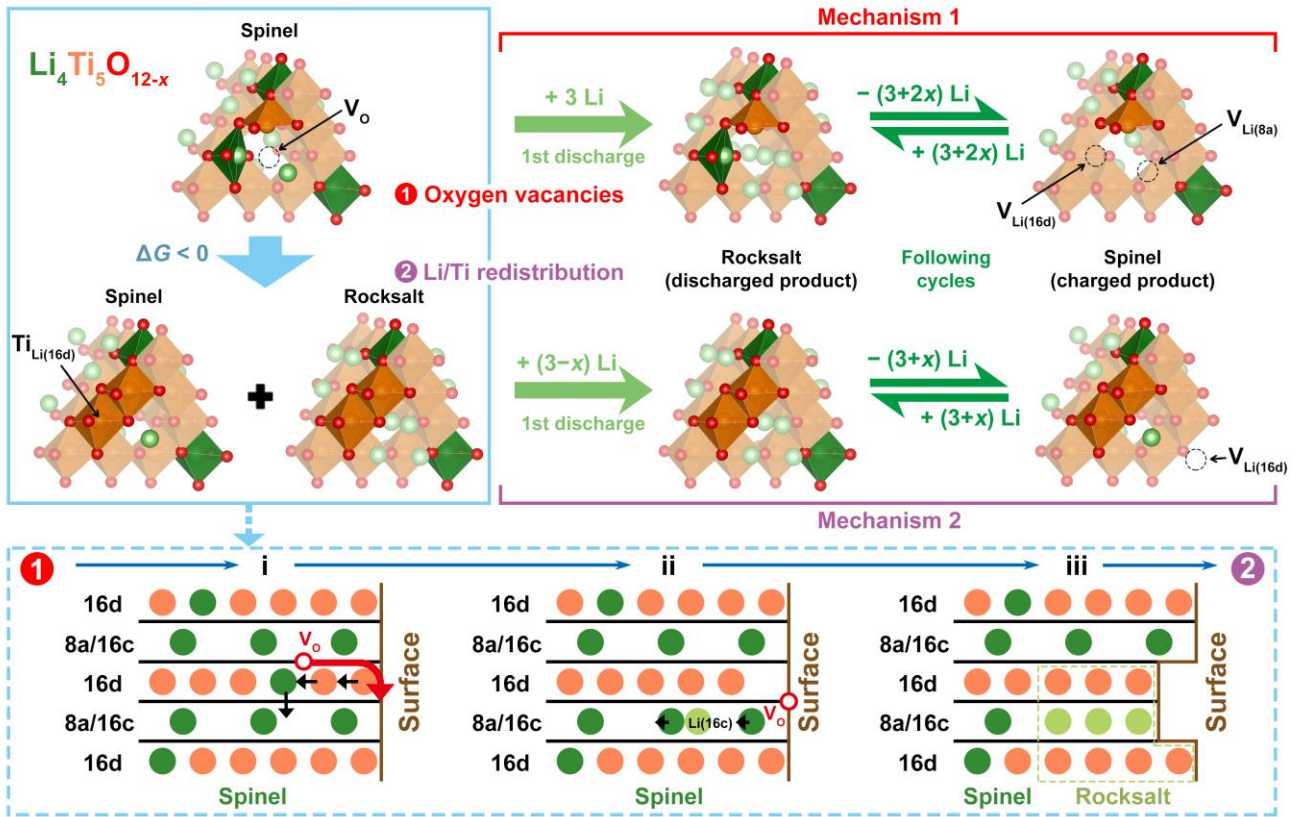
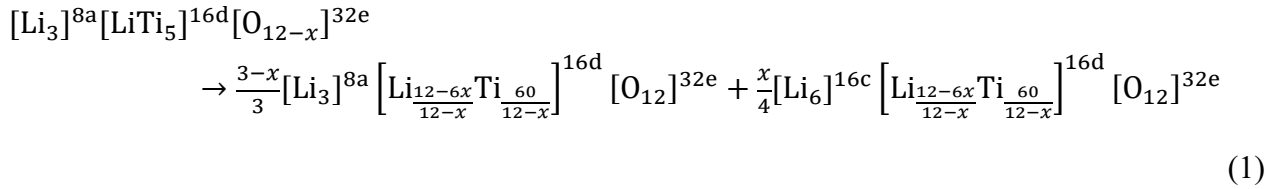


Fig. 1 | The influence of V_O and cation redistribution on the capacity of LTO. $Li_4Ti_5O_{12-x}$ is taken as the initial state, which has a tendency to be transformed into a configuration with Li/Ti redistribution (blue solid rectangle). The transformation involves the diffusion of V_O to the surface and the synergistic displacement of cations (blue dashed rectangle). In Mechanism 1, every x V_O per f.u. of $Li_4Ti_5O_{12-x}$ leads to an excess capacity of $2x$ Li/f.u. after the first discharge. In Mechanism 2, assuming that the stoichiometry of $Li_4Ti_5O_{12-x}$ is maintained after Li/Ti redistribution, an excess capacity of x Li/f.u. would be expected.

Superconcentrated V_O could facilitate atomic rearrangement so as to relieve internal stress. One viable avenue is to squeeze the vacancies out of the bulk phase and concurrently push the Li ions located at 16d sites to the 16c sites (blue dashed rectangle in Fig. 1). As a result, the anion sublattice retains its perfect structure while the Li/Ti ratio on 16d sites deviates from 1:5. It is worth emphasizing that the stoichiometry of $Li_4Ti_5O_{12-x}$ and the Ti oxidation state are supposed to be kept constant during this structural transition. Hence, the process of V_O elimination is different from the classical

microscopic picture of external oxygen incorporated into the vacant site, which sees no need for the redistribution of other ions. Since Li at the 16c sites in a spinel structure is unstable, the following reaction will take place:



with the first and second terms being the spinel and rocksalt phases, respectively. After the first cycle, the extractable content of Li would become $3+x$ per unit of $\text{Li}_4\text{Ti}_5\text{O}_{12-x}$ (Mechanism 2 in Fig. 1, detailed formulation given in the Supporting Information), indicating that 1 at.% of original V_O can produce 4% increase in the capacity after the atomic rearrangement. A lower capacity than Mechanism 1 is therefore anticipated for Mechanism 2 with the same amount of original V_O . Nevertheless, Reaction (1) tends to be exothermic according to the DFT calculation results ($\Delta G = -1.1$ eV/f.u. at $x = 0.57$, see Supplementary Fig. 3), which suggests improved thermodynamic stability after the atomic rearrangement, and consequently, a high likelihood of Mechanism 2 is encountered.

Characterization of the ice-water-quenched LTO

Now that we know it is theoretically possible to enhance the capacity of LTO via the increase in V_O concentration, it would be reasonable to pursue the defect-enriched structure in the preparation of LTO. The equilibrium population of vacancies in a crystal is given by $n = N \exp(-\Delta G_\text{V}/kT)$ ¹⁸, where N is the total number of normally occupied atom sites, ΔG_V is the Gibbs free energy for the formation of a vacancy, k is the Boltzmann constant and T is temperature. Accordingly, oxygen deficiency is likely to appear upon heating. We employed in-situ thermogravimetric analysis (TGA) to keep track of the

mass change during alternating slow heating and cooling of LTO (Fig. 2a). The periodic fall and rise of the TGA curve imply the release and uptake of oxygen¹⁹. In-situ X-ray absorption near-edge structure (XANES) was utilized to probe the oxidation states of Ti ions at various temperatures (Fig. 2b). The systematic shift of the Ti K-edge to lower energies at elevated temperatures proves the reduction of Ti^{4+} ions to Ti^{3+} (Fig. 2c)^{20, 21}, thus adding credence to the idea that V_O is formed during heating. The average oxidation state of Ti, reaching +3.5 at 800 °C, goes back to around +3.9 upon natural cooling to room temperature (Fig. 2d,e), which suggests the annihilation of V_O and the recovery of the structure close to pristine $\text{Li}_4\text{Ti}_5\text{O}_{12}$. Another justification of the depletion of lattice O ions at high temperatures comes from the in-situ X-ray absorption fine structure (XAFS) measurements, which reveal the continuous decrease in amplitudes of Ti-O and Ti-Ti peaks during heating (Supplementary Fig. 4). This trend can be rationalized by the formation of V_O , and is reversed when the sample is naturally cooled down (Supplementary Fig. 5)²⁰.

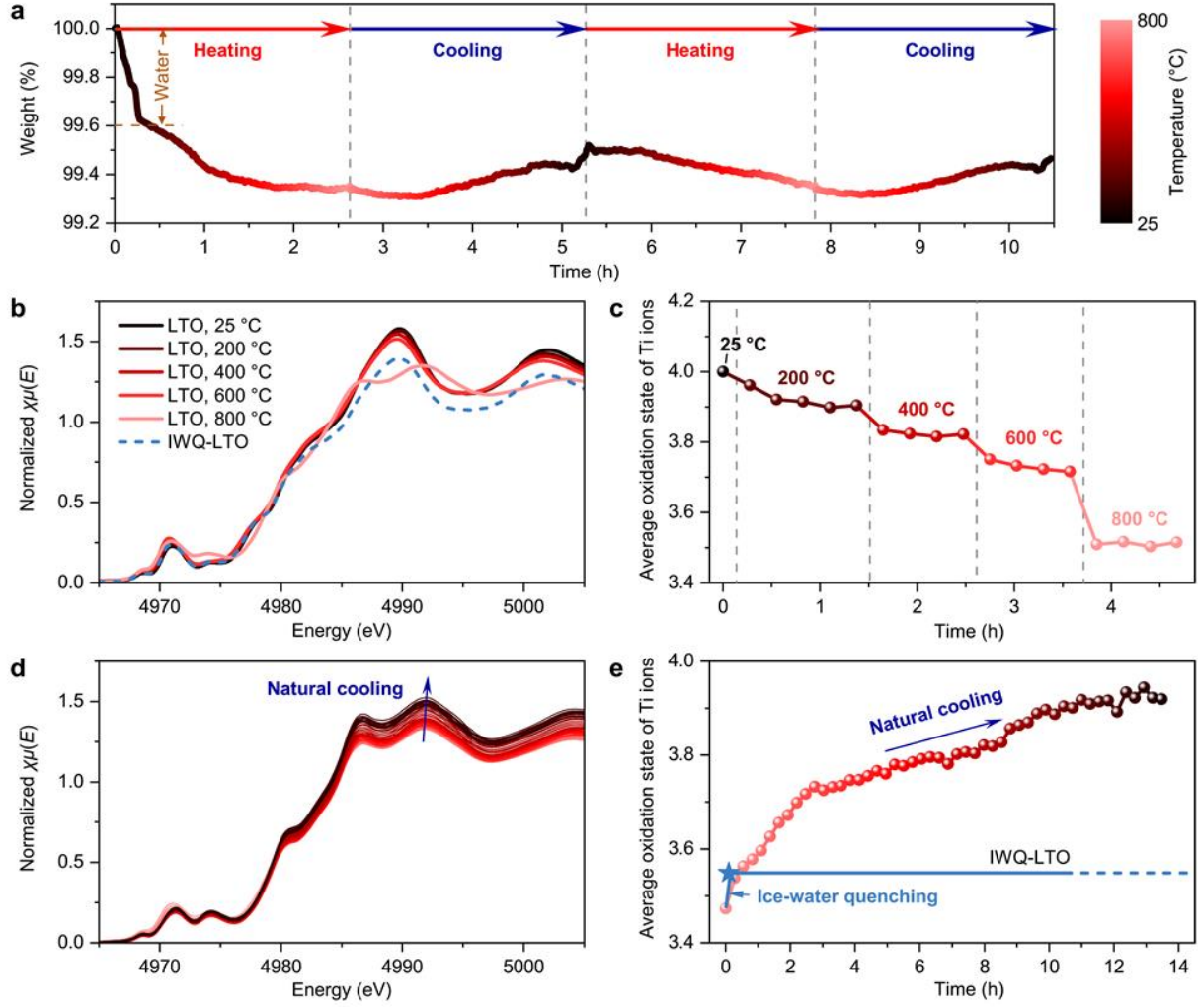


Fig. 2 | Effect of temperature on V_O content and Ti oxidation states in LTO. **a**, In-situ TGA curve of LTO under alternating slow heating and cooling sequences. The intensity of red and black color of the data points and curves analogically indicates the temperatures of the samples. **b**, In-situ XANES spectra of LTO heated to different temperatures. **c**, The oxidation states of Ti ions as deduced from the in-situ XANES spectra of LTO at elevated temperatures. **d,e**, The evolution of XANES spectra of LTO during natural cooling (**d**) and the corresponding oxidation states of Ti (**e**). The XANES spectrum of LTO after ice-water quenching is also plotted in **b**, and the corresponding valency of Ti is provided in **e**.

With the defective LTO achievable via heating, the remaining issue would be to maintain this state to low temperature. Rapid quenching is a straightforward means to this end. As compared to natural

cooling that permits the recombination of V_O and external oxygen in the cooling process, the rapidly-quenched samples do not have enough time to be restored to their perfect crystal structure. This defective structure encompassing large quantities of V_O as well as the possible Li/Ti redistribution is stable after quenching due to the limited kinetics of Ti and O ions at room temperature.

As a proof of concept, we heated a commercial LTO powder to 800 °C, and then dropped it in ice water to produce a rapidly-quenched sample. Scanning electron microscopy (SEM) images reveal the formation of micro-spherical secondary particles (3~6 μm), which comprise relatively loose aggregates of nano-sized grains (Supplementary Fig. 6). Remarkably, a substantial discrepancy between the pristine and quenched samples is witnessed in the XANES spectra (Fig. 2b). The oxidation state of Ti in this ice-water-quenched LTO (IWQ-LTO) is estimated to be +3.5 (Fig. 2e), indicating the enrichment of V_O or extensive Li/Ti redistribution. The high-resolution X-ray photoelectron spectroscopy (XPS) O 1s spectrum of IWQ-LTO (Fig. 3a) can be deconvoluted into lattice O (529.7 eV), V_O (531.3 eV) and adsorbed O (532.3 eV)²². In the XPS Ti 2p spectrum (Fig. 3b), a new peak emerges at 458.2 eV, indicative of Ti^{3+} ions²². This result is compatible with the Raman spectra showing the blue shift of the peak at $\sim 140\text{ cm}^{-1}$ that implies the reduction of Ti^{4+} (Supplementary Fig. 7)²³. The TGA data of IWQ-LTO at 800 °C in N_2 atmosphere (Supplementary Fig. 8) reveal a lower mass loss than pristine LTO, which is attributable to a concentration of V_O being closer to its equilibrium value at high temperature. The results of XAFS (Supplementary Fig. 4) are consistent with the above analysis, in which a less pronounced Ti-O peak in IWQ-LTO than the pristine sample is most probably linked with the removal of lattice O ions²⁰.

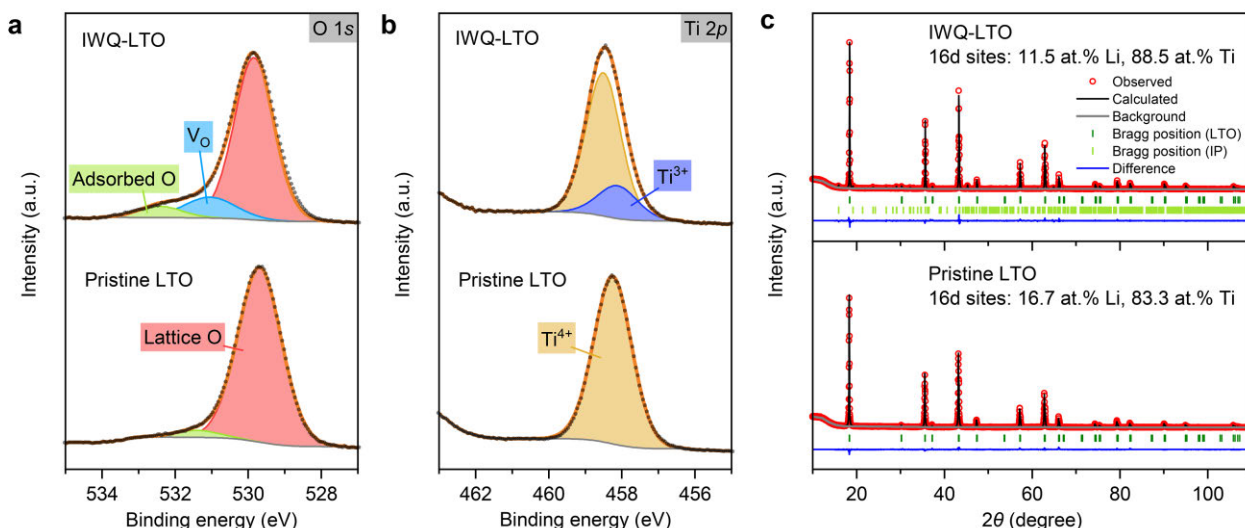


Fig. 3 | Characterization of IWQ-LTO and pristine LTO. **a,b**, XPS O 1s (**a**) and Ti 2p (**b**) spectra of IWQ-LTO (top) and pristine LTO (bottom). **c**, XRD patterns and Rietveld refinement of IWQ-LTO (top) and pristine LTO (bottom). The Li/Ti ratios at 16d sites are 88.5 and 83.3 at.% for IWQ-LTO and pristine LTO, respectively.

Nearly all the X-ray diffraction (XRD) peaks of the IWQ-LTO sample can be assigned to a spinel structure with a space group of $Fd-3m^{24}$ (Fig. 3c). Rietveld refinement of the XRD data has unveiled the V_O -induced cation rearrangement, showing that the Ti content at 16d sites is increased from 83.3 at.% in pristine LTO to 88.5 at.% after ice-water quenching. The corresponding amount of V_O leading to this rearrangement is 5.8 at.% ($x = 0.7$ in Eq. 1), which can yield up to 23% larger capacity than the theoretical value of pristine LTO, demonstrating the potential role of Li/Ti redistribution in the capacity of IWQ-LTO. Although there exist some impurity phases (IP), all of which can be indexed to an orthorhombic structure, their amount is negligibly small ($< 5\%$) and can hardly influence the capacity on a large scale. It is worth noting that, unlike the Li/Ti ratio, the concentration of V_O and the proportion of Ti^{3+} ions cannot be accurately quantified from the spectroscopic measurements, which precludes us

from directly assessing the individual contributions of both mechanistic pathways. Nevertheless, a robust conclusion can still be drawn that the experimentally obtained IWQ-LTO is severely off-stoichiometric with significant participation of V_O and Li/Ti redistribution as the key factors that differ its structure from that of pristine LTO.

Moreover, we found a perceptible color change of the LTO samples from white (pristine) to green (IWQ), which is in agreement with the dramatic difference in the ultraviolet-visible (UV-Vis) absorption spectra (Supplementary Fig. 9). The existence of deep defect levels in the rapidly-quenched sample, as inferred from the UV-Vis results (Supplementary Fig. 10), is consistent with the DFT calculations for the defective LTO (Supplementary Fig. 11). The high concentration of V_O is again justified, and an improvement in electronic conductivity is expected as well.

We have used transmission electron microscopy (TEM) to examine the surface structure of IWQ-LTO (Supplementary Fig. 12). In comparison with the pristine and naturally-cooled LTO samples where evident lattice fringes are displayed near the (111) surface, some of the IWQ-LTO particles possess a subsurface region with relatively low crystallinity. This region is only 3 nm thick, and such a limited amount can rule out the possibility that this amorphous-like region can alter the capacity to a noticeable degree. The breakdown of crystallinity is likely associated with the prevailing formation of V_O on the surfaces of LTO at high temperatures and the consequent appearance of a disordered structure, which is preserved during rapid quenching.

Electrochemical performance of the ice-water-quenched LTO

The performance of IWQ-LTO electrode was analyzed in a half-cell. The galvanostatic charge-discharge test of IWQ-LTO at 1C shows a specific capacity of 202 mAh/g between 1.0 V and 2.5 V

(Fig. 4a), which exceeds the capacity limit of traditional LTO (175 mAh/g) by ~15%, and is 33% greater than the experimental value of the pristine sample in this study (152 mAh/g). In a test between 0 V and 2.5 V at 1C, the discharge capacity of IWQ-LTO further increases to 360 mAh/g (Supplementary Fig. 13). While the discharge capacity between 0 V and 1.0 V is mainly from the additional occupancy of Li at 8a sites near the surfaces of the rocksalt product, the length of the voltage plateau at ~1.5 V should be related to the amount of reversibly extractable Li inside the bulk phase²⁵. The increased capacity for IWQ-LTO as compared to pristine LTO at this voltage plateau corroborates our hypothesis that the defective structure of LTO can result in a higher degree of delithiation upon charge.

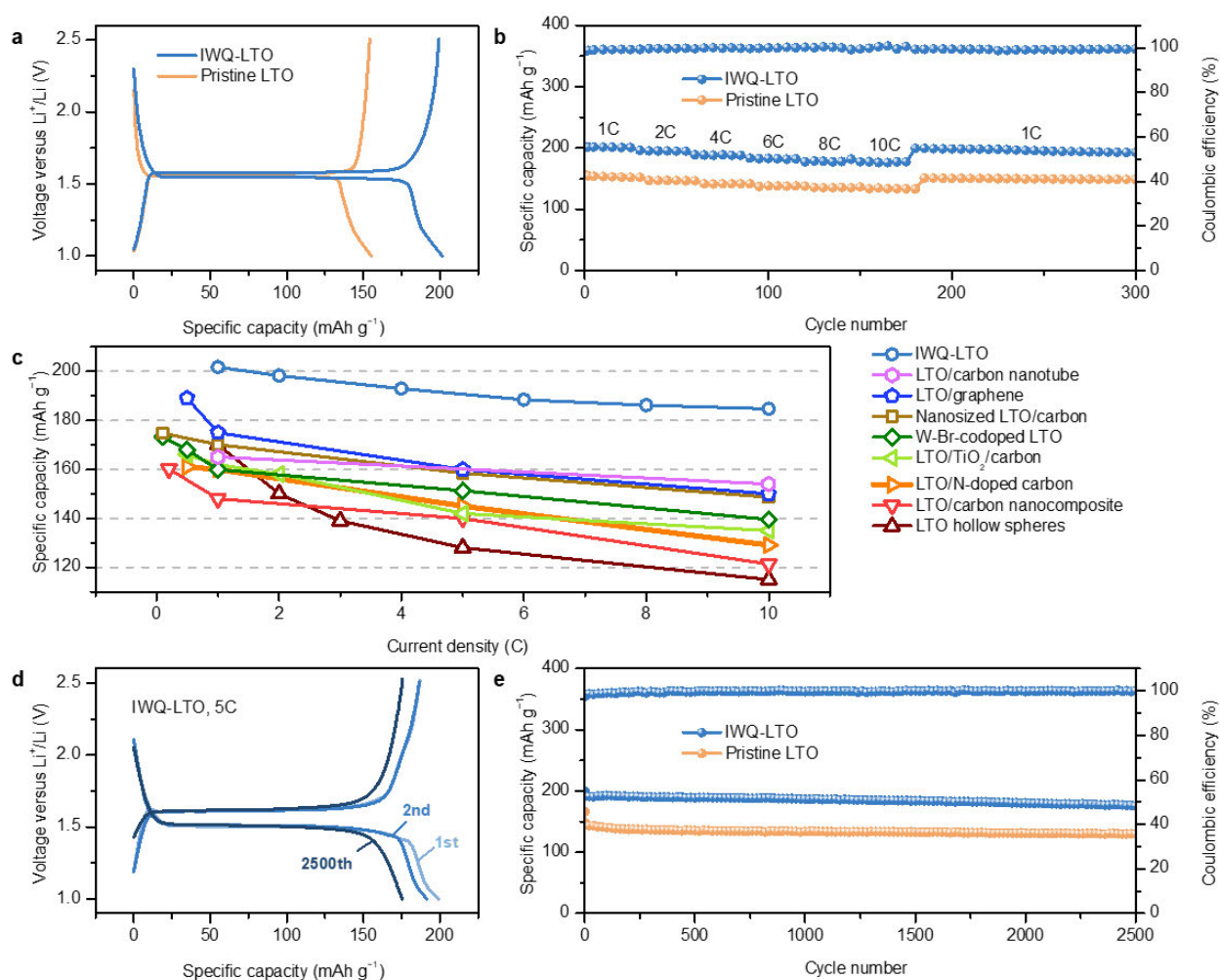


Fig. 4 | Electrochemical performance of IWQ-LTO electrode. **a**, Voltage profiles of IWQ-LTO and pristine LTO in the 1.0–2.5 V range at 1C. **b**, Rate performance comparison between IWQ-LTO and pristine LTO. **c**, Comparison of the capacity of IWQ-LTO to those of state-of-the-art LTO-based anodes as reported in the literature: LTO/carbon nanotube¹⁴, LTO/graphene²⁶, nanosized LTO/carbon²⁷, W-Br-codoped LTO²⁸, LTO/TiO₂/carbon²⁹, LTO/N-doped carbon³⁰, LTO/carbon nanocomposite³¹, and LTO hollow spheres³². **d**, Voltage profiles of IWQ-LTO for the 1st, 2nd and 2500th at 5C. **e**, Cycling performance comparison between IWQ-LTO and pristine LTO at 5C.

Interestingly, the rate capability and cyclability of IWQ-LTO are also outstanding. When working at 10C, IWQ-LTO can deliver a capacity of 176 mAh/g (Fig. 4b) between 1.0 V and 2.5 V, which is over 40 mAh/g higher than that of pristine LTO. For all rates tested, the capacity of this rapidly-quenched product is, to the best of our knowledge, the highest among all the LTO-based anodes (Fig. 4c and Supplementary Table 1). After 2500 cycles at 5C, the IWQ-LTO electrode retains ~88% of the original capacity without discernible change in the voltage plateau, and has an average Coulombic efficiency of ~99.95% (Fig. 4c,d). SEM images show negligible morphology evolution after 300 cycles (Supplementary Fig. 14). Samples with different heating durations display similar long-term cycling stability (Supplementary Fig. 15), suggesting that this superior performance is by no means fortuitous. In addition, the cyclic voltammetry (CV) measurements indicate a slightly less pronounced polarization for IWQ-LTO than pristine LTO (Supplementary Fig. 16), which can be attributed to the enhanced electronic conductivity in the defective structure. This finding coincides with the outcomes from the analysis of electrode impedance spectra before cycling (Supplementary Fig. 17).

The oxidation states of Ti ions in the first cycle are estimated from the ex-situ XANES spectra (Fig 5a-c). At the initial state, the average valency of Ti in IWQ-LTO is much lower than that of pristine

LTO. After the first discharge, the discrepancy in oxidation states between both samples is reduced. Given that the valence change of Ti is linearly correlated with the amount of Li intercalation, this result is indicative of less intercalated Li in IWQ-LTO than pristine LTO, which agrees well with the theoretical expectation ($3-x$ Li/f.u.) for the case of Li/Ti redistribution (Fig. 1). Here, caution has to be exercised when considering the actual capacity of the first discharge, as shown in Fig. 4d, since a proportion of the capacity likely stems from surface reactions. During the subsequent charge, most of the Ti^{3+} ions are oxidized to Ti^{4+} , resulting in fairly close average oxidation states for both IWQ-LTO and its counterpart. We note that a larger valence change of Ti is observed for IWQ-LTO at this time, meaning that the amount of deintercalated Li in IWQ-LTO exceeds pristine LTO. It can be drawn that a certain amount of native Li in the bulk of the as-prepared IWQ-LTO will be lost after the first discharge-charge cycle, which is exactly in line with the mechanistic scenario outlined above for the acquisition of additional capacity. XAFS spectra (Fig. 5d,e) show the elongation of Ti-Ti bonds after the first discharge, which can be ascribed to the expansion of the lattice upon Li intercalation. After the charge, the Ti-Ti bond length in IWQ-LTO shrinks to a value lower than its initial value, in sharp contrast to the pristine LTO where the bond length change is essentially irreversible. This result is parallel to the trend of Ti oxidation state and implies a higher degree of delithiation in IWQ-LTO. Also, the Ti 2p XPS spectra of the IWQ-LTO and P-LTO electrodes after 50 cycles at rate of 5 C were studied and shown in Supplementary Fig. 18. Compared with P-LTO electrode, the higher content of Ti^{3+} ions can be observed in the IWQ-LTO electrodes after 50 cycles, indicating that the defect state will not disappear during the charging and discharging process. The more Ti^{3+} ions in the LTO benefits for Li^+ reversible de-intercalation and help to improve electrochemical performance, this conclusion is consistent with the ex-situ XAS results (Fig. 5)

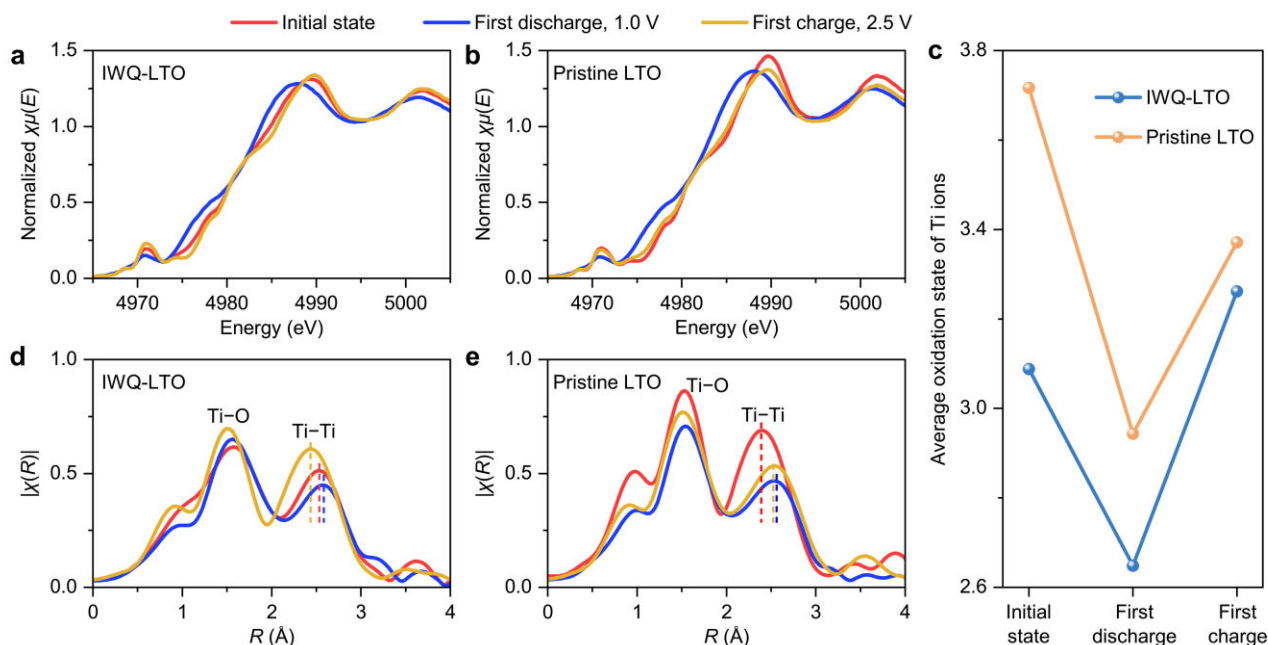


Fig. 5 | Li (de)intercalation in the first cycle. a-c, Ex-situ XANES spectra of IWQ-LTO (a) and pristine LTO (b) at the initial, 1.0 V discharged and 2.5 V charged states, and the corresponding oxidation states of Ti ions (c). d,e, XAFS spectra of IWQ-LTO (d) and pristine LTO (e) in the first discharge-charge cycle.

Effective tuning of defect concentration and electrochemical performance

The concentration of V_O and the Li/Ti ratio on 16d sites can be effectively tuned by the quenching agent, which enables the modulation of the electrochemical performance of the rapidly-quenched LTO anodes. As a demonstration, we have replaced ice water with liquid nitrogen. It is noteworthy that although the temperature of liquid nitrogen is below that of ice water, the cooling rate of substances in liquid nitrogen is lower than in ice water due to the Leidenfrost phenomenon³³. The liquid-nitrogen-quenched LTO (LNQ-LTO) exhibits morphological features similar to IWQ-LTO according to the SEM images (Supplementary Fig. 19). The concentration of Ti^{3+} ions and V_O can be roughly quantified

by XANES and XPS measurements, respectively, from which it appears that LNQ-LTO is less defective than IWQ-LTO (Fig. 6a,b, Supplementary Fig. 20 and 21). XRD refinement suggests a Ti content of 87.6 at.% at 16d sites in LNQ-LTO (Fig. 6c), meaning that the Li/Ti redistribution is less prominent than in IWQ-LTO. The Li/Ti redistribution level in LNQ-LTO can contribute to a maximum increase of 19% in capacity with respect to pristine LTO.

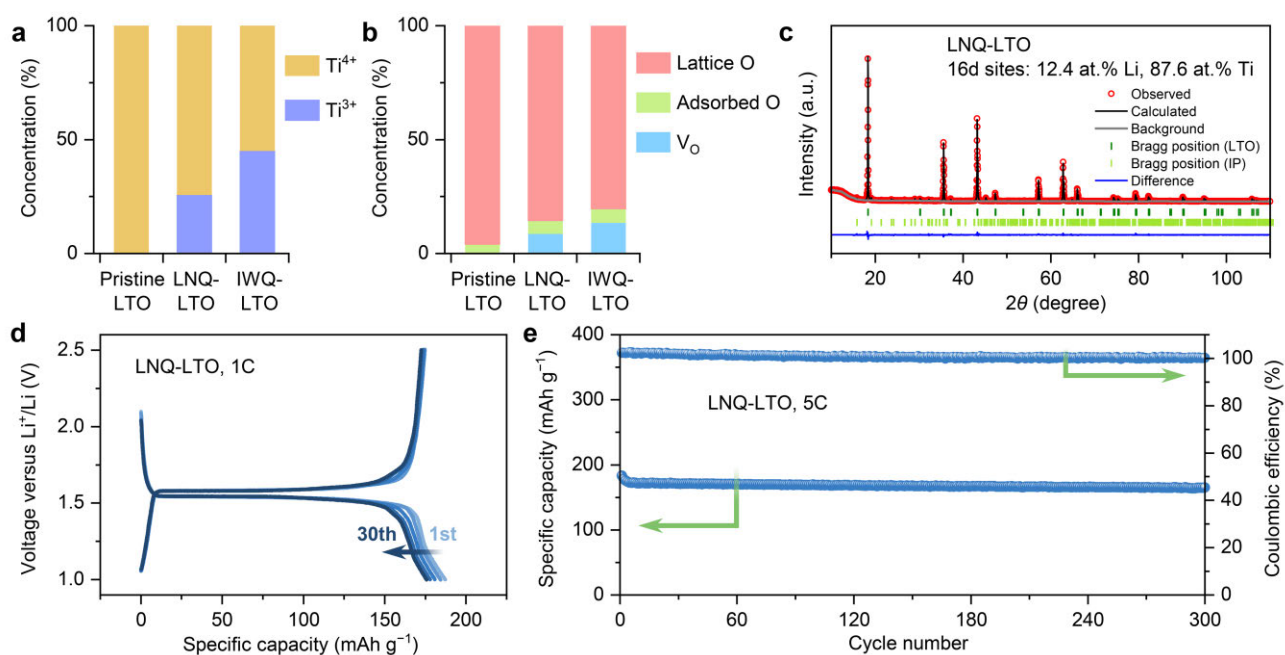


Fig. 6 | Characterization and electrochemical performance of LNQ-LTO. **a**, Concentration of Ti^{3+} as estimated from XANES. **b**, Concentration of V_O as estimated from XPS. **c**, XRD pattern and Rietveld refinement of LNQ-LTO. **d**, Voltage profile of LNQ-LTO between 1.0 V and 2.5 V at 1C. **e**, Cycling performance of LNQ-LTO at 5C for 300 cycles.

A reversible capacity of 187 mAh/g is achieved in LNQ-LTO over the 1.0-2.5 V range at a current rate of 1C (Fig. 6d). An extended cycling test at 5C shows that LNQ-LTO can output 165 mAh/g after 300 cycles (Fig. 6e), which is higher than pristine LTO, but beneath that of IWQ-LTO. The inferior

electrochemical performance of LNQ-LTO in comparison to IWQ-LTO corroborates our reasoning that the excess specific capacity of the rapidly-quenched product arises from V_O and Li/Ti redistribution and hence is proportional to the degree of structural defectiveness. Furthermore, based on the above findings, it is feasible to fine-tune the structural defectiveness via the adjustment of quenching conditions, which offers hope for the optimization of such quasi-equilibrium defective structures for the design of highly performing LIB electrodes.

Conclusion

In this work, we have demonstrated the opportunities offered by intrinsic defects to activate Li ions that are conventionally not extractable in an electrode material. As exemplified by the LTO anode, a defective structure with abundant V_O and cation redistribution can be realized via a heating-quenching treatment. In-situ and ex-situ spectroscopy techniques have confirmed the oxygen off-stoichiometry with which native Li ions in LTO can readily be extracted during delithiation owing to the introduction of excess electrons. By virtue of the stabilized defects after ice-water quenching, a sustained reversible capacity of 202 mAh/g is achieved between 1.0 V and 2.5 V, reaching 115% (133%) of the theoretical (experimental) capacity of pristine LTO. A specific capacity of 176 mAh/g is retained even at 10C. The tunable defect concentration depending on the choice of quenching agent, allows us to further optimize the electrochemical performance. We believe that our discovery can be generalized to other materials systems, and the rapid quenching treatment can be implemented as a cost-effective strategy for intrinsic defect engineering, which can be leveraged to promote the energy density of existing electrodes in future studies.

Methods

DFT calculations. DFT calculations were performed using Vienna ab initio simulation package (VASP)^{34, 35}. The electron-core interactions were treated in the projector augmented wave method³⁶ with a cutoff energy of 520 eV. The Perdew-Burke-Ernzerhof exchange-correlation functional³⁷ was employed with Hubbard U corrections (PBE+U) to take account of the on-site Coulomb interaction³⁸. The value of 4.2 eV for the U parameter of Ti ion was adopted from the previous studies³⁹. The *k*-point sampling density of at least 1000/(the number of atoms per cell) within the Monkhost-Pack scheme⁴⁰ was found sufficient for energy convergence.

Material preparations. The IWQ-LTO sample was prepared from commercial LTO powder (Tianjin Jiewei). Pristine LTO (5g) was first sonicated in 3 mol/L NaCl solution for several hours. After centrifugation and removing the supernatant solution, the sample was dried at 60 °C for 3 h, heated at 800 °C for 0.5 h in the muffle furnace, and then thrown into ice water immediately. At last, the quenched sample was dried at 80 °C for 6 h. LNQ-LTO was prepared within the same method and a different quenching agent.

Material characterization. The X-ray absorption near-edge structure (XANES) spectra at Ti K-edge was collected in transmission mode and XANES data reduction and analysis were processed by Athena software. The X-ray photoelectron spectroscopy (XPS) spectra were conducted on a multifunctional imaging electron spectrometer (Thermo ESCALAB 250XI, Monochromatized Al K α resource). Scanning electron microscopy (SEM, SU8020) and high-resolution transmission electron microscopy (HRTEM, Tecnai G20) were conducted to characterize the morphology and structure of the obtained LTO. XRD pattern was collected on a Cu-K α radiation (λ = 1.5405 Å) and the diffraction pattern with Rietveld refinement was performed by the RIETAN-2000 program. Raman spectra were examined on a Renishaw system 100 Raman fiber spectrometer and UV-vis diffusion reflectance spectra were collected on a Thermo Nicolet Evolution 500 UV Vis spectrophotometer.

Electrochemical measurements. The galvanostatic charge-discharge cycling was studied on a LAND-CT2001A

battery tester at different rates ($1C = 175 \text{ mA g}^{-1}$) within the voltage range of 1-2.5 V. The electrolyte was 1M LiPF_6 in a 1:1:1 (w/w) mixture solution of ethyl carbonate (EC), ethyl methyl carbonate (EMC) and dimethyl carbonate (DMC). Working electrodes (around 1 mg/cm^2 in loading) were prepared by mixed LTO, carbon black and polyvinylidene fluoride (PVDF) in a weight ratio of 7:2:1, with N-methyl pyrrolidinone as the dispersant, on a copper foil and dried at 60°C for 24 h. CV and electrochemical impedance spectroscopy (EIS, frequency 100 kHz to 10 MHz) were carried on a CHI660D electrochemical workstation.

Data availability

All data that support the findings of this study are included in the article and its Supplementary Information file.

Acknowledgments

We are grateful for the financial support from the Australia Research Council Discovery Projects DP170103721 and DP180102003, the National Key R&D Program of China (2016YFB0700600), the Chemistry and Chemical Engineering Guangdong Laboratory (Grant No.1922018), and the Shenzhen Science and Technology Research Grant (No. JCYJ20200109140416788).

Author contributions

Z.S. and S.Z. conceived the idea for this project. Z.S. prepared the materials and conducted the materials characterization and electrochemical experiments. M.L., S.L. and F.P. performed the DFT calculations. L.M., T.Z. and J.L. conducted the in-situ XANES measurements. S.Q. assisted with the presentation of artworks. C.D. assisted with the XRD analysis. Z.S. and S.L. drafted the manuscript, with advice from J.L., F.P. and S.Z. All the authors discussed the results, analyzed the data and edited the paper.

Competing interests

An Australian Patent No 2019903786 has been Approved and Authorized.

An international patent No PCT AU2020 051080 has been filed

Additional information

Supplementary information is available for this paper.

Reference

1. Tuller, H. L., Bishop, S. R. Point defects in oxides: tailoring materials through defect engineering. *Annu. Rev. Mater. Res.* **41**, 369-398 (2011).
2. Li, X., Lu, K. Playing with defects in metals. *Nat. Mater.* **16**, 700-701 (2017).
3. Su, Z. *et al.* Defect engineering in titanium-based oxides for electrochemical energy storage devices. *Electrochem. Energy Rev.* **3**, 286-343 (2020).
4. Hallam, B. J. *et al.* Advanced bulk defect passivation for silicon solar cells. *IEEE J. Photovolt.* **4**, 88-95 (2013).
5. Ruiz-Morales, J. C. *et al.* Disruption of extended defects in solid oxide fuel cell anodes for methane oxidation. *Nature* **439**, 568-571 (2006).
6. Taylor, F. H., Buckeridge, J., Catlow, C. R. A. Defects and oxide ion migration in the solid oxide fuel cell cathode material LaFeO_3 . *Chem. Mater.* **28**, 8210-8220 (2016).
7. Zhang, Y. *et al.* Defect engineering on electrode materials for rechargeable batteries. *Adv. Mater.* **32**, 1905923 (2020).
8. Liu, H. *et al.* Defect Engineering of 2D Materials for Electrochemical Energy Storage. *Adv. Mater. Interfaces* **7**, 2000494 (2020).
9. Zhang, J.-N. *et al.* Trace doping of multiple elements enables stable battery cycling of LiCoO_2 at 4.6 V. *Nat. Energy* **4**, 594-603 (2019).
10. Liu, Q. *et al.* Approaching the capacity limit of lithium cobalt oxide in lithium ion batteries via lanthanum and aluminium doping. *Nat. Energy* **3**, 936-943 (2018).
11. Li, J. *et al.* Structural origin of the high-voltage instability of lithium cobalt oxide. *Nat. Nanotechnol.*, 1-7 (2021).
12. Prakash, A. *et al.* Solution-combustion synthesized nanocrystalline $\text{Li}_4\text{Ti}_5\text{O}_{12}$ as high-rate performance Li-ion battery anode. *Chem. Mater.* **22**, 2857-2863 (2010).
13. Wagemaker, M., van Eck, E. R., Kentgens, A. P., Mulder, F. M. Li-ion diffusion in the equilibrium nanomorphology of spinel $\text{Li}_{4+x}\text{Ti}_5\text{O}_{12}$. *J. Phys. Chem. B* **113**, 224-230 (2009).
14. Liu, J., Song, K., van Aken, P. A., Maier, J., Yu, Y. Self-supported $\text{Li}_4\text{Ti}_5\text{O}_{12}$ -C nanotube arrays as high-rate and long-life anode materials for flexible Li-ion batteries. *Nano Lett.* **14**, 2597-2603 (2014).
15. Verde, M. G. *et al.* Elucidating the phase transformation of $\text{Li}_4\text{Ti}_5\text{O}_{12}$ lithiation at the nanoscale. *ACS Nano* **10**, 4312-4321 (2016).
16. Wang, F. *et al.* Excess lithium storage and charge compensation in nanoscale $\text{Li}_{4+x}\text{Ti}_5\text{O}_{12}$. *Nanotechnology* **24**,

- 424006 (2013).
17. Zhen, C. *et al.* Nonstoichiometric rutile TiO₂ photoelectrodes for improved photoelectrochemical water splitting. *Chem. Commun.* **49**, 6191-6193 (2013).
 18. Smart, L. E., Moore, E. A. *Solid state chemistry: an introduction*. CRC press (2016).
 19. Pan, X., Yang, M.-Q., Fu, X., Zhang, N., Xu, Y.-J. Defective TiO₂ with oxygen vacancies: synthesis, properties and photocatalytic applications. *Nanoscale* **5**, 3601-3614 (2013).
 20. Thomas, A. *et al.* Comparison of the electronic structure of anatase and rutile TiO₂ single-crystal surfaces using resonant photoemission and x-ray absorption spectroscopy. *Phys. Rev. B* **75**, 035105 (2007).
 21. Wu, Q., Zheng, Q., van de Krol, R. Creating oxygen vacancies as a novel strategy to form tetrahedrally coordinated Ti⁴⁺ in Fe/TiO₂ nanoparticles. *J. Phys. Chem. C* **116**, 7219-7226 (2012).
 22. Ou, G. *et al.* Tuning defects in oxides at room temperature by lithium reduction. *Nat. Commun.* **9**, 1-9 (2018).
 23. Xu, C., Zhang, P., Yan, L. Blue shift of Raman peak from coated TiO₂ nanoparticles. *J. Raman Spectrosc.* **32**, 862-865 (2001).
 24. Fang, W. *et al.* Facile preparation of Li₄Ti₅O₁₂/AB/MWCNTs composite with high-rate performance for lithium ion battery. *Electrochim. Acta* **94**, 294-299 (2013).
 25. Chiu, H. C. *et al.* Capacity fade mechanism of Li₄Ti₅O₁₂ nanosheet anode. *Adv. Energy Mater.* **7**, 1601825 (2017).
 26. Kim, J. *et al.* Single-layer graphene-wrapped Li₄Ti₅O₁₂ anode with superior lithium storage capability. *Carbon* **114**, 275-283 (2017).
 27. Shen, L., Zhang, X., Uchaker, E., Yuan, C., Cao, G. Li₄Ti₅O₁₂ nanoparticles embedded in a mesoporous carbon matrix as a superior anode material for high rate lithium ion batteries. *Adv. Energy Mater.* **2**, 691-698 (2012).
 28. Zhang, Q. *et al.* W⁶⁺ & Br⁻ codoped Li₄Ti₅O₁₂ anode with super rate performance for Li-ion batteries. *J. Mater. Chem. A* **3**, 13706-13716 (2015).
 29. Rahman, M. M., Wang, J. Z., Hassan, M. F., Wexler, D., Liu, H. K. Amorphous carbon coated high grain boundary density dual phase Li₄Ti₅O₁₂-TiO₂: A nanocomposite anode material for Li-ion batteries. *Adv. Energy Mater.* **1**, 212-220 (2011).
 30. Zhao, L., Hu, Y. S., Li, H., Wang, Z., Chen, L. Porous Li₄Ti₅O₁₂ coated with N-doped carbon from ionic liquids for Li-ion batteries. *Adv. Mater.* **23**, 1385-1388 (2011).
 31. Wang, C. *et al.* Combining fast Li-ion battery cycling with large volumetric energy density: grain boundary induced high electronic and ionic conductivity in Li₄Ti₅O₁₂ spheres of densely packed nanocrystallites. *Chem. Mater.* **27**, 5647-5656 (2015).
 32. Yu, L., Wu, H. B., Lou, X. W. Mesoporous Li₄Ti₅O₁₂ hollow spheres with enhanced lithium storage capability. *Adv. Mater.* **25**, 2296-2300 (2013).
 33. Jehl, B., Bauer, R., Dörge, A., Rick, R. The use of propane/isopentane mixtures for rapid freezing of biological specimens. *J. Microsc.* **123**, 307-309 (1981).
 34. Kresse, G., Furthmüller, J. Efficiency of ab-initio total energy calculations for metals and semiconductors using a plane-wave basis set. *Comp. Mater. Sci.* **6**, 15-50 (1996).
 35. Kresse, G., Furthmüller, J. Efficient iterative schemes for ab initio total-energy calculations using a plane-wave basis set. *Phys. Rev. B* **54**, 11169 (1996).
 36. Kresse, G., Joubert, D. From ultrasoft pseudopotentials to the projector augmented-wave method. *Phys. Rev. B* **59**, 1758 (1999).
 37. Perdew, J. P., Ernzerhof, M., Burke, K. Rationale for mixing exact exchange with density functional approximations. *J. Chem. Phys.* **105**, 9982-9985 (1996).
 38. Dudarev, S., Botton, G., Savrasov, S., Humphreys, C., Sutton, A. Electron-energy-loss spectra and the structural stability of nickel oxide: An LSDA+ U study. *Phys. Rev. B* **57**, 1505 (1998).

39. Morgan, B. J., Watson, G. W. A DFT+ U description of oxygen vacancies at the TiO_2 rutile (1 1 0) surface. *Surf. Sci.* **601**, 5034-5041 (2007).
40. Monkhorst, H. J., Pack, J. D. Special points for Brillouin-zone integrations. *Phys. Rev. B* **13**, 5188 (1976).

Supporting information

Outperforming the capacity limit of lithium titanate anode via quenching-induced oxygen vacancies and cation redistribution

Zhong Su¹, Meng Li^{1,2}, Shunning Li², Lu Ma³, Shangshu Qian¹, Tao Zhang³, Cheng Dong², Jun Lu³✉, Feng Pan²✉, Shanqing Zhang¹✉

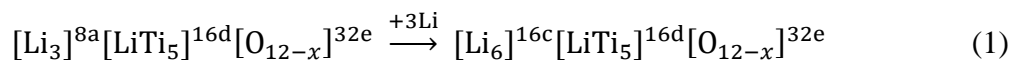
¹ Centre for Clean Environment and Energy, School of Environment and Science, Griffith University, Gold Coast Campus, Gold Coast, Queensland 4222, Australia. ² School of Advanced Materials, Peking University, Shenzhen Graduate School, Shenzhen, 518055, China. ³ Chemical Sciences and Engineering Division, Argonne National Laboratory, Lemont, IL, USA.

✉ e-mail: junlu@anl.gov; panfeng@pkusz.edu.cn; s.zhang@griffith.edu.au.

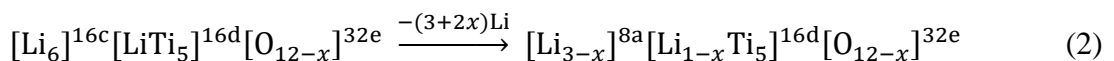
Reactions on charge and discharge

The discharged product of LTO anodes is assumed to be the rocksalt phase, in which all the 16d and 16c sites are occupied by cations. For defective LTO anodes, the charged product is in spinel structure with some of the Li ions at 8a and 16d sites deintercalated until all the Ti ions are oxidized to +4 state. We have performed DFT calculations to identify the energetically favorable configuration at the delithiated limit, as shown in Supplementary Fig. 2. It turns out that Li ions in the vicinity of V_O are more likely to be deintercalated, indicating simultaneous extraction of Li at both 8a and 16d sites, while in a Li/Ti redistributed structure without V_O , delithiation at 16d sites will occur prior to that at 8a sites. Accordingly, the reactions on charge and discharge of **LTO with V_O** are as follows:

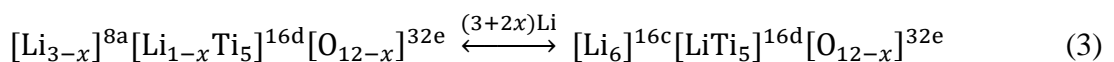
1st discharge



1st charge



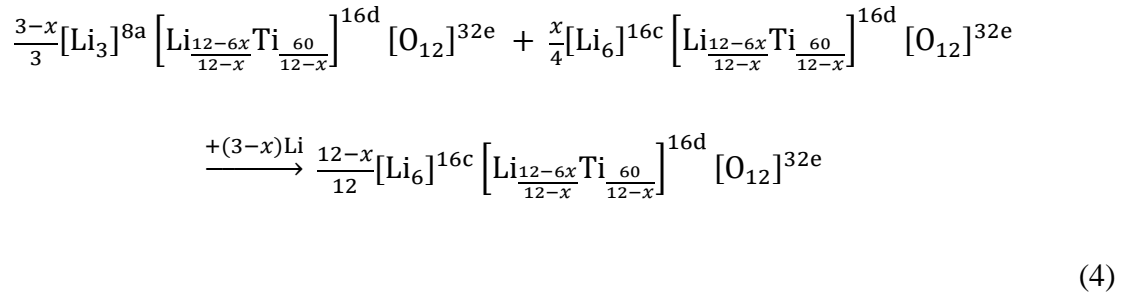
Subsequent cycles



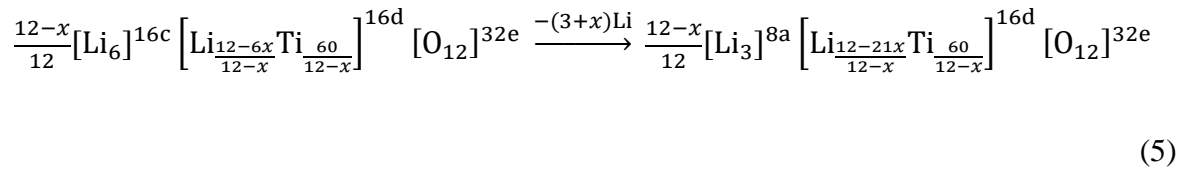
The capacity is increased from 3 Li/f.u. to $3+2x$ Li/f.u.

During Li/Ti redistribution in LTO, $[Li_3]^{8a}[LiTi_5]^{16d}[O_{12-x}]^{32e}$ per f.u. is transformed into $\frac{3-x}{3}[Li_3]^{8a}\left[Li_{\frac{12-6x}{12-x}}Ti_{\frac{60}{12-x}}\right]^{16d}[O_{12}]^{32e} + \frac{x}{4}[Li_6]^{16c}\left[Li_{\frac{12-6x}{12-x}}Ti_{\frac{60}{12-x}}\right]^{16d}[O_{12}]^{32e}$, which is the initial state for discharge. In this context, the electrochemical reactions in **Li/Ti redistributed LTO** can be summarized as follows:

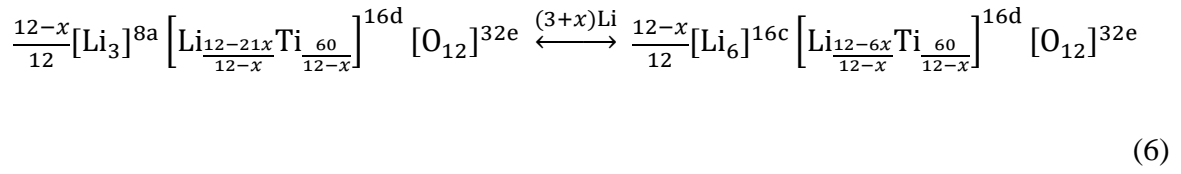
1st discharge



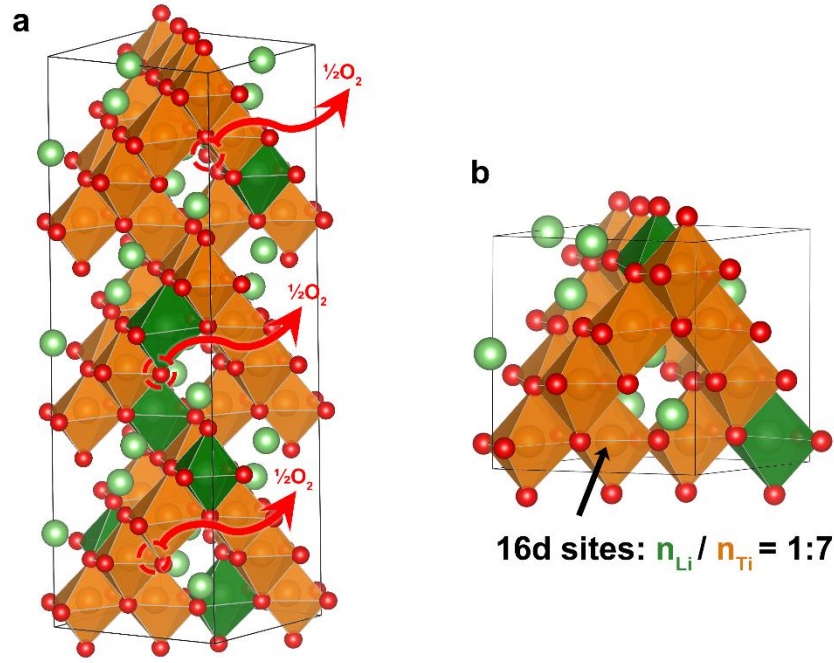
1st charge



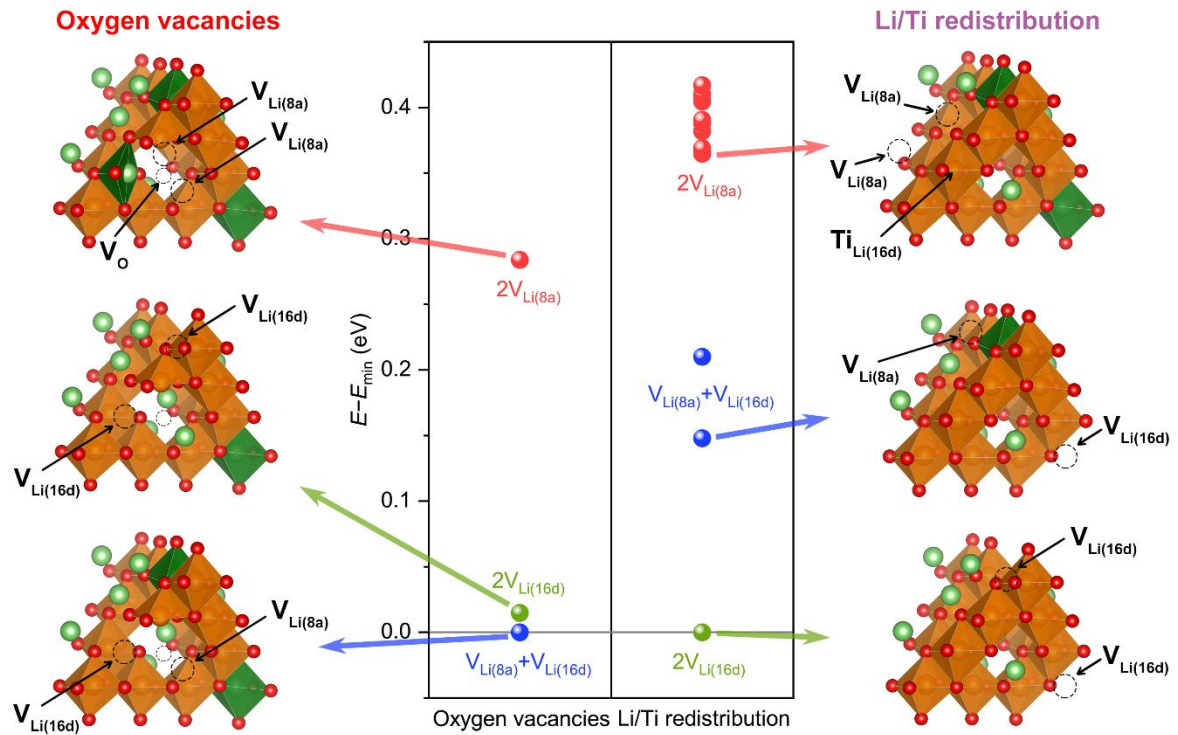
Subsequent cycles



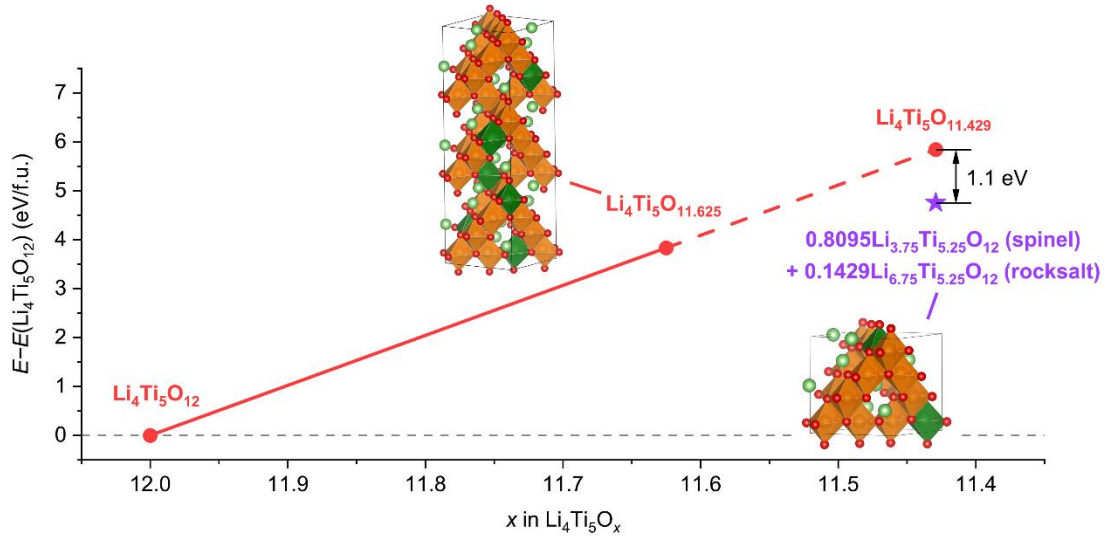
The capacity is increased from 3 Li/f.u. to 3+x Li/f.u.



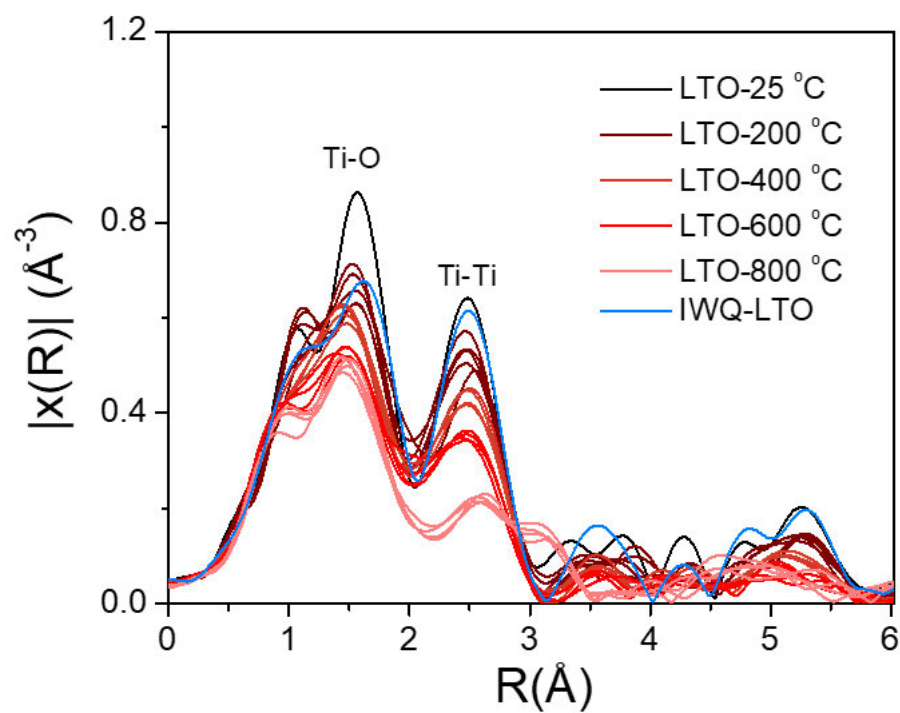
Supplementary Fig. 1 | Simulation cells constructed for DFT calculations. a, Supercell with 8 formula units containing 3 V_{O} , corresponding to a composition of $\text{Li}_4\text{Ti}_5\text{O}_{11.625}$. **b,** Unit cell of $\text{Li}_{10}\text{Ti}_{14}\text{O}_{32}$ with Li/Ti ratio of 1:7 at 16d sites, corresponding to $[\text{Li}_3]^{8a}[\text{Li}_{0.75}\text{Ti}_{5.25}]^{16d}[\text{O}_{12}]^{32e}$. In comparison, the structure of pristine LTO is $[\text{Li}_3]^{8a}[\text{Li}_1\text{Ti}_5]^{16d}[\text{O}_{12}]^{32e}$.



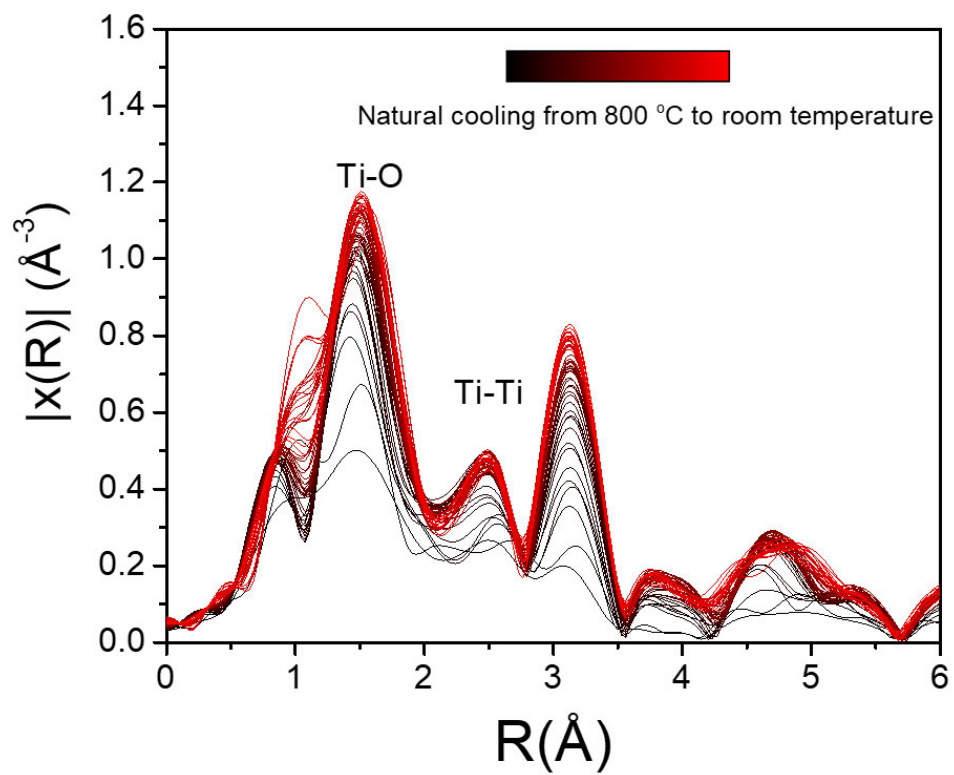
Supplementary Fig. 2 | DFT total energies of different configurations at the delithiated limit as referenced to the lowest-energy configuration. The delithiated product of LTO containing V_o is $[Li_{13-x}]^{8a}[Li_{1-x}Ti_5]^{16d}[O_{12-x}]^{32e}$, while the delithiated product with Li/Ti redistribution is $[Li_3]^{8a}[Li_{(12-21x)/(12-x)}Ti_{60/(12-x)}]^{16d}[O_{12}]^{32e}$.



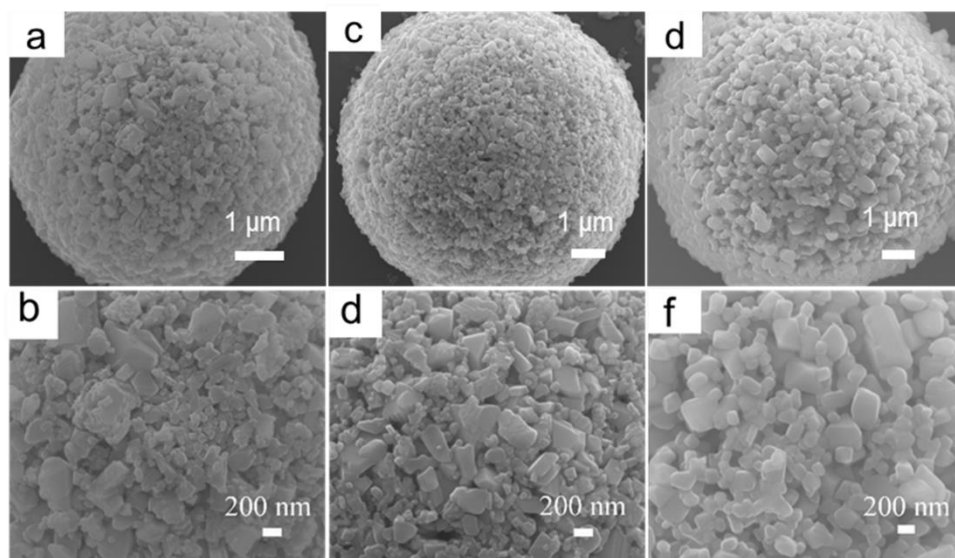
Supplementary Fig. 3 | Energy difference between the configuration with V_O and the configuration after Li/Ti redistribution while maintaining the same composition. Assuming that the energy of oxygen-deficient LTO is linearly correlated with the concentration of V_O at dilute levels, the energy of $\text{Li}_4\text{Ti}_5\text{O}_{11.429}$ can be obtained by extrapolation from the composition of $\text{Li}_4\text{Ti}_5\text{O}_{11.625}$, the structure of which was constructed and shown in Supplementary Fig. 1a. According to Equation 1 in the manuscript, one formula unit of $\text{Li}_4\text{Ti}_5\text{O}_{11.429}$ will be transformed into $0.8095\text{Li}_{3.75}\text{Ti}_{5.25}\text{O}_{12} + 0.1429\text{Li}_{6.75}\text{Ti}_{5.25}\text{O}_{12}$ after Li/Ti redistribution, the energy of which was derived by summing up the contributions from both spinel and rocksalt phases based on the simulation cell of $[\text{Li}_3]^{8a}[\text{Li}_{0.75}\text{Ti}_{5.25}]^{16d}[\text{O}_{12}]^{32e}$ shown in Supplementary Fig. 1b.



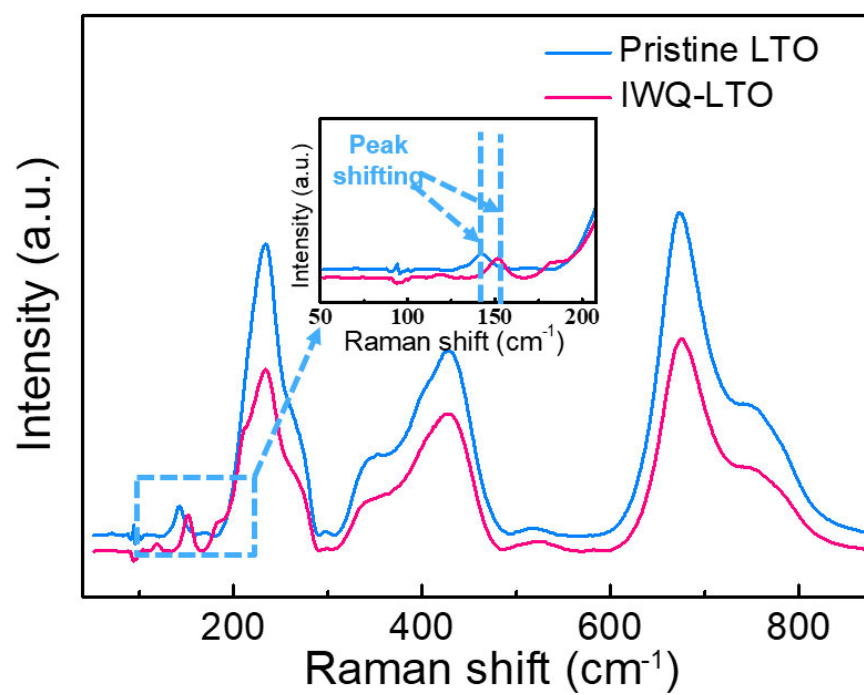
Supplementary Fig. 4 | In-situ extended XAFS spectra of LTO at different temperatures from 25 °C to 800 °C.



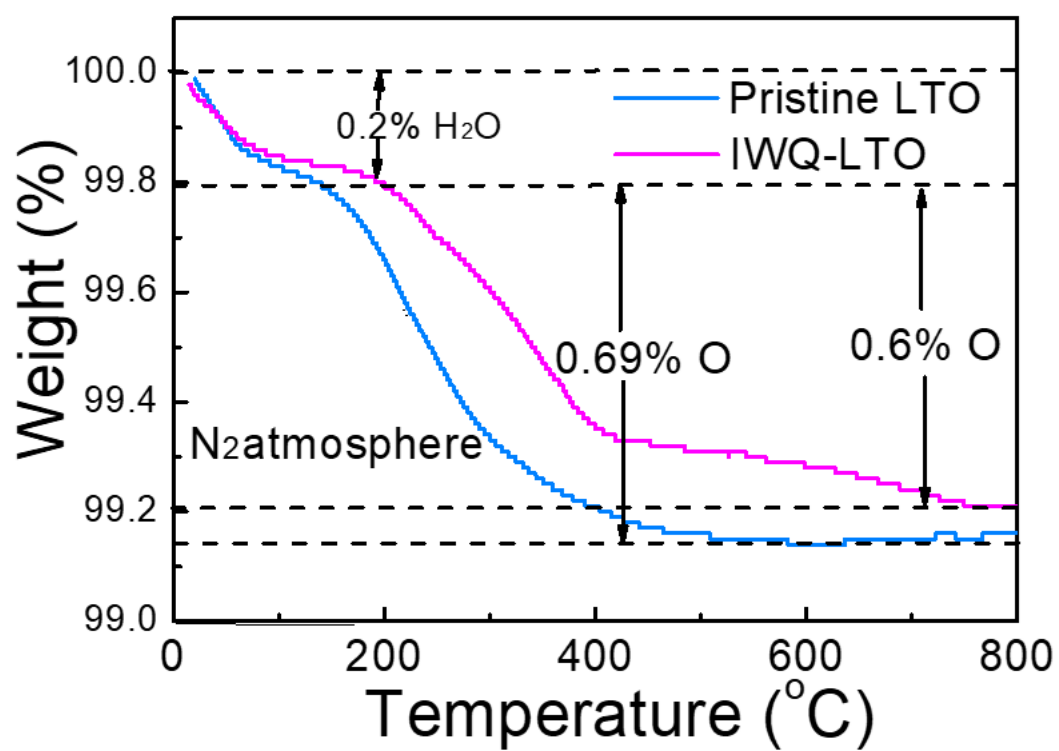
Supplementary Fig. 5 | In-situ extended XAFS spectra of LTO during natural cooling.



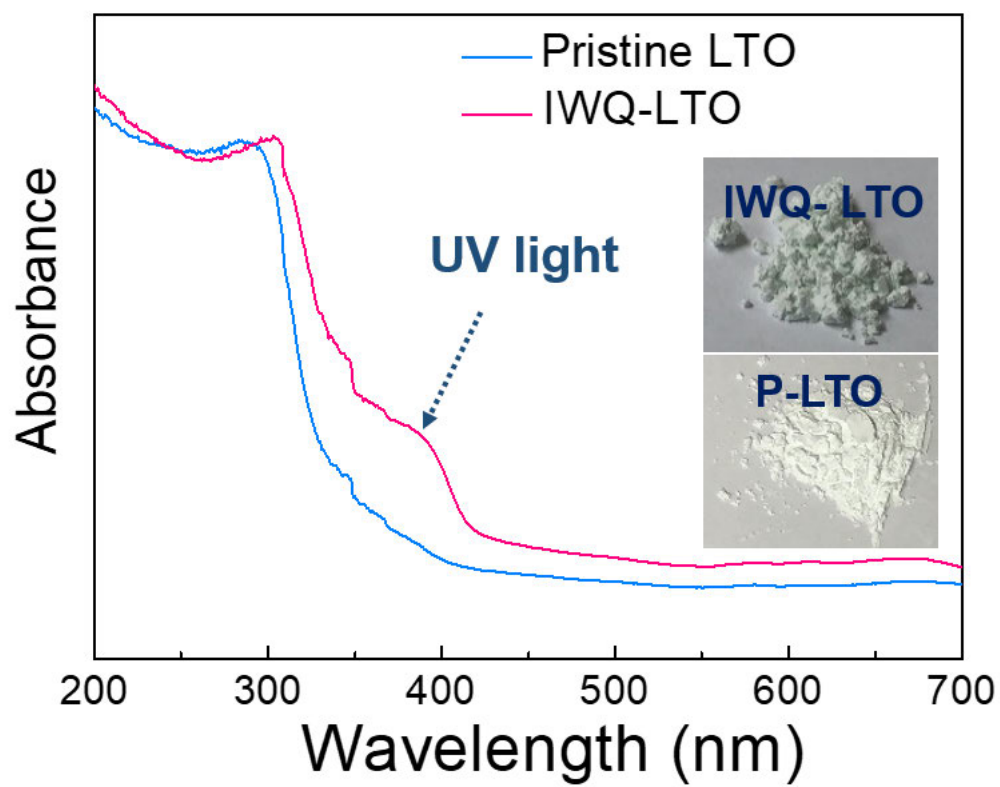
Supplementary Fig. 6 | SEM images. a,b, Pristine LTO. **c,d**, LTO naturally cooled down from 800 °C. **e,f**, IWQ-LTO.



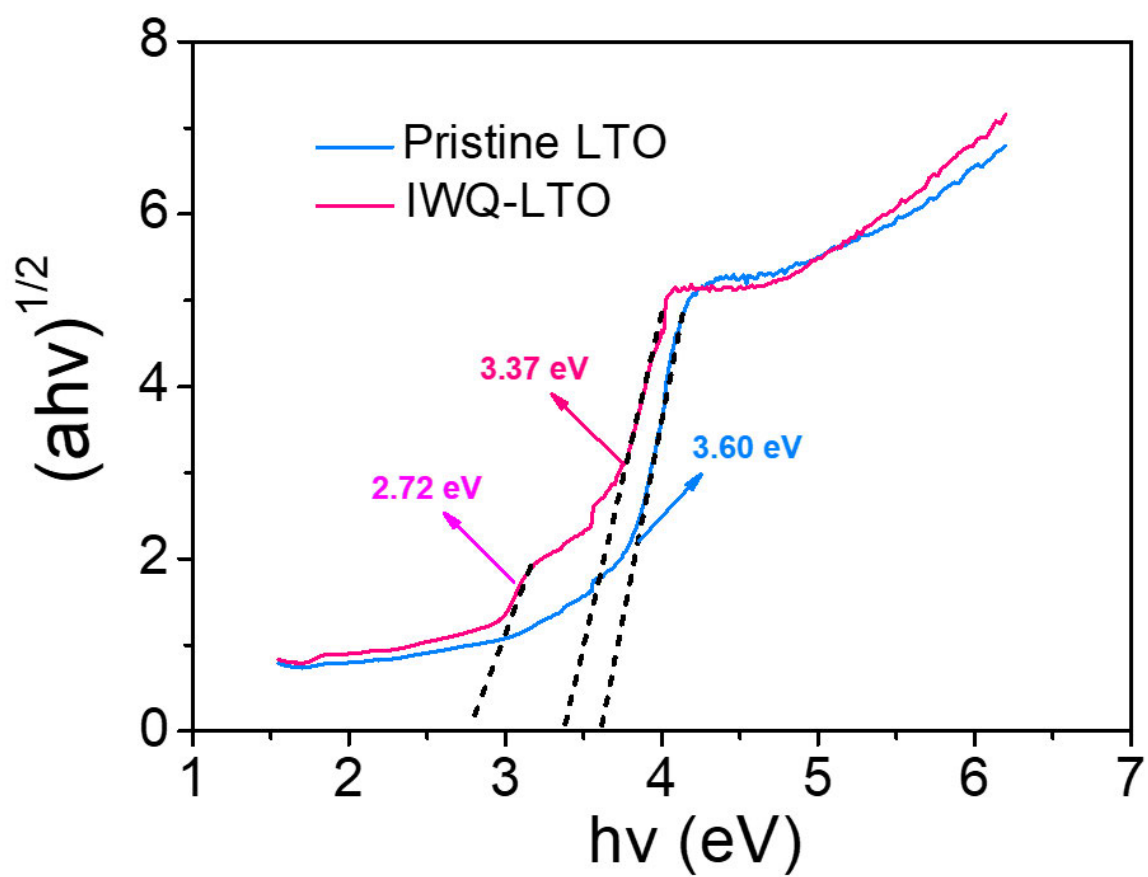
Supplementary Fig. 7 | Raman spectra of IWQ-LTO and pristine LTO.



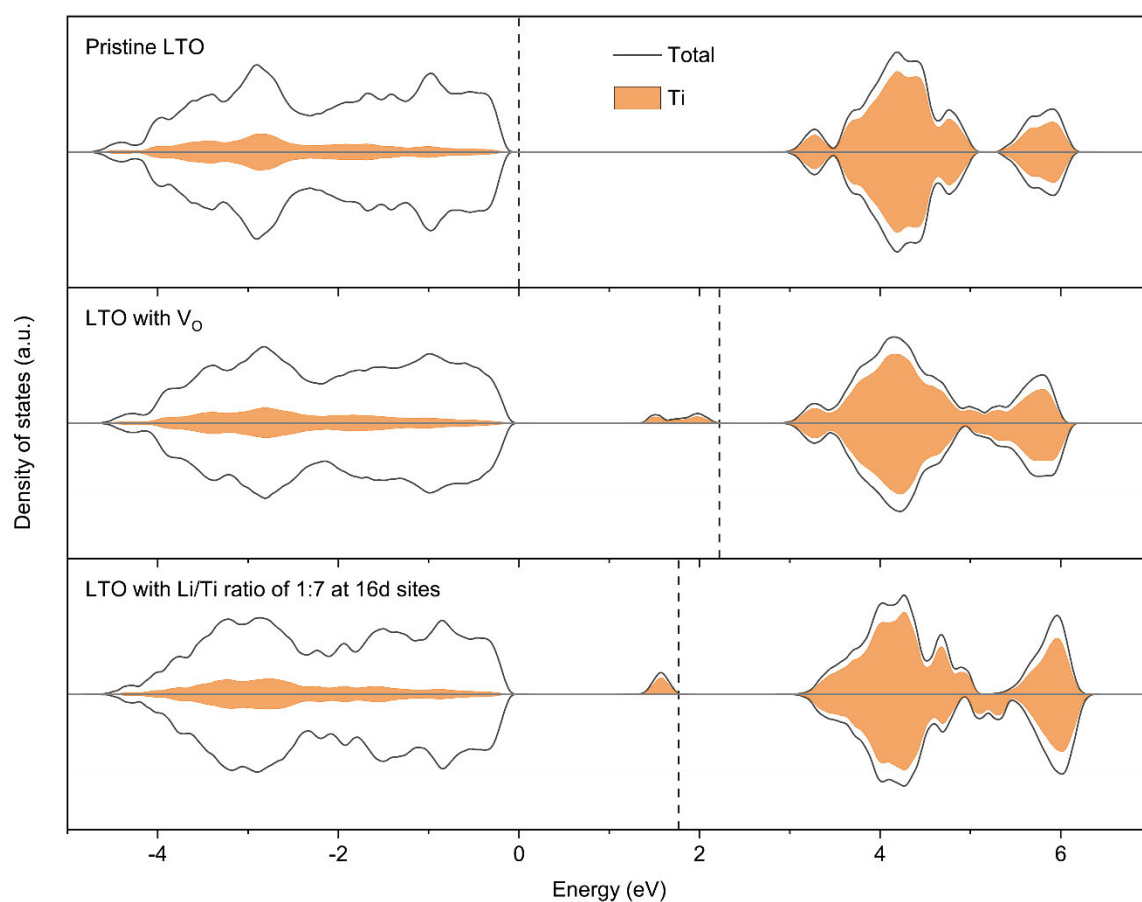
Supplementary Fig. 8 | TGA curve of IWQ-LTO and pristine LTO at N₂ atmosphere.



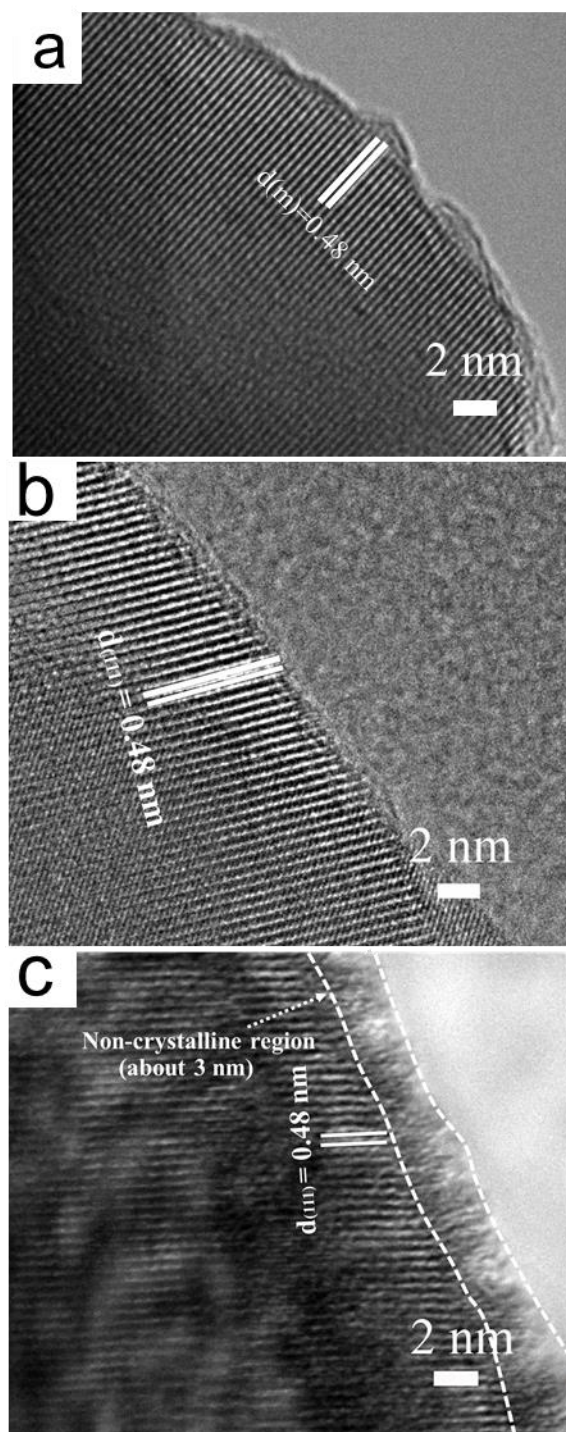
Supplementary Fig. 9 | UV-Vis absorption spectra and photographs of IWQ-LTO and pristine LTO.



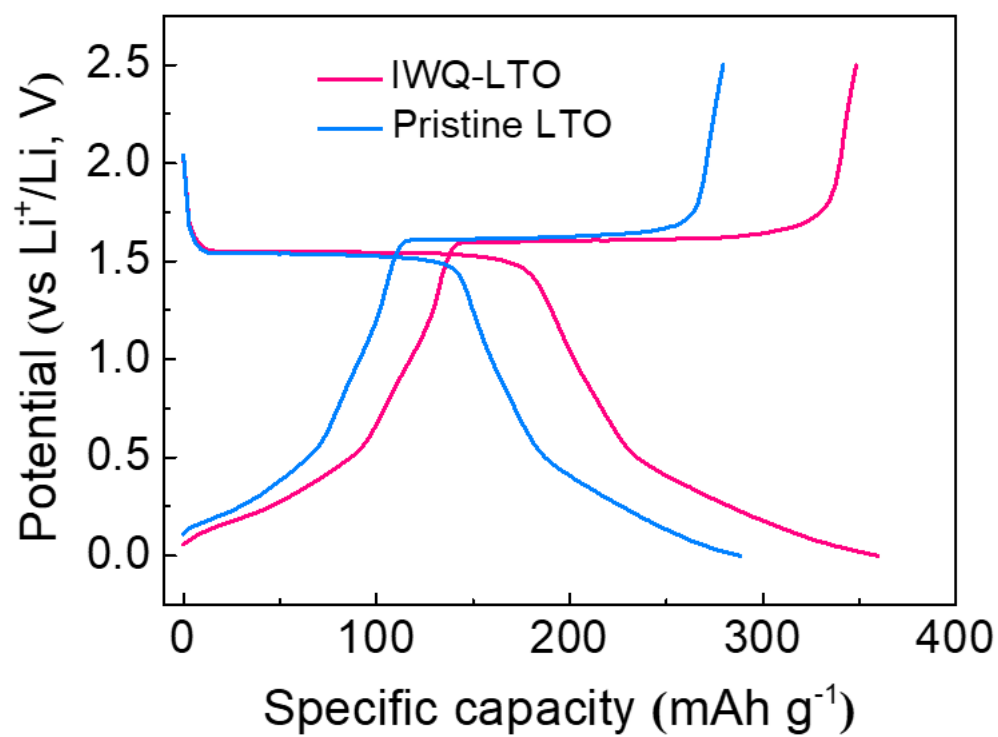
Supplementary Fig. 10 | Optical energy band gaps of IWQ-LTO and pristine LTO.



Supplementary Fig. 11 | Electronic density of states for pristine LTO, $\text{Li}_4\text{Ti}_5\text{O}_{11.625}$ with V_O and $\text{Li}_{3.75}\text{Ti}_{5.25}\text{O}_{12}$ with Li/Ti ratio of 1:7 at 16d sites. Energies are aligned according to the core level of O atoms and referenced to the valence band maximum of pristine LTO. Fermi level is indicated by a dash line.



Supplementary Fig. 12 | TEM images near the surface. a, Pristine LTO. **b,** Naturally-cooled LTO. **c,** IWQ-LTO.

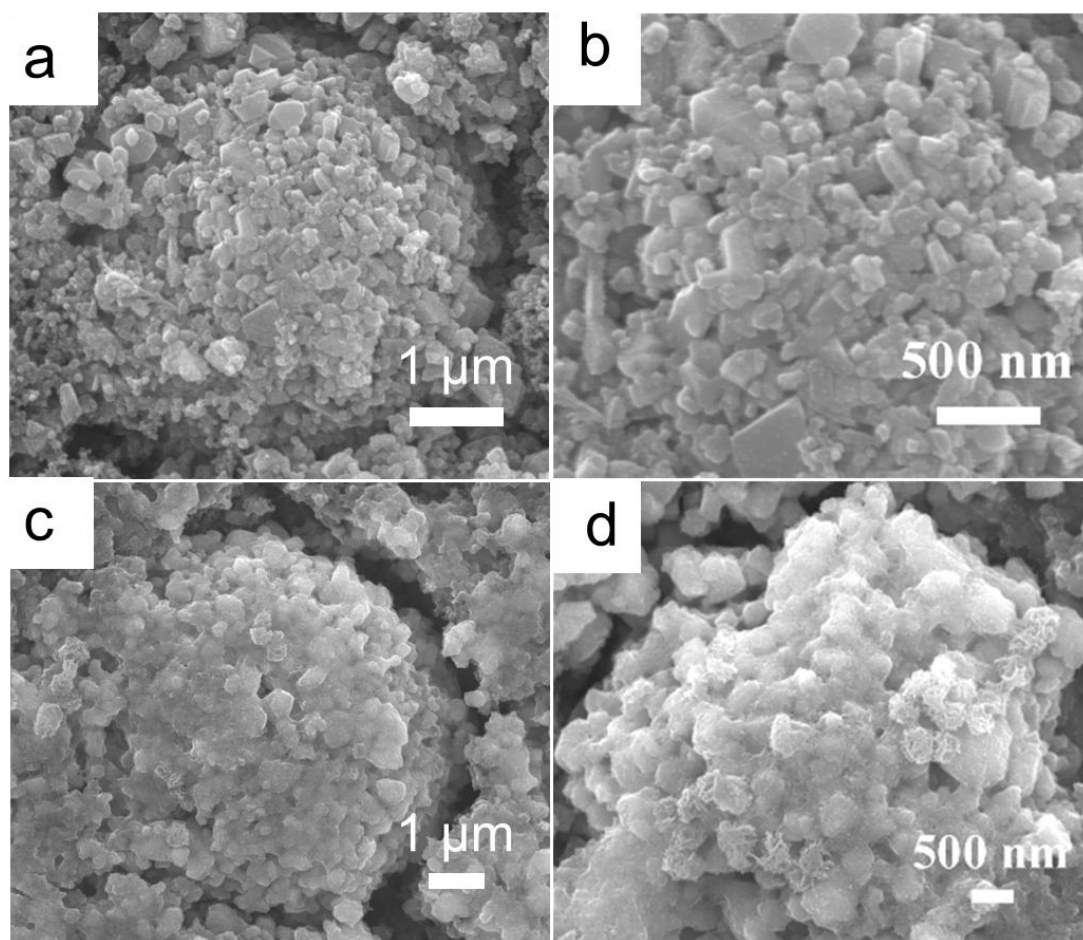


Supplementary Fig. 13 | Voltage profiles of IWQ-LTO and pristine LTO in the 0–2.5 V range at 1C.

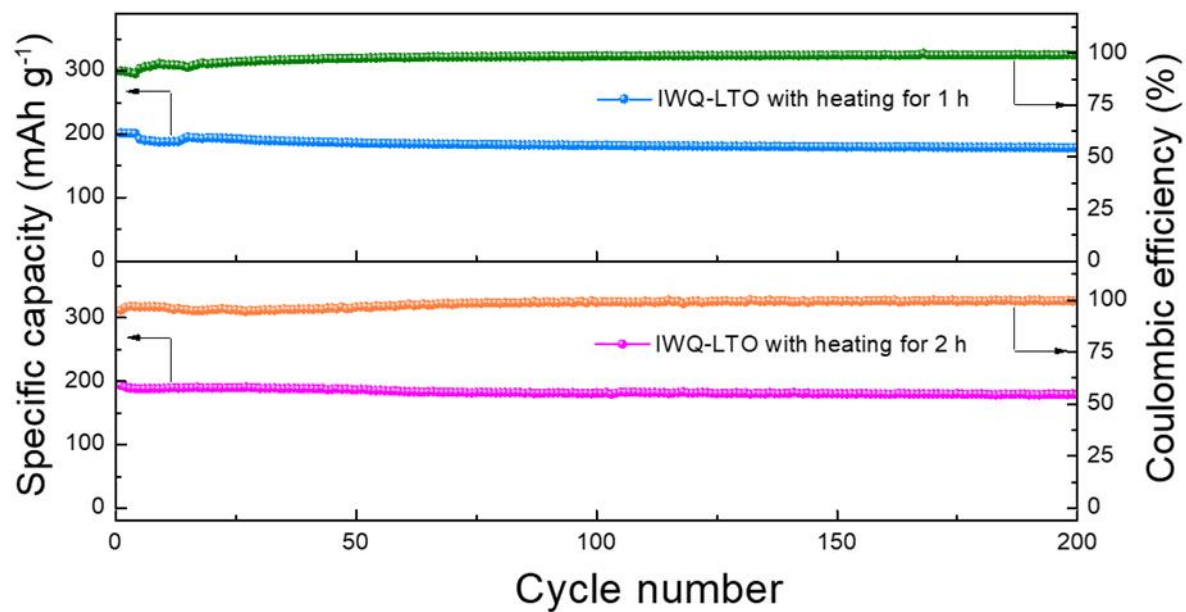
Supplementary Table 1 | Comparison of the capacity of IWQ-LTO electrode to those of previously reported LTO-based anodes shown in Fig. 4c in the manuscript.

LTO-based anodes	Compositions (AM:CC:BI) [#]	Loading density (mg cm ⁻²)	Capacity at 1C (mAh g ⁻¹)	Capacity at 10C (mAh g ⁻¹)
This work	70:20:10	1.0	202	176
LTO/carbon nanotube	100:0:0	0.42	165	154
LTO/graphene	80:10:10	1.5	175	150
Nanosized LTO/carbon	90:02:08	--	170	149
W-Br-codoped LTO	80:10:10	--	160	140
LTO/TiO ₂ /carbon	80:10:10	--	162	135
LTO/N-doped carbon	80:10:10	--	160	129
LTO/carbon nanocomposite	80:10:10	1.5	148	121
LTO hollow spheres	70:20:10	--	170	115

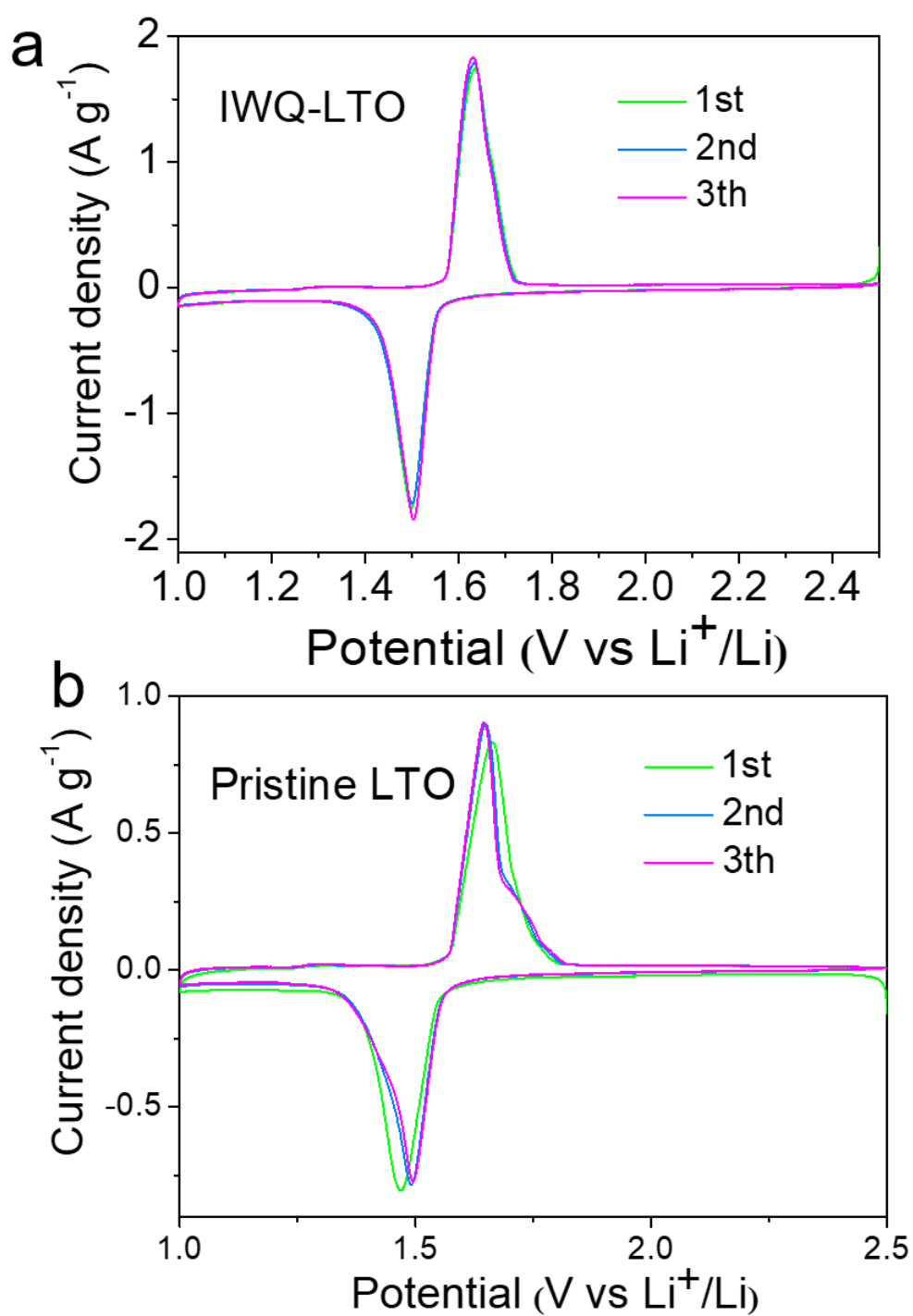
[#] AM: active materials; CC: conductive carbon; BI: binder.



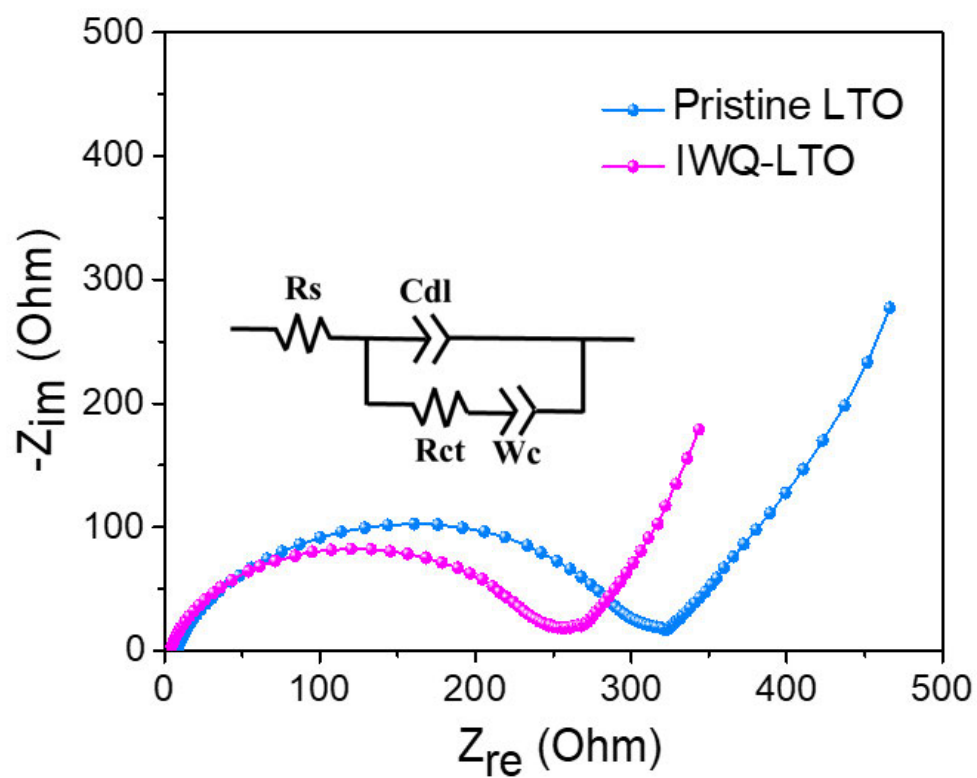
Supplementary Fig. 14 | SEM images of pristine LTO and IWQ-LTO after 300 cycles. a,b, Pristine LTO. c,d, IWQ-LTO.



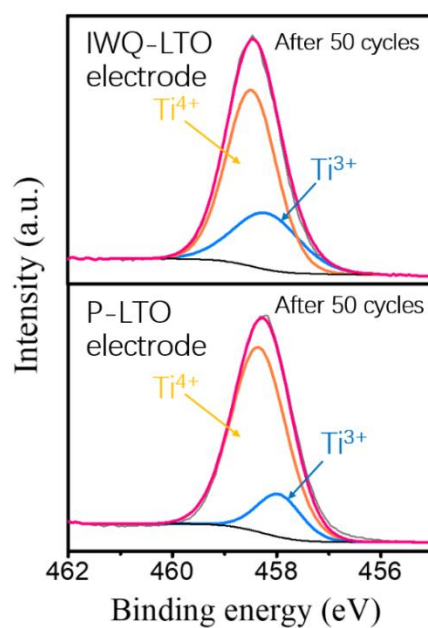
Supplementary Fig. 15 | Long-term cycling performance (current rate: 5C) of IWQ-LTO with different heating durations. In the preparation of IWQ-LTO, the samples were heated at 800 °C for 1 h or 2 h.



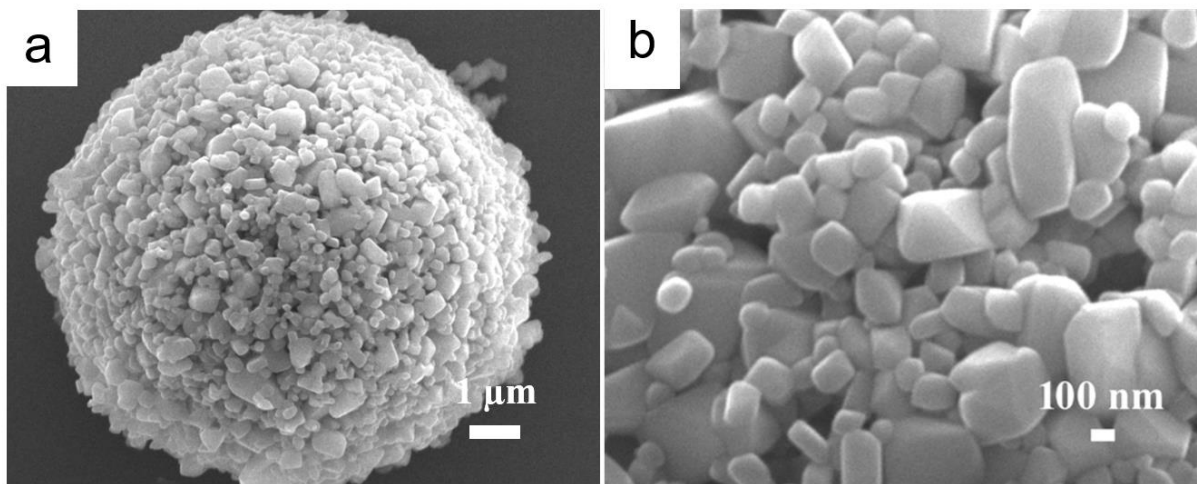
Supplementary Fig. 16 | CV curves at the rate of 0.1 mV S^{-1} . a, IWQ-LTO. b, Pristine LTO.



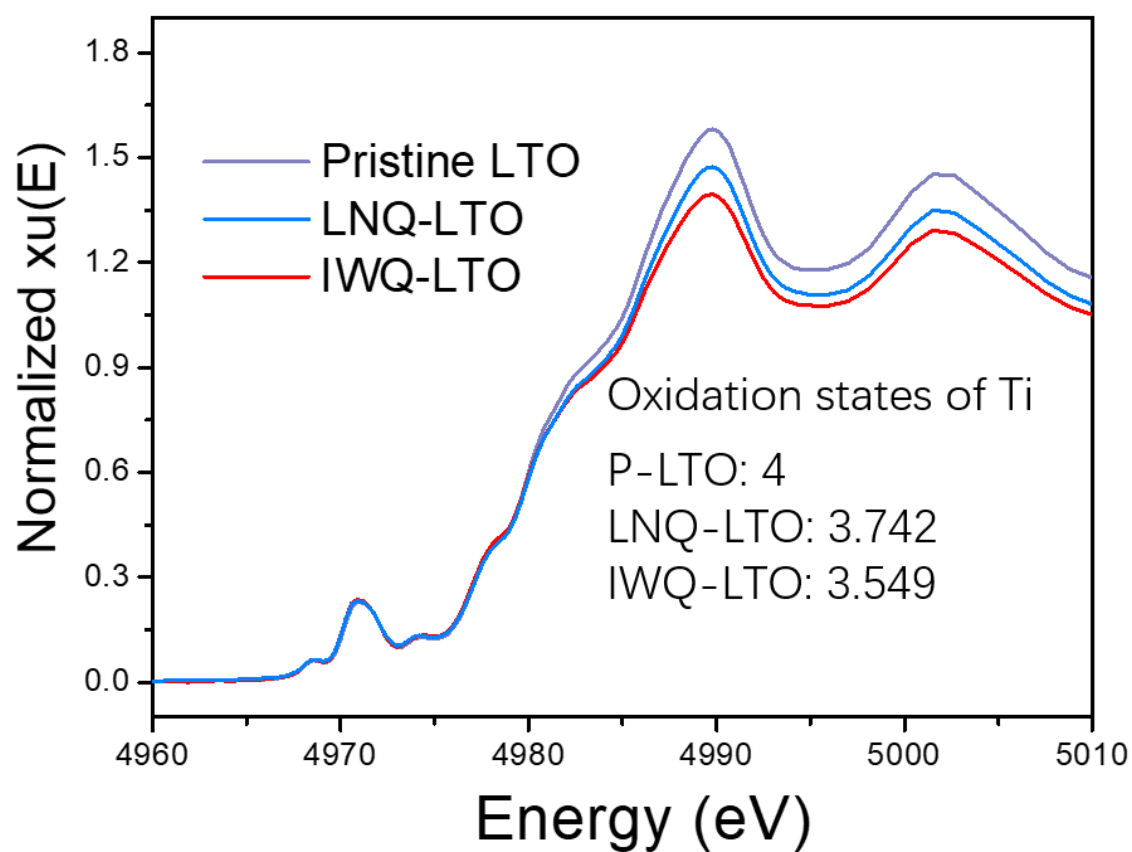
Supplementary Fig. 17 | The Nyquist plots of IWQ-LTO and pristine LTO.



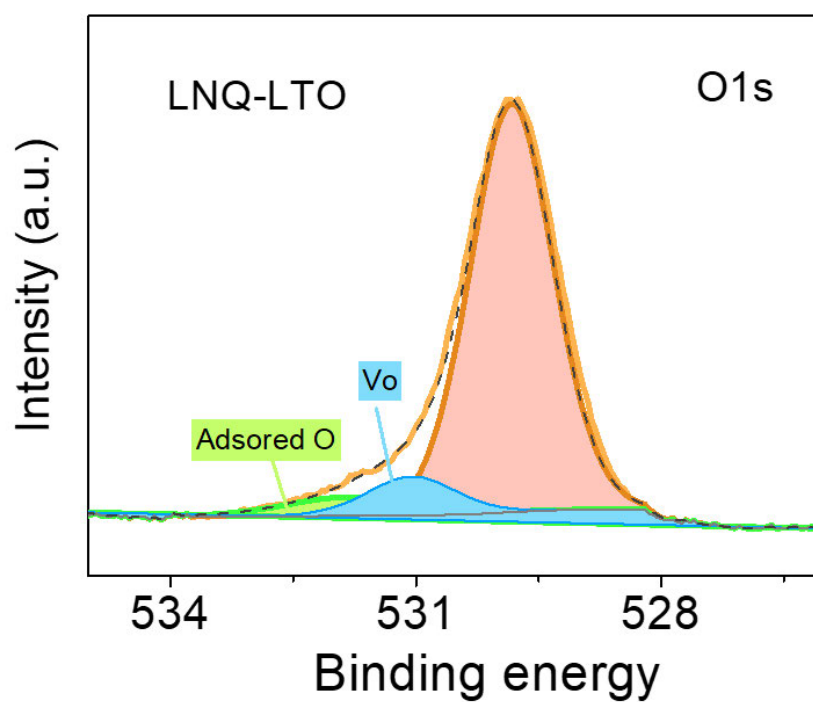
Supplementary Fig. 18 | XPS Ti 2p spectra of IWQ-LTO electrode (top) and pristine LTO electrode (bottom) at rate of 5 C after 50 cycles.



Supplementary Fig. 19 | SEM images of LNQ-LTO.



Supplementary Fig. 20 | XANES spectra of LNQ-LTO, IWQ-LTO and pristine LTO.



Supplementary Fig. 21 | XPS O 1s spectra of LNQ-LTO.

CHAPTER 4

TUNING DEFECTS IN METAL OXIDES VIA REDOX REACTION FOR LITHIUM ION BATTERY

To be Submitted to *Nature Communications* (2021)

4.1. INTRODUCTORY REMARKS

This chapter is written in an article form for submission to *Nature Communications* in 2021.

The article shows a universal defect preparation method through a simple redox reaction at room temperature. N-Butyllithium, as a powerful reducing agent and nucleophile, is selected in this system to deprive oxygen atoms from oxides, and a series of defective oxides including LTO, TiO₂, SnO₂, CeO₂, Sb₂O₅, and Nb₂O₅ were prepared. Spontaneous redox reaction at room temperature avoids complicated operations and rigorous conditions and is a breakthrough innovation in terms of the preparation of defective oxides. More importantly, such a simple redox reaction of soaking in n-BuLi solution realizes the control of defect concentration by adjusting the reaction time. Here, we take defective LTO as a representative to test electrochemical performance at low temperature. A highly reversible specific discharge capacity of 109.9 mAh g⁻¹ can be obtained at a rate of 10 C after 200 cycles even at -10 °C. Such excellent performance can be attributed to the improvement of defect-induced intrinsic properties for enhancing the kinetic behavior of Li⁺ charge storage.

4.2 STATEMENT OF CONTRIBUTION

This chapter includes one first-authored paper. The bibliographic details of the co-authored paper, including all authors, are:

Zhong Su, Meng Li, Shangshu Qian, Lu Ma, Tao Zhang, Chao Lai, Jun Lu, Shanqing Zhang*

Tuning defects in metal oxides via redox reaction for lithium ion battery

To be submitted to *Nature Communications*, 2021

My contribution to the paper included:

Conducting experiments, data collection and analysis, writing of manuscript.

(Signed) _____ (Date) 15/04/2021

Name of Student: Zhong Su

(Countersigned) _____ (Date) 15/04/2021

Corresponding author of paper: Shanqing Zhang

(Countersigned) _____ (Date) 15/04/2021

Supervisor: Shanqing Zhang

4.3. ARTICLE 3

Tuning defects in metal oxides via redox reaction for lithium ion battery

Zhong Su¹, Meng Li¹, Shangshu Qian¹, Lu Ma², Tao Zhang², Chao Lai¹, Jun Lu^{2*}, Shanqing Zhang^{1*}

¹ Centre for Clean Environment and Energy, School of Environment and Science, Griffith University, Gold Coast Campus, Gold Coast, Queensland 4222, Australia. ² Chemical Sciences and Engineering Division, Argonne National Laboratory, Lemont, IL, USA.

* e-mail: junlu@anl.gov; s.zhang@griffith.edu.au.

Abstract

Defects in metal oxides, especially oxygen vacancies (V_o), generate oxygen off-stoichiometry, which is a vital quantity regulating material behaviours, such as electronic and ionic conductivity, catalytic activity, dielectric and optical properties. Defect engineering is a complex technology and an effective strategy to optimize oxides' intrinsic properties used in applications such as lithium-ion batteries, catalytic membrane reactors, electrochemical supercapacitors, and electrochromic films. Here we employed a universal defect preparation strategy via a facile redox reaction at room temperature and obtained a series of defective oxides, including $\text{Li}_4\text{Ti}_5\text{O}_{12}$, TiO_2 , CeO_2 , SnO_2 , Sb_2O_5 , and Nb_2O_5 . Defect concentration in oxides can be easily controlled by adjusting soaking time. To further understand the influence of defects in enhancing electronic and ionic conductivity, $\text{Li}_4\text{Ti}_5\text{O}_{12}$ (LTO) with tuned defects was investigated, especially in low temperatures. A highly reversible discharge specific capacity of 109.9 mAh g^{-1} is obtained at the rate of 10 C in a severe environment of -10°C after 200 cycles, which is significantly better than that of the pristine LTO. Such excellent electrochemical performance at low temperatures can be attributed to the enhanced kinetic migration behaviour of electrons and ions. This simple, efficient, and universal defect introducing method is a major disruptive innovation in defect engineering development and has significantly contributed to a wide range of areas, such as energy storage, catalysis, sewage treatment, and so on.

Keywords: oxygen vacancies, metal oxides; N-butyllithium; low-temperature performance

Introduction

Within the constant attention towards defect engineering of metal oxides in the material science, defect-induced partial structural distortion typically produces charge imbalance and active region and eventually changes the intrinsic physical and chemical properties of metal oxides^{1, 2, 3}. Compared with metal cations, anionic oxygen is a typical volatile element that tends to leave its lattice sites forming vacancies⁴. In fact, oxygen vacancies (Vo) in the metal oxide have been extensively studied in a broad range of catalysts, water splitting, and energy storage. For instance, Wang et al. reported oxygen-deficient hematite with markedly improved photoelectrochemical (PEC) performance through reducing defect formation energy by calcined at high temperature in N₂ atmosphere⁵; Furthermore, a series of reducing agents such as H₂⁶, NaBH₄⁷, and metal-reducing agent⁸ were introduced to capture the oxygen atoms in the oxides forming structural defects while reducing the formation energy of defects at high temperature. Moreover, Vo in the oxides has been extensively confirmed by theoretical calculations and experimental characterizations^{9, 10}. However, it remains a challenge for the strategies mentioned above regarding controllable Vo formation in the oxide materials.

For oxygen vacancies, their formation mechanism should be mentioned first. According to the Schottky defect theory, vacancy concentration increases with temperature exponentially, especially near the crystal surface. High-temperature calcination is usually under a particular low oxygen partial pressure environment, promoting oxygen in the lattice structure to escape. Also, high-cost reducing agents are added in this heat treatment process to assist in removing lattice oxygen, further increasing the vacancy concentration in the oxides. However, once cooling down in contact with cold air or water, these newly generated Vo will partially be re-occupied by dissociated oxygen from outside, resulting in colour recovery. Considering the challenge of generation and preservation of Vo, controllable Vo concentration is still an unreachable region.

N-butyllithium (n-BuLi) is a conventional organolithium reagent, widely used as a polymerization initiator and a strong base in the synthesis of organic compounds¹¹. Also, n-BuLi is a powerful nucleophile and reductant¹², conveying unique advantages over other common reductants, such as H₂, NaBH₄, and metal lithium. Hence, a facile preparation method of Vo is presented through soaking in n-BuLi and rinsing in hexane, water, and ethanol for removing extra n-BuLi and reaction products. With the super reducibility of n-BuLi, complicated operations have been avoided, and a series of metal oxides were prepared with high concentration Vo, including Li₄Ti₅O₁₂ (LTO), TiO₂, SnO₂, Nb₂O₅, Sb₂O₅, and CeO₂. It is worth noting that Vo concentration can be manipulated by controlling the reaction time. Our previous research has shown that Vo can provide additional lithium storage sites and increasing reversible capacity. Thus, LTO with various Vo concentrations was employed as an anode to study further Vo's role in the charging and discharging process.

Results and discussion

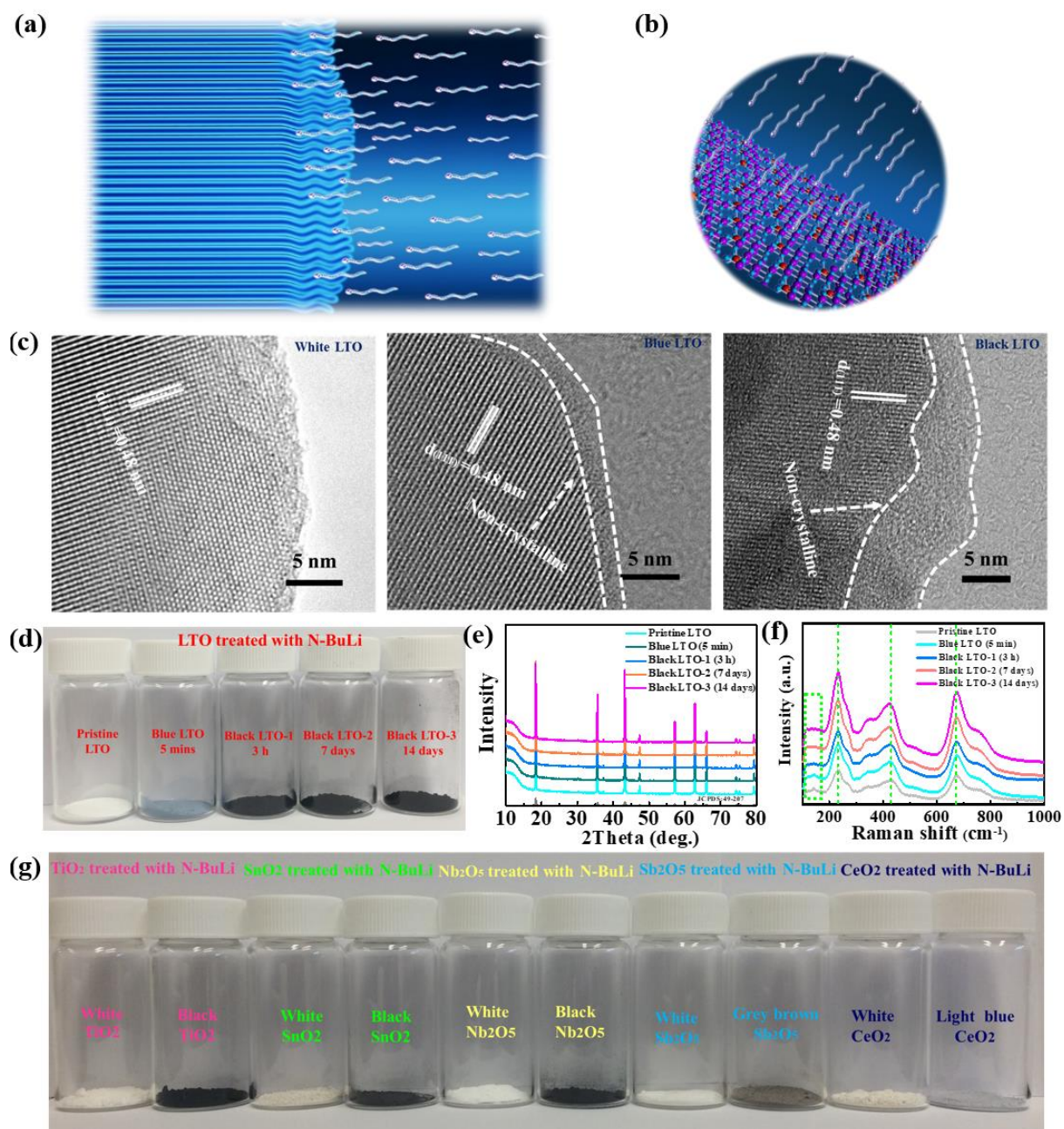
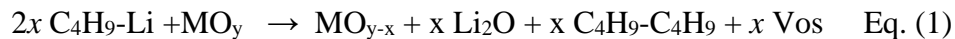


Fig. 1 (a-b) Reaction mechanism diagram of LTO with butyl lithium; (c) HRTEM images of $\text{Li}_4\text{Ti}_5\text{O}_{12}$; Pristine LTO (left); Blue LTO (middle); Black LTO-3 (14 days, right); (d) Photograph of pristine and n-BuLi reduced LTO; the XRD patterns (e) and Raman patterns (f) of the obtained LTO; (g) Photograph of n-BuLi reduced oxide nanoparticles, TiO_2 , SnO_2 , Nb_2O_5 , Sb_2O_5 , and CeO_2 , respectively.

The formation mechanism of Vo is shown in Fig. 1a and 1b. A series of oxides are immersed in a solution of n-butyl lithium, conducting redox reactions with oxides and gradually depriving oxygen atoms from the surface layer to the inside based on the formula of Eq. (1)



As a robust reducing agent and nucleophile, n-BuLi can react with many metal oxides at room temperature, including $\text{Li}_4\text{Ti}_5\text{O}_{12}$ (LTO), TiO_2 , SnO_2 , Nb_2O_5 , Sb_2O_5 , and CeO_2 . Such a violent redox reaction releases a lot of heat, enough to make the solution boil. The energy released helps overcome the activation energy and accelerate reaction rates. Here, we take LTO nanoparticles as an example to create defects through this simple redox process. After adding LTO nanoparticles to the n-BuLi solution, an ordered surface structure becomes amorphous, shown in TEM images (Fig. 1c). The newly generated disordered surface layer improves the absorption of visible light, causing the colour of LTO from white to blue. As disordered areas increase with reaction time, which further strengthens the absorption of visible light, LTO eventually turns black (Fig 1d). Fig 1e shows no apparent difference in peaks after treatment, as well as the morphology of LTO (Fig. S1). The evidence indicates that this redox process only involves around the nanoscale surface layer and does not affect the morphology and crystal structure of LTO particles. Fig. 1f shows the Raman spectra of LTO samples, and a small peak approximately at 143 cm^{-1} gradually disappeared as the increasing defect concentration of the disordered surface¹³. Fig. S2 shows the UV-Vis NIR diffuse reflectance spectra of the obtained LTO at different reacting times. It is evident that the absorption of visible light and near-infrared light of defective LTO gradually enhances with the increasing defect concentration¹⁴. The bandgap has also been reduced from the initial 3.61 eV in the pristine LTO to 1.90 eV in the defective LTO reacting for 14 days (Fig. S3).

Other defective oxides, including TiO_2 , SnO_2 , Nb_2O_5 , Sb_2O_5 and CeO_2 , have also been prepared through this method, and all of them show a distinct black colour change (Fig. 1g). The enhanced visible absorption of these oxides can still be found in the UV-Vis-NIR diffuse reflectance spectra (Fig. S4a-e). Similarly, the lattice structure (Fig. S5a-e) and particle morphology (Fig. S6-10) did not change after the redox reaction. But the disordered surface layer can be observed in the TEM images of all defective oxides (Fig. S6-10). It is also worth noting that the Raman spectra peaks have shifted to varying degrees due to these generated disordered surface layers (Fig. S11a-e), which shows that this method is delicate and tuneable.

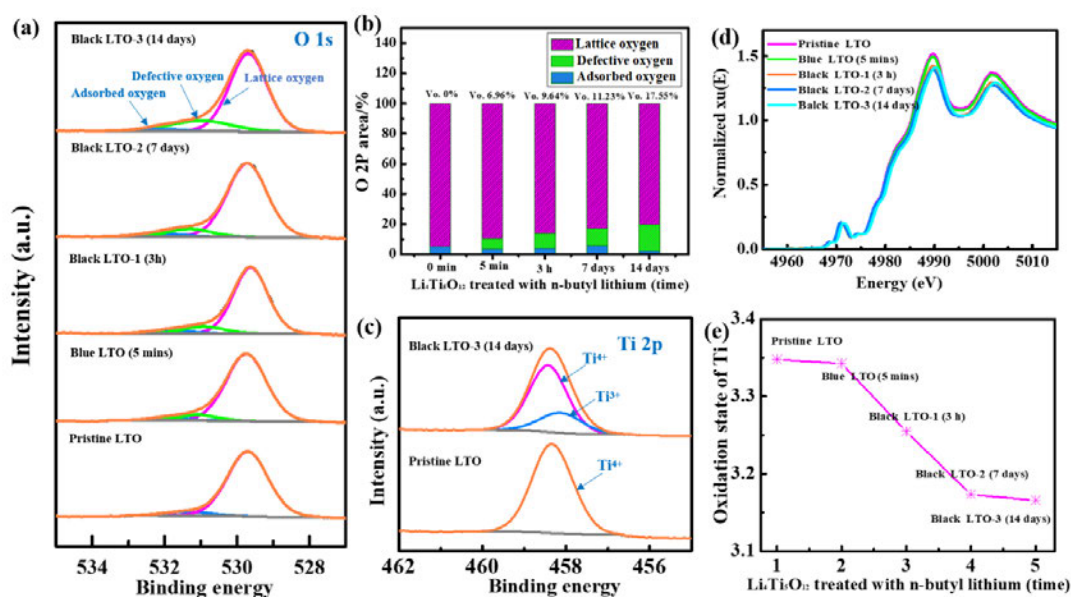


Fig. 2 The high-resolution XPS spectra of O1s (a) and corresponding percentage of Valence state calculated based on O 1s area (b); the high-resolution XPS spectra of Ti (c); the X-ray absorption near edge structure) spectra of obtained LTO (d) and the corresponding evolution of the Ti oxidation state (e).

X-ray photoelectron spectroscopy (XPS) testing is carried out to analyze the valence state distribution and characterize N-butyl lithium reduced LTO, and typical Li 1s, Ti 2p and O 1s peaks locate at 36.4 eV, 457.8 eV and 529.4 eV, respectively, in the whole spectra of obtained samples¹⁵ (shown in Fig. S12a). For the high-resolution O1s XPS spectra shown in Fig. 2a,

three typical oxygen peaks at 529.7 eV, 531.2 eV, 532.3 eV can be found in the defective LTO, corresponding to the lattice oxygen, defective oxygen, and adsorbed oxygen, respectively⁸. Also, there is no significant change in the Li 1s and Ti 2p XPS spectra, but an additional broad peak indicates that the oxygen defects gradually appear in the O1s XPS spectra of reduced LTO (Fig. S12b-d). More remarkably, the content of defective oxygen increases obviously with the reaction time of n-butyl lithium (shown in Fig. 2b), demonstrating the fact that n-butyl lithium can efficiently capture partial oxygen atoms and remain Vo in the LTO lattices. Another interesting point is that the concentration of oxygen defects can be adjusted and controlled by the reaction time, gradually increasing from the initial 0% to 17.5% after 14 days of reacting (Fig. 2b). While oxygen atoms are being removed under the attack of n-butyl lithium, the adjacent Ti⁴⁺ is reduced to Ti³⁺ and retained in the crystal lattice (Fig. 2c). Moreover, based on the insensitivity of XPS for Ti³⁺, X-ray Absorption Near-Edge Structure (XANES) measurement was selected to further determine the valence change in the defective LTO lattice. As shown in Fig. 2d, no significant difference can be observed in the XANES figure, and the whole spectra slightly shifted to lower energy with increased reaction time. Such a result implies a gradual deepening of the reduction process^{16, 17}. Specifically, Ti's oxidation number gradually decreased from initial 3.930957 to 3.624425 after soaking in n-butyl lithium for 14 days, consistent with the XPS results (Fig. 2a and 2b). Furthermore, identical to the LTO reduction process, other oxides, such as TiO₂, N₂O₅, SnO₂, Sb₂O₅, and CeO₂, present similar defective structures under the attack of n-butyl lithium. Different concentrations of Vo can be observed in the O1s XPS spectra of these oxides (Fig. S13 and S14), which indicates that n-butyl lithium successfully captures the oxygen atoms in these oxides and retain these Vo in the lattice. For the cationic XPS spectra shown in Fig. S15, pronounced peak shifting to lower energy can be observed in these oxides, which come from the newly generated disordered surface after being reduced by n-butyl lithium. The XANES of defective TiO₂ was presented

in Fig. S13c-d, verifying the reduction effect of n-butyl lithium. Similar to the results of defective LTO, the tetravalent titanium is gradually reduced to a lower valence state.

Fig. 3a and 3b show the refinement fit profile of the neutron powder diffraction data of black LTO (14 days) and pristine LTO powders, respectively. Benefiting from the high sensitivity towards light elements, we determine the atomic positional parameter and site occupancy of the O within the spinel structure (Table S1). The results suggest that, in addition to the larger lattice parameters, black LTO has more O vacancies and larger Ti-O bond length, indicating weaker Ti-O bond energy and lower oxidation states of Ti¹⁸. These results highly coincide with those from XPS and XANES.

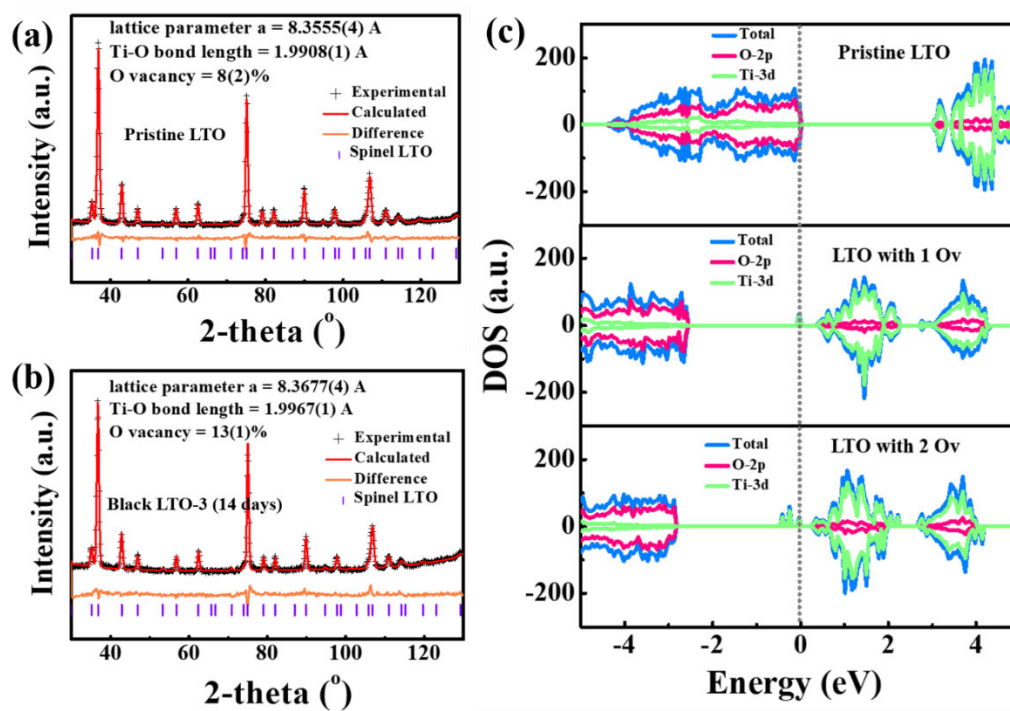


Fig. 3 The Refinement fit profiles against NPD data of (a) pristine and (b) black LTO-3. (c) DFT calculations: Density of states of pristine $\text{Li}_4\text{Ti}_5\text{O}_{12}$ (top), $\text{Li}_4\text{Ti}_5\text{O}_{11.875}$ (middle), and $\text{Li}_4\text{Ti}_5\text{O}_{11.75}$ (bottom).

To fully explain the influence of Vo on LTO material intrinsic property, DFT calculations were carried out and shown in Fig. S16 and Fig. 3c. According to crystal field theory, the five-fold degenerate $3d$ orbits of Ti split into two groups, t_{2g} (d_{xy}, d_{xz}, d_{yz}) and e_g ($d_{x^2-y^2}, d_{z^2}$) and the $2p$ orbits of O decomposed into p_σ and p_π , the molecular-orbital bonding diagram was shown in Fig. S16. The electronic structure of $\text{Li}_4\text{Ti}_5\text{O}_{12}$ is clearly illustrated by Fig. 3c, which is in accordance with the molecular orbital theory (Fig. S16): the O p_σ states and the Ti e_g states form the bonding σ states in the low energy region of the valence band (VB), and the anti-bonding σ^* states in the high energy region of the conduction band (CB); the middle region of VB and CB are the weak π bonding between the O p_π states and the Ti t_{2g} states. The valence band maximum (VBM) and the conduction band minimum (CBM) are non-bonding O p_π and Ti t_{2g} states, respectively. The Fermi energy locates a little above the VBM and the gap between VBM and CBM is almost 3 eV, smaller than the experimental value (3.61 eV, shown in Fig. S3). This difference is due to the strong on-site Coulomb interaction of localized electrons of Ti-3d states, which LDA or GGA does not correctly describe. Usually, DFT+U corrections can be introduced with $U = 2.5$ eV^{19, 20} to get a larger bandgap value. However, this will not change our conclusions here as the relative positions of each state will not change. The experimental value and calculated one are in reasonable conformity with previous results indicating that $\text{Li}_4\text{Ti}_5\text{O}_{12}$ is an insulator^{21, 22}. For LTO with Vo ($\text{Li}_4\text{Ti}_5\text{O}_{11.875}$), as the electronegativity of Ti (1.54) is larger than Li (0.98), these excess electrons are more likely to be captured by d_{xy} orbit of Ti forming donor states next to the CB. These electrons have weak connections with Ti than those in the VB and can easily enter the CB (impurity excitation), as the donor ionization energy is minimal. In sharp contrast, exciting electrons in the VB to the CB can be very hard for insulators. These donor states, also new Ti t_{2g} states with the width of about 0.10 eV, appear in the middle of the bandgap, 2.40 eV away from VBM and 0.29 eV away from CBM. With more Vo ($\text{Li}_4\text{Ti}_5\text{O}_{11.75}$), these introduced gap states locate

2.32 eV away from VBM and 0.18 eV away from CBM. The more V_o introduced, the broader the absorption spectrum of LTO will be, and the color of LTO will become darker. In the end, LTO with a large number of V_o will show black in the white light, as well as a smaller band gap and better electronic conductivity.

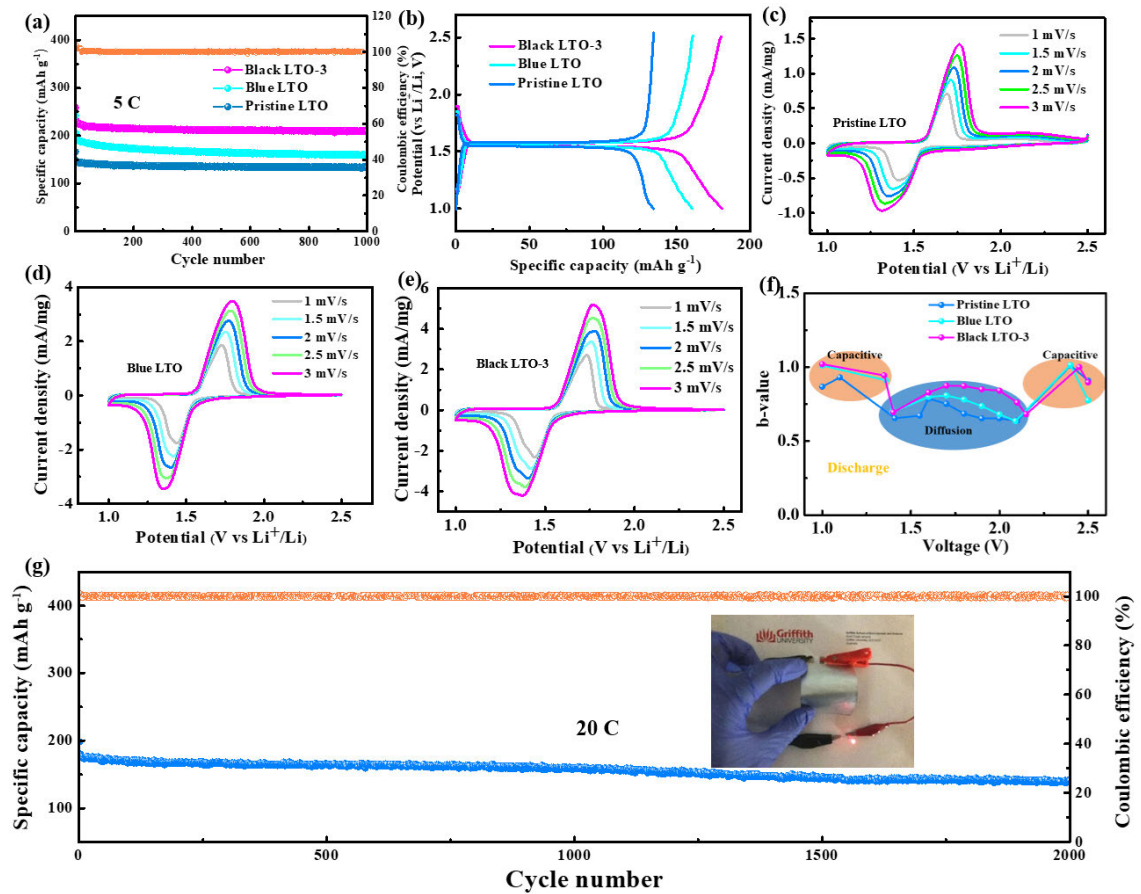


Fig. 4 (a) the performance of the obtained LTO at the rate of 5 C (1 C=175 mA g⁻¹); (b) the charge–discharge profiles of LTO at the rate of 5 C after 800 cycles; The CV curves of the (c) pristine LTO, (d) blue LTO and (e) black LTO-3; (f) the b value trend of pristine LTO, blue LTO, and black LTO-3 in the voltage of 1-2.5V (g) the long cycle performance of black LTO-3 at rate 20 C.

The electrochemical performance of the obtained LTO was tested and shown in Fig. 4. As shown in Fig. 4a, the black LTO-3 (14 days) shows a stable discharge capacity of 181 mAh g⁻¹ after 800 cycles at the rate of 5 C (1 C=175 mA g⁻¹), which is much better than blue LTO and

pristine LTO. There is such a fantastic fact that super theoretical capacity can be achieved due to the additional lithium storage site induced by Vo based on our previous research. Fig. 4b shows the capacity voltage curves of LTO with typical voltage at 1.55V after 800 cycles, indicating the intrinsic properties of LTO in electrochemical energy storage area: excellent cycle reversibility and stability. Towards defective LTO anodes with enhanced kinetics, cyclic voltammetry (CV) was adapted to reveal lithium ions' diffusion process in the LTO anode. The apparent polarization phenomenon can be observed in all LTO anodes with increasing scan rate (shown in Fig 4c-e). Fig. 4f compares the calculated b values of obtained LTO anodes at the discharge process according to their CV results with different scan rates. When b is 0.5, the electrochemical process obeys the diffusion-control mechanism; when b is equal to 1, the capacitive-control process is dominated²³. As shown in Fig. 4f, it is evident that the b value of black LTO-3 is higher than that of blue LTO and pristine LTO, which indicates that the disordered surface layers in the defective LTO are beneficial for the Li⁺ diffusion and accelerates the transportation of electrons. The enhanced ionic and electron conductivity and the additional storage sites endow defective LTO the ability to store electric energy through redox and pseudocapacitive process, breaking through the theoretical capacity of 175 mAh g⁻¹. Fig. 4g shows the long cycle performance of black LTO-3 at the rate of 20 C with a high discharge capacity of 141 mAh g⁻¹ after 2,000 cycles. Such excellent electrochemical performance can be attributed to the optimized electronic structure, the enhanced Li⁺ diffusion rate, and additional lithium storage sites in the defective LTO.

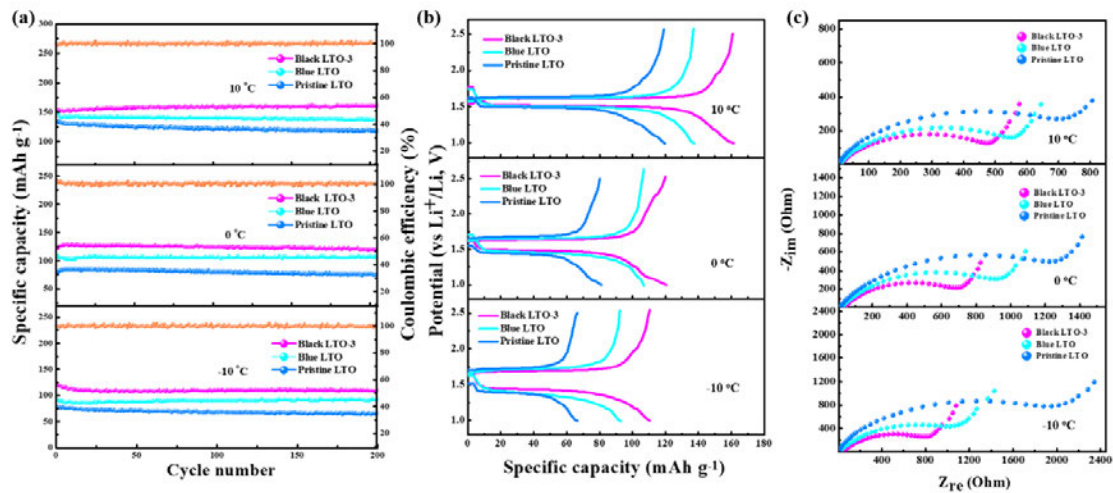


Fig. 5 (a) The low-temperature performance of the obtained LTO at the rate of 10 C; (b) the low-temperature discharge/charge voltage profiles at the rate of 10 C after 200 cycles; (c) the EIS curves of the obtained LTO at the low-temperature.

Low-temperature performance is an essential parameter of the battery, mainly affected by the Li⁺ ion diffusion rate. Here, we conduct low-temperature performance tests on defective LTO, considering its excellent kinetic performance. As shown in Fig. 5a, after 200 cycles at the rate of 10 C, the black LTO-3 exhibits a high discharge capacity of 161.3 mAh g⁻¹, 120.5 mAh g⁻¹, and 109.9 mAh g⁻¹ at the temperature of 10 °C, 0 °C, and -10 °C, respectively, which are far better than the performance of blue LTO and pristine LTO. Fig. 5b shows the capacity voltage of obtained LTO samples at different temperatures. The voltage plateau of pristine LTO is slightly lower than that of blue LTO and black LTO-3, especially at -10 °C. The slower voltage drop of defective LTO indicates its excellent kinetic migration of Li⁺ at the liquid-solid interface²⁴. It also proves that the disordered surface layers are beneficial for the desolvation of Li⁺ even at low temperatures. Moreover, the defective LTO possesses a much narrower potential gap at different temperatures than blue LTO and pristine LTO, indicating an excellent kinetic process of Li⁺ ions at low temperatures. We also took the electrochemical impedance spectroscopy (EIS) test to analyze the charge-transfer process (Fig. 5c). The value of charge-

transfer resistance (R_{ct}) of black LTO-3 is significantly lower than that of the blue LTO and pristine LTO. All the results at different temperatures indicate the rapid Li^+ migration process at the disordered solid-liquid interface in the defective LTO²⁵.

Conclusion

In brief, a series of defective oxides are synthesized through a simple redox process at room temperature. To our knowledge, we first achieve controllable defect concentration in this universal defect preparing method. As a strong nucleophile and reducing reagent, n-butyl lithium can easily deprive oxygen from oxides forming defective phases of Vo . The n-BuLi reduction method can also help form a uniform defective structure in the oxides and control defect concentration easily by altering soaking time. We take defective LTO as an example to further analyze the role of Vo in electrochemical energy storage. The defective LTO shows excellent super-theoretical capacity with a remarkable kinetic process than pristine LTO at room temperature, which can be attributed to the additional lithium storage sites induced by Vo , according to our previous research. When etching by n-butyl lithium, the crystal surface becomes amorphous, which can accelerate Li^+ desolvation and enhanced Li^+ migration rate at the crystalline-amorphous interface, even at low temperatures. Our research also confirms this method's broad applicability by preparing a series of defective metal oxides, which significantly increased its practical value.

Experimental Section

Material preparations. The defective LTO was prepared through a simple redox process at room temperature in a glove box filled with Ar. Pristine LTO (Tianjin Jiewei, 1g) powder was added to 10ml of 2.5ml/l n-butyl lithium solution and was soaked for 14 days. Then hexane is used to remove the butyl lithium solution, followed by centrifuging and washing through acetone, ethanol, and water. The obtained LTO powders were collected and dried for 12 h in

vacuum. LTO with different defect concentrations was prepared by controlling different soaking times, including 5 mins, 3 h, and 7 days. In this study, other defective oxides, including TiO_2 , CeO_2 , SnO_2 , Sb_2O_5 , and Nb_2O_5 , were also prepared through the redox process described above.

Structural characterization The prepared samples' morphology and structure were characterized through Scanning electron microscopy (SEM, SU8020) and high-resolution transmission electron microscopy (HRTEM, Tecnai G20). X-ray Absorption Near-Edge Structure spectra at Ti K-edge were collected on a 9BM-C beam line of Argonne Advanced Photon Sources through a transmission mode, and Athena software were performed for further analysis. The X-ray photoelectron spectroscopy (XPS) spectra (Thermo ESCALAB 250XI), Raman spectra (Renishaw system 100 Raman fibre spectrometer), and UV-vis diffusion reflectance spectra (Thermo Nicolet Evolution 500 UV Vis spectrophotometer) were used to study the obtained samples. The prepared oxides' crystal structure was characterised by X-ray diffraction (XRD) and neutron powder diffractometer (NPD). The XRD data were collected on the Burker D8 advance diffractometer at the Cu Ka radiation ($\lambda = 1.5405 \text{ \AA}$) in a range of 10° - 80° with a scan rate of 5 min^{-1} . High-resolution NPD was measured on the high-resolution neutron powder diffractometer, ECHIDNA, with 4° - 164° 2θ angular range and 0.05° step size at Australian Nuclear Science and Technology Organization (ANSTO). Based on the La11B6 NIST standard reference material 660b, the neutron beam's wavelength was set to $1.6214(4) \text{ \AA}$. The collected data were then analysed with Rietica ver. 1.77 with refined parameters such as background coefficients, zero-shift and peak-shape parameters, lattice parameters, O positional parameters, and isotropic atomic displacement parameters.

Electrochemical measurement The electrochemical behaviour of the obtained LTO was conducted on a LAND-CT2001A battery tester with the voltage range of 1-2.5 V. The working electrode is prepared by mixing LTO powder, carbon black and PVDF at a ratio of 7:2:1 with

N-methyl pyrrolidinone (NMP) as dispersant, followed by vacuum drying for 12 h at 60 °C. The approximate loading is 1mg/cm². Lithium metal was used as the reference electrode and polyethene as a separator. The electrolyte was 1mol of LiPF₆ dissolved in a 1:1:1 (w/w) mixture solution of ethyl carbonate (EC), ethyl methyl carbonate (EMC) and dimethyl carbonate (DMC) with 20% fluoroethylene carbonate (FEC) as an additive. The self-assembly process of the coin cell is carried out in a glove box filled with argon gas. Cyclic Voltammetry (CV) and electrochemical impedance spectroscopy (EIS, frequency 100 kHz to 10 MHz) were performed on an electrochemical workstation (CHI 660A).

DFT calculations Our first-principle calculations were performed using generalized gradient approximation (GGA) parameterized by Perdew-Burke-Ernzerhof (PBE) exchange-correlation functional^{26, 27} as implemented in the Vienna Ab Initio Simulation Package (VASP)^{28, 29}. The interaction potentials of the core electrons were replaced by projector augmented wave (PAW)³⁰ pseudopotentials (Li: 1s²2s¹, Ti: 3p⁶3d²4s², O: 2s²2p⁴). The cut-off energy is 600 eV and a Γ -centered 3×3×1 Monkhorst-Pack k-point mesh was used for Brillion zone sampling with a small broadening width of Gaussian smearing (0.05 eV). With semiempirical dispersion correction, namely zero damping DFT-D3 method^{31, 32}, all atoms were relaxed until the maximum energy difference and residual force is less than 10⁻⁶ eV and 0.01 eV/Å, respectively. All these parameters were carefully tested to ensure the convergence and accuracy. Li₄Ti₅O₁₂ belongs to the $Fd\bar{3}m$ space group (No. 227). The unit cell contains eight formula units of [Li]_{8a}[Li_{1/3}Ti_{5/3}]_{16d}[O₄]_{32e} (Wyckoff positions). The Li atoms occupy all the tetrahedral 8a sites and 1/6 of the octahedral 16d sites; the Ti atoms occupy the rest 5/6 of the 16d sites; O atoms occupy the tetrahedral 32e sites. However, the arrangement of these atoms is not clear and we adopt the structure reported by Tsai et al³³, which model has the lowest energy compared to others³⁴.

Acknowledgements

We are grateful for the financial support from the Australia Research Council Discovery Projects DP170103721 and DP180102003.

Additional information

Supplementary information is available for this paper.

References

1. Setvín, M., Wagner, M., Schmid, M., Parkinson, G. S., Diebold, U. Surface point defects on bulk oxides: atomically-resolved scanning probe microscopy. *Chem. Soc. Rev.* **46**, 1772-1784 (2017).
2. Su, Z. *et al.* Defect engineering in titanium-based oxides for electrochemical energy storage devices. *Electrochem. Energy Rev.* **3**, 286-343 (2020).
3. Kalinin, S. V., Spaldin, N. A. Functional ion defects in transition metal oxides. *Science* **341**, 858-859 (2013).
4. Greiner, M. T., Chai, L., Helander, M. G., Tang, W. M., Lu, Z. H. Transition metal oxide work functions: the influence of cation oxidation state and oxygen vacancies. *Adv. Funct. Mater.* **22**, 4557-4568 (2012).
5. Wang, Z. *et al.* Understanding the roles of oxygen vacancies in hematite-based photoelectrochemical processes. *Angew. Chem., Int. Ed.* **58**, 1030-1034 (2019).
6. Barzan, C., Groppo, E., Bordiga, S., Zecchina, A. Defect sites in H₂-reduced TiO₂ convert ethylene to high density polyethylene without activator. *ACS Catalysis* **4**, 986-989 (2014).
7. Zhang, W. *et al.* Defect-engineering of mesoporous TiO₂ microspheres with phase junctions for efficient visible-light driven fuel production. *Nano Energy* **66**, 104113 (2019).
8. Ou, G. *et al.* Tuning defects in oxides at room temperature by lithium reduction. *Nat. Commun.* **9**, 1-9 (2018).
9. Tilocca, A., Selloni, A. DFT-GGA and DFT+ U simulations of thin water layers on reduced TiO₂ anatase. *J. Phys. Chem. C* **116**, 9114-9121 (2012).
10. Jiang, X. *et al.* Characterization of oxygen vacancy associates within hydrogenated TiO₂: a positron annihilation study. *J. Phys. Chem. C* **116**, 22619-22624 (2012).
11. Reich, H. J. Role of organolithium aggregates and mixed aggregates in organolithium mechanisms. *Chem. Rev.* **113**, 7130-7178 (2013).
12. Kim, S., Ahn, K. H. Ate complex from diisobutylaluminum hydride and n-butyllithium as a powerful and selective reducing agent for the reduction of selected organic compounds containing various functional groups. *The Journal of organic chemistry* **49**, 1717-1724 (1984).
13. Xu, C., Zhang, P., Yan, L. Blue shift of Raman peak from coated TiO₂ nanoparticles. *J. Raman Spectrosc.* **32**, 862-865 (2001).
14. Naldoni, A. *et al.* Effect of nature and location of defects on bandgap narrowing in black TiO₂ nanoparticles. *J. Am. Chem. Soc.* **134**, 7600-7603 (2012).

15. Xu, H. *et al.* Highly porous $\text{Li}_4\text{Ti}_5\text{O}_{12}/\text{C}$ nanofibers for ultrafast electrochemical energy storage. *Nano Energy* **10**, 163-171 (2014).
16. Thomas, A. *et al.* Comparison of the electronic structure of anatase and rutile TiO_2 single-crystal surfaces using resonant photoemission and x-ray absorption spectroscopy. *Phys. Rev. B* **75**, 035105 (2007).
17. Wu, Q., Zheng, Q., van de Krol, R. Creating oxygen vacancies as a novel strategy to form tetrahedrally coordinated Ti^{4+} in Fe/TiO_2 nanoparticles. *J. Phys. Chem. C* **116**, 7219-7226 (2012).
18. Pang, W. K., Peterson, V. K. A custom battery for operando neutron powder diffraction studies of electrode structure. *Journal of Applied Crystallography* **48**, 280-290 (2015).
19. Gao, Y., Wang, Z., Chen, L. Stability of spinel $\text{Li}_4\text{Ti}_5\text{O}_{12}$ in air. *J. Power Sources* **245**, 684-690 (2014).
20. Hu, Z., Metiu, H. Choice of U for DFT+ U calculations for titanium oxides. *J. Phys. Chem. C* **115**, 5841-5845 (2011).
21. Verde, M. G. *et al.* Elucidating the phase transformation of $\text{Li}_4\text{Ti}_5\text{O}_{12}$ lithiation at the nanoscale. *ACS Nano* **10**, 4312-4321 (2016).
22. Song, H. *et al.* Anomalous decrease in structural disorder due to charge redistribution in Cr-doped $\text{Li}_4\text{Ti}_5\text{O}_{12}$ negative-electrode materials for high-rate Li-ion batteries. *Energy Environ. Sci.* **5**, 9903-9913 (2012).
23. Yang, C. *et al.* Flexible aqueous Li-ion battery with high energy and power densities. *Adv. Mater.* **29**, 1701972 (2017).
24. Lin, T. *et al.* Faster Activation and Slower Capacity/Voltage Fading: A Bifunctional Urea Treatment on Lithium-Rich Cathode Materials. *Adv. Funct. Mater.* **30**, 1909192 (2020).
25. Yang, L. Y. *et al.* $\text{Li}_4\text{Ti}_5\text{O}_{12}$ nanosheets as high-rate and long-life anode materials for sodium-ion batteries. *J. Mater. Chem. A* **3**, 24446-24452 (2015).
26. Perdew, J. P., Burke, K., Ernzerhof, M. Generalized gradient approximation made simple. *Phys. Rev. Lett.* **77**, 3865 (1996).
27. Langreth, D. C., Mehl, M. Beyond the local-density approximation in calculations of ground-state electronic properties. *Phys. Rev. B* **28**, 1809 (1983).
28. Kresse, G., Furthmüller, J. Efficiency of ab-initio total energy calculations for metals and semiconductors using a plane-wave basis set. *Comp. Mater. Sci.* **6**, 15-50 (1996).
29. Kresse, G., Furthmüller, J. Efficient iterative schemes for ab initio total-energy calculations using a plane-wave basis set. *Phys. Rev. B* **54**, 11169 (1996).
30. Blöchl, P. E. Projector augmented-wave method. *Phys. Rev. B* **50**, 17953 (1994).
31. Grimme, S., Antony, J., Ehrlich, S., Krieg, H. A consistent and accurate ab initio parametrization of density functional dispersion correction (DFT-D) for the 94 elements H-Pu. *J. Chem. Phys.* **132**, 154104 (2010).
32. Grimme, S., Ehrlich, S., Goerigk, L. Effect of the damping function in dispersion corrected density functional theory. *J. Comput. Chem.* **32**, 1456-1465 (2011).
33. Tsai, P.-c., Hsu, W.-D., Lin, S.-k. Atomistic structure and ab initio electrochemical properties of $\text{Li}_4\text{Ti}_5\text{O}_{12}$ defect spinel for Li ion batteries. *J. Electrochem. Soc.* **161**, A439 (2014).
34. Zahn, S., Janek, J., Mollenhauer, D. A simple ansatz to predict the structure of $\text{Li}_4\text{Ti}_5\text{O}_{12}$. *J. Electrochem. Soc.* **164**, A221 (2016).

Supporting information

Tuning defects in metal oxides via redox reaction for lithium ion battery

Zhong Su¹, Meng Li¹, Shangshu Qian¹, Lu Ma², Tao Zhang², Chao Lai¹, Jun Lu^{2*}, Shanqing Zhang^{1*}

¹ Centre for Clean Environment and Energy, School of Environment and Science, Griffith University, Gold Coast Campus, Gold Coast, Queensland 4222, Australia. ² Chemical Sciences and Engineering Division, Argonne National Laboratory, Lemont, IL, USA.

* e-mail: junlu@anl.gov; s.zhang@griffith.edu.au.

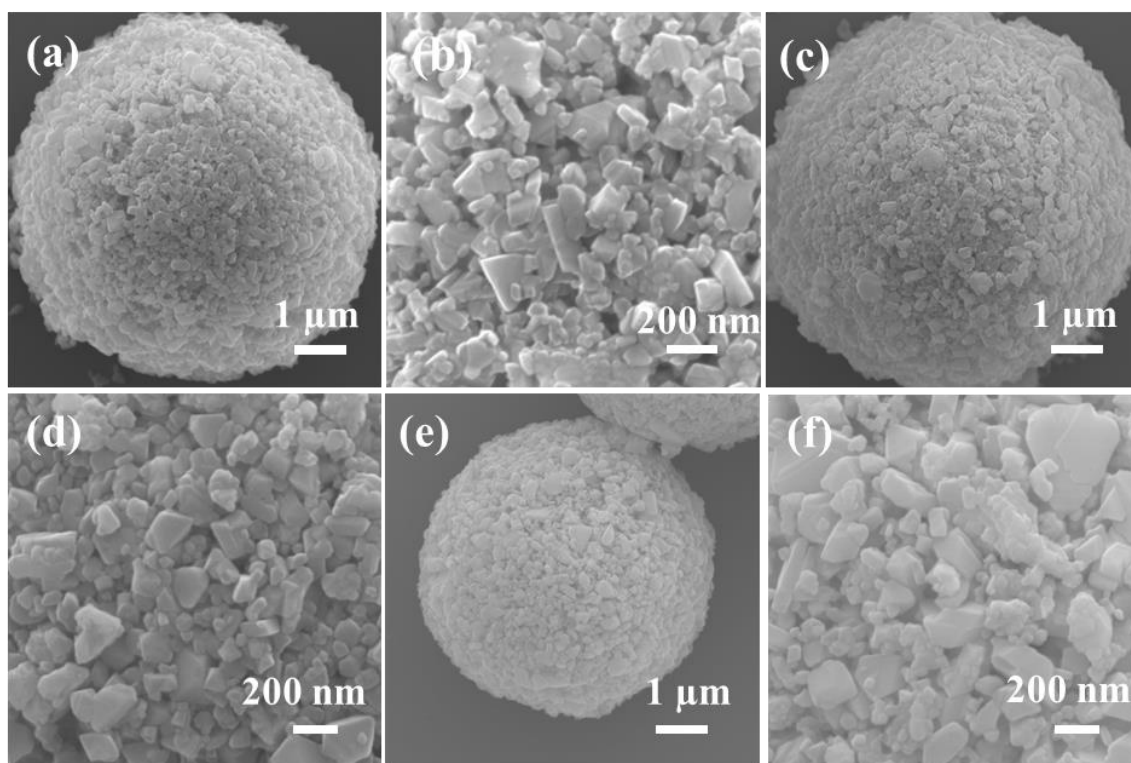


Fig. S1 SEM images of pristine LTO (a,b); Blue LTO (c,d); Black LTO-3 (e,f).

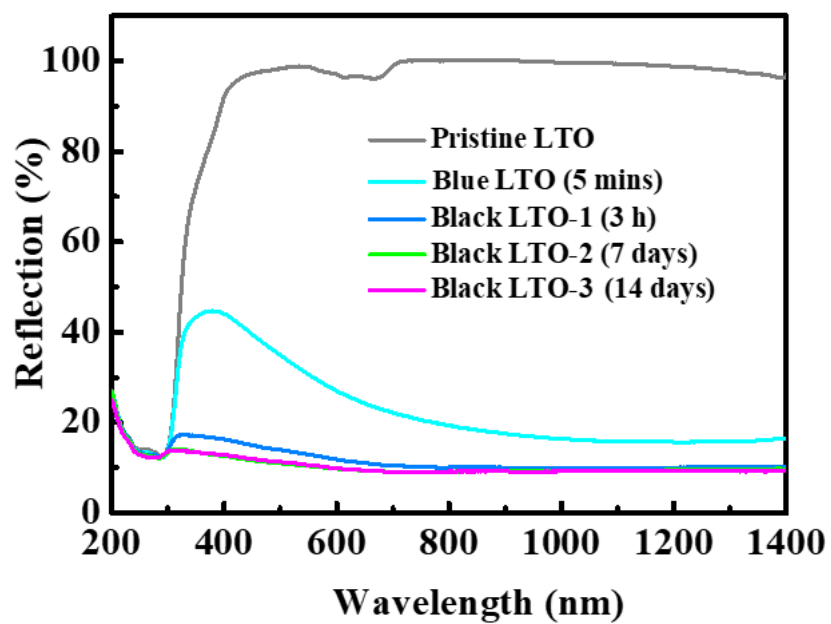


Fig. S2 UV-Vis-NIR diffuse reflectance spectra of Pristine and n-butyl lithium treated LTO.

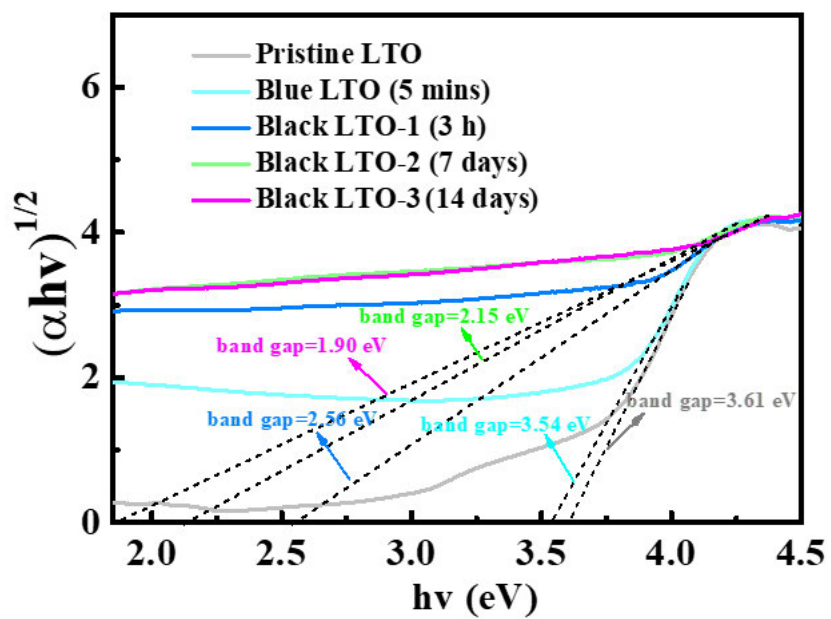


Fig. S3 Tauc plots of Pristine and n-butyl lithium treated LTO. The bandgap was fitted according to the Tauc plot.

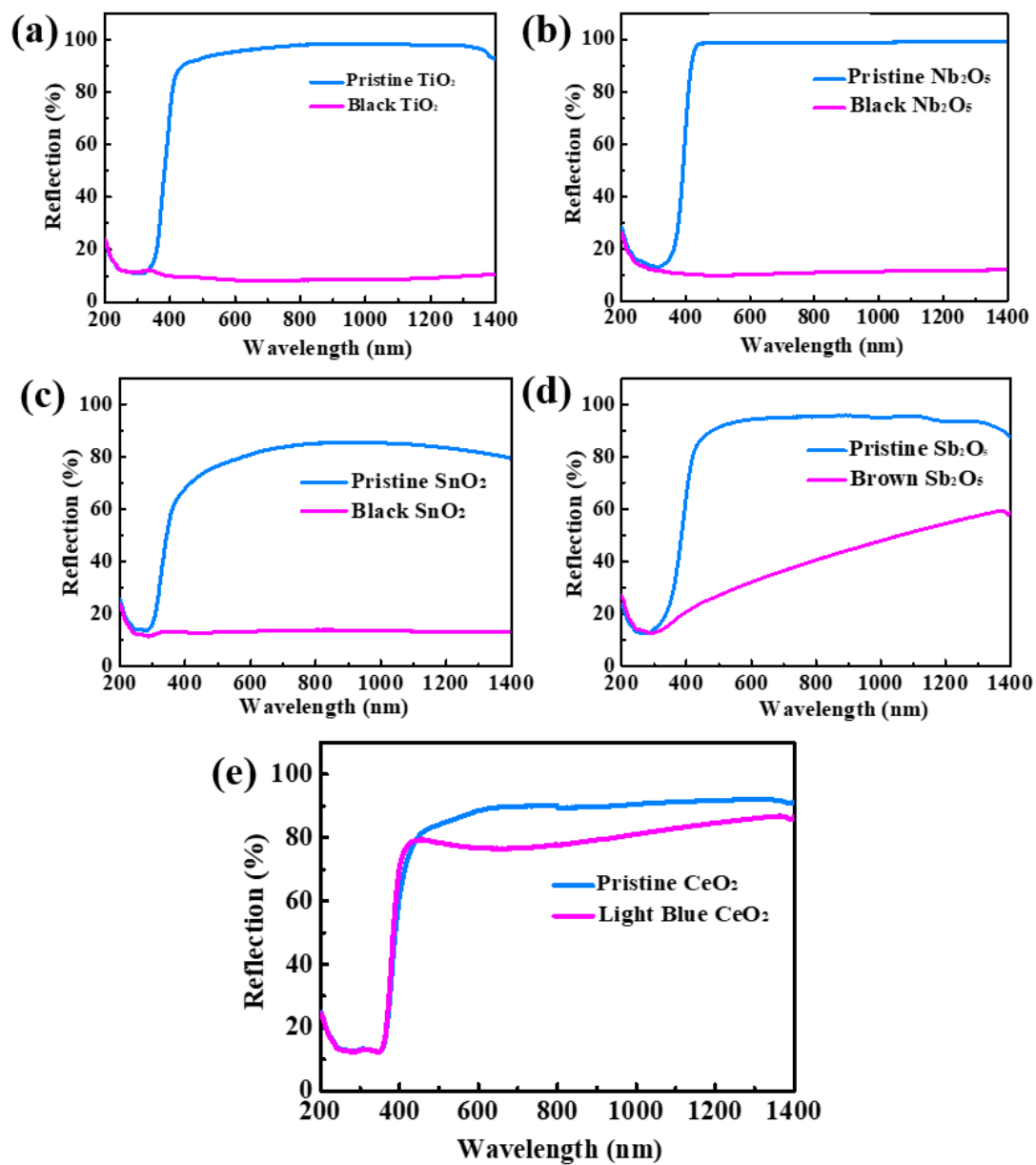


Fig. S4 UV-Vis-NIR diffuse reflectance spectra of Pristine and n-butyl lithium treated oxide nanoparticles. a, TiO_2 . b, Nb_2O_5 . c, SnO_2 . d, Sb_2O_5 . e, CeO_2

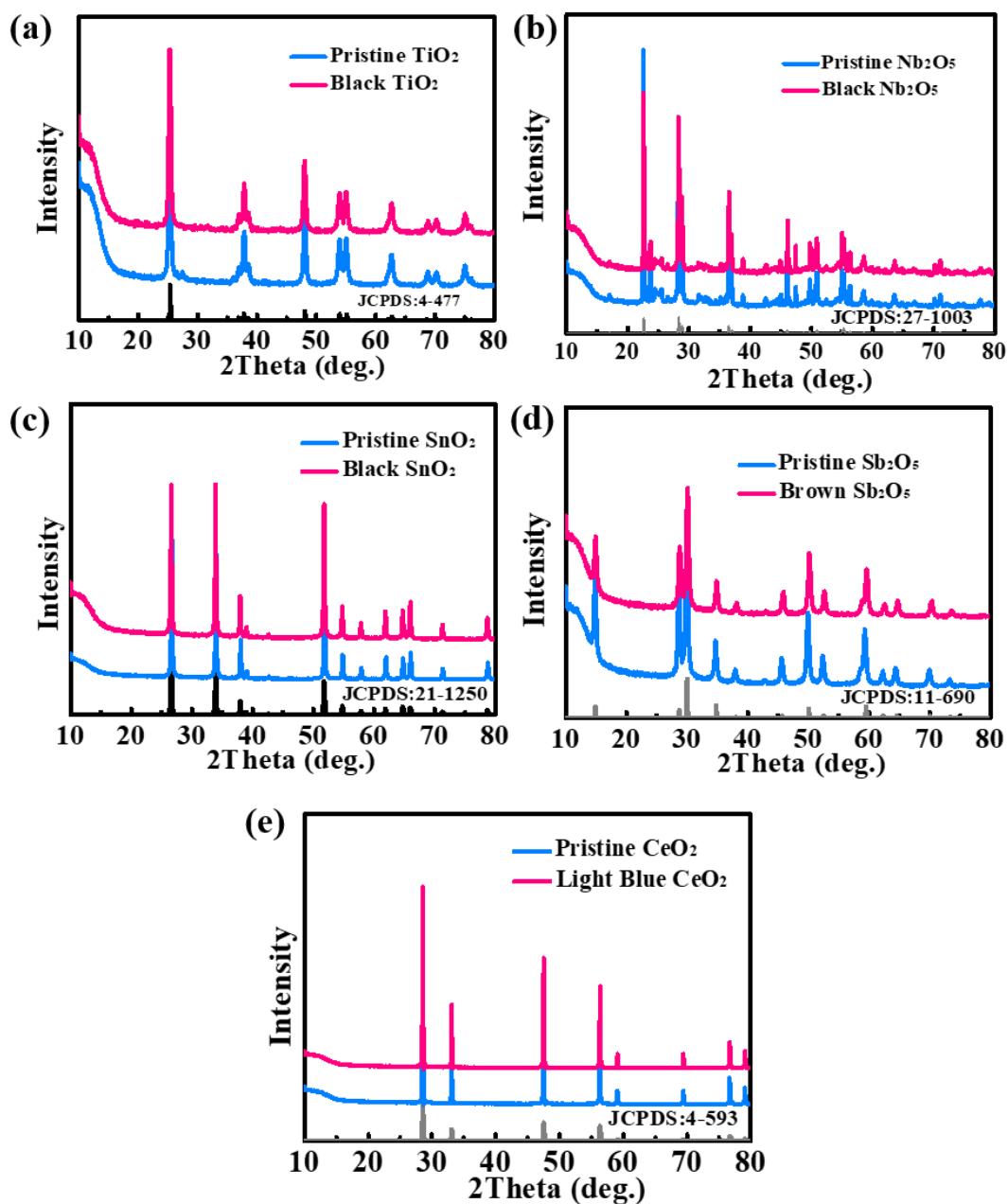


Fig. S5 The XRD spectra of Pristine and n-butyl lithium treated oxide nanoparticles. a, TiO_2 . b Nb_2O_5 . c, SnO_2 . d, Sb_2O_5 . e, CeO_2 .

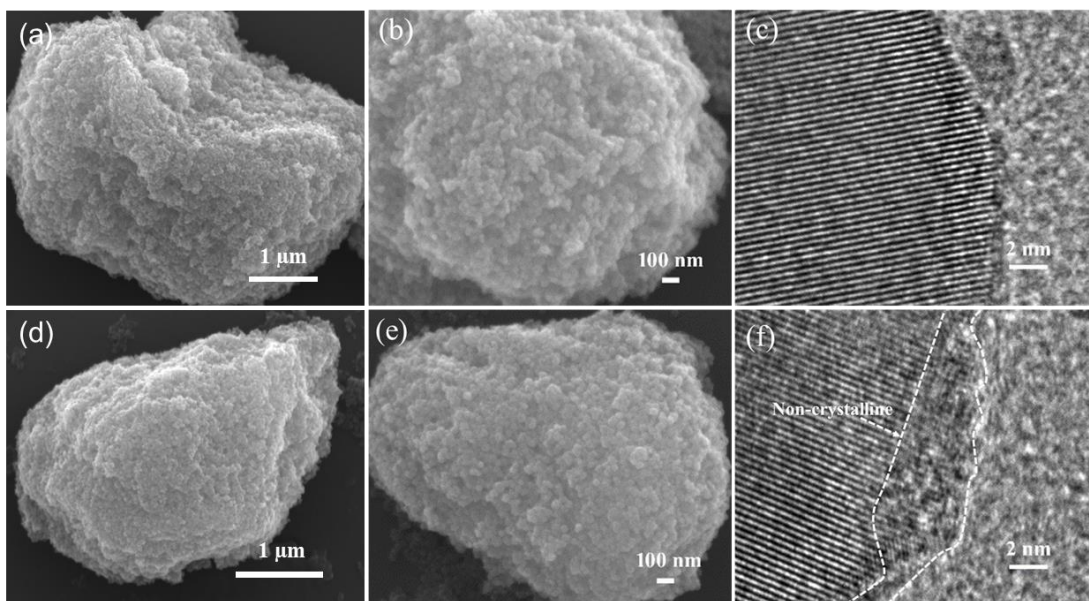


Fig. S6 SEM and HRTEM images of pristine and n-butyl lithium treated TiO₂: a-c, pristine TiO₂; d-f, black TiO₂.

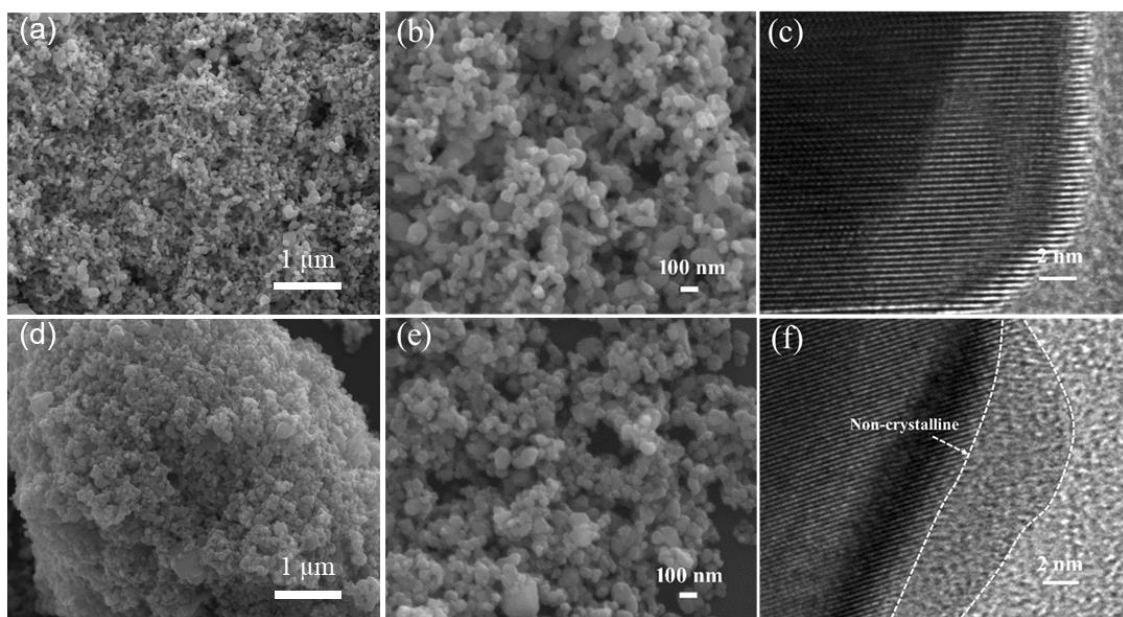


Fig. S7 SEM and HRTEM images of pristine and n-butyl lithium treated SnO₂: a-c, pristine SnO₂; d-f, black SnO₂.

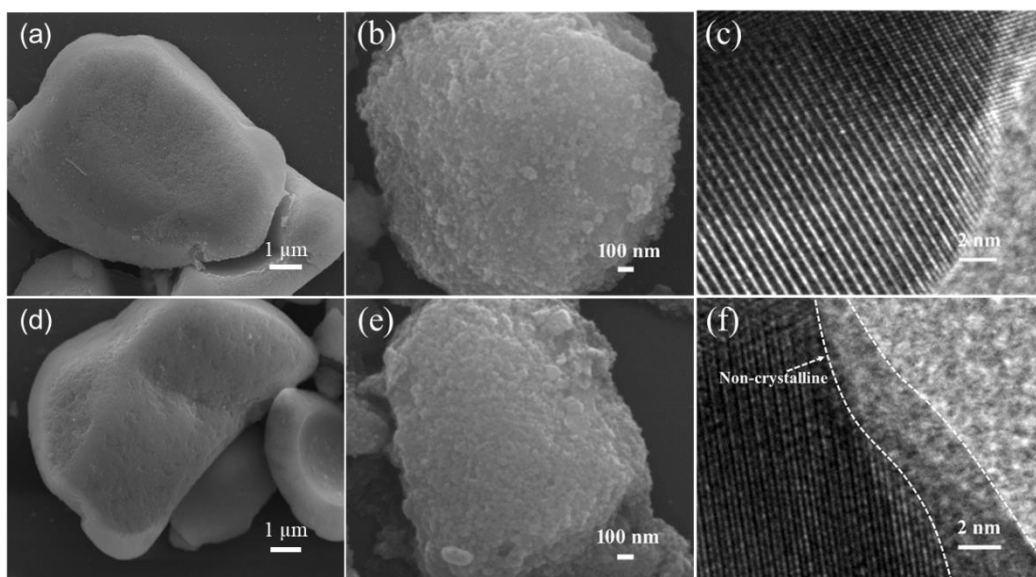


Fig. S8 SEM and HRTEM images of pristine and n-butyl lithium treated Sb_2O_5 : a-c, pristine Sb_2O_5 ; d-f, brown Sb_2O_5 .

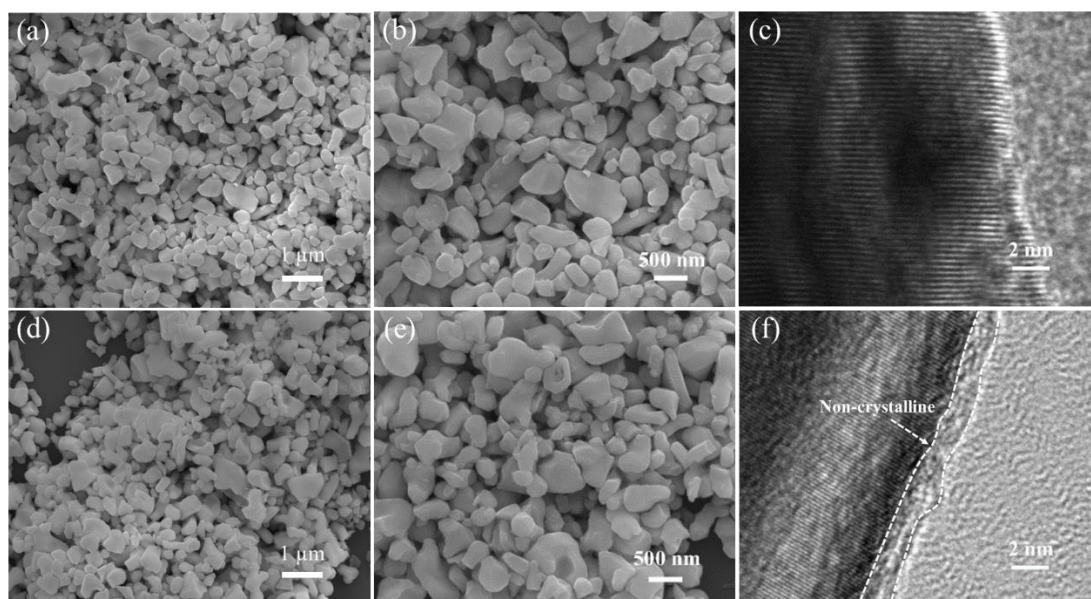


Fig. S9 SEM and HRTEM images of pristine and n-butyl lithium treated TiO_2 : a-c, pristine CeO_2 ; d-f, light blue CeO_2 .

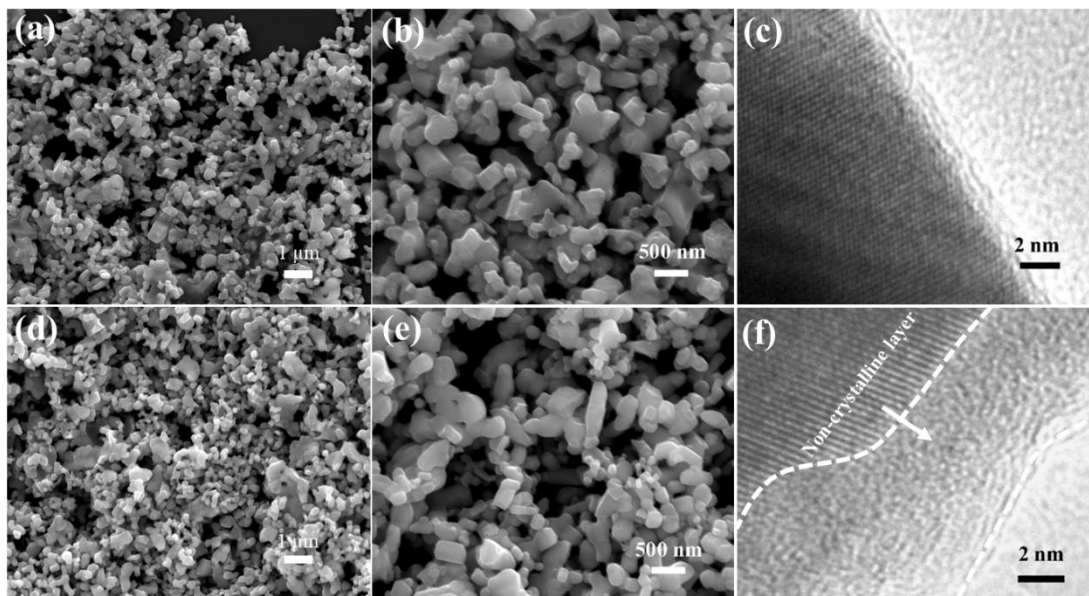


Fig. S10 SEM and HRTEM images of pristine and n-butyl lithium treated Nb_2O_5 : a-c, pristine Nb_2O_5 ; d-f, black Nb_2O_5 .

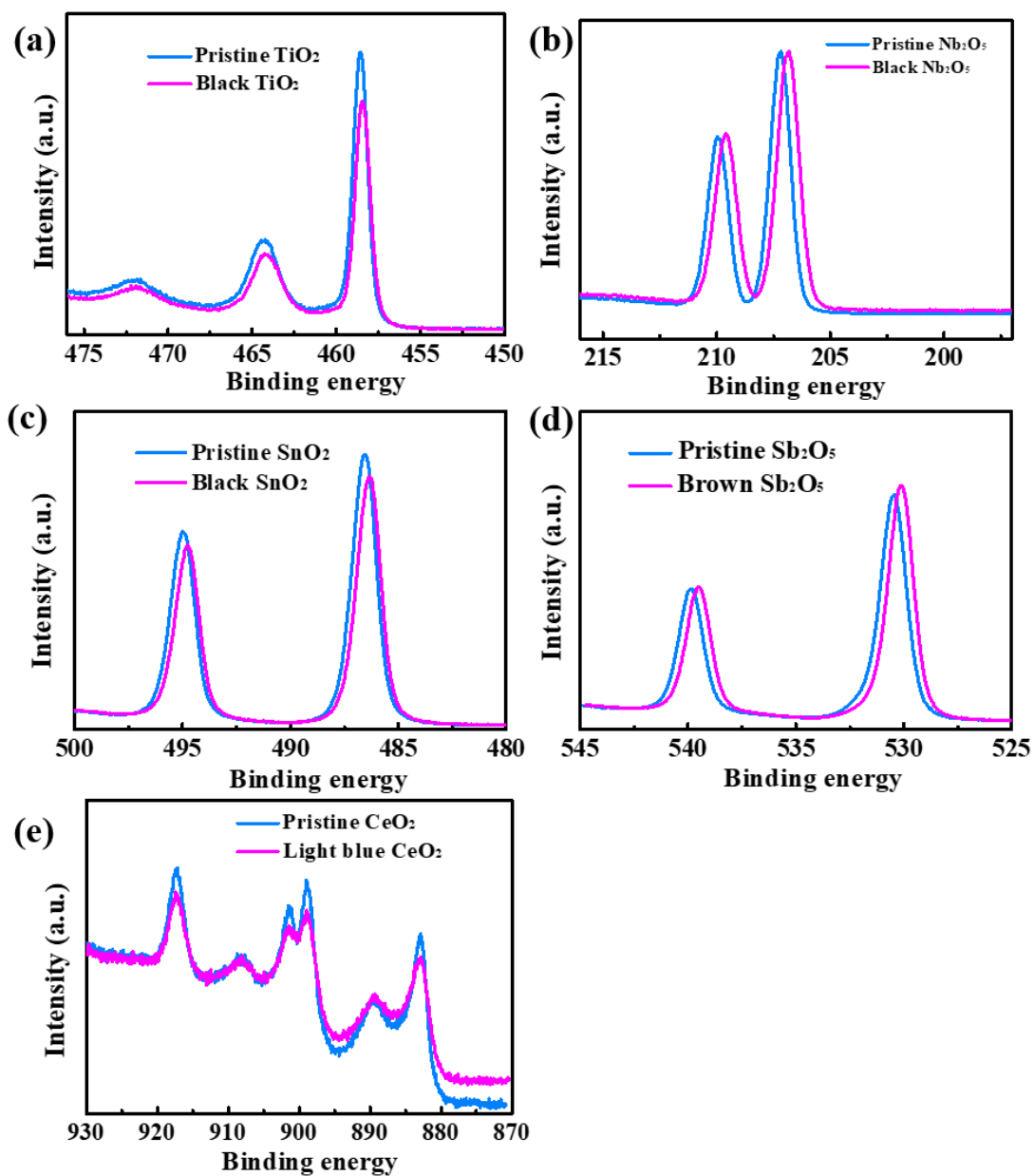


Fig. S11 The Raman spectra of Pristine and n-butyl lithium treated oxide nanoparticles. a, TiO_2 . b Nb_2O_5 . c, SnO_2 . d, Sb_2O_5 . e, CeO_2 .

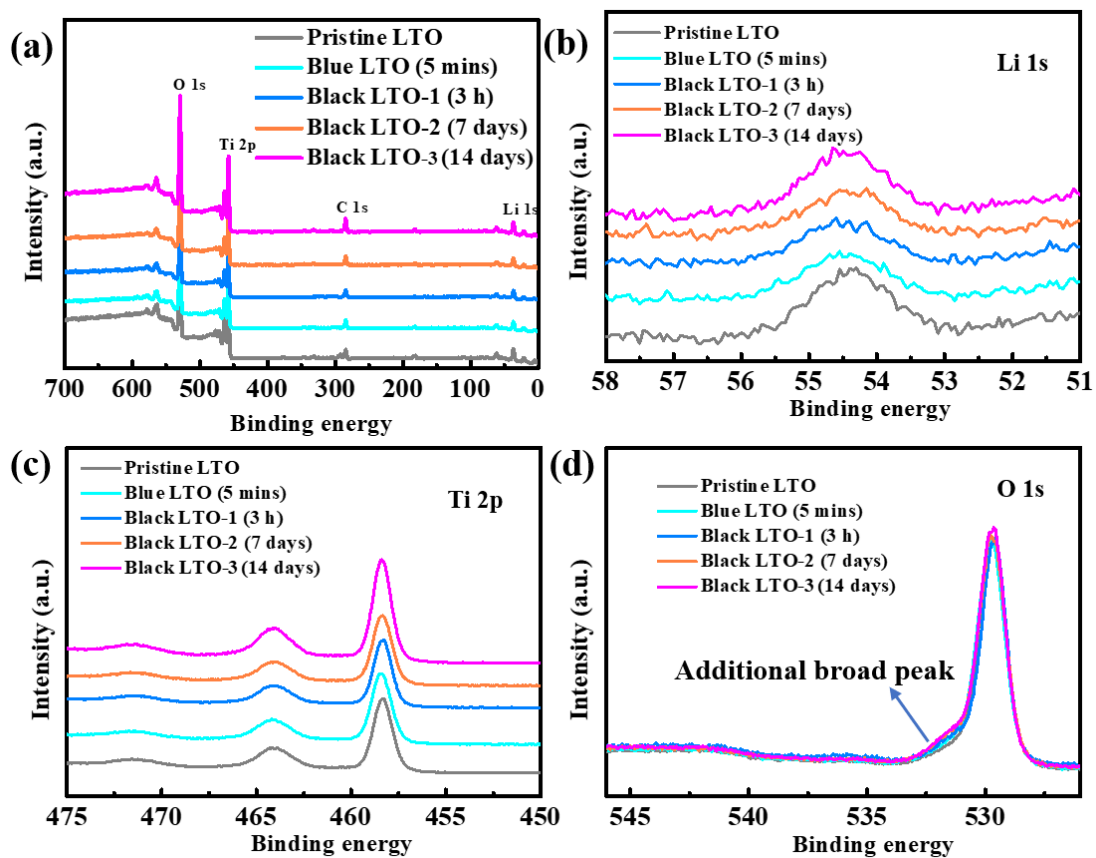


Fig. S12 The whole XPS spectra of obtained LTO samples (a), and corresponding Li 1s (b), Ti 2p (c) and O 1s (d) XPS spectra.

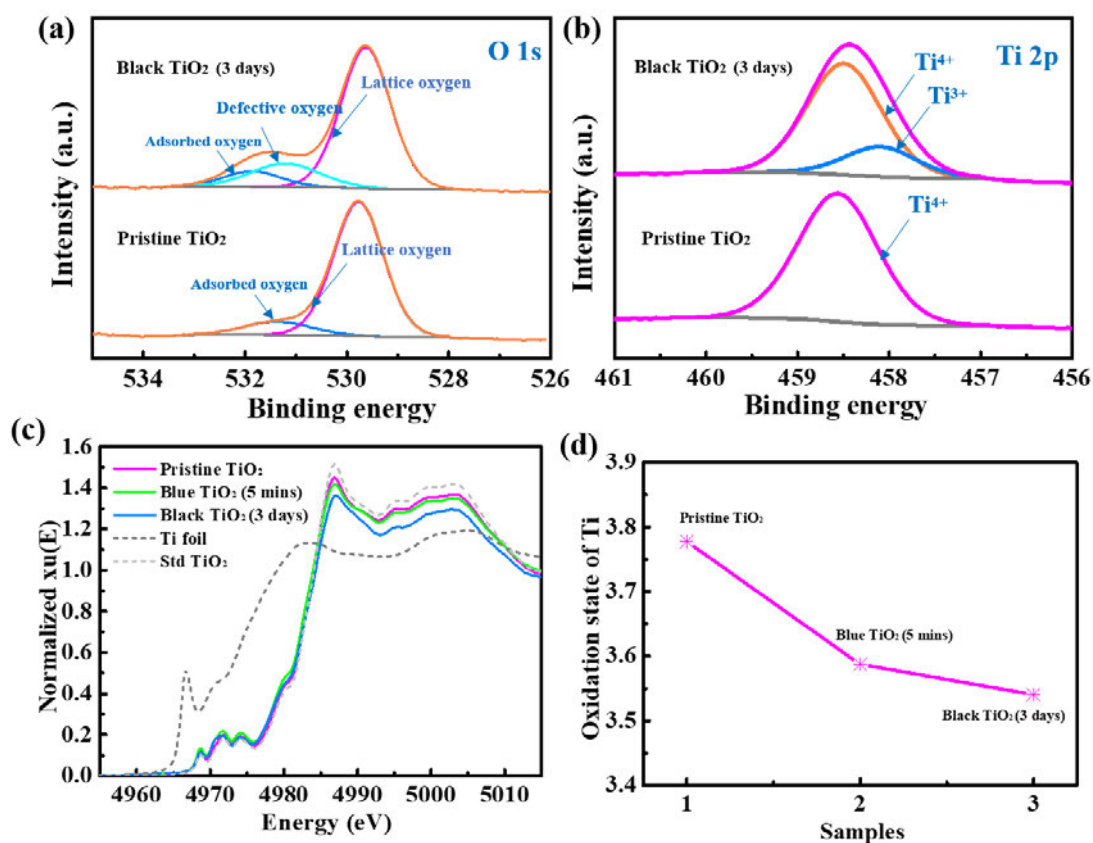


Fig. S13 The high-resolution XPS spectra of O1s (a) and the high-resolution XPS spectra of Ti (b) of TiO₂; the X-ray absorption near edge structure spectra of obtained defect TiO₂ (c) and the corresponding evolution of the Ti oxidation state (d)

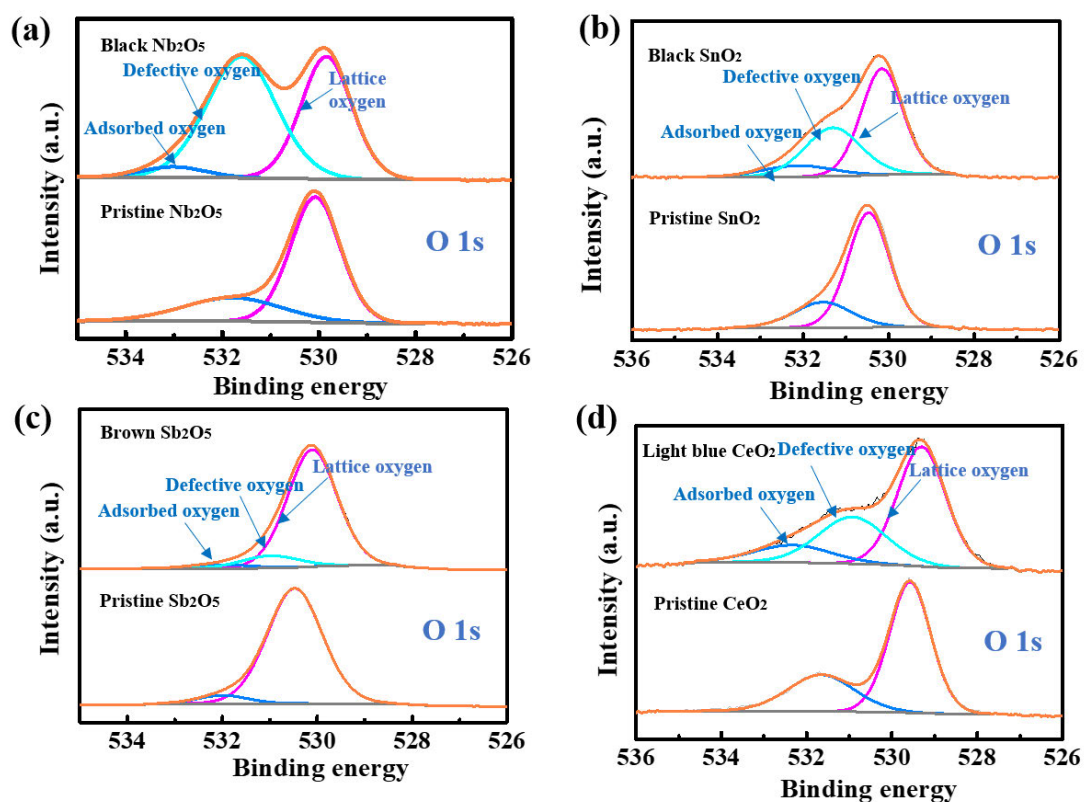


Fig. S14 XPS spectra (O1s) of pristine and n-butyl lithium treated oxide nanoparticles. a, Nb₂O₅. b, SnO₂. c, Sb₂O₅. d, CeO₂.

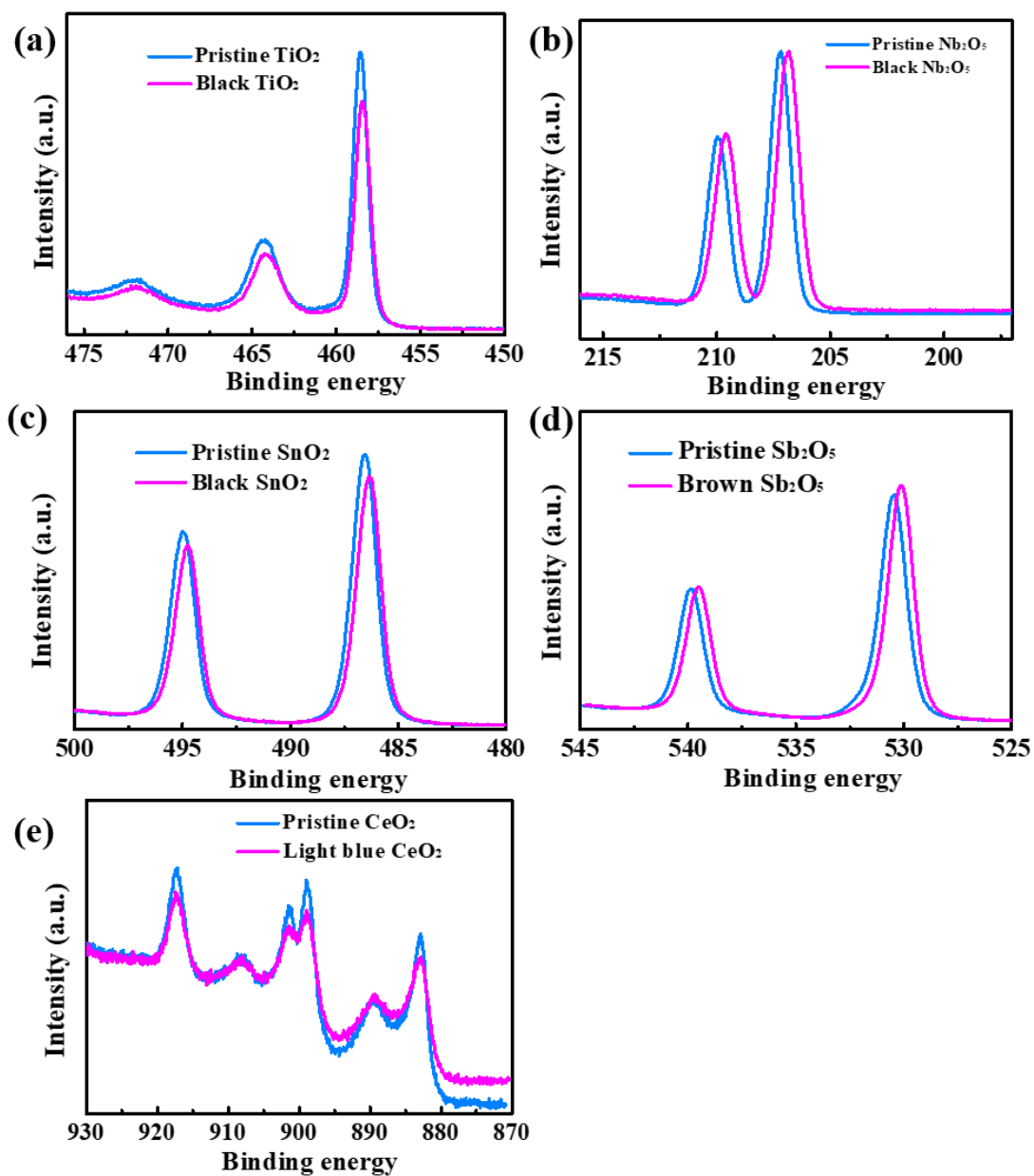


Fig. S15 XPS spectra of pristine and lithium reduced oxide nanoparticles. a, Ti 2p of TiO_2 . b, Nb 3d of Nb_2O_5 . c, Sn 3d of SnO_2 . d, Sb 3d of Sb_2O_5 . e, Ce 3d of CeO_2 .

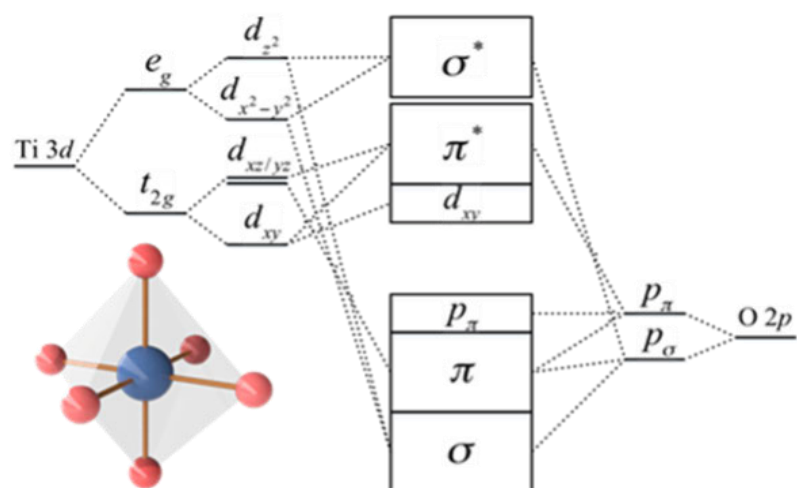


Fig. S16 The molecular-orbital bonding diagram for TiO_6 octahedron according to crystal field theory.

Table s1. Crystallographic details revealed in NPD

As-prepared pristine LTO Space group = $Fd-3m$						
$a = 8.3556(4) \text{ \AA}$, volume = $583.34(8) \text{ \AA}^3$						
Atom	Wyckoff site	x	y	z	$U_{\text{iso}} (\text{\AA}^2)$	Site occupancy factor (x 100%)
Li	$8a$	0.125	0.125	0.125	0.014(6)	1
Li	$16d$	0.5	0.5	0.5	0.016(1)*	0.167
Ti	$16d$	0.5	0.5	0.5	0.016(1)*	0.833
O	$32e$	0.2624(2)	0.2624(2)	0.2624(2)	0.011(1)	0.92(2)

As-prepared defected LTO Space group = $Fd-3m$						
$a = 8.3677(4) \text{ \AA}$, volume = $585.89(8) \text{ \AA}^3$						
Atom	Wyckoff site	x	y	z	$U_{\text{iso}} (\text{\AA}^2)$	Site occupancy factor (x 100%)
Li	$8a$	0.125	0.125	0.125	0.018(6)	1
Li	$16d$	0.5	0.5	0.5	0.018(2)*	0.167
Ti	$16d$	0.5	0.5	0.5	0.018(2)*	0.833
O	$32e$	0.2620(1)	0.2620(1)	0.2620(1)	0.012(1)	0.87(1)

CHAPTER 5

**ENGINEERING DEFECTS INTO NATURAL SiO₂ FOR SUSTAINABLE
LITHIUM STORAGE**

(To be Submitted to Nature Sustainability)

5.1 INTRODUCTORY REMARKS

This chapter is written in an article form for submission to *Nature Sustainability* in 2021.

The chapter reports defect-decorated electroactive SiO₂-based electrodes realised through simple quenching and carbon reduction methods. Crystalline SiO₂ is inactive for Li intercalation due to its poor intrinsic conductivity and has been excluded as a promising electrode. Here, we employed a facile quenching and carbon-reduction method to successfully realize defect-modified crystalline SiO₂. The developed electrodes achieved a surprising breakthrough in terms of Li insertion and a higher reversible capacity of 2774.3 mAh g⁻¹ at a current of 100 mA g⁻¹. Such outstanding lithium storage performance can be ascribed to the oxygen vacancies that activate the Li-ion insertion, and carbon coating that increases conductivity and suppresses volume expansion during alloying reactions. The crystalline SiO₂ in this work is extracted from natural montmorillonite and sand highlighting great innovation and broad commercial application prospects.

5.2. STATEMENT OF CONTRIBUTION

This chapter includes one first-authored paper. The bibliographic details of the co-authored paper, including all authors, are:

Zhong Su, Meng Li, Shangshu Qian, Chao Lai*, Jun Lu*, Shanqing Zhang*

Engineering Defects into natural SiO₂ for sustainable Lithium storage

Submitted to *Nature Sustainability*, 2021

My contribution to the paper included:

Conducting experiments, data collection and analysis, writing of the manuscript.

(Signed) _____ (Date) 15/04/2021

Name of Student: Zhong Su

(Countersigned) _____ (Date) 15/04/2021

Corresponding author of paper: Shanqing Zhang

(Countersigned) _____ (Date) 15/04/2021

Supervisor: Shanqing Zhang

5.3 ARTICLE 4

Engineering Defects into natural SiO₂ for sustainable Lithium storage

Zhong Su¹, Meng Li¹, Shangshu Qian¹, Chao Lai¹, Jun Lu^{*2}, Shanqing Zhang^{*1}

¹ Centre for Clean Environment and Energy, School of Environment and Science, Griffith University, Gold Coast Campus, Gold Coast, Queensland 4222, Australia. ² Chemical Sciences and Engineering Division, Argonne National Laboratory, Lemont, IL, USA.

* e-mail: junlu@anl.gov; s.zhang@griffith.edu.au.

Abstract

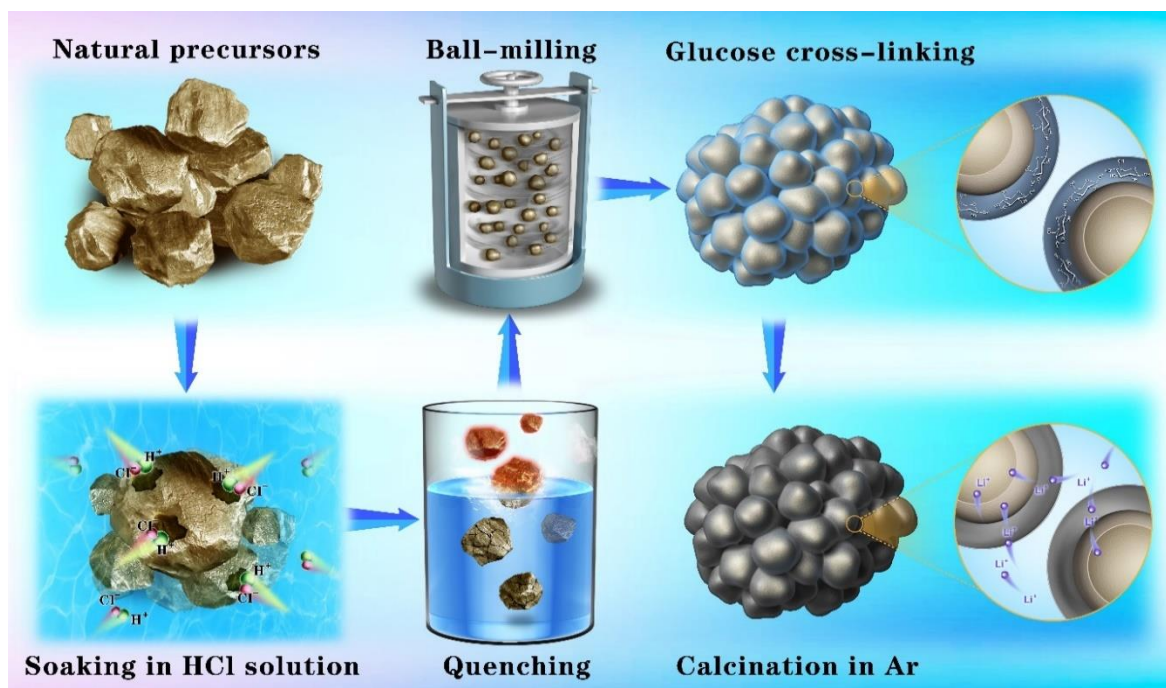
Crystalline SiO_2 has been excluded as an anode for Li-ion batteries due to its poor intrinsic electrical conductivity and inability for lithium-ion storage. To order to address this problem, we propose to use quenching, ball-milling and carbon-reduction methods to induce oxygen vacancy to natural SiO_2 (montmorillonite and sand), forming a highly electroactive SiO_2 (named as QMC- SiO_2) nanocomposites. In particular, the defect-decorated QMC-K30 from montmorillonite (K30) delivers a high capacity of $2774.3 \text{ mAh g}^{-1}$ at a current of 100 mA g^{-1} and excellent cycle stability (734.8 mAh g^{-1} at 500 mA g^{-1} after 200 cycles). Furthermore, the defect-decorated QMC-sand also shows a highly reversible capacity of 558.1 mAh g^{-1} at 500 mA g^{-1} after 500 cycles with superior cycling stability. Such outstanding lithium storage performance can be ascribed to the oxygen vacancies that activate the Li-ion insertion and facilitate the transfer of both electrons and Li-ions. Besides, the buffering layer generated through the carbon reduction can effectively restrain the volume expansion during the lithiation process and stabilize the electrode structure. More importantly, the wide availability of the natural SiO_2 makes the production of the proposed SiO_2 active materials green and sustainable.

Keywords: electroactive SiO_2 , oxygen vacancies, lithium ion battery, conductivity, natural precursor

Introduction

Under such overwhelming superiority of long cycle life, environment-friendly and high energy density, lithium-ion batteries (LIBs) serve as an essential energy storage system in the spotlight has successfully been applied into portable electronic devices^{1, 2, 3}. Yet, it is still far dissatisfied with the demand for electric vehicles and large-scale energy storage for pursuing high energy density. To address this urgent need, various novel anode materials with high energy density have been selected and studied to replace the commercial graphite anode (372 mAh g⁻¹).

Among these anode materials, silicon-based materials have been proposed as promising anodes due to their high energy density, abundant resources, and low cost^{4, 5, 6, 7}. Silicon (4200 mAh/g in theoretical capacity) is known to ten times higher than that of graphite. However, colossal volume change (>400%) induced by alloying reaction during the Li-ion intercalation process makes Si electrode materials pulverized and leads to poor electrical contact with the collector. Silicon oxides (SiO₂) possess relatively more minor volume expansion and much better than silicon. Particularly, for the initial Li-inserting process, the presence of O atoms in silicon oxides facilitates the in situ formation of an inert buffer matrix phase (Li₂O and Li₄SiO₄) around the silicon particles, thus effectively release the stress caused by volume expansion to some extent and protect the active silicon nanoparticles to avoid contact with the electrolyte during the subsequent Li-ion de-intercalation process^{8, 9, 10}. Nevertheless, crystalline SiO₂ possesses poor intrinsic conductivity and is deemed to be electrochemical inactive for inserting lithium. Towards the above challenge, amorphous SiO_x (0 ≤ x ≤ 2) offers a promising chance to enhance electrochemical performance^{11, 12, 13, 14}. The ultrafine nano-Si particles (a-Si) were uniformly dispersed in the SiO_x matrix and had more electrochemical active lithium storage phase. The generated Li₂O and Li₄SiO₄ matrix via initial lithiation buffer volume expansion and can act as a fast diffusion channel for lithium ions migration to silicon particles and optimized cycle and rate performance. However, the preparation process for amorphous SiO_x is normally complicated and costly.



Schemes 1. The preparation of defect-decorated QMC-SiO₂ nanocomposites (Note: QMC here stands for quenching, ball milling, and carbon reduction processes)

Faced with the challenges of crystalline SiO₂ in the Li⁺ charge storage, defect-decorated QMC-SiO₂ was designed to improve the electronic conductivity and electrochemical activity for Li⁺ inserting, as shown in Scheme 1. Firstly, we extract crystalline SiO₂ from natural precursors by soaking in HCl solution, followed by repeated quenching processes. Based on our previous research, vacancy concentration increases with temperature exponentially and quenching can preserve the defects generated at high temperature in the crystal lattice¹⁵. The intense stress produced from the instantly significant temperature changes could frost the vacancy and/or cause the lattice distortion of objects, thus resulting in forming abundant oxygen vacancy (Ov) active sites and amorphous layer on the surface of crystalline SiO₂¹⁶. The ball-milling and carbon reduction process is conducted on quenched samples to further improve the reactivity and electronic conductivity. Ball-milling enables nanoparticles to pulverize to increases the reaction area and shorten Li⁺ migration distance. And the external carbon layer derived from carbon reduction (C-reduction) is beneficial for improving electrical conductivity and further enhance structural toughness for repetitive volume expansion and contraction during Li-ion

de-intercalation processes, also C-reduction at a high temperature can further increase the number of defective oxygen sites and facilitate surface disorder, enhancing Li-ion diffusion rate and kinetic performance.

Results and discussion

The morphologies and structure of the obtained SiO₂ composites derived from montmorillonite (K30) were characterized by SEM and TEM (Figure 1). As shown in Figure 1a, from where the large irregular bulk structure of pristine K30 (P-K30) can clearly be observed. The pulverization of particles occurs when encountered by quenching (Figure 1b) and ball milling (Figure 1c), respectively. Interestingly, the relative uniform nanoparticles are forming when subjected to the cooperative effect of quenching and ball milling (Figure 1d and 1e). To further reveal the influence of quenching on SiO₂, the high-resolution transmission electron microscopy (HRTEM) is applied and the obvious amorphous layer can be observed on the surface of crystalline SiO₂ (Figure 1f, marked as QM-K30). It is worth noting that the amorphous SiO₂ layer with more defective sites (oxygen vacancies, Ovs) help the Li-ion insertion and diffusion, and provide a promising chance to tightly crosslink the external carbon layer. Figure 1g-i shows the SEM and TEM images of the obtained QMC-K30 and it is noticeable from these pictures that after C-reduction all the SiO₂ nanoparticles are uniformly coated with a thin carbon layer (5-10 nm), which also can be further confirmed by the EDS mapping of QMC-K30 (Figure S1). This thin carbon layer is very helpful in improving electrical conductivity and enhancing the bearing ability for the stress generated by repeated expansion and contraction during Li-ion de-intercalation processes¹⁷. To further determine the effects of C-reduction, ball-milling and quenching on K30 nanoparticles, respectively. The C-reduced K30 (C-K30), Ball-Milling and C-reduced K30 (MC-K30) and Quenched and C-reduced K30 (QC-K30) samples were synthesized and their SEM picture were shown in Figure S2. To all appearances, no significant effect on K30 particles during the C-reduction process but the ball-milling pulverize and reduce the size of nanoparticles via mechanical collision. For quenching, more clastics were formed on the surface of large bulk under the transient high temperature generated by substantial contact stress.

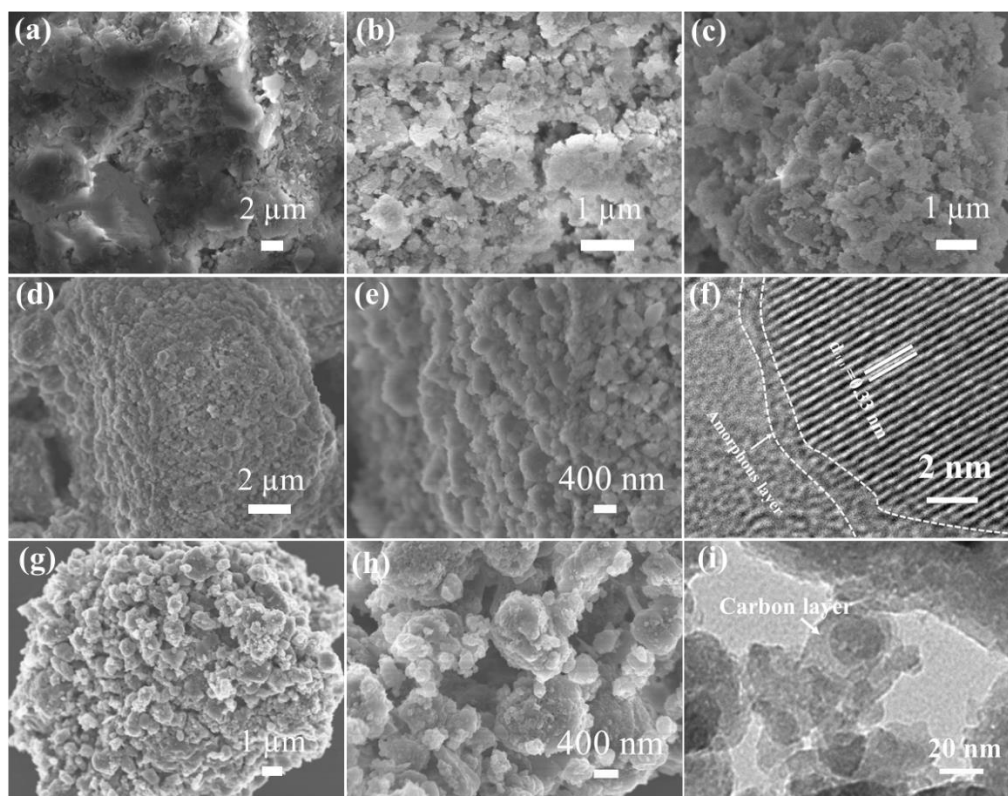


Figure 1 SEM of (a) Pristine K30 (P-K30), (b) K30 after dealing with HCl and quenching at 900 °C, (c) K30 after dealing with HCl and ball milling at 400 r/min; (d), (e), (f) SEM and HRTEM of K30 after dealing with HCl, quenching at 900 °C and ball milling at 400 r/min (marked as QM-K30); (g), (h), (i) SEM and HRTEM of carbon coating of quenched and milled K30 at 900 °C for 2 h (Marked as QMC-K30).

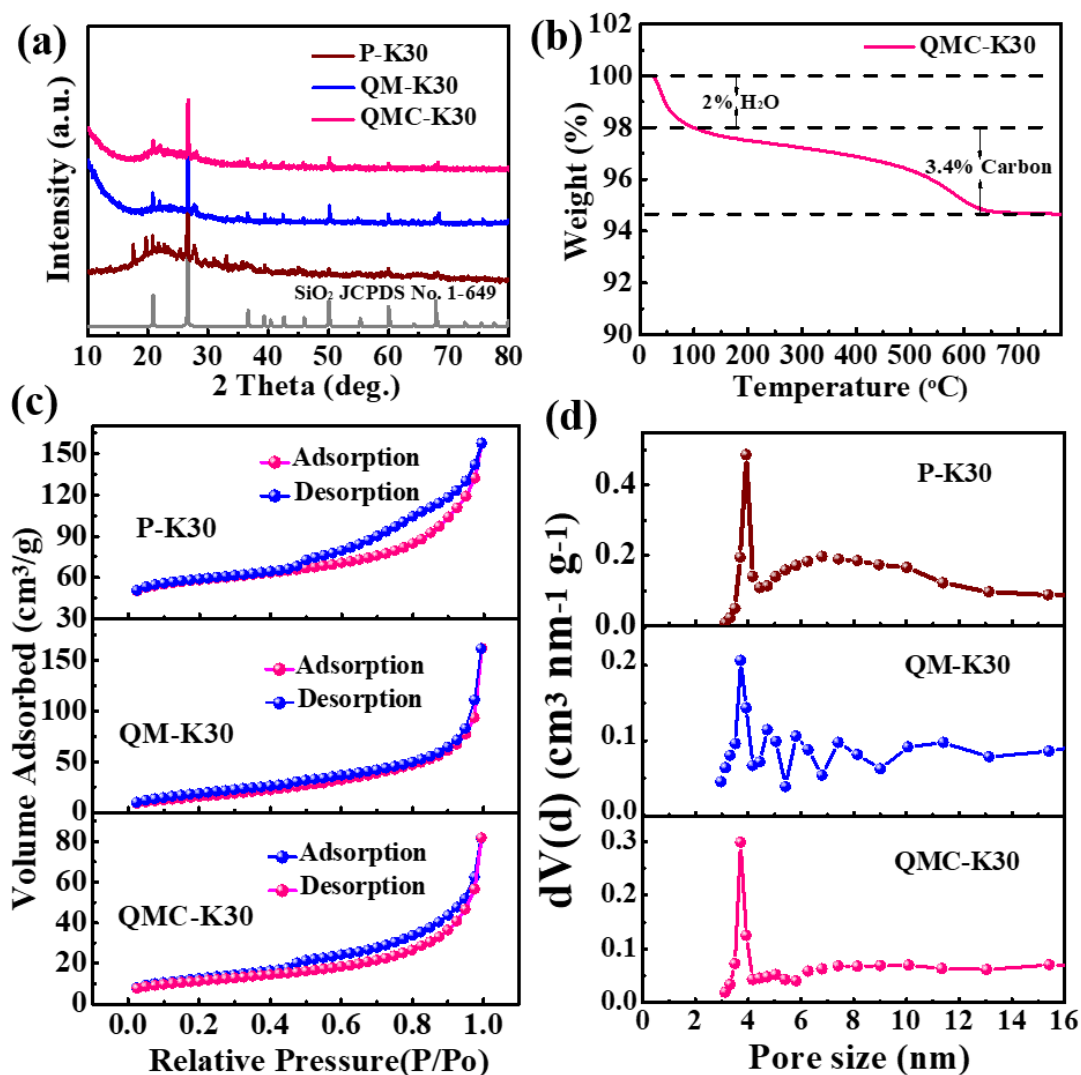


Figure 2 (a) XRD of the obtained K30; (b) the TGA of QMC-K30; and the N₂ adsorption/desorption curves (c) and the pore size distribution (d) of the obtained K30.

To reveal the phase composition of the obtained K30, powder X-ray diffraction (XRD) analysis was carried out (shown in Figure 2a). It is worth noting that well-resolved diffraction peaks of all K30 samples can be indexed to the standard card of SiO₂ (JCPDS No. 1-649), indicating that the highly crystalline SiO₂ can be well preserved¹⁸. The removal of impurity peaks in the P-K30 means that the impurity oxide (FeO, Al₂O₃ and MgO) has been washed by hydrochloric acid (Figure S3 and Table S1), which further ensures the pure phase of SiO₂. Besides, from thermogravimetric analysis (TGA) in the air (Figure 2b), a higher SiO₂ content up to 94.8wt% can be obtained in the final product. Figure 2c and

2d show the N₂ adsorption-desorption and the corresponding pore size distribution curve of the obtained K30 composites. A typical type IV characteristic with a higher hysteresis loop can be observed and correspond to the mesoporous structure¹⁹. Notably, the surface area increased from 75.359 m² g⁻¹ to 106.493 m² g⁻¹ due to the particle pulverization of P-K30 after treating with hydrochloric acid, quenching and ball-milling, while reducing to 38.806 m² g⁻¹ when coating with a crosslink carbon layer. This further reveals that the formation of the carbon layer was tightly attached to the SiO₂ nanoparticles, and this is consistent with the TEM results (Figure 1i).

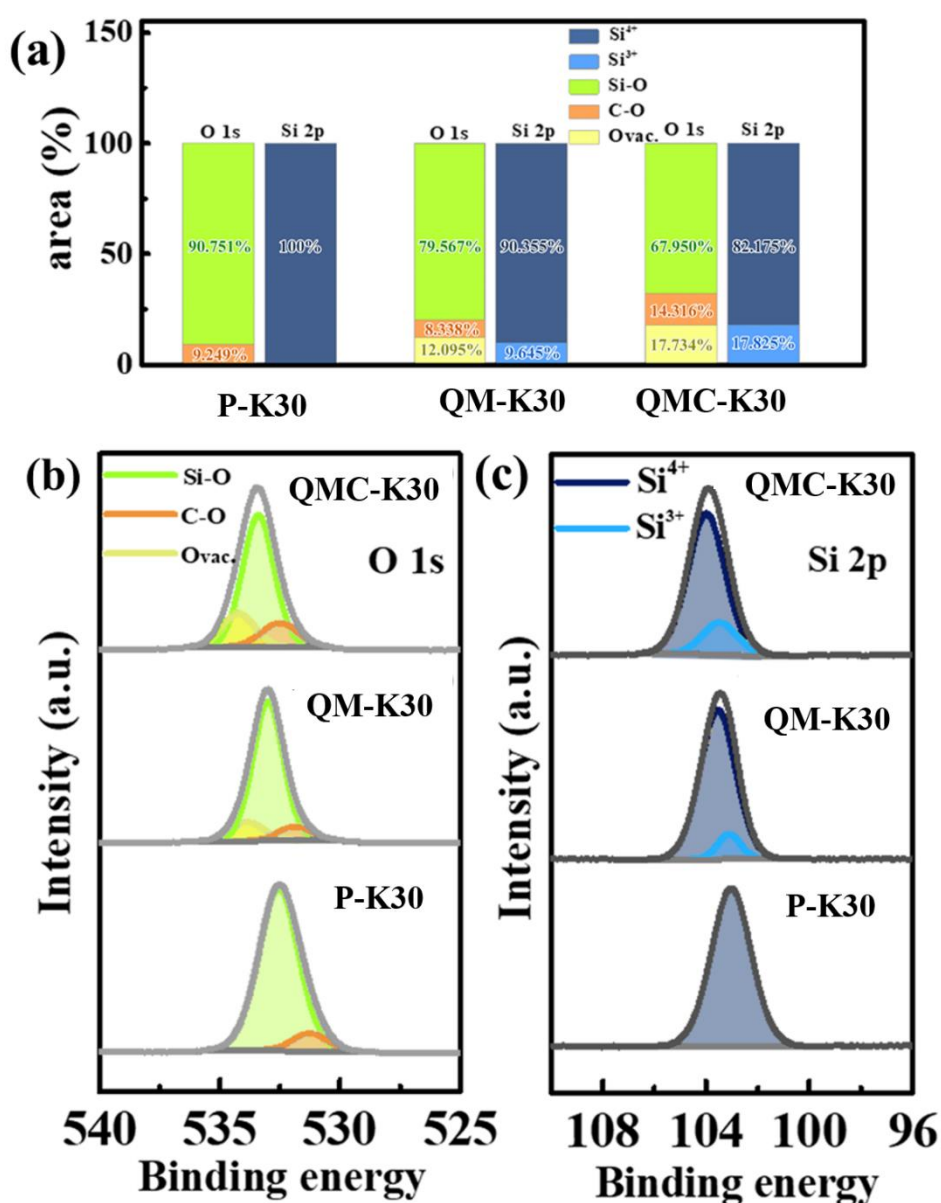


Figure 3 (a)The percentage of Valence state calculated based on O 1s area and Si 2p area; the high-resolution XPS spectra of O1s (b) and Si2p (c).

To further illustrate the effects of quenching and carbon reduction on crystalline SiO₂, the chemical states of O and Si in all the obtained SiO₂ samples are analysed by the XPS spectrum. As shown in Figure S4a, all the samples show the typical peaks of O1s, Si2p and C1s in the survey spectra. From the high-resolution O1s XPS spectra (Figure 3b), the extra peaks observed in both QM-K30 and QMC-K30 samples near 533.9 eV are related to oxygen vacancies, with the corresponding concentration of 12.095% and 17.734%, respectively (Figure 3a)²⁰. Another two typical O1s peaks around at 531.2 eV and 532.5 eV can be attributed to the C-O and Si-O bonding^{21, 22}. For the Si2p XPS spectra shown in Figure 3c, as expected, the typical Si³⁺ peaks (103.1 eV) occur in the QM-K30 and QMC-K30 samples^{21, 23}, and their concentrations are 9.645% and 17.825%, respectively (Figure 3a). Remarkably, the formation of Vo and Si³⁺ peaks in the QM-K30 certifies that oxygen vacancies and Si³⁺ caused by lattice distortion at high temperatures can be preserved after the rapid cooling process. Also, C-reduction can further increase Vo and Si³⁺ and deepen the disorder layer via reducing SiO₂ in situ. Furthermore, the gradual peak shifting to higher energy in both O1s and Si2p XPS spectra illuminates the effect of the disorder layer after undergoing quenching and C-reduction (shown in Figure S4b-c).

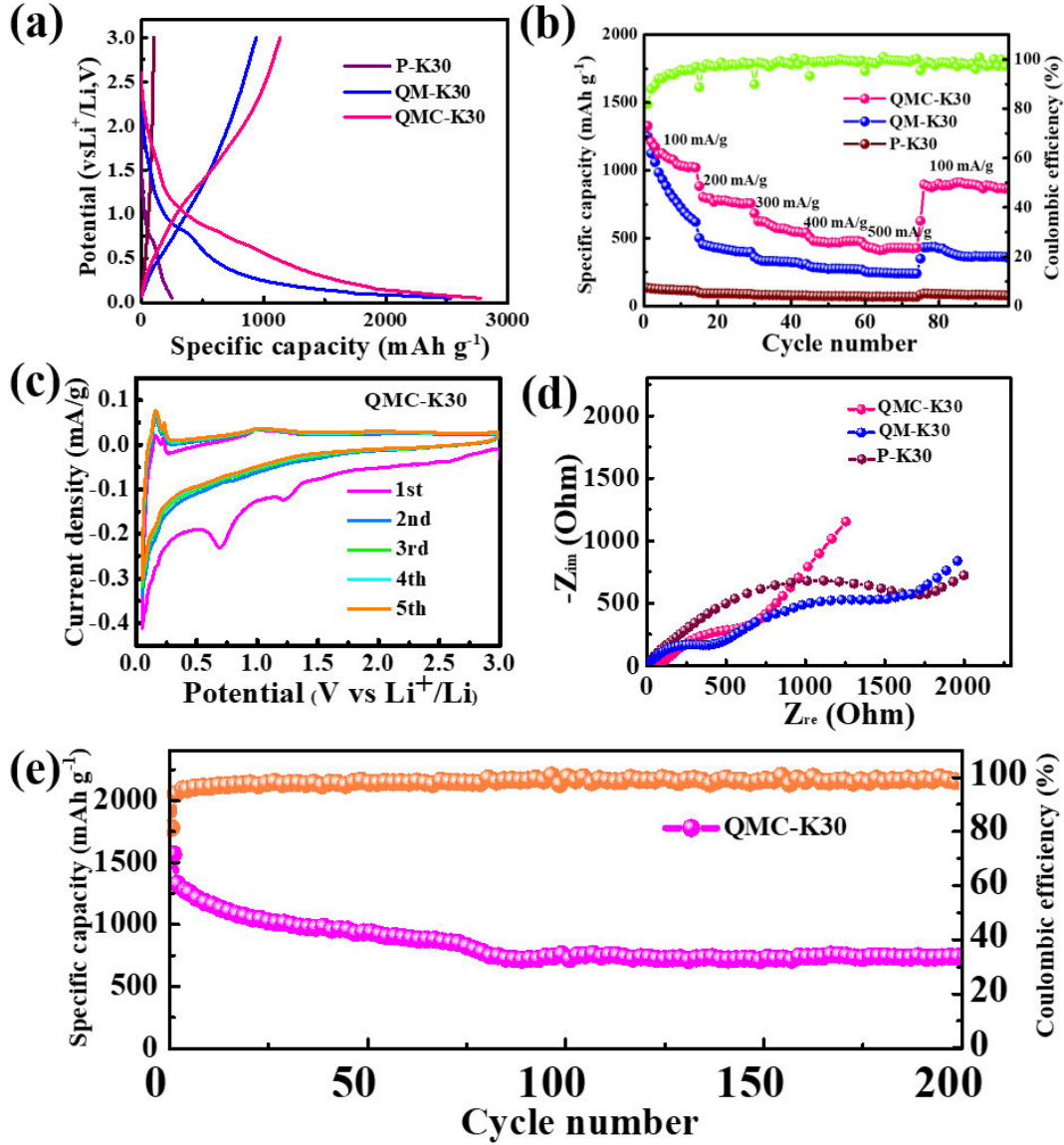


Figure 4 (a) The initial charge-discharge profiles of the obtained K30 at 100 mA g⁻¹; (b) the performance of obtained K30 at different rate after initial activation; (c) the CV curves of QMC-K30; (d) EIS of QMC-K30, QM-K30 and P-K30 after 30 cycles; and (e) the long cycle performance of QMC-K30 at 500 mA g⁻¹.

The Li⁺ charge storage performance of the obtained K30 electrodes was tested via self-assembling half batteries between 0.05 V and 3 V. Figure 4a shows the discharge/charge curves of the obtained K30 electrodes. The QMC-K30 sample presents a higher initial discharge capacity of 2774.3 mAh g⁻¹ at the current of 100 mA g⁻¹ with a lower coulomb efficiency (40.91%), but much better than the MC-K30 and P-K30. Notably, such a high irreversible capacity can be attributed to the irreversible process in which lithium reacts with SiO₂ to form a buffer matrix phase (Li₂O and Li₂SiO₄)^{8, 23}. Figure 4b

presents the rate performance of the obtained K30 at 100 mA g⁻¹. The QMC-K30 delivers a higher reversible capacity of 1327.8 mAh g⁻¹, 883.2 mAh g⁻¹, 683.3 mAh g⁻¹, 480.9 mAh g⁻¹ and 431.6 mAh g⁻¹ at a different rate of 100 mA g⁻¹, 200 mA g⁻¹, 300 mA g⁻¹, 400 mA g⁻¹, and 500 mA g⁻¹, respectively. It can still obtain a high capacity of 871.1 mAh g⁻¹ when the rate returns to 1C after 100 cycles, which can be ascribed to the middle non-crystalline SiO₂ layer and external carbon layer with abundant active sites to facilitate the transfer of electrons and lithium ions. Besides, to investigate the role of C-reduction, quenching and ball-milling on the electrochemical performance, respectively, the C-K30, MC-K30, and QC-K30 electrodes were prepared and tested the charge and discharge behavior at 100 mA g⁻¹ (Figure S5). Interestingly, QC-K30 with relatively larger particles (as shown in Figure S1) can still deliver a higher capacity of 827.9 mAh g⁻¹ at 100 mA g⁻¹ after 30 cycles, while the MC-K30 and C-K30 present relatively poor capacity of 322.9 mAh g⁻¹ and 236.7 mAh g⁻¹, respectively. These results can fully confirm that Vo in lattice plays a vital role in activating lithium-insertion; reduced particle size via ball-milling can effectively shorten the diffusion path of Li-ions during the charge and discharge process; the carbon layer served as a carrier for electron transfer. These mechanisms together improve electrical conductivity and suppress volume expansion. Therefore, under the combined actions of quenching, milling and C-reduction, the defect-modified crystalline SiO₂ exhibits such remarkable electrochemical properties. In addition, the lithium de-intercalation process of QMC-K30 was further investigated by the CV curves with the voltage range of 0.05-3V at a scan rate of 0.1 mV s⁻¹ (Figure 4c). The three obvious cathodic peaks in the initial discharge process can be observed, the smaller peak around 1.2 V can be attributed to the irreversible reaction of Li and SiO₂ to generate Li₂O, Si and Li₂SiO₄ phase, while the broad peak located at 0.75 V corresponds to the formation of solid electrolyte interphase (SEI) layer^{7, 23}. Both two peaks disappear in the subsequent cycle to verify the reason for initial irreversible capacity. Towards the third peak below at 0.25 V, it represents the alloying reaction between Li and Si, which is also the major energy storage reaction in the subsequent cycle²⁴. The anodic peak at around 0.2 V is responsible for the de-lithiation behavior of Li_xSi^{25, 26}. After the initial irreversible process, the overlapped CV curves indicate a highly reversible alloying reaction of Li and Si. Moreover, similar results of the Li⁺ de-intercalation process can also be found in the CV curves of QM-K30 and P-K30

(Figure S6 and Figure S7). Electrochemical Impedance Spectroscopy (EIS) testing was performed to explore the interfacial impedance of the obtained K30 electrodes before and after cycling. As shown in Figure S8 (before cycling), all the Nyquist plots show a single semicircle at high-frequency region and an inclined line at low-frequency regions²⁷, but a much smaller charge-transfer resistance (R_{ct}) can be achieved in the QMC-K30 compared with another two samples. This indicates that the middle amorphous SiO_2 layer with abundant structural defects (V_o and Si^{3+}) and the external carbon layer can greatly improve the electrical conductivity. After cycling 30 cycles at 100 mA g^{-1} , no obvious change in R_{ct} but an additional semicircle is found in the QMC-K30 and QM-K30 samples. Simultaneously, P-K30 only presents a larger single semicircle (Figure 4d), suggesting the buffering media can help to stabilize the electrode structure and form a stable solid electrolyte interface (SEI) layer²⁸. Also, the first semicircle of QMC-K30 is significantly smaller than that of QM-K30, indicating that the external carbon layer is beneficial to electron charge transfer and significantly reduces the interface impedance of the electrode. The long cycle life of QMC-K30 is evaluated at the current of 500 mA g^{-1} (Figure 4e). A higher initial reversible capacity of $1567.5 \text{ mAh g}^{-1}$ can be achieved, and remain 734.8 mAh g^{-1} after 200 cycles with superior cycling stability. In addition, the charge-discharge curves of QMC-K30 at 1st, 2nd, 50th, 100th, 150th and 200th cycles exhibit a highly reversible alloying reaction at a high current of 500 mA g^{-1} (Figure S9).

For the sake of gaining insight into the electrochemical active of structural defects and the effect of the buffering layer for the electrode structural stability, the mechanism of Li^+ de-intercalation behaviour in QMC-K30 electrode and P-K30 electrode were shown in Figure 5a. For the P-K30 electrodes, repeated Li^+ de-intercalation in the cycle process makes the P-K30 electrode continuously expand and contract, in turn leading to pulverization of the electrode surface. While the buffering layer (amorphous SiO_2 layer and carbon layer) helps to relieve stress changes cause by Li^+ de-intercalation process and ensures the structural stability of the QMC-K30 electrode. This conjecture can be confirmed by the SEM image of QMC-K30, QM-K30 and P-K30 electrodes after 30 cycles (Figure 5b-d). Obvious cracks can be found on the P-K30 electrodes while the QM-K30 and QMC-K30 electrodes present a relatively flat surface. Also, the smooth electrode surface contributes to the formation of the stable solid

electrolyte interface (SEI) layer²⁸. To verify that oxygen vacancies help activate Li inserting into crystalline SiO₂ lattice, ex-situ XPS was performed to characterize the Li⁺ charge storage mechanism of the obtained QMC-K30 and P-K30 electrodes (shown in Figure 5e and 5f). The obvious two peaks observed in the QMC-K30 electrode near 101.68 eV and 98.5 eV are related to LiSiO₄ and Si²⁹, while those two peaks cannot be found in the P-K30 electrode. Such an opposite result indicating that oxygen vacancy indicates that oxygen vacancy helps Li⁺ intercalate into crystalline SiO₂, followed by alloying reactions mechanism in energy storage.

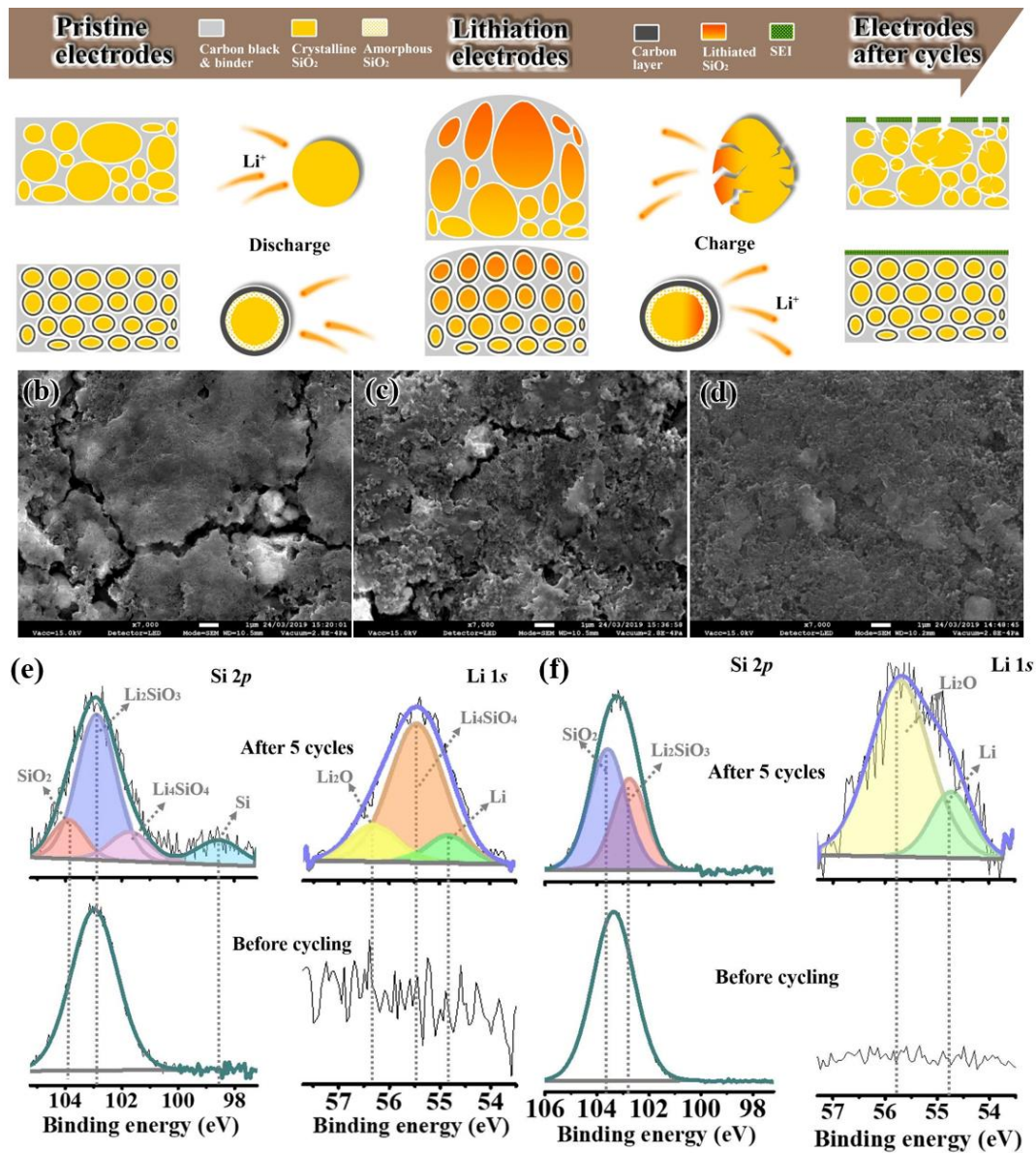


Figure 5 (a) Reaction mechanism of Li⁺ de-intercalation in QMC-K30 electrode and P-K30 electrode. SEM of (b) P-K30 electrodes, (c) QM-K30 electrodes, (d) QMC-K30 electrodes after cycling 30 cycles at 100 mA g⁻¹; the high-resolution XPS spectra of Si 2p and Li 1s in QMC-K30 electrodes (e) and P-K30 electrode (f)

In order to improve the commercial application prospect of SiO₂ and further reduce the production cost, natural sand is selected and treated by the same experimental procedures as above. From the SEM image shown in Figure 6a, a larger bulk irregular structure can be seen clearly in the pristine sand (P-sand) after treating with hydrochloric acid, quenching and ball-milling, the relatively uniform smaller nanoparticles were formed and shown in Figure 6b (marked as QM-Sand). Next, a thin carbon layer was tightly coated onto the surface of QM-Sand after C-reduction (Figure 6c-d, sample marked as QMC-Sand). Similarly, the influence of quenching and ball-milling on the structure of sand was further analysed, respectively and the SEM images are presented in Figure S10-11. Particle pulverization occurs by mechanical collision while quenching produces lots of clastic on the surface of the particles under tremendous stress from the instant temperature change, while no significant change on the morphology by C-reduction. The X-ray diffraction (XRD) was used to analyse the phase composition of the obtained sand (Figure S12), all the obvious diffraction peaks stand for highly crystalline SiO₂ and can be deemed to the standard card of SiO₂ (JCPDS No. 5-490)³⁰. The TGA analysis was tested that a higher SiO₂ content (92.7%) can be preserved in the QMC-Sand samples (Figure S13). XPS spectrum was carried out to further investigate the chemical states of P-Sand, QM-Sand and QMC-Sand samples and the O1s and Si2p spectrum results shown in Figure 6e-g. Similar to K30 results, the extra (V_{os}) peak can be found in the QM-Sand and increase largely in the QMC-Sand, with V_o concentrations of 11.563% and 18.509%, respectively. Correspondingly, the peak of Si³⁺ ion appears in the QM-Sand and QMC-Sand samples with a concentration of 10.239% and 18.246%, respectively. Besides, the survey XPS spectrum of the obtained sand samples was shown in Figure S14a and indicates that all the samples contain the C, Si and O elements. However, a peak shifting to larger of O1s and Si2p can be observed in the QM-Sand and QMC-Sand (Figure S14b-c).

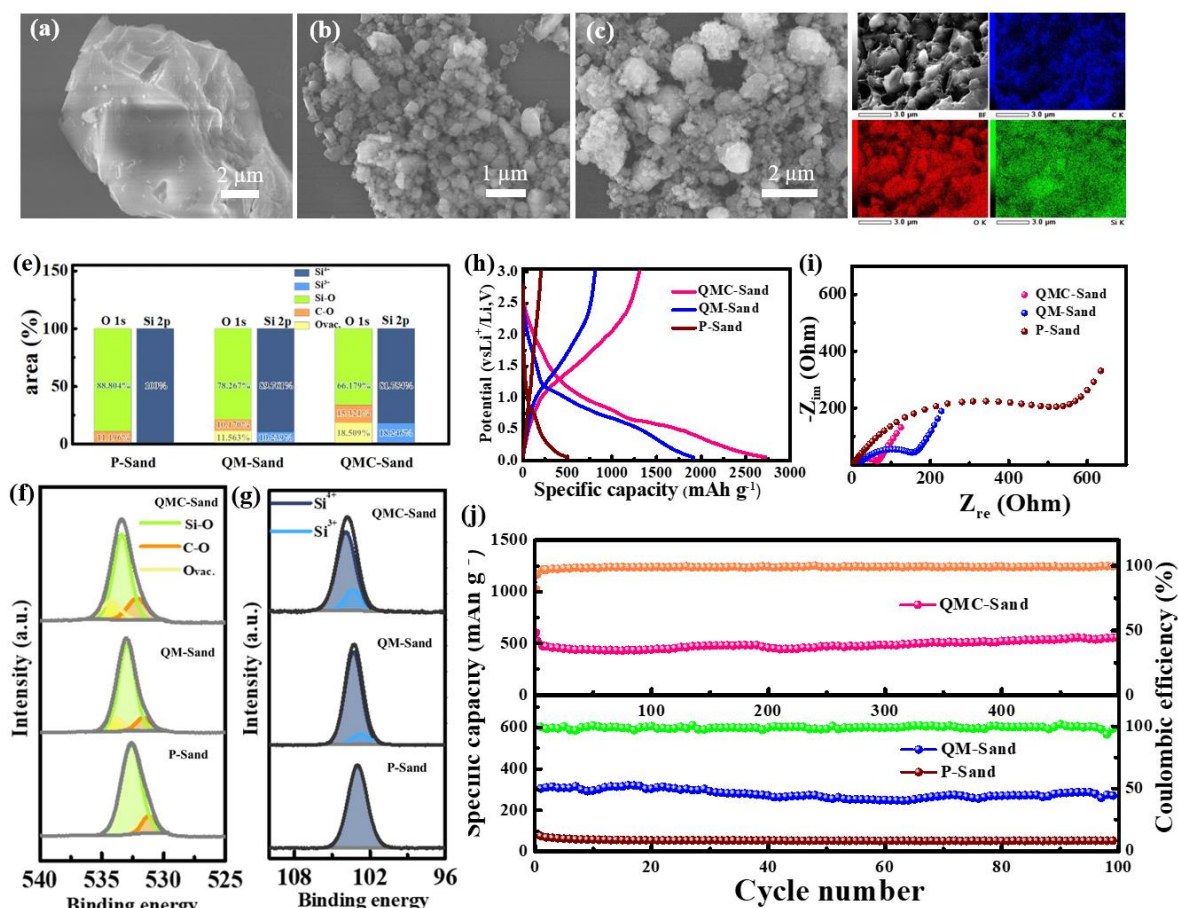


Figure 6 (a) SEM of pristine sand; (d) the SEM of sand after dealing with HCl, quenching at 900 °C and ball milling at 400 r/min (marked as QM-Sand); (c) the SEM of QM-Sand after C-reduction (marked as QMC-Sand); (d) the mapping of QMC-Sand; (e-g) the percentage of Valence state of the obtained sand calculated based on O 1s area and Si 2p area and the high-resolution XPS spectra of O1s and Si2p; (h) the charge-discharge profiles of the obtained sand at 100 mA/g; (i) the EIS of the obtained Sand; and (j) the long cycle performance of QMC-Sand at 500 mA g⁻¹.

Also, self-assembled batteries were investigated to analyse the electrochemical performance of the obtained sand samples. Figure 6h shows the initial discharge-charge curves of the QMC-Sand, QM-Sand and P-sand at 100 mA g⁻¹. The QMC-Sand delivers a discharge capacity of 2725.4 mAh g⁻¹ and a charge capacity of 1307.4 mAh g⁻¹, which are higher than that of the QM-Sand and P-Sand. Such a high initial irreversible capacity can be attributed to the formation of Li₂O and Li₄SiO₄ matrix and the stable SEI layer^{7, 23}. Figure 6i shows the EIS results to illustrate the interfacial impedance of QMC-Sand, QM-Sand and P-Sand. The QMC-Sand present a lower charge-transfer resistance (R_{ct}), which means that

QMC-Sand possesses a better-conducting electron and Li-ion characteristic²⁷. Also, the QMC-Sand reveals a superior long cycle life at 500 mA g⁻¹ after initial activation and the capacity can be maintained at 558.1 mAh g⁻¹ after 500 cycles with lowering the capacity fade (only 0.0156% per cycle, Figure 6j). This can be further confirmed by the charge-discharge curves of QMC-Sand at different cycles (Figure S15). Such stable long cycle performance convinces that the middle amorphous SiO₂ layer and the external carbon layer can effectively active the Li-ion insertion, improve the electron and ionic conductivity, and more importantly inhibit the volume expansion caused by the alloying reaction during the charge and discharge processes. These play together to ensure a stability of the electrode structure.

Conclusion

In brief, in order to address three intrinsic issues of crystalline SiO₂, including poor electrical conductivity, electrochemically inactive for inserting lithium and volume expansion, the defect-modified electroactive SiO₂-based anodes were successfully designed and synthesized through simple quenching and C-reduction methods. The oxygen vacancies in the SiO₂ lattice help to enhance electronic conductivity and active lithium insertion. While the external carbon layer induced from C-reduction not only improves the electrical conductivity but also further reduces SiO₂ to increase defective sites and deepen the middle amorphous layer. More importantly, this ingenious protected buffering layer design can effectively inhibit the volume expansion caused by Li-ion de-intercalation processes and help to stabilize the electrode structure. Therefore, under the protection of a unique protected buffering layer, the defect-decorated QMC-K30 derived from montmorillonite exhibits an outstanding capacity (871.1 mAh g⁻¹ after 100 cycles at a different rate) and superior cycling stability (734.8 mAh g⁻¹ at 500 mA g⁻¹ after 200 cycles). In addition, the defect-decorated QMC-Sand extracted from natural sand also presents excellent lithium storage performances, demonstrating a higher reversible capacity of 558.1 mAh g⁻¹ at 500 mA g⁻¹ after 500 cycles. The promising lithium storage performances of defect-decorated natural SiO₂ fully shed light on the advantages of defect engineering in activating Li-ion insertion and optimizing electronic structure. Moreover, SiO₂ extracted from montmorillonite and sand is cheap and abundant in resources, indicating considerable potential in commercial applications.

Acknowledgements

We are grateful for the financial support from the Australia Research Council Discovery Projects DP170103721 and DP180102003.

Additional information

Supplementary information is available for this paper.

Reference

1. Dunn B, Kamath H, Tarascon J-M. Electrical energy storage for the grid: a battery of choices. *Science* **334**, 928-935 (2011).
2. Tang Y, Zhang Y, Li W, Ma B, Chen X. Rational material design for ultrafast rechargeable lithium-ion batteries. *Chem. Soc. Rev.* **44**, 5926-5940 (2015).
3. Janek J, Zeier WG. A solid future for battery development. *Nat. Energy* **1**, 1-4 (2016).
4. Liu H-K, Guo Z, Wang J, Konstantinov K. Si-based anode materials for lithium rechargeable batteries. *J. Mater. Chem.* **20**, 10055-10057 (2010).
5. Son IH, *et al.* Silicon carbide-free graphene growth on silicon for lithium-ion battery with high volumetric energy density. *Nat. Commun.* **6**, 1-8 (2015).
6. Magasinski A, Dixon P, Hertzberg B, Kvit A, Ayala J, Yushin G. High-performance lithium-ion anodes using a hierarchical bottom-up approach. *Nat. Mater.* **9**, 353-358 (2010).
7. Liu Z, *et al.* Silicon oxides: a promising family of anode materials for lithium-ion batteries. *Chem. Soc. Rev.* **48**, 285-309 (2019).
8. Zhang Y, Li Y, Wang Z, Zhao K. Lithiation of SiO₂ in Li-ion batteries: in situ transmission electron microscopy experiments and theoretical studies. *Nano Lett.* **14**, 7161-7170 (2014).
9. Fu R, Zhang K, Zaccaria RP, Huang H, Xia Y, Liu Z. Two-dimensional silicon suboxides nanostructures with Si nanodomains confined in amorphous SiO₂ derived from siloxene as high performance anode for Li-ion batteries. *Nano Energy* **39**, 546-553 (2017).
10. Wang J, *et al.* Size effect on the growth and pulverization behavior of Si nanodomains in SiO anode. *Nano Energy* **78**, 105101 (2020).

11. Zhang L, *et al.* Hierarchically designed SiOx/SiOy bilayer nanomembranes as stable anodes for lithium ion batteries. *Adv. Mater.* **26**, 4527-4532 (2014).
12. Hu YS, *et al.* Superior storage performance of a Si@ SiOx/C nanocomposite as anode material for lithium-ion batteries. *Angew. Chem. Int. Ed.* **47**, 1645-1649 (2008).
13. Yu Q, *et al.* Ultrafine SiOx/C nanospheres and their pomegranate-like assemblies for high-performance lithium storage. *J. Mater. Chem. A* **6**, 14903-14909 (2018).
14. Liu Z, *et al.* Monodisperse and homogeneous SiOx/C microspheres: A promising high-capacity and durable anode material for lithium-ion batteries. *Energy Storage Mater.* **13**, 112-118 (2018).
15. Varotsos P, Alexopoulos K. On the possibility of the enthalpy of a Schottky defect decreasing with increasing temperature. *J. Phys. C: Solid State Phys.* **12**, L761 (1979).
16. Sushko P, Mukhopadhyay S, Stoneham A, Shluger A. Oxygen vacancies in amorphous silica: structure and distribution of properties. *Microelectron. eng.* **80**, 292-295 (2005).
17. Li H, Zhou H. Enhancing the performances of Li-ion batteries by carbon-coating: present and future. *Chem. Commun.* **48**, 1201-1217 (2012).
18. Kaminskas R, Barauskas I. Autoclaved aerated concrete waste as a micro-filler for portland cement. *Rev. Rom. Mater.* **49**, 244-250 (2019).
19. Voegtlin A, Matijasic A, Patarin J, Sauerland C, Grillet Y, Huve L. Room-temperature synthesis of silicate mesoporous MCM-41-type materials: influence of the synthesis pH on the porosity of the materials obtained. *Micropor. Mater.* **10**, 137-147 (1997).
20. Jiang X, *et al.* Characterization of oxygen vacancy associates within hydrogenated TiO₂: a positron annihilation study. *J. Phys. Chem. C* **116**, 22619-22624 (2012).
21. Hollinger G, Jugnet Y, Pertosa P, Duc TM. X-ray photoelectron spectroscopy of thermally grown silicon dioxide films on silicon. *Chem. Phys. Lett.* **36**, 441-445 (1975).
22. Thøgersen A, Selj JH, Marstein ES. Oxidation effects on graded porous silicon anti-reflection coatings. *J. Electrochem. Soc.* **159**, D276 (2012).
23. Chang W-S, Park C-M, Kim J-H, Kim Y-U, Jeong G, Sohn H-J. Quartz (SiO₂): a new energy storage anode material for Li-ion batteries. *Energy Environ. Sci.* **5**, 6895-6899 (2012).
24. Kirklin S, Meredig B, Wolverton C. High-throughput computational screening of new Li-ion battery anode materials. *Adv. Energy Mater.* **3**, 252-262 (2013).

25. Tian H, Tan X, Xin F, Wang C, Han W. Micro-sized nano-porous Si/C anodes for lithium ion batteries. *Nano Energy* **11**, 490-499 (2015).
26. Kim YM, *et al.* Titanium silicide coated porous silicon nanospheres as anode materials for lithium ion batteries. *Electrochim. Acta.* **151**, 256-262 (2015).
27. Barai A, Chouchelamane GH, Guo Y, McGordon A, Jennings P. A study on the impact of lithium-ion cell relaxation on electrochemical impedance spectroscopy. *J. Power Sources* **280**, 74-80 (2015).
28. Eom K, Joshi T, Bordes A, Do I, Fuller TF. The design of a Li-ion full cell battery using a nano silicon and nano multi-layer graphene composite anode. *J. Power Sources* **249**, 118-124 (2014).
29. Chen J, *et al.* Electrolyte design for LiF-rich solid–electrolyte interfaces to enable high-performance micro-sized alloy anodes for batteries. *Nat. Energy* **5**, 386-397 (2020).
30. Iqbal Y, Lee WE. Fired porcelain microstructures revisited. *J. Am. Chem. Soc.* **82**, 3584-3590 (1999).

Supporting information

Engineering Defects into natural SiO₂ for sustainable Lithium storage

Zhong Su¹, Shangshu Qian¹, Meng Li¹, Chao Lai¹, Jun Lu^{*2}, Shanqing Zhang^{*1}

¹ Centre for Clean Environment and Energy, School of Environment and Science, Griffith University, Gold Coast Campus, Gold Coast, Queensland 4222, Australia. ² Chemical Sciences and Engineering Division, Argonne National Laboratory, Lemont, IL, USA.

*e-mail: junlu@anl.gov; s.zhang@griffith.edu.au.

Experimental Section

Preparation of QMC-K30 materials: Firstly, montmorillonite (K30) was repeatedly soaked and washed with HCl (1 mol/L) until the solution appears transparent to ensure the removal of impurity oxides. Followed by washing with water and drying at 60 °C, the obtained K30 was repeatedly quenched as following process (10 times): calcined at 900 °C for 1 h in the muffle furnace and then immediately thrown into liquid nitrogen. Next, the quenched k30 was transferred to the ball mill-tank and ball-milling at 400r/min for 3h. After that, the quenched and milled K30 was soaked in glucose solution (1 mol/L) accompanied by ultrasound for 2 h. After centrifugation and dry at 60 °C, the obtained QM-K30@glucose was disposed by further C-reduction via calcined at 900 degrees for 2h in Ar atmosphere and thus to form the final QMC-K30. As a comparison and analysis of quenching, ball grinding and carbon reduction on the K30, a series of samples including the Quenched K30 (Q-K30), Ball-milled K30 (M-K30), C-reduced K30 (C-K30), Quenched and Ball-milled K30 (QM-K30), Ball-Milled and C-reduced K30 (MC-K30) as well as Quenched and C-reduced K30 (QC-K30) were synthesized separately through the same process described above.

Preparation of QMC-Sand materials: the natural sand was collected at Qingdao, China. After washing with water, the QMC-Sand was successfully synthesized in the same way as K30 described above. Also, as a comparison, the Quenched Sand (Q-Sand), Ball-milled Sand (M-Sand), C-reduced Sand (C-Sand), Quenched and Ball-milled Sand (QM-Sand), Milled and C-reduced Sand (MC-Sand) as well as Quenched and C-reduced Sand (QC-Sand) were prepared by the same method.

Materials characterization: The scanning electron microscopy (SEM, SU8020) and transmission electron microscopy (TEM, Tecnai G2 F20) images were collected to analyze the morphology and structure of obtained samples. X-ray diffraction (XRD) patterns were conducted on a Bruker D8 Advance diffractometer with Cu Ka radiation ($\lambda=1.5418 \text{ \AA}$). Brunauer-Emmett-Teller (BET) surface areas were tested by the Quantachrome Instruments Autosorb-iQ instrument. The carbon content of obtained samples were calculated by the Thermo-gravimetric analysis (TGA, Rigaku Thermoflex PTC-10A thermal analyzer) at heating rate of $5 \text{ }^{\circ}\text{C min}^{-1}$ in air. The chemical state of the obtained samples

were performed via X-ray photoelectron spectroscopy (XPS) analyser (Thermo ESCALAB 250XI). The composition of the prepared sample is measured from a fluorescence spectrometer (Bruker S2 Ranger)

Electrochemical measurement: the SiO_2 electrode (almost $1\text{mg}/\text{cm}^2$) was prepared by mixed the active materials (70%), superconducting carbon (20%), and polyvinylidene fluoride (PVDF, 10%) with N-methyl pyrrolidinone as the dispersant, while Lithium metal served as a reference electrode. The electrolyte was the 1 M LiPF_6 dissolved in the mixture solution of ethyl carbonate (EC), ethyl methyl carbonate (EMC), and dimethyl carbonate (DMC) with a volume ratio of 1:1:1. The charge and discharge process was tested by a LAND-CT2001A galvanostatic tester at room temperature with a voltage range from 0.05 V to 3 V. The cyclic voltammetry (CV) and electrochemical impedance spectroscopy (EIS) tests were performed on a Solartron 1287 electrochemical workstation.

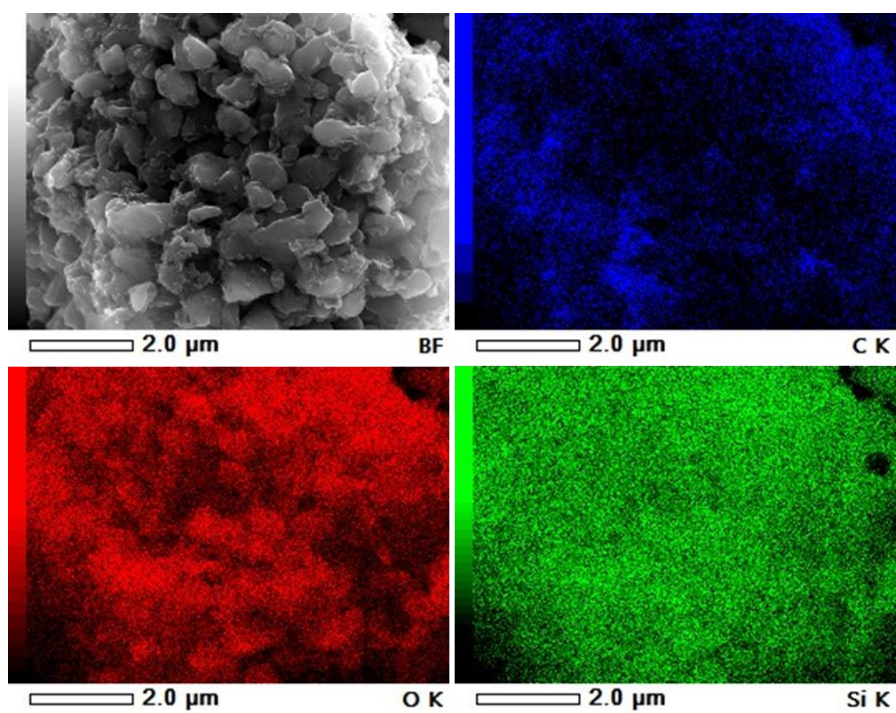


Figure S1 EDS mapping of QMC-K30

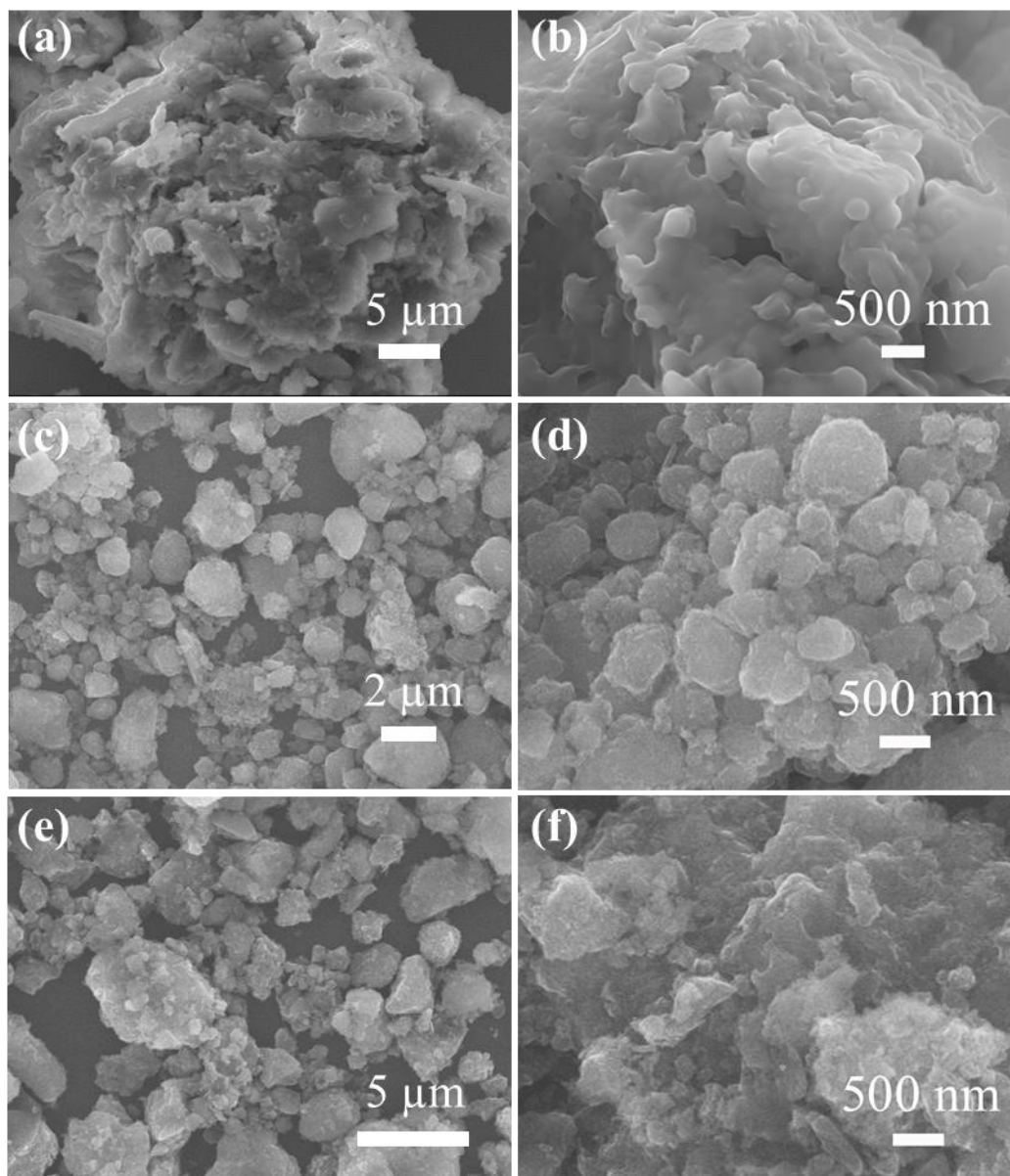


Figure S2 SEM of (a), (b) C-K30; (c), (d) MC-K30; (e), (f) QC-K30

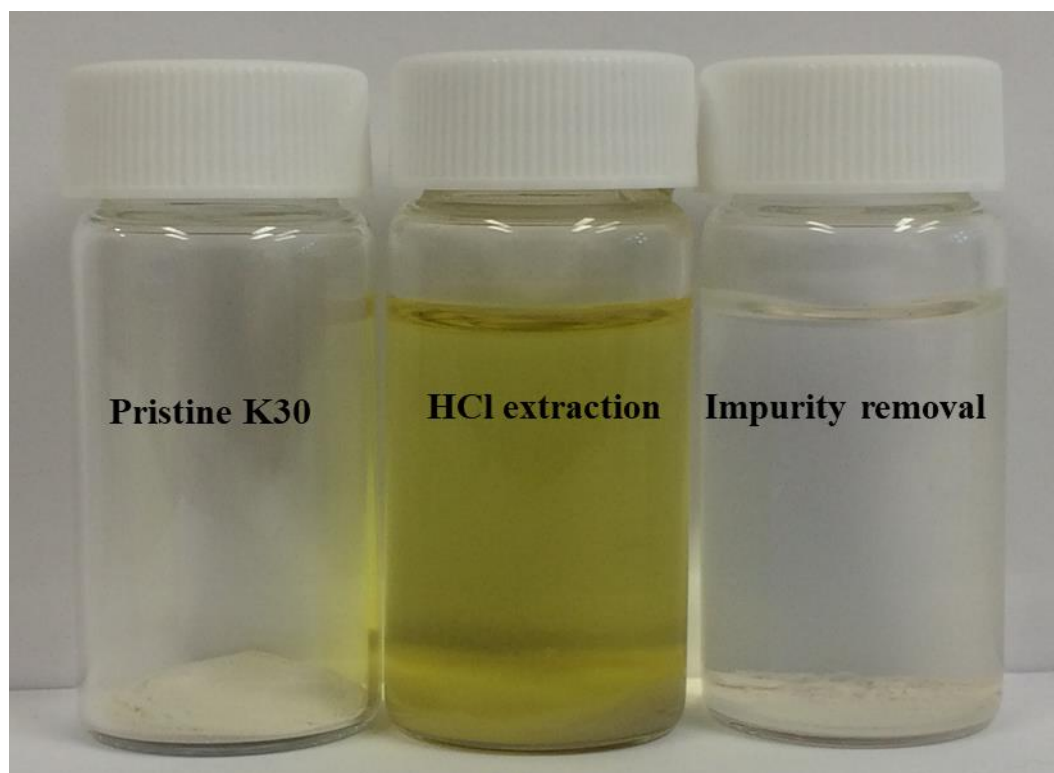


Figure S3 the pristine K30 (left); soak in HCl to remove impurities (middle); Impurities have been removed by HCl (right)

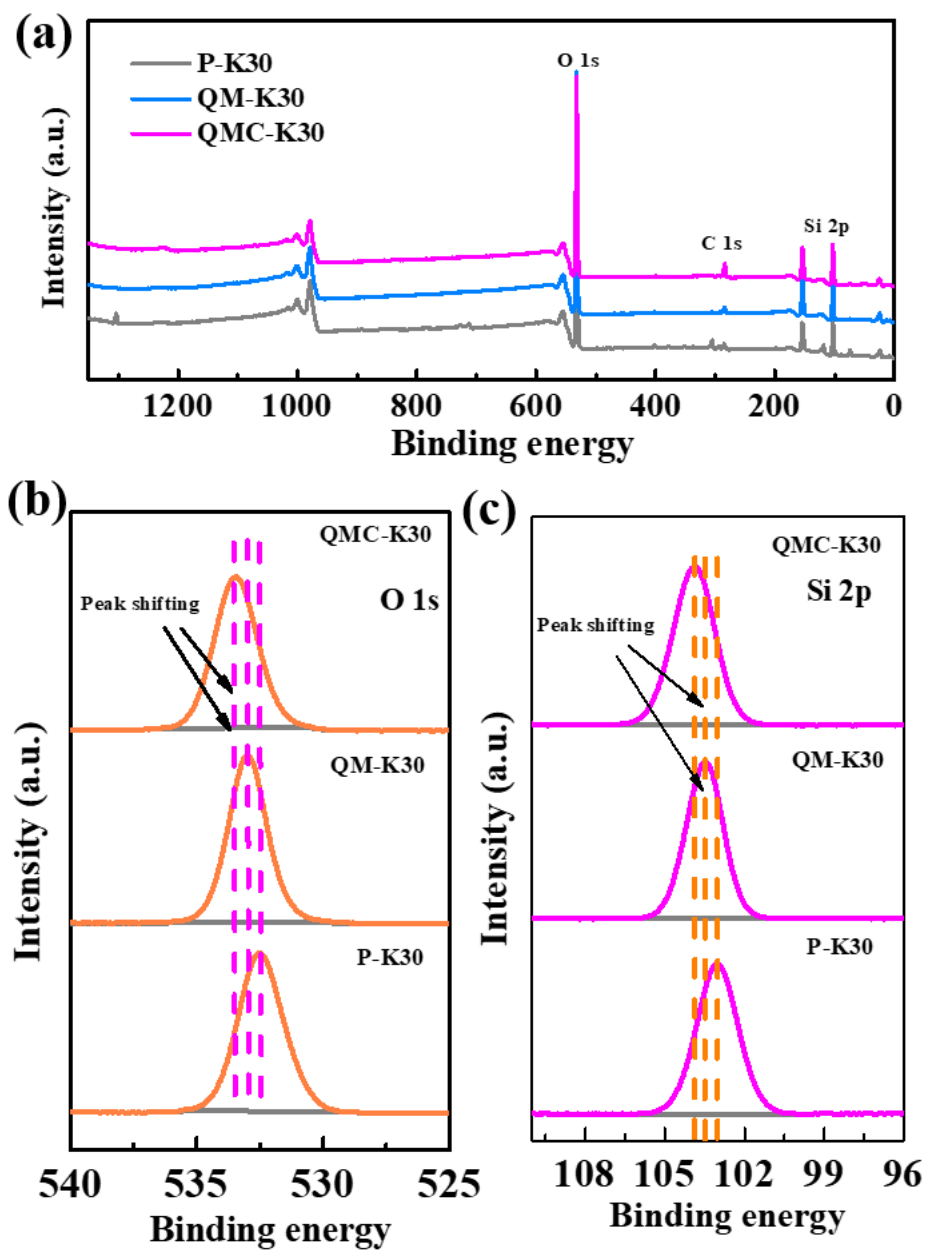


Figure S4 The survey XPS spectra of obtained K30 (a); the high-resolution XPS spectra of O1s (b) and Si2p (c).

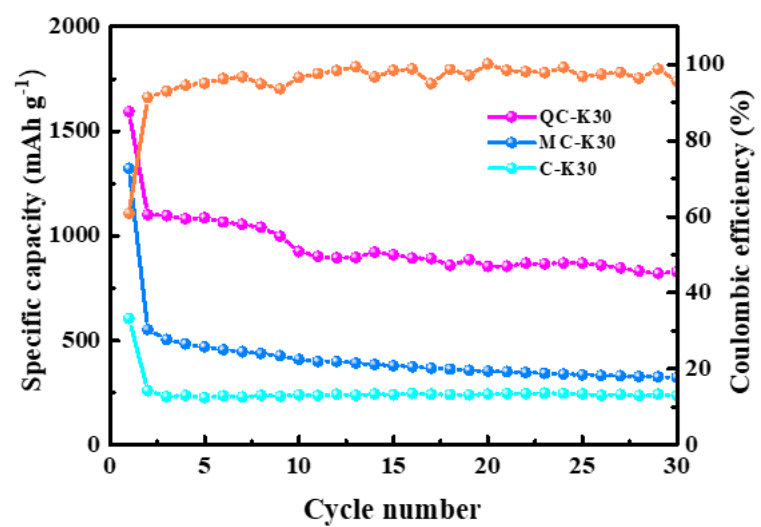


Figure S5 the cycle performance of the C-K30; MC-K30; QC-K30 at 100 mA g⁻¹

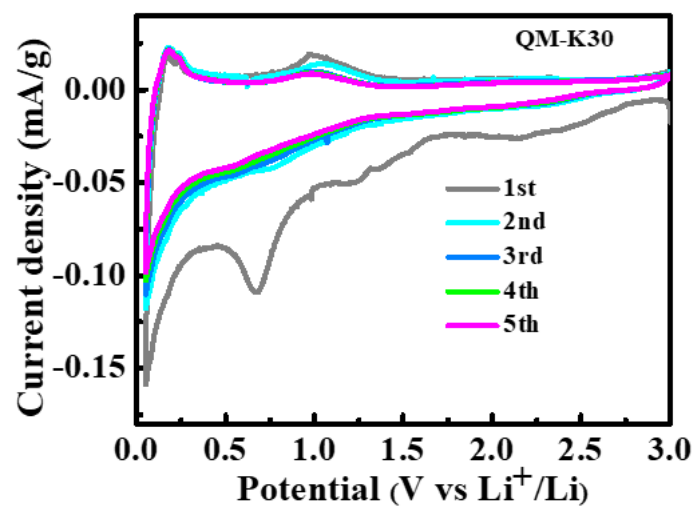


Figure S6 the CV curves of QM-K30 at scan rate of 0.1 mV S^{-1}

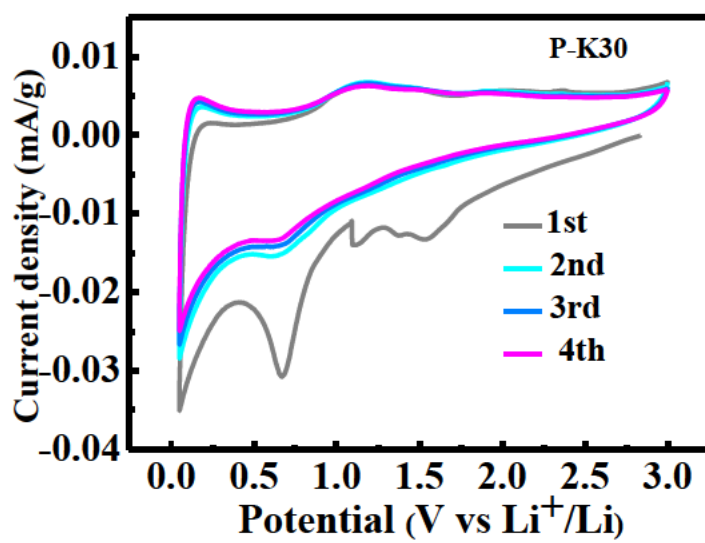


Figure S7 the CV curves of P-K30 at scan rate of 0.1 mV S⁻¹

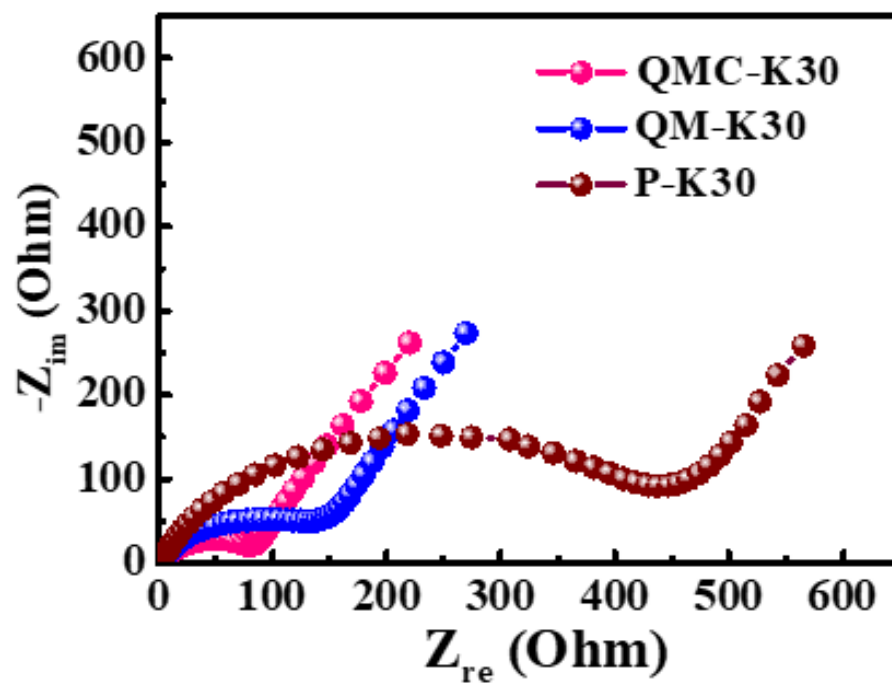


Figure S8 EIS of QMC-K30, QM-K30 and P-K30 before cycling.

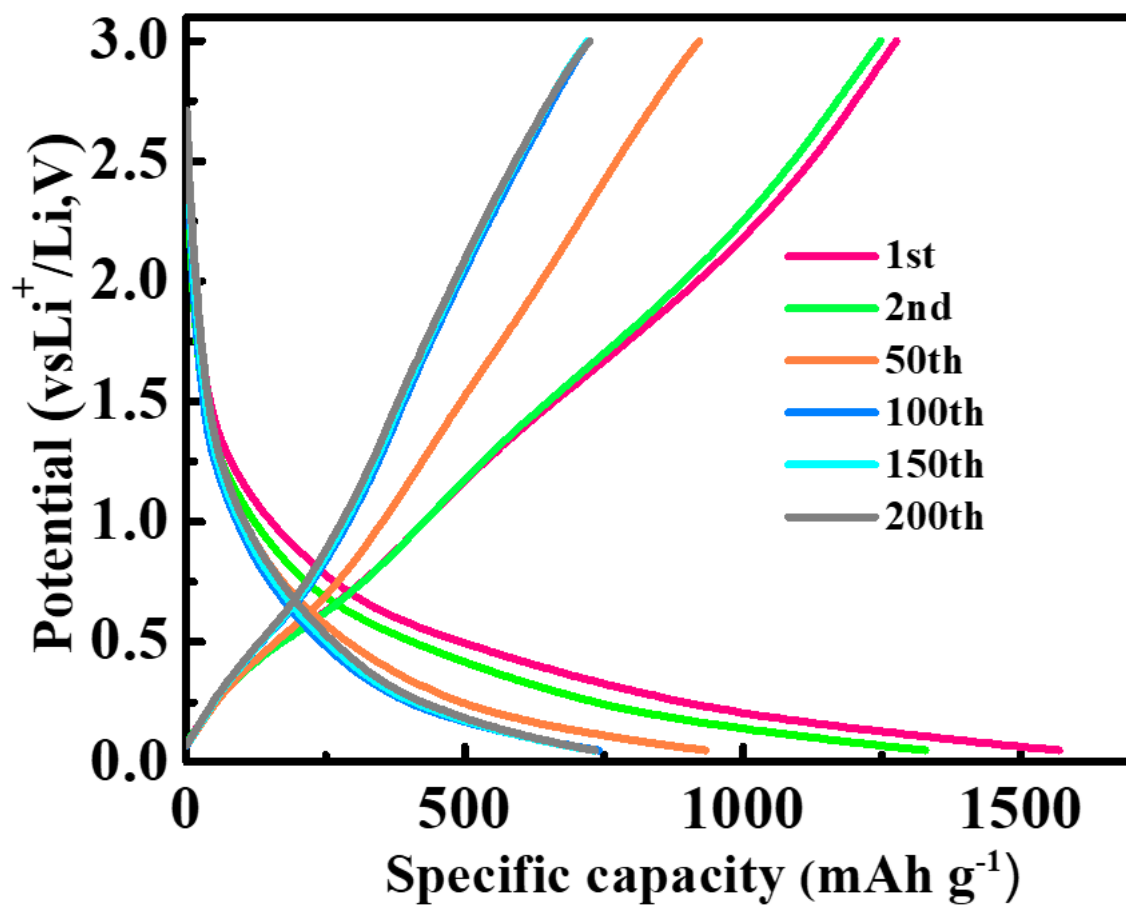


Figure S9 the charge-discharge curves of QMC-K30 at different cycles at 500 mA g⁻¹

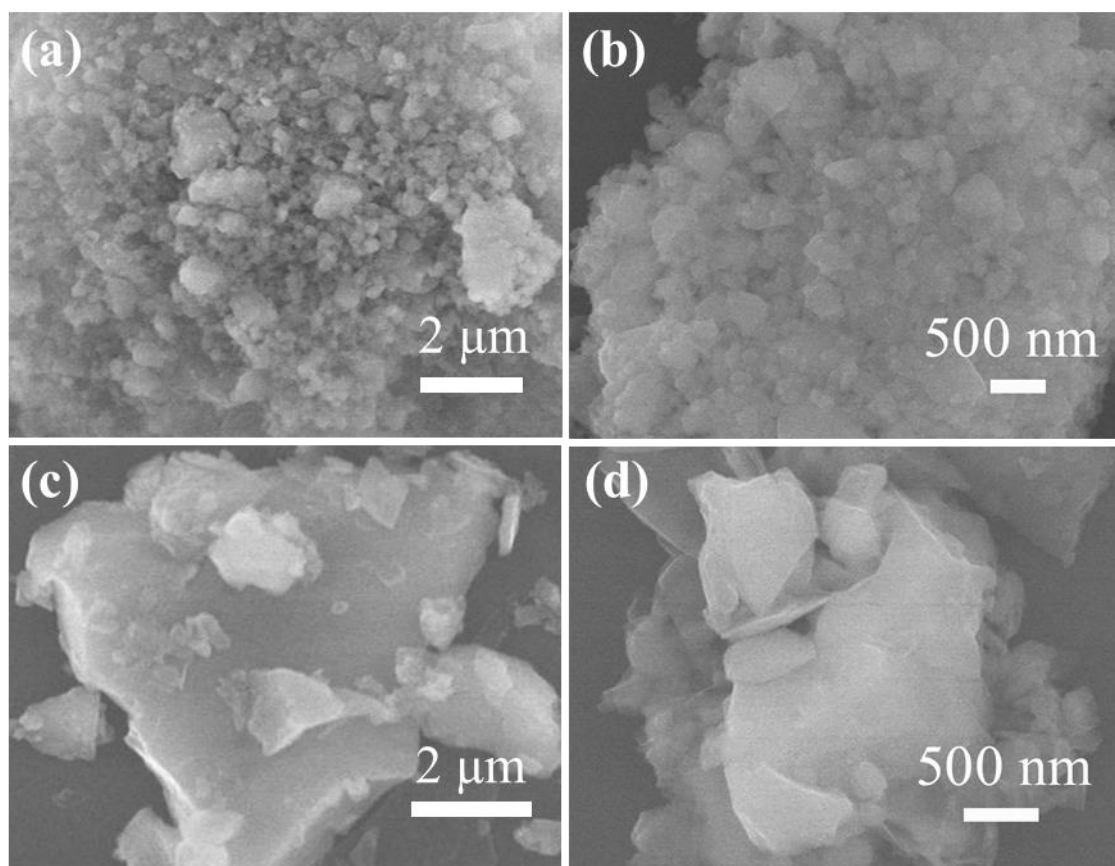


Figure S10 SEM of (a), (b) Milled sand at 400 r/min for 3h; (c), (d) Quenched Sand at 900 °C for 10 times.

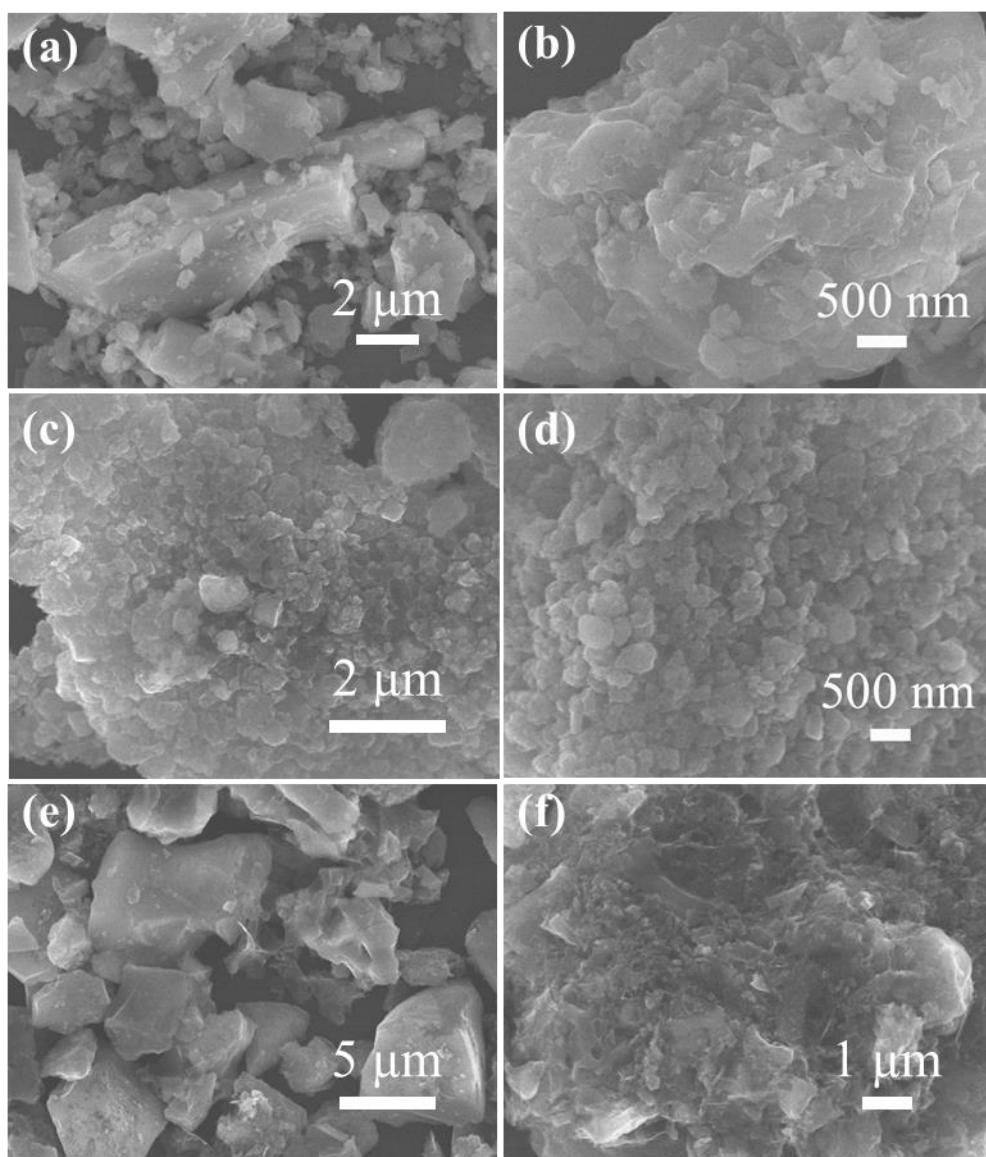


Figure S11 SEM images of (a), (b) C-Sand; (c), (d) MC-Sand; (e), (f) QC-Sand

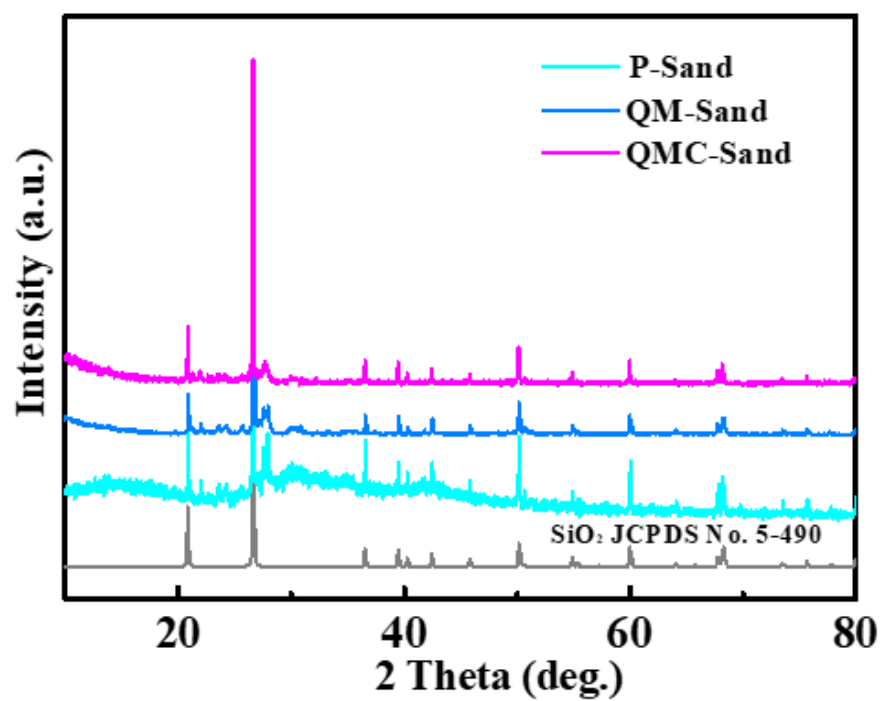


Figure S12 the XRD pattern of the obtained sand

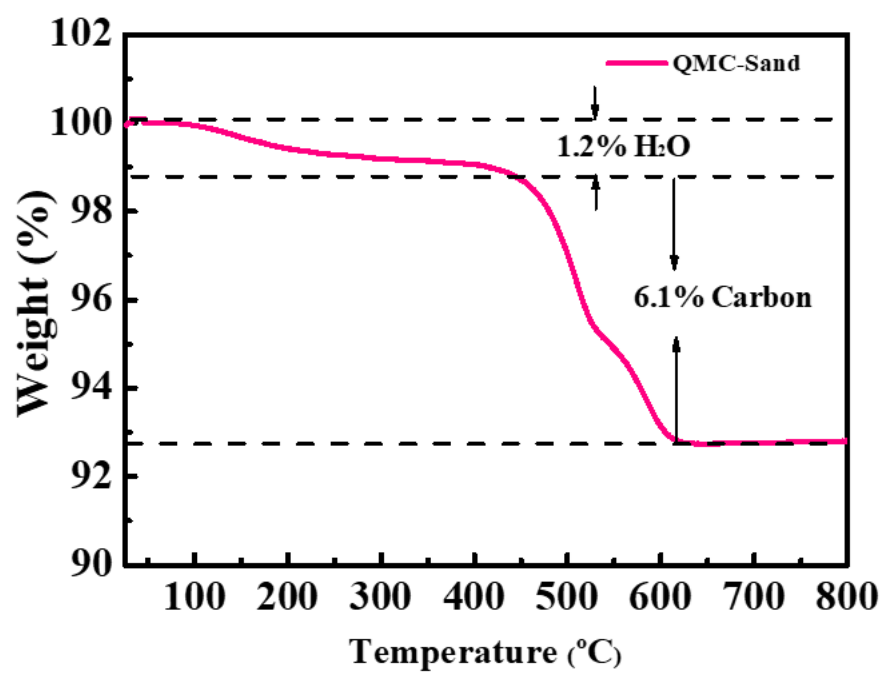


Figure S13 The TGA curves of QMC-Sand

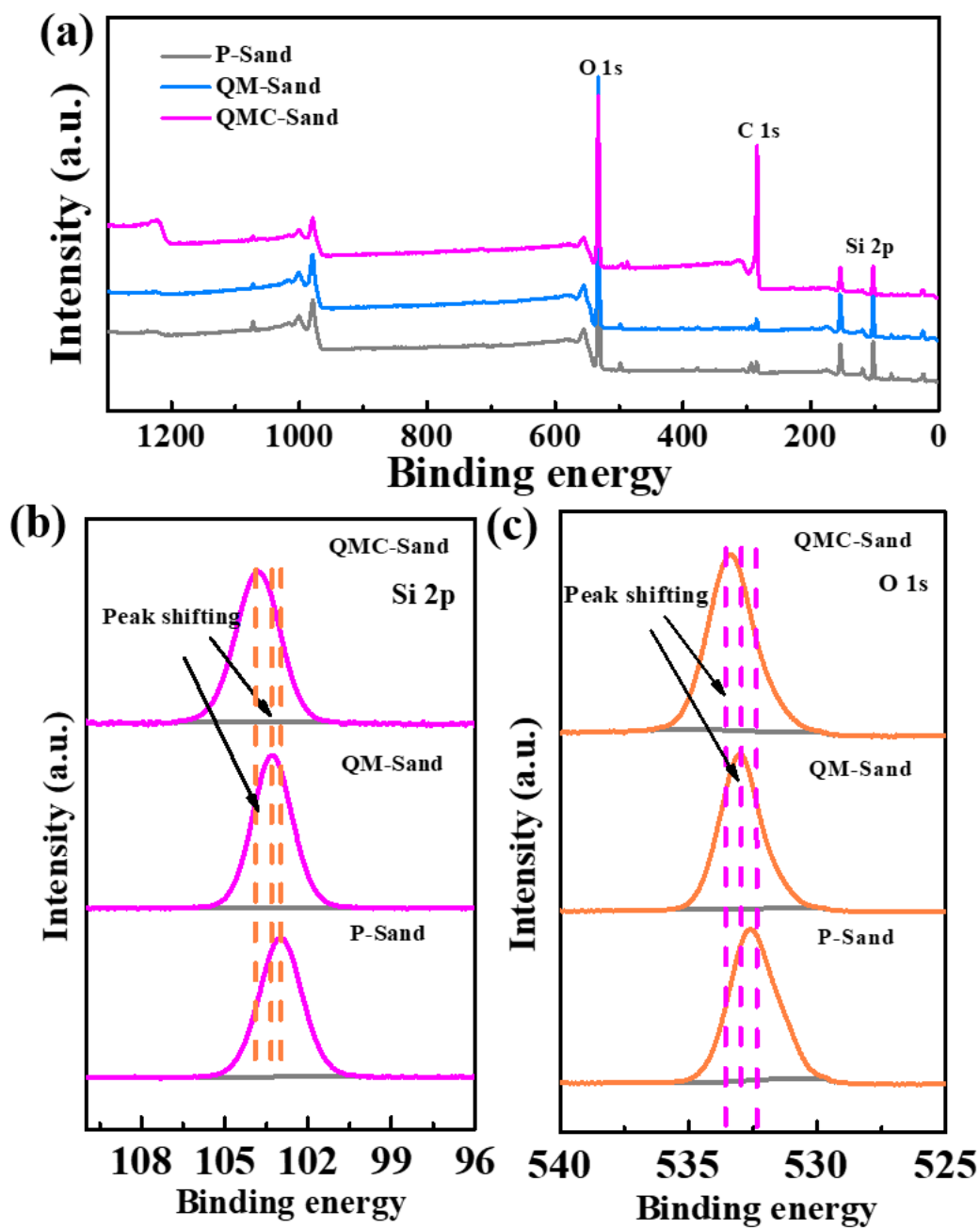


Figure S14 The survey XPS spectra of obtained sand (a); the high-resolution XPS spectra of O1s (b) and Si2p (c).

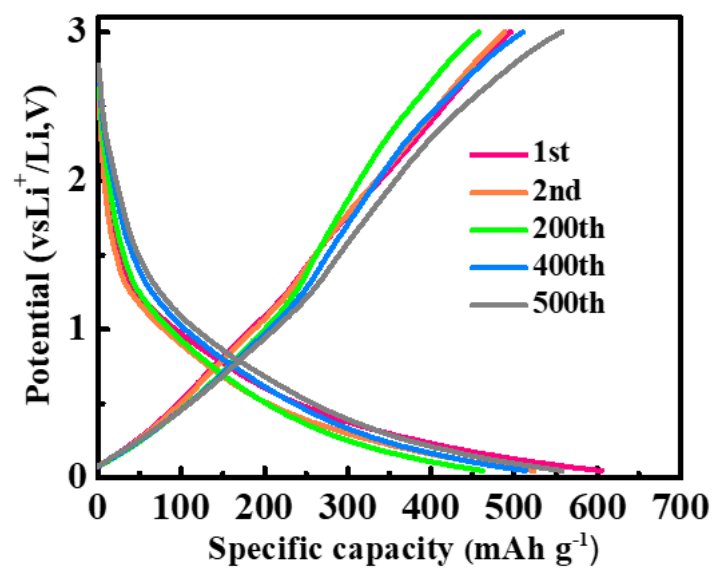


Figure S15 The charge-discharge curves of QMC-Sand at different cycles at 500 mA g⁻¹

Table S1 the component of the obtained K30 from the fluorescence spectrometer

Montmorillonite		Montmorillonite with HCl washing	
SiO ₂	69.58%	SiO ₂	94.18%
Al ₂ O ₃	13.31%	Al ₂ O ₃	0.7%
MgO	3.89%	MgO	0.395%
CaO	1.84%	CaO	0.26%
Fe ₂ O ₃	1.544%	Fe ₂ O ₃	0.71%
K ₂ O	0.385%	K ₂ O	0.28%
Na ₂ O	0.29%	Na ₂ O	0.159%
Substrate	8.99%	Substrate	3.03%

Table S2 the component of the obtained Sand from the fluorescence spectrometer

Natural Sand		Sand with HCl washing	
SiO ₂	64.6%	SiO ₂	93.03%
Al ₂ O ₃	16.18%	Al ₂ O ₃	0.78%
MgO	0.957%	MgO	0.255%
CaO	2.47%	CaO	0.313%
Fe ₂ O ₃	3.334%	Fe ₂ O ₃	0.682%
K ₂ O	4.59%	K ₂ O	0.43%
Na ₂ O	4.18%	Na ₂ O	0.381%
Substrate	2.18%	Substrate	3.25%

CHAPTER 6

CONCLUSIONS AND FUTURE WORK

6.1. GENERAL CONCLUSIONS

Given the current challenges in the development of defect engineering, we successfully developed a series of simple and universal defect preparation methods and constructed a series of defective oxides. Specifically, quenching is a simple and effective strategy to preserve defects at high temperatures in the oxide lattice and this technology is very promising for commercial applications, but the stress change during the quenching process is still worthy of attention, especially the influence on the morphology of the material. For the N-BuLi oxidation-reduction reaction, which is a simple and universal defect preparation strategy at room temperature and the strict experimental operation must be observed considering the high activity and potential safety hazards of n-butyl lithium. Although some limitations still exist, sufficient evidence has shown that defect engineering is able to optimize the intrinsic properties of oxides, and those defect-optimized properties are extremely effective strategies to solve the key issues of Li^+ charge storage in the oxide electrode. The major findings from the research in this thesis can be summarized as follows:

1. Atoms vibrating away from their equilibrium position under high activation energy conditions usually means the formation of defects, which leads to an exponential change in defect concentration with temperature. However, these defects will gradually “heal” completely when a slow cooling process is applied and become ordered crystallinity again. In this work, we took LTO as an example and found that instantly cooling can "solidify" these defects formed at high temperatures, thus retaining a high vacancy concentration in the LTO crystal lattice, also known as the supersaturated defect at room temperature. More importantly, these defects (Li/Ti redistribution and oxygen vacancies) in the LTO lattice contribute additional lithium storage sites and quenched LTO delivers an extraordinary

capacity of 201.7 mAh g⁻¹ in the 1.0-2.5 V charge/discharge range, surpassing the theoretical value of pristine bulk LTO (175 mAh g⁻¹).

2. Defect engineering is usually accompanied by high activation energy, which means that defect preparation usually requires a complicated high-temperature calcination process. In addition, costly reducing agents are usually added in the heat treatment process to help accelerate the formation of defects. In this work, a simple and universal defect preparation strategy is presented through a simple redox reaction at room temperature. The oxygen atoms in oxides including LTO, TiO₂, CeO₂, SnO₂, Sb₂O₅, Nb₂O₅ were captured under the attack of n-butyl lithium, and oxygen vacancies were preserved in these crystal lattices. More importantly, to the best of our knowledge, controllable defect concentration was achieved in this work for the first time by adjusting the reaction time. Defective LTO was selected to study Li⁺ charge storage and shows a highly reversible discharge specific capacity of 109.9 mAh g⁻¹ at a rate of 10 C after 200 cycles even at -10 °C, whereas pristine LTO exhibits a serious irreversible fading capacity.
3. Crystalline SiO₂ is not considered an ideal anode material due to its intrinsic poor electrical conductivity, electrochemical inactivity for inserting lithium, and volume expansion. In this work, we introduce defects into crystalline SiO₂ through quenching and carbon reduction methods to provide suitable electroactive properties for Li⁺ insertion. Specifically, the defect-modified crystalline SiO₂ derived from montmorillonite exhibits a high reversible capacity of 734.8 mAh g⁻¹ at 500 mA g⁻¹ after 200 cycles while defect-modified sand also presents excellent lithium storage performance (558.1 mAh g⁻¹ at 500 mA g⁻¹ after 500 cycles).

6.2. FUTURE WORKS

This thesis focused on the preparation and design of defect engineering based on oxide materials for rechargeable lithium-ion batteries. Although the aims of the defect research in this thesis have been achieved, all the experimental steps were carried out in the laboratory. Further research and expansion of this work to an industrialized scale, including the preparation of defective oxides and the assembly of flexible packaging batteries, are needed to truly realize industrial production and commercialization. These details are summarized as follows:

1. The amount of LTO to be quenched can be expanded to the kilogram level for real application or industrialization and studies of the effect of quenching at a larger scale. In addition, the loading of coated defective LTO powder can be increased to test the actual energy density of the battery in a flexible package.
2. The intrinsic properties of defective oxides, including TiO_2 , CeO_2 , SnO_2 , Sb_2O_5 , Nb_2O_5 should be further studied. It is also worth exploring and studying the application of these defective oxides in other fields, including catalysis, sewage treatment, and energy storage.
3. For crystalline SiO_2 , the low coulombic efficiency resulting from the initial irreversible reaction is a potential challenge, especially for commercial applications. Defect engineering (oxygen vacancy) to lower the oxygen content in SiO_2 is an effective strategy to improve the initial coulombic efficiency, which is because the loss of oxygen in SiO_x ($0 < x < 2$) means the increase of electrochemically active Si phase. However, the lower of X value in SiO_2 will reduce the irreversible matrix of Li_2O and Li_4SiO_4 and in turn, the volumetric expansion stress cannot be effectively released, causing rapid capacity decay. Therefore, the optimal X value of SiO_x ($0 < x < 2$) may require further research to balance the initial coulomb efficiency and stress relief. Apart from the low initial coulomb

efficiency, enhancing SiO₂ conductivity should also be considered to balance electron and Li⁺ migration during the redox process, thereby improving the coulombic efficiency.

4. Commercialized crystalline SiO₂ should be used to replace natural precursors to avoid the influence of other impurities and the role of oxygen vacancies verified. DFT calculations should also be adopted to further theoretical analysis of the mechanism of oxygen vacancies in activating Li intercalation. Considering the low cost of montmorillonite and sand, I believe the replacement trials of the highly electroactive SiO₂-based electrode for commercial silicon anodes and graphite anodes could be conducted for the assembly of flexible packaging batteries. As this is a product with commercial prospects, it is worth exploring the parameters of the assembled commercial soft-package batteries.
5. Furthermore, it would be one step closer to commercialization if we could co-operate with an industrial partner in terms of the large-scale production of electrode materials production and pouch cell testing of the large battery applications.